

Dissertation
submitted to the
Combined Faculties of the Natural Sciences and
Mathematics
of the Ruperto-Carola-University of Heidelberg, Germany
for the degree of
Doctor of Natural Sciences

Put forward by
Mathias Neidig
Born in Bad Friedrichshall
Oral examination: 24.05.2017

Many-Body Pairing in a Two-Dimensional Fermi Gas

Referees:

Prof. Dr. Selim Jochim

Prof. Dr. Markus Oberthaler

Abstract:

This thesis reports on experiments conducted in a single layer, quasi two-dimensional, two-component ultracold Fermi gas in the strongly interacting regime. Ultracold gases can be used to simulate key aspects of more complicated systems like for example cuprates which show high- T_c superconductivity.

The momentum distribution of a sample of bosonic dimers in a quasi-2D square lattice geometry was measured to obtain the coherence properties. For shallow lattices, sharp peaks in the momentum distribution, indicating coherence, were observed at zero momentum as well as at positive and negative lattice momenta along each axis. For deeper lattices, heating impeded the ability to prepare a Mott-insulator.

A spatially resolved radio-frequency spectroscopy was employed for a quasi-2D Fermi gas in the normal phase throughout the BEC-BCS crossover. The interaction induced energy shifts were measured in the strongly interacting region where they can be on the order of the Fermi energy and thus the local resolution is crucial. Furthermore, the onset of pairing in the strongly interacting region was measured as a function of temperature and it was shown that the fraction of free atoms decreases faster than expected from thermal non-interacting theory. At last, the pairing gap was measured using an imbalanced sample. On the BEC side it was found to be in very good agreement with two-body physics as expected. In the strongly interacting regime, however, a deviation from two-body physics indicates that here many-body effects play a role and thus further studies are required.

Zusammenfassung:

Diese Arbeit beschreibt Experimente die in einer einzelnen Lage eines quasi zweidimensionalen, zweikomponentigen ultrakalten Fermi Gas im stark wechselwirkenden Bereich ausgeführt wurden. Ultrakalte Gase können benutzt werden um Schlüsselaspekte komplizierter Systeme wie zum Beispiel Kupraten, welche Hochtemperatursuperleitung zeigen, zu simulieren.

Die Impulsverteilung einer Probe von bosonischen Dimeren in einer quasi-2D quadratischen Gittergeometrie wurde gemessen um die Kohärenzeigenschaften zu bestimmen. Für flache Gitter wurden steile Peaks, die auf Kohärenz hinweisen, in der Impulsverteilung sowohl bei Null-Impuls als auch bei positivem und negativem Gitterimpuls entlang jeder Achse gemessen. Für tiefere Gitter verhinderte Heizen die Präparation eines Mott-Insulators.

Eine orts aufgelöste Radiofrequenz-Spektroskopie wurde für ein quasi-2D Fermi Gas in der normalen Phase im gesamten BEC-BCS Übergangsbereich angewendet. Die durch Wechselwirkung hervorgerufene Energieverschiebung wurde im stark wechselwirkenden Bereich gemessen und gezeigt dass sie auf der Größenordnung der Fermi-Energie liegen kann, was die Ortsauflösung unabdingbar macht. Desweiteren wurde das Einsetzen der Paarung im stark wechselwirkenden Bereich als Funktion der Temperatur gemessen und es wurde gezeigt, dass der Anteil freier Atome schneller abnimmt als von einer thermischen, nicht-wechselwirkenden Theorie hervorgesagt. Als letztes wurde die Paarungslücke mithilfe einer nicht ausgeglichenen Probe gemessen. Auf der BEC-Seite waren die Ergebnisse in sehr guter Übereinstimmung mit der Zwei-Körper Physik. Im stark wechselwirkendem Bereich hingegen wurde eine Abweichung festgestellt die darauf hinweist dass hier Mehrkörperphysik eine Rolle spielt was weitere Untersuchungen rechtfertigt.

Contents

1. Introduction	1
2. Theory	5
2.1. Entering the Quantum Regime	5
2.1.1. Distribution Functions in Harmonic Traps	7
2.2. Tuning the Interactions	13
2.2.1. Elastic Scattering of Ultracold Atoms	14
2.2.2. Feshbach Resonances in Atomic Physics	18
2.3. Strongly Interacting Fermi Gases as a Tunable Many-Body System	22
2.3.1. BKT Transition and the 2D BEC-BCS Crossover	24
2.4. Pairing in the Normal Phase	27
2.5. Particles in Periodic Potentials	29
2.5.1. Non-Interacting Particles and Band Structure	29
2.5.2. The Hubbard Model in Deep Lattices	31
3. Experimental Setup and Tools	35
3.1. Preparation of a Degenerate Quasi-2D Sample	35
3.1.1. Standing Wave Trap (SWT)	39
3.1.2. Lattice	45
3.1.3. Preparation of a ¹³ C-Mixture	46
3.2. Detection of Ultracold Gases	47
3.2.1. Absorption Imaging	48
3.2.2. Experimental Imaging Setup	50
3.2.3. Imaging Calibration	52
3.2.4. Image Composition and Error Estimation	64
3.2.5. Imaging Two Hyperfine States within an Experimental Cycle	69
4. Superfluidity in a Shallow Quasi-2D Square Lattice	73
4.1. Probing the Momentum Distribution of a Strongly Interacting Gas	73
4.2. Observation of a Superfluid in the Quasi-2D Square Lattice	75
4.3. Heating in the Lattice	77
5. Pairing in the Normal Phase of a Quasi-2D Fermi Gas	81
5.1. RF Spectroscopy as a Tool	82
5.1.1. Coherent RF Transitions	83
5.1.2. Incoherent RF Transitions in Interacting Systems	85
5.1.3. Interaction Shifts	86
5.1.4. Lineshape	88
5.1.5. Spatially Resolved RF Spectra	91

5.1.6. The ${}^6\text{Li}$ System	93
5.2. Mean-Field Treatment of the Crossover Region	94
5.3. Experimental Implementation and Methods	98
5.3.1. Data Preparation	98
5.3.2. Tuning the Interaction Strength and Temperature	99
5.3.3. Creating Spin Imbalance	99
5.3.4. Determination of the Free-Free Transition	102
5.3.5. Frequency Resolution	102
5.3.6. Thermometry	104
5.3.7. Atoms in Adjacent Layers	107
5.3.8. Modeling the Spectra	110
5.4. Determination of Initial State Interaction Shifts	112
5.5. Onset of Pairing at High Temperatures in the Crossover Region	119
5.6. Many-Body Pairing above the Critical Temperature	122
6. Conclusion and Outlook	129
A. Appendix	133
A.1. Polylogarithmic Function	133
Bibliography	134

1. Introduction

The discovery of conventional superconductivity at the beginning of the last century [Onn11] as well as the discovery of so-called high- T_c superconductors in cuprates [Bed86, Wu87] have been important technological milestones as they enable to drive currents with zero resistance. In conventional superconductors the critical temperature is on the order of a few Kelvin whereas for the more exotic high- T_c superconductors the critical temperature can reach up to 130 K [Sch93]. Thus, liquid helium has to be used as a cooling agent for conventional superconductors, whereas the much cheaper and easily producible liquid nitrogen can be used for high- T_c superconductors making them potentially a superior alternative in the future¹. Examples for the application of superconductors in technology range from the creation of sensitive SQUID magnetometers to strong magnets which are used in Magnetic Resonance Imaging (MRI) in medicine, for beam-steering in particle accelerators like the Large Hadron Collider (LHC) at CERN or to confine the hot plasma in fusion reactor experiments.

A fascinating aspect of superconductivity in metals as well as in these cuprate systems is that the charge carriers are electrons which are fermionic. Superconductivity, however, is linked to the formation of long range phase coherence which stems from bosonic degrees of freedom. This seemingly paradox was solved in the fifties by Bardeen, Cooper and Schrieffer [Bar57] who showed that electrons with an arbitrarily weak attractive interaction can form so-called 'Cooper' pairs in momentum space which then condense. Hence, superconductivity in fermionic systems is deeply connected to pairing. An intriguing question is whether the pairing and condensation are two distinct phenomena happening at different temperature scales or if they occur simultaneously. Or in other words, how does the superconducting phase emerge from the normal phase?

In conventional superconductors which can be described by weakly coupled BCS theory, the pairing and condensation occur simultaneously. Experiments conducted with high- T_c cuprates, however, have shown a so-called 'pseudogap' region in the normal phase at temperatures $T^* > T_c$ where a multitude of anomalies occur [Joh89, All89, War89, Din96]. These are possibly connected to the superconducting state and thus to fermionic pairing [Che05]. However, a thorough theoretical understanding of this pseudogap region in these cuprates is difficult as their physics is very complex [Nor05, Nor11]. The parent compound of the cuprates is in a Mott-insulating state and the charge carriers themselves are confined to quasi-two dimensional planes and hence additional factors like doping play an integral part.

A common approach in physics to gain understanding of a phenomenon is to study

¹Therefore, technological challenges like the critical current density in these materials have to be solved.

the simplest system where it occurs. For the case of superconductivity/superfluidity² of a fermionic system this is a balanced mixture of interacting spin-up and spin-down fermions. In the lab such a system can be created artificially using ultracold Fermi gases in a trap. Such ultracold atomic systems have emerged in the last two decades as an important tool to simulate quantum systems [Fey82, Blo12]. Neutral atoms can be trapped in optical potentials allowing for a wide array of trapping geometries, ranging from lattice structures to strong anisotropic trapping geometries effectively creating lower dimensional systems. Furthermore, due to the low energies involved in the scattering processes, the atoms can be described as structureless fermions or bosons with a contact potential [Dal98]. Hence, the interaction in the system can be described by a single parameter, the scattering length a which is also tunable via magnetic Feshbach resonances [Ino98]. This simplifies the Hamiltonians in these systems allowing for very good comparability to theoretical predictions.

Although the physics of such a two-component Fermi gas is much less complex than that of the cuprates, it nevertheless shows already a rich phase diagram. At positive scattering lengths, corresponding to repulsive mean-field interactions, the atoms are bound in two-body dimers. As their size is small compared to the inter-particle distance, they can be treated as bosons and thus can undergo a phase transition into a superfluid Bose-Einstein condensate. At negative scattering lengths the mean field interactions are attractive and the system can be described by BCS theory. Here the fermions can form Cooper pairs in momentum space at the critical temperature and condense. As the scattering length can be continuously tuned by applying an external magnetic field, the experimental study of this so-called BEC-BCS crossover transition is possible and has been done extensively for a 3D system [Reg04, Bar04, Chi04, Zwi05, Gre05, Sch08a] as well as for a quasi-2D system [Rie15b, Mur15, Boe16, Fen16, Mit16].

The most powerful technique to study pairing in a Fermi gas is radio-frequency (rf) spectroscopy. Here a radio frequency pulse is applied to the sample to drive a transition from one internal state to a previously unoccupied one. As the rf photon has negligible momentum, the atom momentum is conserved and one obtains insight into the single-particle spectral function $A(\mathbf{k}, \omega)$. Thereby one can observe the energy gap between paired and free atoms. Radio-frequency spectroscopy can be done both momentum resolved, spatially resolved or averaged over the trap and has been applied both for 3D [Chi04, Sch07a, Sch08b, Sch08a, Sch09, Gae10, Sag15] as well as quasi-2D systems [Fel11, Frö11, Bau12, Frö12, Kos12, Som12, Zha12]. Using these techniques first clues of the existence of a pseudogap region both in 3D [Chi04, Gae10, Sag15] as well as in 2D [Fel11] have been measured, however a definite picture has not yet been reached [Nga13, Mar15, Lev15, Mue17].

In this thesis a contribution to this ongoing research is done by investigating a quasi-2D Fermi gas of ${}^6\text{Li}$ using spatially resolved rf spectroscopy. Thereby we can look at the response of locally homogeneous subsystems and disentangle density dependent effects. We measure the interaction induced shifts for balanced mixtures across the crossover region and reduce final state effects by employing two different Fermi mixtures. Furthermore, we measure the onset of pairing in the crossover

²Phenomenologically a superconductor is just a charged superfluid.

region at large temperatures and compare it to expectations of thermal equilibrium physics. At last, we investigate the pairing gap in an imbalanced mixture. On the BEC side where the fermions form deeply bound molecules, a constant pairing gap as a function of temperature was measured in accordance with the two-body binding energy. In the strongly interacting region, a deviation of the pairing gap from the two-body binding energy was observed although a clear temperature dependence as predicted for a pseudogap has not been observed.

Apart from these rf spectroscopy measurements, also a superfluid in a shallow 2D square lattice geometry has been observed during this thesis using a momentum imaging technique. These measurements were our first step towards realizing two-dimensional lattice systems. Although some issues with unresolved heating remain, we aim to realize low entropy two-dimensional systems like e.g. a Mott-insulator of molecules.

Outline

This thesis is organized as follows: chapter 2 provides a brief introduction about the theory of ultracold quantum gases. The ideal Bose and Fermi gas are introduced and the low energy scattering both for two- and three-dimensions is derived. Subsequently the many-body physics of an interacting Fermi gas is explained on the basis of the BEC-BCS crossover and the concept of the pseudogap is introduced. At last, the behavior of particles in periodic potentials is discussed.

In chapter 3 a brief overview over the experimental setup used to produce a single realization of a quasi two-dimensional, two-component ultracold Fermi gas is presented. Next, the detection method using absorption imaging is explained and a detailed description of its calibration is given. In this context also the newly implemented technique to image two spin states in short succession is introduced.

In chapter 4 the experiments conducted in a quasi-2D lattice geometry are discussed. Here the in-situ momentum distribution of the sample is measured using a time-of-flight evolution in a weak harmonic potential. The momentum distribution contains information of the coherence of the system and we observe the system to be in a superfluid state in shallow lattices. For deeper lattices heating was observed which shows up as a loss of coherence.

In Chapter 5 experiments performed using spatially resolved rf spectroscopy in the normal phase of a quasi-2D Fermi gas are discussed. The chapter starts with an introduction to the basics of rf spectroscopy including the effects interactions have on the observed lineshape and transition energies. Next, a qualitative picture of the strongly interacting region by means of a BCS mean-field theory and its implication in rf spectroscopy is given. Then our experimental procedure and the data analysis are presented. At last our results are discussed which include the measurement of the density and interaction dependent energy shifts, the investigation of the onset of pairing at large temperatures in the strongly interacting region and the temperature dependent evolution of the pairing gap both on the BEC side as well as in the strongly interacting regime.

Chapter 6 then concludes with a summary of the results obtained in this thesis and gives an outlook of what we plan to achieve in the future.

2. Theory

The experiments in this thesis are performed with a quasi two-dimensional Fermi gas in the strongly interacting regime. The reduced dimensionality is achieved by confining the sample strongly along one axis, thus effectively suppressing excitations along this dimension. This has similarities to solid state systems like graphene or high- T_c cuprates, where the electron gas is also confined in two-dimensional planes [Nor11, Jos13]. Furthermore, we also conducted experiments where the atoms are in addition subject to an optical lattice in the plane of weak confinement.

This chapter summarizes the main principles needed to understand ultracold atomic systems. It starts in section 2.1 by reviewing the conditions necessary to enter the quantum regime and how there the fundamentally different behavior of bosons and fermions shows up. Furthermore, the density profiles of non-interacting samples in harmonic traps are discussed. Then, in section 2.2 interactions are introduced and the low-energy scattering of atoms both in a 3D and 2D geometry is reviewed. Additionally, the concept of Feshbach resonances as a means to change the interaction strength in the sample is summarized and shown for the explicit case of ^6Li encountered in the experiment. This tunability of the interaction strength can be used to explore superfluid phase transitions in a wide range of parameter regimes. This is embodied in the so-called BEC-BCS crossover which smoothly connects the limit of Bose-Einstein condensation (BEC) of molecular dimers with the BCS limit where many-body Cooper pairs leads to the existence of a pairing gap and hence superfluidity. This crossover is reviewed both for the 3D and 2D case in section 2.3 and the notion of pairing in the normal phase above superfluidity is discussed in section 2.4. At last, the behavior of particles in periodic potentials and the Bose Hubbard-model are presented in section 2.5.

2.1. Entering the Quantum Regime

In classical physics all particles are considered distinguishable. This means that when looking for example at a scattering process between particles, it is possible to keep track of the trajectories of each particle and the system can be described by classical mechanics. This assumption however breaks down when entering the quantum regime. Then identical¹ particles become indistinguishable. This means that when evaluating now e.g. at a scattering process, it is not possible to predict which trajectory each particle took and one now has to take all possibilities into account as shown in Figure 2.1. This is referred to as the superposition principle as one has to add up the different possibilities linearly.

¹Particles are said to be identical if they occupy the same internal state.

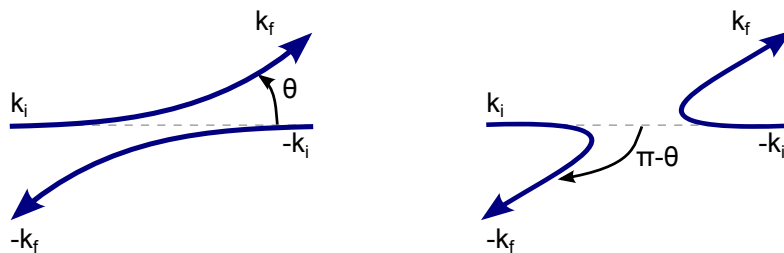


Figure 2.1.: For indistinguishable particles the two scattering processes are equivalent and thus the wave function has to be symmetrized (anti-symmetrized) in the bosonic (fermionic) case. The picture is adapted from [Dal99].

The regime where this happens depends on the system properties. Whereas for example quantum effects can be observed in metals already at room temperature, in ultracold quantum gas systems one has to reach temperatures of the order 100 nK before seeing these effects. This is due to the different densities and thus the interparticle spacing. In physics, each particle can be described by a quantum mechanical wave function. The size of the wave function is of the order of the de Broglie wavelength [Bro23] which is related to the particle momentum p via $\lambda_{\text{dB}} = h/p$. Hence in a thermal gas, the size of the wave function of each particle is approximately

$$\lambda_{\text{dB}} = \frac{h}{\sqrt{2\pi m k_B T}}, \quad (2.1)$$

where h is Planck's constant, m is the mass of the particle and T is the temperature of the system. For macroscopic systems where the mass of the involved particles is large, the size of the wave function is negligible and classical physics can be applied as a limiting case of quantum physics. In microscopic systems, however, the extent of the wave function can become comparable to the interparticle spacing when lowering the temperature. Then, the wave functions overlap and the particles become indistinguishable. As stated earlier, the temperature where this transition occurs depends on the interparticle spacing and hence the density of the system. Since the interparticle spacing scales as $n^{-1/3}$ in three dimensions, one can define the phase-space density $\rho_{3D} = n\lambda_{\text{dB}}^3$ as a parameter to quantify if the system is in the quantum regime.

The indistinguishability of the particles has the consequence that all observables in a system of N particles described by the wavefunction $\Psi(x_1, x_2, \dots, x_N)$ have to remain unchanged when interchanging particles via the operator $P_{i,j}$. This is e.g. applicable for the density of the system which is given by $n = |\Psi|^2$. Mathematically this can be expressed as

$$\begin{aligned} |P_{i,j}\Psi(x_1, \dots, x_i, \dots, x_j, \dots, x_N)|^2 &= |\Psi(x_1, \dots, x_j, \dots, x_i, \dots, x_N)|^2 \\ &= |\Psi(x_1, \dots, x_i, \dots, x_j, \dots, x_N)|^2, \end{aligned} \quad (2.2)$$

where x_i is a representation of both the spatial coordinate as well as internal quantum numbers of each particle [Wen13]. There are two eigenstates of the operator

$P_{i,j}$ with eigenvalues ± 1 . These two eigenstates define two distinct classes of particles depending on if they are symmetric or anti-symmetric under the exchange of particles. This is directly linked to the inherent spin² of a particle [Pau40].

Fermions are particles with half-integer spin. They are the solutions with eigenvalue -1 and transform anti-symmetrically under the interchange of particles. This has far reaching implications on their behavior. Imagine two particles occupying the same state x . Then, according to equation 2.2, $\Psi(x, x) = -\Psi(x, x)$ which can be only fulfilled if $\Psi(x, x) = 0$. Hence two identical fermions can never occupy the same state. This is known as the Pauli exclusion principle [Pau25].

Bosons are particles with integer spin. They are the solutions with eigenvalue $+1$ and behave symmetrically under the exchange of particles. Hence no restriction for the occupation of a single state exists and each state can be occupied by any number of bosons.

In nature, all known constituents of matter like quarks, electrons and neutrinos are fermionic. The force carriers like the photon, graviton or W and Z particles on the other hand are bosonic. Composite particles like neutral atoms can be either fermionic or bosonic depending on the total spin of their components. This can be seen for example in lithium and its two isotopes. ${}^6\text{Li}$ consists of 3 neutrons, 3 protons and 3 electrons which are all fermionic³. Hence the total spin is half-integer and ${}^6\text{Li}$ behaves as a fermion. ${}^7\text{Li}$ on the other hand has 4 neutrons and thus the overall spin is integer, making it behave like a boson. This is of course only valid if the process we are investigating does not resolve the internal structure. In our cold gas experiments, this is valid since the scattering occurs at low energies.

In the following we will now look at an ideal⁴ gas consisting of either bosons or fermions in a harmonic trapping potential like we use them in the experiment. The derivations can be found in many textbooks (e.g. [Lan81, Fet03]) and we will follow the reasoning along the lines in [Wen13]. The analysis is done here both for the 3D and the 2D case. Interactions and their implications to the observed physics are then introduced later in this chapter in section 2.2 and 2.3.

2.1.1. Distribution Functions in Harmonic Traps

In experiments, one often deals with large systems consisting of thousands of atoms. There it is justifiable to assume the thermodynamic limit of large particle numbers and use statistical mechanics [Lan96, Sch00, Fet03] to obtain insights about the system. The system can then be described as a grand canonical ensemble with a volume V , the chemical potential μ and the temperature T . The chemical potential μ fixes the particle number N and can be thought of as the energy required to add a particle at a fixed entropy and volume. In bosonic systems, adding a particle increases the entropy and thus according to the definition of the chemical potential one has to take energy out of the system in order to satisfy the fixed entropy restriction, leading to the condition $\mu \leq 0$. For fermionic systems, however, due to the Pauli principle

²The spin of a particle is given in units of the Planck constant h . This is always implied when talking about particle spin in this thesis.

³Protons and neutrons consist of 3 quarks each and are themselves fermionic.

⁴This means that no interactions are considered.

2.1. Entering the Quantum Regime

$\mu > 0$ is possible since e.g. at $T = 0$ all the lowest energy levels are occupied by a single particle and hence putting a particle at the next lowest unoccupied state does not increase the entropy but costs energy. The expected mean occupation number $\langle n \rangle$ of particles in each discrete energy state E_i is then given via the Bose-Einstein and Fermi-Dirac distribution functions as

$$f_{\text{boson}} \equiv \langle n \rangle_{\text{boson}} = \frac{1}{e^{\beta(E_i - \mu)} - 1} \quad \text{and} \quad f_{\text{fermion}} \equiv \langle n \rangle_{\text{fermion}} = \frac{1}{e^{\beta(E_i - \mu)} + 1}, \quad (2.3)$$

where $\beta = 1/(k_B T)$. Since the exponential function is strictly positive, one can already see that for fermions the Pauli exclusion principle is fulfilled since $f_{\text{fermion}} \leq 1$. In the case of bosons the behavior is different. We can set the ground state energy $E_0 = 0$ without loss of generality. To avoid the unphysical behavior $f_{\text{boson}} < 0$, we can see that the chemical potential has to be $\mu \leq 0$ as discussed above. This implies a striking difference at low temperatures $T \rightarrow 0$ as depicted in Figure 2.2 for particles in a harmonic oscillator. Whereas for bosons all particles occupy the lowest state, for fermions each state is occupied only by a single fermion up to the Fermi energy E_F . Despite their different quantum statistics, both distribution functions should converge into the classical Maxwell-Boltzmann distribution at large temperatures. In this limit, the exponential function dominates and the second term ∓ 1 in the denominator in equation 2.3 can be neglected. One then obtains the thermal distribution function

$$f_{\text{th}} = e^{-\beta(E_i - \mu)}. \quad (2.4)$$

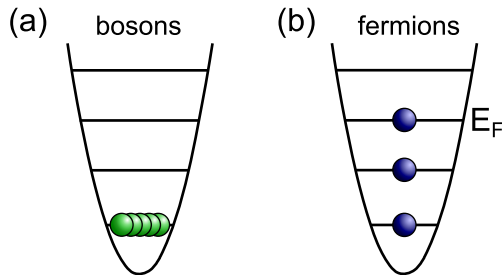


Figure 2.2.: The ground state of a few particle system at $T \rightarrow 0$ in a harmonic potential is shown. In the bosonic case all particles occupy the lowest state (a). In the fermionic case the Pauli exclusion principle forbids this and each state is only occupied by a single fermion up to the Fermi energy E_F . Taken from [Wen13].

From the distribution functions one can then obtain the density distribution $n(\mathbf{r})$ in a harmonic trap. This is of importance as it can be measured in experiments using e.g. absorption imaging techniques. Hence knowledge of the expected distribution lets one infer many properties like the temperature, particle number or others. In a three-dimensional geometry the spatial coordinates and of the particles and their momenta are given as vectors \mathbf{r} and $\mathbf{p} = \hbar\mathbf{k}$ where \mathbf{k} is the wave vector. The

trapping potential $V_{\text{trap}}(\mathbf{r})$ in terms of the harmonic trapping frequencies ω_i is then given as

$$V_{\text{trap}}(\mathbf{r}) = \frac{1}{2}m(\omega_x x^2 + \omega_y y^2 + \omega_z z^2). \quad (2.5)$$

In such a system, the energies of the single-particle levels $\alpha = \{n_x, n_y, n_z\}$ are given by [Sch07b]

$$E_{n_x, n_y, n_z} = \hbar \sum_{\alpha} \omega_{\alpha} \left(n_{\alpha} + \frac{1}{2} \right). \quad (2.6)$$

Hence the spacing between energy levels is given by the harmonic trap frequencies ω_i . In most cases, the thermal energy $k_B T$ is much larger than the level spacing, making a semi-classical approach viable. One then replaces the single-particle levels E_i by the classical Hamiltonian $H = \frac{\hbar^2 k^2}{2m} + V_{\text{trap}}(\mathbf{r})$ to evaluate the quantum statistical distribution functions and performs an integral over the six dimensional phase-space $\{\mathbf{r}, \mathbf{k}\}$ instead of a sum over the discrete levels E_i . In a system of N particles, the chemical potential μ is then defined via

$$N = \frac{1}{(2\pi\hbar)^3} \int d\mathbf{r} d\mathbf{k} f(\mathbf{r}, \mathbf{k}), \quad (2.7)$$

where $1/(2\pi\hbar)^3$ is the density of states per unit volume. The real-space density distribution is then given by

$$n(\mathbf{r}) = \frac{1}{(2\pi\hbar)^3} \int d\mathbf{k} f(\mathbf{r}, \mathbf{k}). \quad (2.8)$$

For a thermal gas, this results in a density profile

$$n_{\text{th}}(\mathbf{r}) = \frac{N}{(2\pi)^{3/2} \sigma_x \sigma_y \sigma_z} e^{-\left(\frac{1}{2} \sum_i x_i^2 / \sigma_i^2\right)}, \quad \text{where } \sigma_i^2 = \frac{k_B T}{m\omega_i^2}. \quad (2.9)$$

Hence for non-degenerate, non-interacting systems one can directly infer the particle number and temperature by fitting a Gaussian profile to the measured density distribution if one knows the trap parameters ω_i . The assumption of a non-interacting thermal gas is also often used in the wings of the trap where the density and thus interactions are small.

Ideal Bose Gas

To obtain the density distribution of the thermal gas, we made the assumption that we can replace the discrete sum over all energy levels by an integral over the phase space. However, as we have already discussed above the ground state in a Bose gas gets macroscopically occupied for $T \rightarrow 0$. Hence it makes sense to treat the ground state separately from the rest of the states. We can then rewrite equation 2.7 as

$$N = N_0 + N_{\text{exc}} = N_0 + \frac{1}{2(\hbar\bar{\omega})^3} \int_0^{\infty} dE \frac{E^2}{\exp[\beta(E - \mu)] - 1}, \quad (2.10)$$

where we introduced the density of states $g_{3D}(E) = \frac{E^2}{2(\hbar\bar{\omega})^3}$ with the mean trapping potential $\bar{\omega} = (\omega_x\omega_y\omega_z)^{1/3}$. Evaluating the integral in equation 2.10, the number of atoms in the excited state is given by

$$N_{\text{exc}} = \left(\frac{k_B T}{\hbar\bar{\omega}}\right)^3 Li_3\left(\exp\left[\frac{\mu}{k_B T}\right]\right), \quad (2.11)$$

where $Li_3(z)$ is the polylogarithmic function as defined in Appendix A.1. At large temperatures the occupation of the ground state is negligible and $N = N_{\text{exc}}$ holds. The critical temperature T_c where the macroscopic occupation of the ground state sets in is then given at the point where $\mu = 0$. At this point $N_0 = 0$ and we can set $N_{\text{exc}} = N$. Plugging this into equation 2.11 then leads to

$$k_B T_c = \hbar\bar{\omega} \left(\frac{N}{Li_3(1)}\right)^{\frac{1}{3}} \approx 0.94 (\hbar\bar{\omega}) N^{\frac{1}{3}}, \quad (2.12)$$

where the relation $Li_3(1) \approx 1.202$ was used. For temperatures $T < T_c$, the ground state population N_0 then grows as

$$\frac{N_0}{N} = 1 - \left(\frac{T}{T_c}\right)^3. \quad (2.13)$$

This phase transition is called Bose-Einstein condensation (BEC) and was first observed in 1995 [And95, Dav95].

In accordance to the derivation of the density distribution of the thermal gas in equation 2.9, we can also derive an expression for the uncondensed part of a Bose gas as

$$n_{\text{B,th}}(\mathbf{r}, T) = \frac{1}{\lambda_{\text{dB}}^3} Li_{3/2}\left(\exp\left[\frac{\mu - V_{\text{trap}}(\mathbf{r})}{k_B T}\right]\right). \quad (2.14)$$

Compared to the thermal Gaussian profile, the polylogarithmic function has an increased weight at the center. This is often referred to as bosonic enhancement in the literature. Hence at temperatures $T < T_c$, the gas can be described as the sum of a condensed part $n_{\text{B},0}(\mathbf{r})$ and a thermal part $n_{\text{B,th}}(\mathbf{r})$. From the density profile $n_{\text{B,th}}(\mathbf{r})$ in equation 2.14 we can also infer the maximum phase space density before condensation occurs to be $\rho_{3D,\text{max}} = Li_{3/2}(1) \approx 2.612$. The phase transition into a BEC is also accompanied by spontaneous symmetry breaking. This means that the condensate part can be described by an effective single particle wave function $\hat{\Psi}_0(\mathbf{r}) = \sqrt{n_0(\mathbf{r})}e^{i\phi}$ with a spontaneously chosen constant phase ϕ . One can define the first order correlation as [Had11]

$$g_1(\mathbf{r}_0 + \mathbf{r}, \mathbf{r}_0) = \frac{\langle \hat{\Psi}^\dagger(\mathbf{r}_0 + \mathbf{r}) \hat{\Psi}(\mathbf{r}_0) \rangle}{\langle \hat{\Psi}^\dagger(\mathbf{r}_0 + \mathbf{r}) \rangle \langle \hat{\Psi}(\mathbf{r}_0) \rangle}, \quad (2.15)$$

where $\hat{\Psi}^\dagger(\mathbf{r}), \hat{\Psi}(\mathbf{r})$ are the creation and annihilation operators for a particle at position \mathbf{r} . Inside the condensate, the phase is constant and $g_1(\mathbf{r}) = 1$. Hence there is no decay of first order correlations and the condensate has true long range order

resulting in a superfluid phase. This has to be contrasted to the case of a thermal gas where the first order correlation decays exponentially on a length scale given by the thermal de-Broglie wavelength λ_{dB}^5 and thus only short-range phase correlations exist.

2D Case

In a two-dimensional system, there exists no BEC for a homogeneous system at finite temperature. This has been shown on general grounds by Mermin and Wagner in the sixties [Mer66, Hoh67]. This can be understood when deriving the 2D density $n_{\text{B,th}}^{2\text{D}}$ in analogy to equation 2.8 via

$$n_{2\text{D}}(\mathbf{r}) = \frac{1}{(2\pi\hbar)^2} \int d\mathbf{k} f(\mathbf{r}, \mathbf{k}). \quad (2.16)$$

This then yields for a homogeneous 2D Bose gas

$$n_{\text{B,th}}^{2\text{D}} = -\frac{1}{\lambda_{\text{dB}}^2} \ln\left(1 - e^{\frac{\mu}{k_{\text{B}}T}}\right). \quad (2.17)$$

It can be seen that for all finite densities there exists a $\mu < 0$ such that the equation is fulfilled. Hence no phase transition into a BEC exists in a homogeneous 2D system. This can be attributed to the increase in thermal fluctuations in two dimensions which destroy long range phase coherence for non-zero temperatures⁶.

However, in 2D there exists another mechanism for a transition into a superfluid topologically ordered phase. This is the famous Berenzinskii-Kosterlitz-Thouless (BKT) phase⁷ [Ber72, Kos73] which relies on the ordering of thermally excited vortex and anti-vortex pairs in the system. We will talk about this phase later in more detail in section 2.3.1 when we discuss the BEC-BCS crossover in a two-dimensional Fermi mixture.

Ideal Fermi Gas

In a fermionic system the behavior is very different compared to the bosonic case due to the Pauli principle. In the case of a harmonic trapping potential in three dimensions at zero temperature, the particles occupy the lowest energy levels one by one up to the Fermi energy $E_{\text{F}} \equiv \mu(T = 0, N)$. Using the density of states approach in equation 2.10 together with the normalization in equation 2.7 then yields

$$N = \frac{1}{2(\hbar\bar{\omega})^3} \int_0^{E_{\text{F}}} dE E^2 = \frac{E_{\text{F}}^3}{6(\hbar\bar{\omega})^3} \text{ or } E_{\text{F}} = (6N)^{1/3} \hbar\bar{\omega}. \quad (2.18)$$

The Fermi energy can be interpreted as the natural energy scale of the system and an indicator if the system is in the quantum regime. Therefore it is useful to define

⁵For typical experimental parameters this length scale is approximately a few μm .

⁶In a homogeneous 2D system there is still a BEC possible at $T = 0$.

⁷For their ground-breaking work, both J. M. Kosterlitz and D. J. Thouless were awarded with the Nobel prize of physics in 2016.

the Fermi temperature T_F , Fermi momentum p_F , Fermi wavevector k_F and Fermi radii $x_{i,F}$ as

$$E_F = k_B T_F = \frac{p_F^2}{2m} = \frac{\hbar^2 k_F^2}{2m} = \frac{1}{2} m \omega_i^2 x_{i,F}^2. \quad (2.19)$$

For homogeneous systems, the Fermi energy can also be directly derived from the spatial density $n_{3D}(\mathbf{r})$ as

$$E_{F,3D} = \frac{\hbar^2}{2m} (6\pi^2 n_{3D})^{2/3}. \quad (2.20)$$

This is useful in experiments where one can infer from the measured local density a local Fermi energy under the assumption that the potential varies smoothly such that one can treat the gas locally as a homogeneous system and that no long range order exists. This is referred to as the local density approximation (LDA).

Quantum effects start to play a role when the Fermi distribution f_{fermion} starts to deviate from the thermal Boltzmann distribution f_{th} which usually happens when the relative temperature T/T_F becomes of the order of 1. The real space density distribution $n_F(\mathbf{r}, T=0)$ can be again obtained from equation 2.8 when using the chemical potential $\mu = E_F$ as

$$n_F(\mathbf{r}, T=0) = \frac{8N}{\pi^2 x_F y_F z_F} \left(1 - \sum_{i=x,y,z} \frac{x_i^2}{x_{i,F}^2} \right)^{3/2}. \quad (2.21)$$

For temperatures $T > 0$, one can also derive a general expression for the spatial density $n_F(\mathbf{r}, T)$ given by

$$n_F(\mathbf{r}, T) = -\frac{1}{\lambda_{\text{dB}}^3} Li_{3/2} \left(-\exp \left[\frac{\mu - V_{\text{trap}}(\mathbf{r})}{k_B T} \right] \right). \quad (2.22)$$

In order to make statements about how the density profile changes when reaching the quantum degenerate limit, we have to know μ as a function of T/T_F . This can be achieved using the normalization condition in equation 2.7 and the definition of E_F in equation 2.19 which leads to the implicit definition of the chemical potential as

$$Li_3 \left(-\exp \left[\frac{\mu}{k_B T} \right] \right) = -\frac{1}{6 (T/T_F)^3}. \quad (2.23)$$

Solving this equation numerically as done e.g in [Wei09], we can plot the density profile for different T/T_F as can be seen in Figure 2.3. One can see that there is no significant change from a thermal distribution when entering the quantum degenerate regime $T/T_F < 1$. Only for temperatures $T/T_F \ll 1$ we see deviations in the wing of the cloud and at the center which come from the polylogarithmic function. This makes thermometry in ultracold Fermi gases challenging as the information about the temperature is encoded mostly in the wing of the cloud where the signal strength is weak.

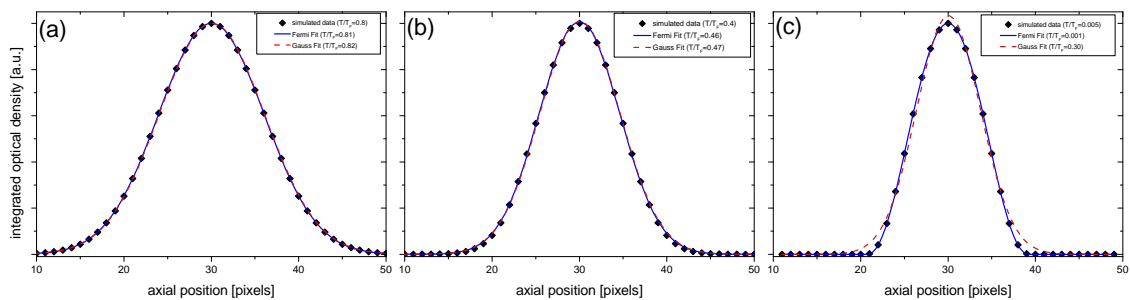


Figure 2.3.: The simulated doubly integrated density distribution of a harmonically trapped ideal Fermi gas is shown for temperatures $T/T_F = 0.8$ (a), $T/T_F = 0.4$ (b) and $T/T_F = 0.005$ (c) is compared to a Fermi fit (blue line) or Gaussian fit (red dashed line) respectively. For temperatures down to $T/T_F \geq 0.4$ both fits provide the same temperature and the density profiles show no deviation from the thermal Gaussian profile. Only for $T/T_F \ll 1$ we see a clear deviation which is mostly pronounced in the wings of the cloud. Adapted from [Wen13].

2D Case

In analogy to the 3D case, the Fermi energy of an ideal 2D Fermi gas can be obtained by solving equation 2.16 for $T = 0$. This results in the Fermi energy $E_{F,2D}$:

$$E_{F,2D} = \frac{\hbar^2}{2m} 4\pi n_{2D}. \quad (2.24)$$

Hence in a two-dimensional gas the Fermi energy is proportional to the density. The density distribution $n_{F,2D}(\mathbf{r})$ of a harmonically trapped 2D Fermi gas can again be obtained by integrating out equation 2.16 using the Fermi-Dirac distribution. This yields

$$n_{F,2D}(\mathbf{r}, T) = \frac{1}{\lambda_{dB}^2} \ln \left(1 + e^{\frac{\mu - V_{\text{trap}}(\mathbf{r})}{k_B T}} \right). \quad (2.25)$$

Similar to the 3D case the profile resembles again a thermal Gaussian profile down to temperatures of the order $T/T_F \sim 0.5$. This makes thermometry also in 2D systems a challenge as the relevant region for the temperature extraction is in the low-density wing where the signal is small.

2.2. Tuning the Interactions

So far we only considered non-interacting systems. Although this makes the description of these system pretty straightforward, it does not capture the physical world which relies on interactions. In ultracold atomic systems, due to a lack of charged particles, these interactions are short-range which simplifies the physics again. Theoretically, the interaction of particles at low energies can be modeled by contact pseudo-potentials and all the scattering properties can be captured by a single parameter, the scattering length a .

In this section, the derivation for the scattering length both in three- and two-dimensional systems is summarized. In addition the tunability of the scattering via so-called Feshbach resonances is explained and the special case of ${}^6\text{Li}$ used in our experiment is highlighted. The existence of a Feshbach resonance comes along with a universal bound dimer state and thus allows to effectively change the system from bosonic dimers to free fermionic atoms in Fermi mixture experiments.

2.2.1. Elastic Scattering of Ultracold Atoms

In typical ultracold atom experiments, the samples are dilute and due to the short range nature of the interaction only two-body collisions have to be considered. Because of the low energies involved, this scattering can then be described by a single parameter, the scattering length $a_{3\text{D}}$ ⁸. The derivation of $a_{3\text{D}}$ can be found in many textbooks (e.g. [Sak10, Bra03]) and will be sketched out in the following:

At low energies, the elastic scattering of two non-identical particles can be described in a non-relativistic framework by the stationary Schrödinger equation for the relative coordinates as

$$\left[-\frac{\hbar^2}{2m_r} \nabla^2 + V_{\text{int}}(r) - E_k \right] \psi_{\mathbf{k}}(\mathbf{r}) = 0, \quad (2.26)$$

where $m_r = \frac{m_1 m_2}{m_1 + m_2}$ is the reduced mass, $\mathbf{r} = \mathbf{r}_1 - \mathbf{r}_2$ is the relative distance between atoms at \mathbf{r}_1 and \mathbf{r}_2 , $V_{\text{int}}(r)$ is the spherically symmetric potential mediated by the van der Waals force between the atoms and $E_k = \hbar^2 \mathbf{k}^2 / (2m_r)$ is the energy of the eigenstate $\psi_{\mathbf{k}}$ with a well-defined wave vector \mathbf{k} . Due to the fast drop off of the van der Waals force as r^{-6} , the potential can be considered to have a finite range r_{eff} . For distances $r \gg r_{\text{eff}}$, the wave function then satisfies the free-space Schrödinger equation and can be written as the sum of an incoming plane wave e^{ikz} and an outgoing spherical wave e^{ikr}/r as

$$\psi_{\mathbf{k}}(\mathbf{r}) \propto e^{ikz} + f_{\mathbf{k}}(\theta) \frac{e^{ikr}}{r}. \quad (2.27)$$

Here the incoming particles are assumed to have momentum along the z -axis and $f_{\mathbf{k}}(\theta)$ is the scattering amplitude which only depends on the polar angle θ due to the symmetry of the system. From the scattering amplitude one can then obtain both the differential and total cross section as

$$\frac{d\sigma_{\mathbf{k}}}{d\Omega} = |f_{\mathbf{k}}(\theta)|^2 \text{ and } \sigma_{\mathbf{k},\text{tot}} = \int_{\Omega} |f_{\mathbf{k}}(\theta)|^2 d\Omega, \text{ where } 0 \leq \theta < \pi. \quad (2.28)$$

So far the derivation assumed non-identical particles. For identical particles, however, one cannot differentiate between certain scattering events as depicted in Figure 2.1. Hence the wave function has to be correctly symmetrized (anti-symmetrized) for the bosonic (fermionic) case which leads to differential cross sections of

$$\left(\frac{d\sigma_{\mathbf{k}}}{d\Omega} \right)_{\text{bosons}} = |f_{\mathbf{k}}(\theta) + f_{\mathbf{k}}(\pi + \theta)|^2 \quad (2.29)$$

⁸We explicitly introduce the scattering length here as $a_{3\text{D}}$ to emphasize that we will later deal with lower dimensional systems.

for identical bosons and

$$\left(\frac{d\sigma_{\mathbf{k}}}{d\Omega}\right)_{\text{fermions}} = |f_{\mathbf{k}}(\theta) - f_{\mathbf{k}}(\pi + \theta)|^2 \quad (2.30)$$

for identical fermions.

As an ansatz to obtain the scattering amplitude, one can expand the wave function into a series of Legendre polynomials as

$$\psi_{\mathbf{k}}(r, \theta) = \sum_{l=0}^{\infty} R_{l,\mathbf{k}}(r) P_l(\cos \theta). \quad (2.31)$$

Plugging this ansatz into equation 2.26 then separates it into a radial and a spherical part. In the limit $r \gg r_{\text{eff}}$ the solutions for $R_{l,\mathbf{k}}$ are identical with the free-space solutions apart from phase shifts $\delta_{l,\mathbf{k}}$ which scale as k^{2l+1} . Hence at large scales the only effect elastic collisions have is introducing a phase shift in the wave function. The scaling of $\delta_{l,\mathbf{k}}$ can be interpreted as the centrifugal barrier. For angular momenta $l > 0$, the introduced phase shifts only become relevant if the energy of the incoming particles lies above the centrifugal barrier E_c . Otherwise collisions only occur in the isotropic s-wave ($l = 0$) channel. In ${}^6\text{Li}$ this centrifugal barrier is on the order of $T \sim 7$ mK and thus we only have to consider s-wave interactions in our experiments. Therefore the scattering amplitude is isotropic and can be expressed as [Sak10]

$$f_{\mathbf{k},l=0} = \frac{1}{k \cot \delta_0 - ik}. \quad (2.32)$$

Since s-wave scattering is independent of the polar angle θ this leads together with equations 2.29 and 2.30 to the fact that low-energy scattering is enhanced for identical bosons and non-existent for identical fermions resulting in the fact that identical fermions are non-interacting at low energies. Hence when working with a fermionic system, one has to either use different internal states or different species to have interactions present.

The scattering amplitude thus only depends on the wave vector k and the phase shift δ_0 and it is possible to describe the whole scattering process by a single parameter, the scattering length $a_{3\text{D}}$. This can be achieved by expanding $k \cot \delta_0$ in k as

$$k \cot \delta_{0,\mathbf{k}} = -\frac{1}{a_{3\text{D}}} + \frac{1}{2} r_{\text{eff}} k^2 + \mathcal{O}(k^4) \quad (2.33)$$

which leads to

$$a_{3\text{D}} \xrightarrow{k \rightarrow 0} -\frac{\tan \delta_0}{k} \quad (2.34)$$

in the case of $kr_{\text{eff}} \ll 1$ which is usually fulfilled in ultracold atom experiments as r_{eff} is identical to the van der Waals range r_{vdW} up to a numerical factor on the order of 1. This leads to a total scattering cross section of

$$\sigma_{\mathbf{k},\text{tot}} = \frac{4\pi a_{3\text{D}}^2}{1 + k^2 a_{3\text{D}}^2} \quad (2.35)$$

for the case of non-identical particles. In the limit of weak interactions $ka_{3\text{D}} \ll 1$ the total cross section becomes energy independent with $\sigma_{\mathbf{k},\text{tot}} = 4\pi a_{3\text{D}}^2$. Hence the

scattering length directly gives a measure for the strength of interactions. In the limit of strong interactions $ka_{3D} \gg 1$ the total cross section reduces to $\sigma_{k,\text{tot}} = 4\pi/k^2$ and is thus explicitly energy dependent. This is also called the unitary regime. In a fermionic system, the typical momentum scale is given by the Fermi momentum k_F and thus $1/k_F a_{3D}$ can be used to describe the scattering strength. For $|1/k_F a_{3D}| \ll 1$ one is in the strongly interacting regime and the Fermi energy E_F becomes the only relevant length scale. Here all relevant system properties are characterized by the Fermi energy E_F rescaled by numerical factors [Car03, Ku12]. On the other hand for $|1/k_F a_{3D}| \gg 1$ one is in the weakly interacting regime.

In low energy scattering, the internal structure of our neutral atoms does not get resolved and one can treat them as either bosonic or fermionic when describing scattering. In a similar fashion, if the de Broglie wavelength $\lambda_{\text{dB}} = 2\pi/k$ is much larger than the effective range of the interaction potential r_{eff} , then the exact short-distance behaviour of the potential does not get resolved and one can treat the potential effectively as a contact potential. Theoretically, the potential can then be modeled as a pseudo-potential of the form

$$V_{\text{int}}(\mathbf{r}) = \frac{4\pi\hbar^2 a_{3D}}{m_r} \delta(\mathbf{r}) \partial_r r, \quad (2.36)$$

where the partial derivative regularizes the potential to avoid divergences in three dimensional systems [Hua57, Hua87]. This simplifies the theoretical description of neutral atomic systems considerably while still being exact. This can be for example used to calculate the interaction energy for a weakly interacting system in a mean-field picture. Looking at a sample of N atoms in a volume V at a density $n = N/V$, one can derive the interaction energy experienced by a single atom by summing up the contributions from all the other atoms in the volume. This results in a mean-field interaction energy [Wei09]

$$E_{\text{int,mf}} = g_{3D}n = \frac{4\pi\hbar^2 a_{3D}}{m_r} n. \quad (2.37)$$

Thus, the sign of the scattering length a_{3D} determines whether the experienced mean field shift is repulsive ($a_{3D} > 0$) or attractive ($a_{3D} < 0$). Note however that the underlying microscopic van der Waals interaction is always attractive even when the overall effect on a test particle is repulsive.

Treatment of Scattering in a Two-Dimensional System

Similar to the three dimensional case, the scattering problem in two dimensions can be solved working with the 2D Schrödinger equation [Lev15]. In an analogous fashion to the 3D derivation, one obtains for the two-dimensional s-wave scattering amplitude $f_{2D}(k)$

$$f_{2D}(k) = \frac{-4}{\cot \delta_0(k) - i}. \quad (2.38)$$

For elastic scattering, the low energy behavior of the phase shift $\delta_0(k)$ is given by [Ran90]

$$\cot \delta_0(k) = -\frac{2}{\pi} \ln(1/ka_{2D}) + \mathcal{O}(k^2), \quad (2.39)$$

where $a_{2D} > 0$ is now the scattering length in two dimensions. Inserting this back into equation 2.39 yields

$$f_{2D}(k) = \frac{-4}{\frac{2}{\pi} \ln(ka_{2D}) - i}. \quad (2.40)$$

From this it is clear that the scattering behavior is remarkably different from the 3D case. For vanishing collision energies the scattering amplitude now goes to zero instead of going to the scattering length as in the 3D case. Also there is no unitary regime where the scattering length diverges and the scattering cross section is only momentum dependent as in 3D. As we will later see, this can be attributed to the presence of a bound dimer state at all scattering lengths a_{2D} . Furthermore, the repulsive or attractive nature of the mediated interaction is now not determined by the sign of the scattering length but the value of $\ln(ka_{2D})$. In a Fermi gas the energy scale for the momenta is given by the Fermi momentum k_F which is directly connected to the density n of the system. Hence one can now also profoundly influence the physics of the system by changing only the density. This is of importance in the context of the BEC-BCS crossover in 2D systems which is discussed in section 2.3.1.

Influence of the Strong Axial Confinement

In the real world, the notion of a two dimensional system is of course superfluous. However, when the confinement width of particles in one direction is much smaller than both the thermal wavelength and the interparticle spacing, the transverse motion is effectively frozen out and the system can be described in a 2D framework [Pet00, Mar10]. Hence equation 2.40 still holds. However there is one subtlety in the quasi-2D case. The length scale of the tight confinement⁹ is given by the harmonic oscillator length $l_z = \sqrt{\hbar/m\omega_z}$ which is typically on the order of 500 nm in our experiments. The effective range of the two-body interaction is however on the order of the van der Waals range which is typically $r_{vdW} \approx 3$ nm. Thus, the two-body interactions are not effected by the confinement and the microscopic scattering process has to be described in three dimensions. Taking this into consideration, one can arrive at an expression for the two-dimensional scattering length a_{2D} which now explicitly depends on a_{3D} [Pet01, Lev15]

$$a_{2D} = l_z \sqrt{\pi/B} \exp\left(-\sqrt{\frac{\pi}{2}} l_z/a_{3D}\right) e^{-\frac{1}{2}\Delta w(k_0^2 l_z^2/2)}, \quad (2.41)$$

where $B \approx 0.905$ [Pet01, Blo08] and $\Delta w(x)$ is a correction dependent on the relevant momentum scale of the system k_0 [Boe16]. In a many-body system this momentum scale is given by $\hbar k_0 = \sqrt{2m\tilde{\mu}}$ and therefore $k_0^2 l_z^2/2 = \tilde{\mu}/\hbar\omega_z$. The correction can be neglected if $k_0 l_z \ll 1$. Note that there are also other definitions of a_{2D} in the literature which deviate slightly [Pet01, Blo08]. In this thesis, however, only equation 2.41 is used.

⁹We define it to be along the z-direction in the rest of this thesis.

2.2.2. Feshbach Resonances in Atomic Physics

In atomic systems, one can often make use of magnetic Feshbach resonances [Fes58] to change the scattering length by simply applying a homogeneous magnetic offset field. In this section the underlying physics will be summarized and the special case of ${}^6\text{Li}$ will be discussed in detail. The ability to tune the scattering length also gives access to universal dimer states whose properties are solely determined by the mass and the scattering length. These will be discussed both for the 3D and quasi-2D systems at the end of this section.

Principle of Feshbach Resonances

Although low-energy scattering can be described simply by the scattering length $a_{3\text{D}}$ without relying on the exact form of the interaction potential V_{int} , the value of $a_{3\text{D}}$ can still be greatly influenced by it. This can be seen for example if a weakly bound dimer state of the potential exists close to the continuum. The interaction is then resonantly enhanced which leads to a large positive scattering length [Lan81]. Similarly, if there is a (virtual) bound state slightly above the continuum the scattering length is large and negative. This phenomenon is sometimes referred to as accidental fine-tuning and can e.g. be seen in ${}^6\text{Li}$, where the scattering length at large magnetic fields is large and negative (see section 2.2.2).

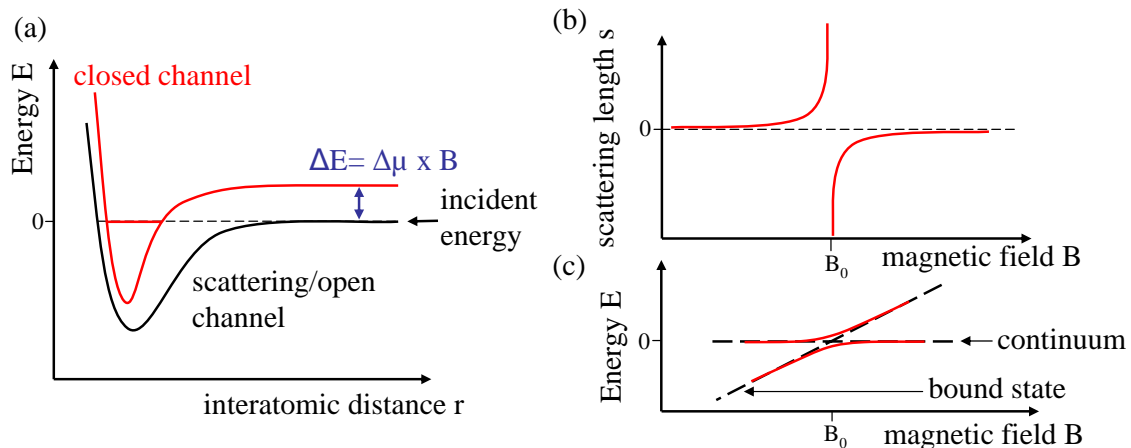


Figure 2.4.: Sketch of the open/closed channel model for scattering (a). If the particles in the open channel can couple to the closed channel, a bound state of the closed channel can be brought to coincide with the open channel continuum by changing the magnetic field. The scattering is then resonantly enhanced and the scattering length diverges at the resonance position B_0 as shown in (b). The coupling also leads to an avoided crossing between a molecular state and the free scattering state (c). Hence one can adiabatically go from a system of molecules to free particles and vice versa by ramping the magnetic field across the resonance. Taken from [Wen08].

These bound states can also be tuned by applying external magnetic fields and thus resonantly enhanced scattering can be achieved. This principle is used in

magnetic Feshbach resonances which have been discussed both theoretically [Fes58, Moe95, Pet02, Pit03] and experimentally [Ino98, Chi10] in great detail. Hence we will give here just a short qualitative picture motivated by Figure 2.4 (a). The scattering process can be described in an open/closed channel model. Imagine two particles with energy slightly above the continuum threshold of their respective interparticle potential (black curve). The particles can then come close together, be repelled by the strong short-range repulsion and separate again. Hence such a channel is called an open or scattering channel. However there also exist different scattering channels with differing initial spin configurations which can have a larger continuum threshold (red curve). If particles initially in the open channel can couple to this channel, they cannot separate again in this channel. Hence it is called a closed channel and particles have to couple back to the open channel making this a second-order process. The closed channel can now e.g. support a bound state close to the energy of the scattering particles and if there is a magnetic moment difference $\Delta\mu$ between the channels, one can tune this bound state to be in the vicinity of the continuum threshold of the open channel. The scattering becomes then resonantly enhanced, diverging at a magnetic field where the bound state lies exactly at the continuum (see Figure 2.4 (b)). In the vicinity of the Feshbach resonance the scattering length a_{3D} is then given as a function of the magnetic field B as [Moe95]

$$a_{3D}(B) = a_{bg} \cdot \left(1 - \frac{\Delta}{B - B_0}\right), \quad (2.42)$$

where a_{bg} defines the background scattering length, Δ describes the width of the resonance and B_0 gives the position of the resonance.

⁶Lithium as a Special Case

⁶Li is a fermionic isotope with a single electron in the outer shell. Therefore it has an electron spin $S = 1/2$ and its nuclear spin is $I = 1$ leading to a hyperfine splitting ($\Delta_{HF} = 228$ MHz) of the ground state with total spins $F = 1/2$ and $F = 3/2$ [Geh03]. When applying a magnetic field, the Zeeman shift lifts the degeneracy of the magnetic sublevels and the energy levels of the ground state can be seen in Figure 2.5 a). Already for magnetic fields above 30 G the electron spin and nuclear spin mostly decouple which leads to a splitting up into two triplets ($m_S = 1/2$ and $m_S = -1/2$ with sublevels $m_I = 0, \pm 1$) whose behavior is dominated by the electron spin. We label these states as $|1\rangle$ to $|6\rangle$ from low to high energy accordingly. The upper branch is referred to as the low-field seeking states since they minimize their energy at low fields. The lower branch are the high-field seeking states, lowering their energy at large magnetic fields in return. In the experiment we use only binary mixtures of the high-field seeking states $|1\rangle - |3\rangle$ since these do not undergo spin-changing collisions when preparing binary mixtures. Binary mixtures are needed since identical fermions do not interact at low-energies and hence distinguishable particles are needed to introduce interactions.

The scattering lengths a_{12}^{3D} , a_{13}^{3D} and a_{23}^{3D} for the different mixtures have been calculated using a coupled channel method in combination with a precise determination of the resonance positions using rf spectroscopy [Zü13]. The results are depicted in

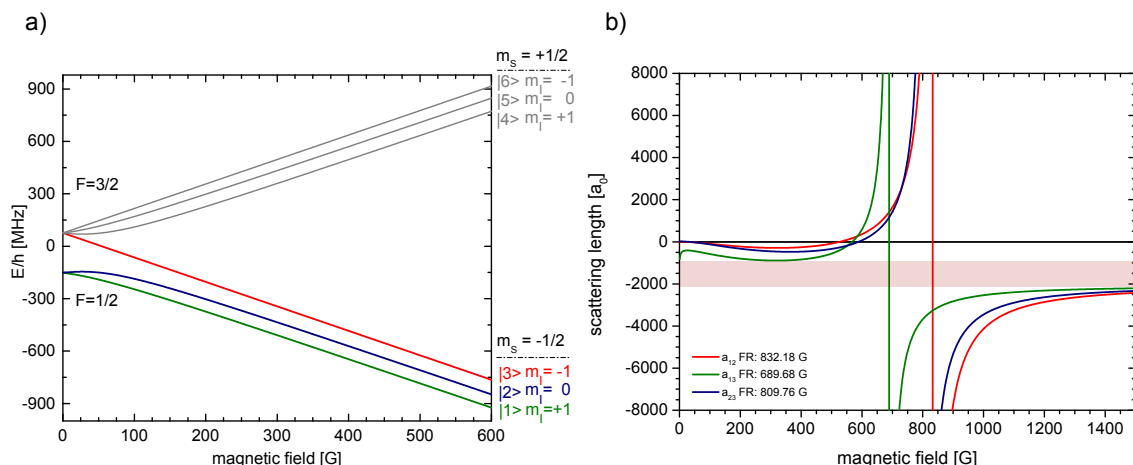


Figure 2.5.: a) Zeeman shifted energy levels of the ${}^6\text{Li}$ electronic ground state $2^2S_{1/2}$. Our experiments are usually performed at large magnetic fields $B > 500$ G where electron and nuclear spin decouple. We use binary mixtures of the lowest three hyperfine states labeled as $|1\rangle$, $|2\rangle$ and $|3\rangle$. b) The scattering length in units of the Bohr radius a_0 is given for all three possible binary mixtures of the high-field seeking states as a function of the applied magnetic offset field in Gauss. In this thesis we use both the 12-mixture as well as the 13-mixture.

Figure 2.5 b). All three mixtures show a broad Feshbach resonance in the vicinity of 800 G which is experimentally accessible. The results are shown in Table 2.1. For large magnetic fields, the background scattering length a_{bg} is dominated by the scattering length of the triplet channel which is resonantly enhanced due to the existence of a virtual bound state slightly above the continuum [Joc04]. This leads to a large negative background scattering length on the order of $a_{\text{bg}} \approx -2000 a_0$. Hence there is a small range of scattering lengths which are not experimentally accessible in ${}^6\text{Li}$ (see red opaque area in Figure 2.5 b)).

As explained in section 2.2.1, the two-dimensional scattering length does not diverge at the resonance position and is always positive. However, the two-dimensional interaction strength given by $\ln(k_F a_{2D})$ changes its sign in the vicinity of B_0 , depending on the density of the system.

Scattering channel	B_0 [G]	Δ [G]
$ 1\rangle 2\rangle$	832.2	262.3
$ 1\rangle 3\rangle$	689.7	166.6
$ 2\rangle 3\rangle$	809.8	200.2

Table 2.1.: Position B_0 and width Δ of the three lowest scattering channels of ${}^6\text{Li}$ as determined in [Zü13].

Universal Dimer States

The existence of a Feshbach resonance is accompanied with a bound dimer state. In a 3D system, the bound state is only present for positive scattering lengths $a_{3D} > 0$ and the binding energy goes to zero directly at the resonance (see Figure 2.6). When the scattering length a_{3D} is much larger than the effective range r_{eff} of the interparticle potential, the binding energy of this dimer becomes universal and is a simple function of the scattering length and the reduced mass of the particles [Pet04]

$$E_{B,3D} = \frac{\hbar^2}{2m_r a_{3D}^2}. \quad (2.43)$$

This dimer state is not in the vibrational ground state¹⁰ of the system and thus can potentially relax into deeper lying states releasing a lot of energy in the process. This leads inevitably to particle losses in the trap. However it was shown [Pet03a, Pet04, Pet05] that these relaxation processes are strongly suppressed in fermionic systems, making the dimers stable on experimental timescales.

In the 2D framework the situation is slightly different. Here $a_{2D} > 0$ is true for all magnetic fields and thus a dimer state exists for all interaction strengths $\ln(k_F a_{2D})$ (see Figure 2.6). The dimer binding energy is similar to the 3D case defined as [Lev15]

$$E_{B,2D} = \frac{\hbar^2}{2m_r a_{2D}^2}. \quad (2.44)$$

However, once again the axial extent l_z of the strongly confined dimension has to be taken into account when one wants to obtain the binding energy under real experimental conditions. The dimer energy $E_{B,q2D}$ can then be calculated¹¹ via the transcendental equation [Pet01, Blo08, Lev15]

$$\frac{l_z}{a_{3D}} = \int_0^\infty \frac{du}{\sqrt{4\pi u^3}} \left[1 - \frac{\exp\left(-\frac{E_{B,q2D} u}{\hbar\omega_z}\right)}{\sqrt{\frac{1}{2u}(1 - \exp(-2u))}} \right]. \quad (2.45)$$

In Figure 2.6 one can see that this solution interpolates between the 3D regime for deeply bound dimers and the true 2D regime for weakly bound dimers. This can be intuitively understood when considering that the 3D dimer size is on the order of the scattering length a_{3D} . Hence for $l_z/a_{3D} \gg 1$ the dimer size is much smaller than the axial confinement and hence the system feels no perturbation, hence approaching the 3D case. For $l_z/a_{3D} \leq 1$ however the influence of the tight confinement becomes stronger and the binding energy $E_{B,q2D}$ approaches the true 2D binding energy $E_{B,2D}$. This behavior has been experimentally verified in two independent experiments using rf spectroscopy [Som12, Bau12]. Note that the confinement induced binding energy $E_{B,q2D}$ has no direct connection to the scattering length a_{2D} .

¹⁰Hence they are also often referred to as Halo molecules due to their size being much larger than the underlying interaction potential.

¹¹If the assumption $(r_{\text{eff}}/l_z)^2 \rightarrow 0$ is fulfilled. This is true in our system where $l_z \approx 500$ nm and $r_{\text{eff}} \approx 3$ nm.

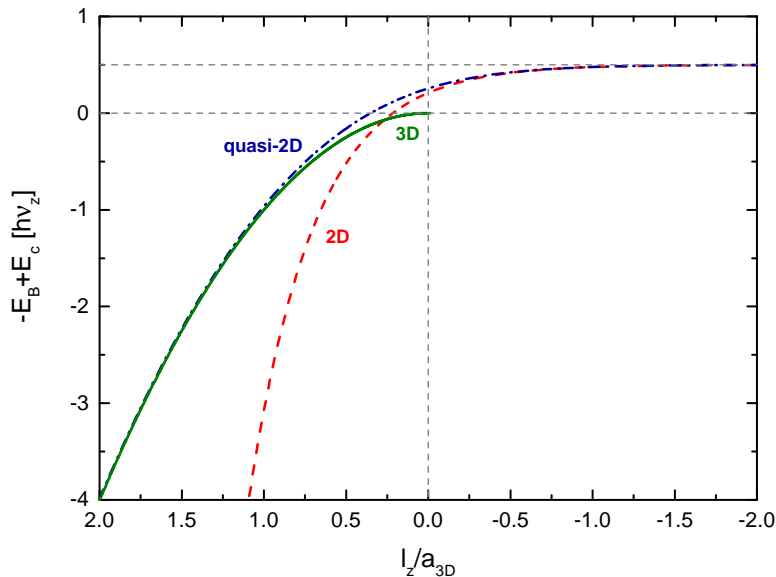


Figure 2.6.: The binding energy of the universal dimer is depicted as a function of l_z/a_{3D} for the 2D (red dashed line), quasi-2D (blue dash dotted line) and 3D (green) case using equations 2.41, 2.43, 2.44 and 2.45. The axial confinement length is set to $l_z = 551.2$ nm. Due to the strong confinement, the continuum energy of both the 2D and quasi-2D case is shifted by $0.5h\nu_z$. Hence this shift is added in this plot in order to compare the 3D and 2D case. For large dimer binding energies, the size of the dimer is negligible compared to the confinement length and the quasi-2D solution converges towards the 3D solution. Close to the resonance $l_z/a_{3D} = 0$, the influence of the confinement length becomes important and the quasi-2D solution interpolates between the 3D and 2D solutions. Above the resonance, a dimer state only exists in the two-dimensional systems. Hence it is often referred to as confinement induced.

2.3. Strongly Interacting Fermi Gases as a Tunable Many-Body System

Fermions provide an interesting playground for many-body physics. At low temperatures, the Pauli principle excludes interactions between identical particles, thus necessitating the usage of mixtures, either in the internal state of the species or by using different species. This absence of interactions between identical fermions makes binary mixtures stable on long timescales [Pet03a] also in the strongly interacting regime as three-body losses are suppressed since always two of the three involved particles in a scattering process are identical. Together with the existence of Feshbach resonances, this enables the creation of strongly correlated systems which is not possible in purely bosonic systems as three-body losses set in at larger interaction strengths.

The prime example of such a rich phase-diagram is the BEC-BCS crossover in a 3D Fermi mixture. There, a phase transition to a superfluid state below a critical temperature T_c exists at all interaction strengths. However, the underlying principle of this superfluid transition changes fundamentally when crossing the Feshbach resonance from a weakly repulsive to a weakly attractive system. The theoretical groundwork of the BEC-BCS crossover was done [Eag69, Leg80] and experimentally it was studied in detail in [Bar04, Reg04, Chi04, Zwi05, Gre05, Sch08a] and has been summarized in various review articles [Ket08, Gio08]. The principle of the BEC-BCS crossover is depicted schematically in Figure 2.7 a) and will be here shortly summarized.

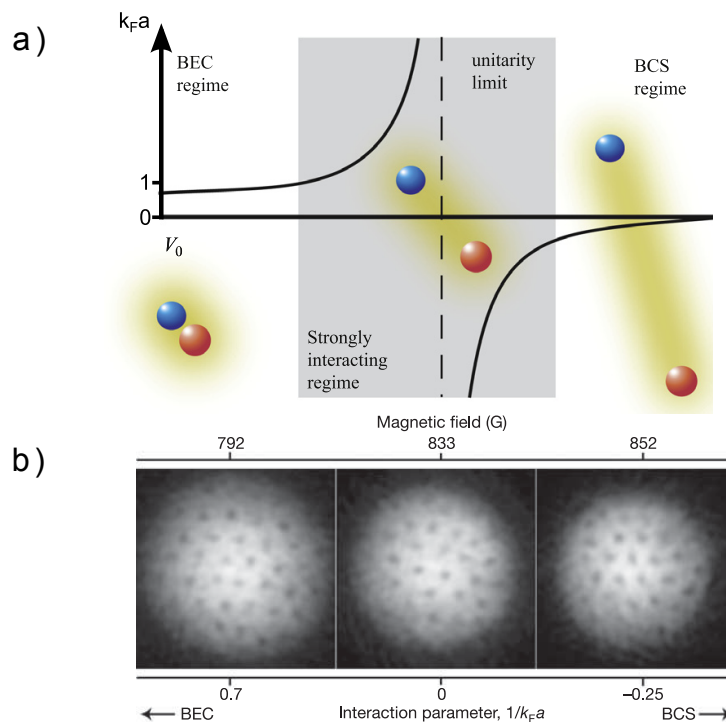


Figure 2.7.: a) The underlying mechanism of the pair formation changes as one crosses the Feshbach resonance. In the BEC regime, atoms of opposite spin form deeply bound dimer states which can undergo Bose-Einstein condensation. In the unitary regime where the scattering length diverges, the pairing is a many-body phenomenon and the pair size is on the order of the inter-particle spacing. In the BCS regime for weak attractive interactions, BCS theory describes the system and the atoms form Cooper-pairs in momentum space. Taken from [Gub13]. b) Experimental data from [Zwi05] showing vortex cores in all regimes when stirring the sample. This is a clear sign of superfluidity and shows that the BEC-BCS crossover is smooth. Taken from [Zwi05].

On the repulsive side of the Feshbach resonance ($a_{3D} > 0$), a universal dimer state exists whose size scales with the scattering length. For weak interactions, the dimer is deeply bound and its size is much smaller than the inter-particle distance. The dimer scattering can then be treated as purely bosonic and the system can be

described by the Gross-Pitaevskii equation [Pit03]. Similar to the non-interacting case, the system then undergoes a phase transition to a Bose-Einstein condensate below a critical temperature T_c . This is often referred to as a molecular BEC (mBEC).

On the attractive side of the Feshbach resonance ($a_{3D} < 0$), no dimer state exists and the system consists of free atoms. However, superfluidity is connected to long range coherence in the system which only exists for bosons as fermions cannot occupy the same state. Thus, fermionic pairing is a necessity for superfluidity. Although there is no dimer state available, Bardeen, Cooper and Schrieffer¹² showed that in such a system so-called Cooper pairs can be formed in momentum space at arbitrarily weak interactions [Bar57]. These Cooper-pairs are formed by atoms with opposite spin and momentum. Note that this pairing mechanism, unlike the simple two-body phenomenon for the dimer state on the BEC side, relies on the presence of the filled Fermi sea below the Fermi surface and is thus often referred to as many-body pairing. This many-body pairing leads to a zero-temperature energy gap in the excitation spectrum close to the Fermi surface of the form [Gor61]

$$\Delta_0 \approx \left(\frac{2}{e}\right)^{7/3} E_F \exp\left[-\frac{\pi}{2k_F |a_{3D}|}\right]. \quad (2.46)$$

It was shown [Gio08] that below a critical temperature $k_B T_c = (e^\gamma/\pi) \Delta_0$ the system is superfluid. Furthermore, in the limit of $a_{3D} \rightarrow 0_-$, the critical temperature for the onset of superfluidity coincides with the critical temperature for Cooper-pair formation T^* .

In the unitary limit close to the Feshbach resonance, the scattering length diverges and for $k_F |a_{3D}| \gg 1$ it exceeds the inter-particle distance. Here, no analytic solution exists for the many-body system but one can extend the standard BCS theory into the unitary regime to get a qualitative understanding [Eag69, Leg80]. It shows that there is still a superfluid state below a critical temperature T_c . Experimentally, this was studied e.g. in [Reg04, Bar04, Chi04, Zwi05, Gre05, Sch08a] and it was shown that the size of these pairs is on the order of the inter-particle spacing. An interesting aspect of the unitary regime is that the scattering cross section there is independent of the scattering length (see equation 2.35). Hence, the inter-particle spacing $d \sim 1/k_F$ becomes the only relevant length scale. Therefore, all thermodynamic properties of the system only depend on the Fermi energy E_F and the degeneracy T/T_F [Gio08].

2.3.1. BKT Transition and the 2D BEC-BCS Crossover

The situation in a two-dimensional system has some subtle differences compared to its 3D counterpart. First of all there now exists a two-body dimer state at all interaction strengths, whose binding energy approaches zero in the limit of weak attractive interactions. Furthermore, the scattering length does not diverge at the Feshbach resonance and thus no unitary regime exists in two dimensions. Nevertheless, the crossover from a system with bosonic degrees of freedom in the form

¹²Their theory is commonly referred to as BCS theory.

of dimers into a system with fermionic degrees of freedom in the form of atoms is still present at finite temperatures due to the vanishing bound state energy of the dimers on the attractive side of the resonance.

In the limit $\ln(k_F a_{2D}) \ll 1$ where deeply bound dimers form on the repulsive BEC side, the condensation of these dimers into a BEC with true long-range order is not possible at finite temperatures [Mer66]. Nevertheless, there still exists a phase transition into a superfluid state in the form of a topological phase transition. This is the famous Berenzinskii-Kosterlitz-Thouless (BKT) transition which was predicted theoretically in the seventies [Ber72, Kos73] and for which both D. Thouless and J. Kosterlitz were awarded a Nobel prize in 2016. It can be qualitatively understood when looking at the thermal vortex excitations of the system [Had11]. Vortices are topological excitations around which the phase θ of the wave function circulates by a multiple of 2π . They also carry a quantized angular momentum and thus can only be produced in pairs of opposite rotation when no additional transfer of angular momentum into the system takes place. These thermal vortices lead to a scrambling of the phase and thus suppress any long range order in the phase. However, below a critical temperature T_{BKT} , the system becomes superfluid as vortices of opposite rotation form bound pairs and thus their influence on the phase almost cancels out. This leads to so-called quasi long-range order (QLRO) in the system and can be seen as an algebraic decay of the first order correlation function [Had11]

$$g_1(r) = n_s \left(\frac{r}{\xi} \right)^{-1/(n_s \lambda_T^2)}, \quad (2.47)$$

where n_s is the superfluid density and ξ is the healing length. The critical temperature T_c in the limit $\ln(k_F a_{2D}) \ll -1$ can be calculated as [Pet03b, Pro01, Pro02]

$$\frac{T_c}{T_F} = \frac{1}{2} \left[\ln \frac{C}{4\pi} + \ln(\ln(4\pi) - 2 \ln(k_F a_{2D})) \right]^{-1}, \quad (2.48)$$

where $C = 380 \pm 3$ is obtained from quantum Monte Carlo simulations. The BKT transition was observed in superfluid Helium films [Bis78] as well as in quasi-2D ultracold Bose gases [Had06, Krü07, Cla09, Des12].

In the limit $\ln(k_F a_{2D}) \gg 1$, where the dimer state energy is negligible, the system can be described as free fermions and BCS theory can be applied. Including the so-called Gor'kov-Melik-Barkhudarov (GMB) corrections to account for particle-hole fluctuations around the Fermi surface, this leads to a critical temperature [Pet03b, Bot06, Lev15]

$$\frac{T_c}{T_F} = \frac{2e^{\gamma-1}}{\pi k_F a_{2D}}, \quad (2.49)$$

where $\gamma \approx 0.577$ is the Euler constant.

Whereas these two limits are well understood theoretically, the interesting region of strong interactions is difficult to describe theoretically due to the increased role of quantum fluctuations in two dimensions. Since in both limits the critical temperature increases monotonically as one approaches the crossover, one expects to find a maximum in T_c as shown schematically in the phase-diagram in Figure 2.8 a).

To obtain a qualitative insight into the crossover, one can again apply zero temperature BCS mean field theory across the whole regime [Lev15]. In contrast to the 3D case where the crossover point from the BEC side to the BCS side is naturally given by the unitary regime where the binding energy approaches zero and the scattering length diverges, there is no divergence of the 2D scattering length and a bound state exists for all interaction strengths. Here, it makes sense to define the crossover point in terms of the chemical potential μ . A necessary condition for the formation of a Fermi surface is $\mu > 0$ and thus it is natural to define the crossover point by this condition. In mean-field theory this crossover point corresponds to $\ln(k_F a_{2D}) = 0$. However, a more accurate QMC calculation yields the crossover point to be at larger values $\ln(k_F a_{2D}) \simeq 0.5$ [Lev15], indicating that strong correlations influence the existence of a Fermi surface significantly. Note that this can also have large implications when perturbing away from the strict 2D limit $E_F \ll \hbar\omega_z$, as the chemical potential can be strongly modified even for weak interactions [Lev15]. This can potentially result in larger critical temperatures when operating between the strict 2D and 3D limit [Fis14].

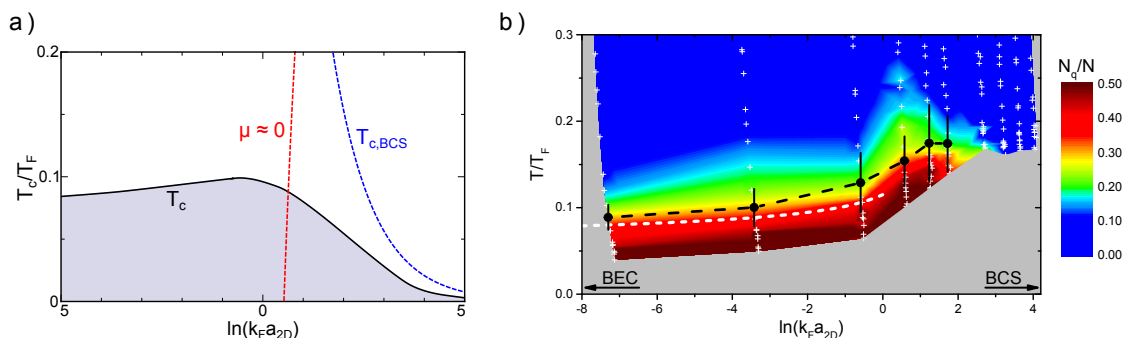


Figure 2.8.: a) A sketch of the expected two-dimensional phase diagram. The critical temperature is given by the black line and the red dashed line indicates the condition $\mu \approx 0$ which is a necessary condition for a Fermi surface to exist. The blue dashed line is a BCS mean-field prediction which indicates the onset of pairing according to the Thouless criterion. Adapted from [Lev15] b) Measured phase-diagram of the critical temperature in the BEC-BCS crossover in quasi-2D [Rie15a]. The phase transition was observed by measuring the zero momentum density in the pair momentum distribution as a function of temperature and interaction strength. The black dots are the experimentally determined critical temperatures including the error. The color scale indicates the non-thermal fraction in the sample. This can be non-zero even above the critical temperature due to Bose-enhancement.

In our group we investigated this transition into a superfluid in the BEC-BCS crossover by measuring the momentum distribution of an inhomogeneous, trapped sample [Rie15a, Mur15]. We observed condensation into a low-momentum phase and were able to extract the critical temperature well into the crossover regime up to $\ln(k_F a_{2D}) \lesssim 2$. This is depicted in the phase diagram in Figure 2.8 b). The ob-

served critical temperatures in the crossover regime where indeed considerably larger than in the 3D case and showed the largest values in the crossover regime. Furthermore, from the momentum distribution we extracted the g_1 -correlation function and observed an algebraic decay below the critical temperature (see Figure 2.9).

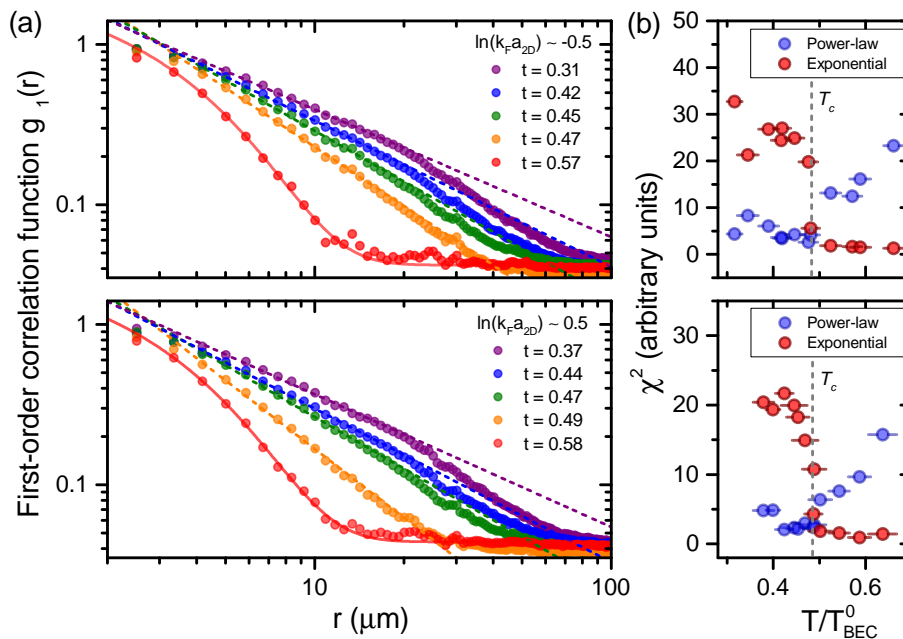


Figure 2.9.: Observation of the BKT phase transition in a strongly interacting quasi-2D Fermi gas. In a) the first order correlation function obtained from a Fourier transform of the momentum space distribution is shown at two interaction strengths in the crossover for different temperatures. Below a critical temperature T_c , the form of the correlation decay changes from an exponential form to an algebraic form as predicted by BKT theory. This is further shown in b) where the χ^2 -value of the fits are shown. One can clearly distinguish the region where the decay is described by an exponential from the region where the decay is algebraic. Taken from [Mur15].

2.4. Pairing in the Normal Phase

Superfluidity can be interpreted as an instability of the normal phase [Nor05] and hence to better understand its origin it is instructive to investigate the normal phase in more detail. In BCS theory, the emergence of a superfluid phase starts right at the point where (many-body) Cooper pairing occurs and leads to a gapped excitation spectrum. This means that the energy Δ_{gap} is required to remove a particle from the paired system leading to a gap with vanishing weight in the density of states right at the Fermi surface. The instability in the normal phase is therefore the instability of the Fermi surface towards pair formation [Alt10]. On the BEC side, the binding energy of the two-body dimers is $E_B \gg k_B T_c$ and thus dimer formation already sets

in far above the critical temperature T_c . The instability in the normal phase is then driven by the pairing of vortices of opposite rotation as described in section 2.3.1.

An open question which is not yet fully understood regards now the pairing mechanism in the strongly interacting fermionic regime. Are many-body pairing and superfluidity distinct phenomena such that one can have many-body pairing already above the critical temperature T_c or does one necessitate the other? In high- T_c cuprates it was shown that it is indeed possible to have a gap at a finite temperature above T_c in an underdoped system without establishing long range order [Din96]. This behavior is referred to as a pseudogap and theoretical investigations imply that this is also expected to occur in strongly interacting atomic Fermi gases [Bau14, Lev15, Mar15]. The pseudogap is then defined by a significant suppression of spectral weight at the Fermi surface starting to form at a crossover temperature $T^* > T_c$ [Bau14]. This results in a gapped excitation spectrum already above T_c with a minimum at a finite momentum k . As this definition of the pseudogap requires the existence of a Fermi surface, the chemical potential μ has to fulfill $\mu > 0$. To understand the pseudogap at least on a qualitative level, its emergence can be illustrated by considering a complex order parameter of the form $\Delta(r) = |\Delta(r)| e^{i\theta(r)}$ [Fel11]. For temperatures below the critical temperature for BKT, quasi-long range order is established, leading to a superfluid gap $\Delta_{\text{gap}} = \langle \Delta \rangle$. Above the critical temperature, quasi-long range order is destroyed by thermal vortices and $\langle e^{i\theta(r)} \rangle = 0$. However, the modulus $\langle |\Delta(r)| \rangle$ remains finite up to the crossover temperature for pairing T^* leading to a pseudogap $\Delta_{\text{pseudogap}} = \langle |\Delta(r)| \rangle > 0$. This is in contrast to standard weak-coupling mean-field BCS theory where the destruction of the superfluid gap is synonymous with pair breaking and thus $T^* = T_c$. In general the pseudogap regime is expected to be particularly large in two dimensions due to the increased role of quantum fluctuations.

Experimentally, pairing above the critical temperature has been observed in quasi-2D systems in the BEC-BCS crossover region [Fel11, Som12]. However due to the existence of a bound state at all interactions strengths in 2D systems, observing pairing alone does not unambiguously identify a pseudogap region. In [Som12] the observed pairing energies up to $\ln(k_F a_{2D}) < 0.5$ are consistent with the two-body binding energy and hence do not show any indication of many-body effects. However it does not probe the region where one would expect $\mu > 0$ and thus a remnant of a Fermi surface to be present. Additionally the temperature regime where the data was taken is on the order of $T/T_F \geq 1$ and hence one is not in the temperature regime one would expect a pseudogap to show up. Similarly the results presented in [Fel11] are in a regime $0 < \ln(k_F a_{2D}) < 0.8$ and hence there is not unambiguously a Fermi surface present [Lev15]. Furthermore, the physical feature used to extract the pseudogap regime can also be reproduced by a thermal virial expansion [Nga13]. This motivates further studies presented in this thesis towards a better understanding of the strongly interacting regime.

2.5. Particles in Periodic Potentials

Apart from the freedom to change the dimensionality of the system in ultracold gases, one can also introduce periodic potentials to mimic solid state systems. In the course of this thesis we therefore investigated a superfluid Fermi gas in a lattice potential. The lattice potential is created by counter-propagating, red-detuned, far off-resonant laser beams which interfere resulting in a standing wave and thus a periodic potential. This section provides a short overview about the behavior of particles confined in a periodic potential as can be found in text books like [Ash76, Lew12] and it furthermore introduces the Hubbard model which is widely used both in condensed matter physics as well as in ultracold gases to describe the lattice physics when adding interactions.

2.5.1. Non-Interacting Particles and Band Structure

For a non-interacting particle its motion in a 1D lattice potential $V(x + d) = V(x)$ with periodicity d is described by the stationary Schrödinger equation

$$\left(\frac{\hat{p}^2}{2m} + V(x) \right) \psi = E\psi. \quad (2.50)$$

This breaks the continuous translation symmetry of the Hamiltonian compared to a particle in free space but replaces it with a discrete translational symmetry such that the Hamiltonian is invariant when shifted by multiples of the periodicity. This leads to a set of eigenfunctions $\psi_{n,q}$ which can be written according to the Bloch theorem as [Ash76]

$$\psi_{n,q}(x) = e^{iqx} u_{n,q}(x), \quad (2.51)$$

where $u_{n,q}(x + d) = u_{n,q}(x)$ is a function representing this translational periodicity, n is the band index for the n -th solution of the Schrödinger equation and q is the quasi-momentum of the particle. The function $u_{n,q}(x)$ can be expressed using a discrete Fourier Series as

$$u_{n,q}(x) = \sum_{l=-\infty}^{\infty} c_{n,q}^{(l)} e^{ilk_L x}, \quad (2.52)$$

$$\psi_{n,q}(x) = \sum_{l=-\infty}^{\infty} c_{n,q}^{(l)} e^{i(lk_L + q)x}, \quad (2.53)$$

where the quasi-momentum q is restricted to the range $q \in \left(-\frac{k_L}{2}, \frac{k_L}{2} \right]$ in units of the reciprocal lattice vector $k_L = 2\pi/d$. The solutions of the wave function are hence plane waves with momentum q differing by integer multiples of the lattice vector. For shallow lattices only the terms $l = 0, \pm 1$ play a role in the expansion.

In the experiment, the optical trapping potential in one dimension is created by a standing wave resulting in a potential of the form

$$V(x) = V \sin^2 \left(\frac{\pi x}{d} \right) = \frac{1}{2} V \left(1 - \cos(k_L x) \right). \quad (2.54)$$

Putting this potential into equation 2.50, the Schrödinger equation can be solved numerically in Fourier space by taking only a finite number of Fourier coefficients into consideration [Lew12]. This results in a band structure as depicted in Figure 2.10 for two different lattice depths. The most striking feature is the opening up of a band gap at the edge of the Brillouin zone. Thus, if a band is completely filled with fermions, a finite energy (the band gap) is needed to create excitations. The system is then insulating and accordingly called a band insulator. Near the center of the Brillouin zone at $q = 0$, the dispersion relation is almost quadratic with an effective mass m^* . Increasing the depth of the lattice potential restricts the movement of particles and leads to an increase in the band gap as well as an increase in the effective mass m^* , resulting in a rather flat dispersion relation. This indicates that the system may be described by an array of independent confining wells with degenerate energy. There the energy of the lowest bands can be estimated by approximating each lattice site by a harmonic confinement with a trap spacing $\hbar\omega = 2\sqrt{V E_r}$ where $E_r = \frac{\hbar^2 k_L^2}{2m}$ is the recoil energy of the lattice photons. This approximation tends to overestimate the energy as the real potential is not harmonic and residual tunneling will lower the energy.

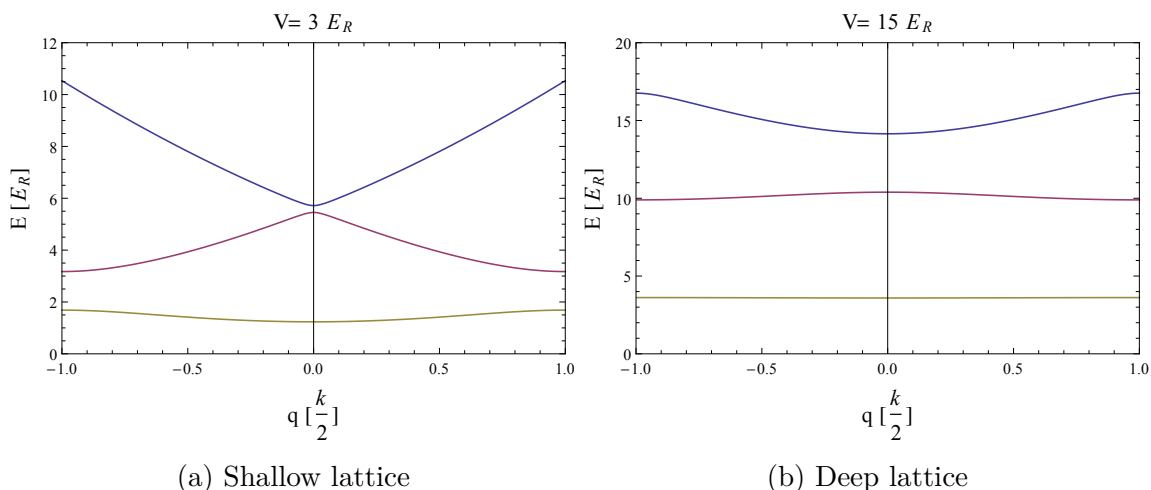


Figure 2.10.: Numerical band structure calculation of a 1D lattice. For (a) $V = 3 E_r$ and (b) $V = 15 E_r$ the lowest three bands are plotted. In the vicinity of $q = 0$ the dispersion relation is harmonic with an effective mass m^* and the bands are separated by the band gap. For deeper lattices, the effective mass increases and the bands become rather flat as $m^* \rightarrow \infty$. This also increases the band gap. Taken from [Bay15].

All these considerations can be extended also to higher dimensional lattices like the 2D square lattice we set up in the experiment. Here the problem is separable in each dimension and the dispersion relations is simply the sum of the 1D lattice dispersion relations. However a difference exists when looking at the higher bands. For the 2D lattice there exist for example momenta q_x, q_y where solutions for $n_x = 1, n_y = 2$ are degenerate to solutions for $n_x = 2, n_y = 1$ and hence these different bands touch each other. Hence there is no band gap between higher bands whereas the band gap between the lowest band and the first excited band still exists.

2.5.2. The Hubbard Model in Deep Lattices

The model of non-interacting particles in a lattice in the previous section was described in the basis of delocalized Bloch waves. This is an intuitive basis in a shallow lattice where the particles can move more or less freely but is not a good basis when describing deep lattices where the particles are more localized and tunneling determines the movement. There the description of particles localized to specific lattice sites becomes more adequate which can be expressed in the basis of so-called Wannier states [Wan37] which are constructed from the Bloch wave functions as

$$w_n(x - x_i) = \frac{1}{\sqrt{N}} \sum_q e^{-iqx_i} \psi_{n,q}(x). \quad (2.55)$$

Here x_i represents the coordinate of a particle localized to a lattice site i , N is the number of lattice sites and n is the band index. In our 2D lattice, the energy gap between the first and second band is on the order of tens of kHz for deep lattices and thus exceeds all other energy scales in the system. Thus, in our case we can only consider the lowest band in the following. Note however that in the direction perpendicular to the lattice, our harmonic confinement is only on the order of several kHz and thus excitations in this direction are still possible. Thus, a more appropriate model would be a system of weakly coupled 1D tubes.

In the following the application of this model to a 1D lattice of interacting bosonic particles is given. The annihilation (creation) of a particle at a position x is then given by the bosonic field operator

$$\hat{\psi}^{(\dagger)}(x) = \sum_i \hat{b}_i^{(\dagger)} w^{(\dagger)}(x - x_i), \quad (2.56)$$

where $\hat{b}_i^{(\dagger)}$ denotes the annihilation (creation) operator of a particle localized at lattice site i obeying the commutation relation $[\hat{b}_i, \hat{b}_i^\dagger] = \delta_{ij}$. The two forces driving the dynamics in the lattice are the kinetic energy of the particles due to tunneling across lattice sites and the interaction between particles. Depending on the depth of the lattice and the ensuing localization of the particles, these can be limited to nearest-neighbor tunneling and on-site interactions which is known as the Bose-Hubbard model

$$H = -J \sum_{\langle i,j \rangle} \hat{b}_i^\dagger \hat{b}_j + U \sum_i \hat{n}_i (\hat{n}_i - 1). \quad (2.57)$$

Here the term J describes the nearest-neighbor tunneling across adjacent lattice sites $\langle i, j \rangle$ and U describes the on-site interaction energy given by the boson number operator $\hat{n}_i = \hat{b}_i^\dagger \hat{b}_i$ at each site. This can be seen sketched in Figure 2.11. The applicability of this model relies on the wave function overlap between particles at neighboring lattice sites to be small. This can be estimated by approximating each lattice site by a harmonic potential with harmonic oscillator length $a_{\text{on-site}} = \sqrt{\hbar/(m\omega_{\text{on-site}})}$ and comparing this to the lattice spacing d . In our system $a_{\text{on-site}} \ll d$ for lattice depths $V \gtrsim 2.5E_r$ and thus there we can apply the Hubbard Model. Note that in this model we explicitly did not consider an external confining potential

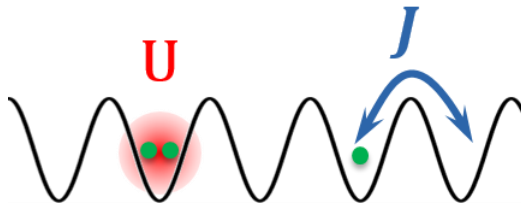


Figure 2.11.: Sketch of particles in a periodic potential obeying the Hubbard model. This model is based on two assumptions: only particles on the same lattice site interact resulting in the on-site energy U . Particles can tunnel only to adjacent lattice sites with a tunneling rate given by J . Taken from [Bay15].

which is present in the experiment. This introduces a lattice site dependent energy offset ϵ_i and thus both the chemical potential μ as well as the on-site trapping frequency change locally. We neglect this in the following derivation.

The tunneling probability J can be calculated as [Lew12]

$$J = - \int dx w^\dagger(x - x_i) \left[\frac{\hbar^2 \nabla^2}{2m} + V(x) \right] w(x - x_i) \quad (2.58)$$

whereas the on-site interaction U is given by

$$U = g \int dx |w(x)|^4 \quad (2.59)$$

where g is the coupling strength.

Although the Hubbard model only has two parameters in the tunneling probability J and the on-site interaction U , its ground state can nevertheless change drastically when changing the ratio U/J . In the limit of weak interactions $U \ll J$, the particles minimize their energy by delocalizing over the whole lattice resulting in a macroscopic occupation of the Bloch state with quasi-momentum $q = 0$. The system is then a superfluid with a fixed phase relation and can be written as a wave function [Blo08]

$$|\psi_{\text{SF}}\rangle = \frac{1}{\sqrt{N!}} \left(\frac{1}{\sqrt{M}} \sum b_i^\dagger \right)^N |0\rangle, \quad (2.60)$$

where N is the particle number and M is the number of lattice sites. Thus, the particle fluctuation at each lattice site is maximal. Increasing the repulsive interaction U now suppresses particle fluctuations at each site as it becomes energetically unfavorable to simultaneously have more than one particle per site. Then the system properties become strongly dependent on the filling factor of the lattice. In case of unity filling where the particle number is equal to the number of lattice sites $N = M$, the system turns into an insulator in the limit $U \gg J$ and each lattice site is exactly occupied by one particle with no number fluctuations present. This

state is known as the Mott-insulator (MI) and its wave function can be written in the limit $U/J \rightarrow \infty$ as a product of Fock states [Blo08]

$$|\psi_{\text{MI}}\rangle = \prod_{i=1}^M b_i^\dagger |0\rangle. \quad (2.61)$$

To create an excitation in the MI the energy U is required, making this state an insulator. The MI persists also for large finite U/J where the ground state is no longer a product state. It can be characterized by its incompressibility $\kappa = \frac{\partial n}{\partial \mu} = 0$. By changing the filling factor of the lattice one can drive the system from a superfluid to a Mott-insulator as is depicted in the zero temperature phase diagram in Figure 2.12. For any non-integer filling of the lattice, the system is in a superfluid state as the excess atoms delocalize to minimize their energy and are hence highly mobile. Therefore by changing the chemical potential μ via the density one can access different MI regimes with a fixed integer occupation number of atoms per site. This is important in the context of experiments as these usually employ an overall harmonic trapping potential in addition to the lattice. Thus, μ changes across the lattice and one can observe the coexistence of different filling factors inside the trap [Bak10]. The critical value for the phase-transition from a superfluid to a Mott-insulator for a 2D square lattice with unity filling has been calculated in mean-field theory to be $(U/J)_c = 23.2$ [Zwe03] whereas QMC calculations yield $(U/J)_c = 16.2$ [Wes04].

In the lattice experiments performed in this thesis, the two-body binding energy E_B is much larger than the other energy scales in the system and thus we expect the Bose-Hubbard model to give a valid description in this regime. In principle one can also access the Fermi-Hubbard model by using free atoms instead of bosonic molecules. There, for a half-filled band one can create the fermionic Mott-insulator where each lattice site is occupied by one spin state. For a fully filled band, each lattice site is occupied by a spin up and spin down fermion and the system is a band insulator.

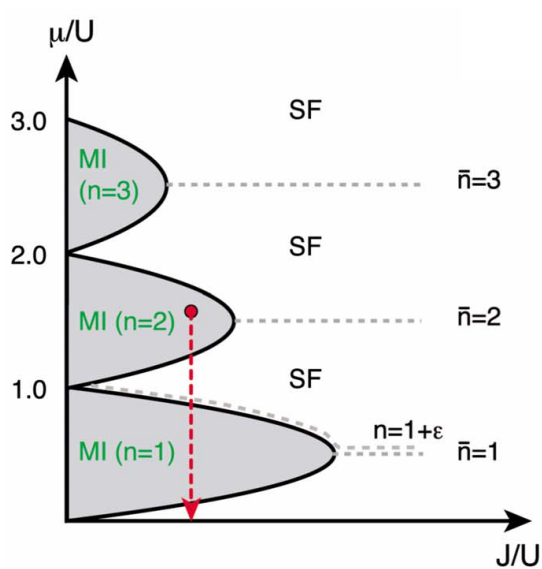


Figure 2.12.: Schematic zero-temperature phase diagram for the homogeneous Bose-Hubbard model. The density is controlled by the chemical potential μ which sets the filling of the lattice. Depending on μ and the ratio J/U one is thus either in a superfluid state or in Mott-insulating state with fixed integer mean atom number per site. Taken from [Blo08].

3. Experimental Setup and Tools

This chapter provides an overview on how we prepare and probe our degenerate Fermi gas systems. The preparation procedure has been described in more detail in previous work [Wen13, Rie15b, Bay15] and thus will be only summarized briefly in section 3.1. The probing of our system is done using an absorption imaging method. The main principle as well as the calibration of our imaging system are described in detail in section 3.2.

3.1. Preparation of a Degenerate Quasi-2D Sample

In this section all the steps required to produce our ultracold sample are briefly explained. Since the detection method is destructive, a new sample has to be prepared for each experimental cycle. A typical cycle of the experiment lasts between 10-15 s.

Vacuum Chamber

In order to achieve the temperatures required to reach quantum degeneracy (~ 100 nK), the atoms have to be isolated extremely well from the environment. Hence, the experiments have to be conducted inside an ultra high vacuum (UHV). The vacuum setup of our apparatus can be seen in Figure 3.1. The pressure, which is measured next to the main chamber (4), is approximately $1 \cdot 10^{-11}$ mbar and it is sustained via a combination of ion-pumps (6) and titanium sublimators (3) next to the main chamber and the oven (1). The main chamber, a spherical octagon, is additionally coated with a non-evaporable getter coating (NEG), reducing the pressure at the location of the atoms furthermore. It provides the required optical access for trapping, cooling and detection via six horizontal viewports¹ (numerical aperture $NA \approx 0.15$) and two vertical re-entrant viewports ($NA \approx 0.88$). More detailed information on the vacuum setup can be found in [Rie10].

Zeeman Slower and Magneto-Optical Trap

In the oven ${}^6\text{Li}$ is heated up to about 350°C . Apertures the direct the resulting atomic gas towards the Zeeman slower (2). Inside the Zeeman slower, atoms are decelerated from an initial longitudinal velocity on the order of 1500 m/s to a final velocity of about 50 m/s using laser cooling. For this purpose a resonant laser beam is directed counter-propagating the atomic beam. This leads to absorption and subsequent re-emission of photons. Since re-emission of photons is a spontaneous process and hence isometric, this leads to a net momentum transfer slowing down the

¹All viewports are anti-reflection coated for the wavelengths used in the experiment.

3.1. Preparation of a Degenerate Quasi-2D Sample

atoms. Since the deceleration also leads to a spatially varying Doppler shift along the Zeeman slower, a spatially varying magnetic field is applied to compensate this by Zeeman shifting the internal energy states of the atoms [Met02]. In our experiment we use a decreasing field configuration. This way, the anti-Helmholtz configuration of the magneto-optical trap (MOT) coils can sustain the Zeeman slower field all the way to the trap position. This leads to a compact design and a very good capture efficiency in the MOT.

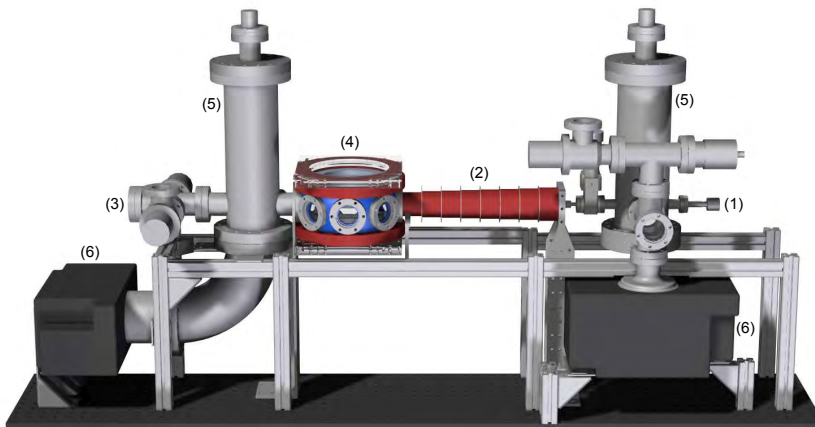


Figure 3.1.: Technical drawing of the vacuum chamber. A small sample of ${}^6\text{Li}$ is heated up in the oven (1). The evaporated atoms then enter the Zeeman slower (2) where they are decelerated by a directed resonant laser beam entering through the window at (3). The atoms are then trapped and investigated in the main chamber (4). The vacuum is sustained by a combination of titanium sublimators (5) and ion pumps (6). Taken from [Rie10].

After this initial drastic reduction in velocity, the atoms can now be trapped inside a MOT. A combination of three retro-reflected near resonant laser beams along three orthogonal directions (red arrows in Figure 3.2) and a magnetic quadrupole field is used to trap the atoms at the zero-crossing of the magnetic field. This is achieved by red-detuning the laser with respect to the resonance and choosing polarizations in such a way that photons are only absorbed from the counter-propagating beam when the atoms drift away from the center of the trap [Met02]. This leads to both a dampening force and a restoring force towards the trap center hence also reducing the temperature. However, the achievable temperature is fundamentally limited [Foo04] by the process of scattering. The minimal achievable temperature is the so-called Doppler temperature T_D and in the case of ${}^6\text{Li}$ is roughly $140 \mu\text{K}$. The MOT lifetime is approximately 23 minutes and thus confirms our very low background pressure.

The required laser light for the steps mentioned above is provided by a tapered amplifier seeded with a diode laser (Toptica TA pro, 200-350 mW depending on the life cycle of the amplifier chip). In the experiment, we make use of the ${}^6\text{Li}$ D2 line which couples the $2^2S_{1/2}$ ground state to the $2^2P_{3/2}$ excited state and has a wavelength of roughly 671 nm. The hyperfine splitting of the excited state is not

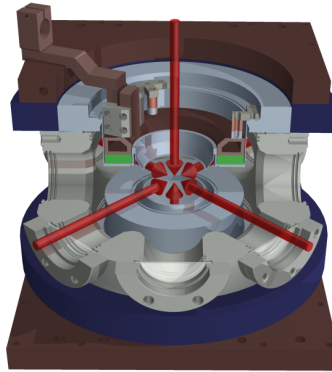


Figure 3.2.: Technical drawing of the main chamber including the MOT beams (red arrows). The linear gradient needed for the MOT is provided by a set coils in anti-Helmholtz configuration (blue). The large homogeneous off-set field needed for adjusting the scattering properties in the experiment is produced via a set of coils in near Helmholtz configuration (green) close to the atoms. All coils are mounted on water-cooled copper heat sinks (brown). Taken from [Wen13].

resolved but the ground state splitting is roughly 228 MHz. Hence, one has to use two laser frequencies labeled cooler and repumper to avoid the accumulation of atoms in an unaddressed dark state. To achieve the required frequency stabilization on the order of 10^{-8} , the TA is beat-offset locked [Sch99] to a separate spectroscopy laser. More details on the spectroscopy laser and the laser setup can be found in [Rie10, Sim10, Peh13].

Optical Dipole Trap and Evaporative Cooling

The achievable phase-space density in the MOT is still several orders of magnitude away from the quantum degenerate regime and hence a different kind of trapping potential is needed which does not rely on resonant photon scattering. One solution is the use of optical potentials [Gri00]. The working principle of an optical dipole trap (ODT) is as follows: although neutral atoms initially do not possess an electrical dipole moment, a far detuned laser beam can induce an electric dipole moment. This induced dipole moment then orients itself in the external laser field to minimize its energy. Depending on the chosen detuning the atoms hence are either trapped in (red detuned) or repelled from (blue detuned) the intensity maximum². Hence, trapping can be achieved by simply focusing a red detuned laser beam. The non-resonant scattering scales as $I\Delta^2$ with the detuning Δ and the intensity I whereas the trap depth scales as I/Δ . Therefore, by choosing a large detuning and large laser power, it is possible to create a trap which is deep enough to trap atoms directly from the MOT without being limited by non-resonant scattering.

In the experiment we use an IPG photonics fiber laser (YLR-200-LP-WC) which provides 200 W at a wavelength $\lambda \approx 1068$ nm. The setup is such that we produce an elliptic beam with an aspect ratio of 1 : 5 using a cylindrical telescope and focus

²Since the trapping is a second order process, the trap depth is proportional to $|E^2|$

it into the chamber. After the chamber, we collimate it again, turn the polarization by 90 degrees to avoid interference using a $\lambda/2$ – waveplate and refocus the beam back into the chamber. There it intersects horizontally with itself under an angle of 12° , producing a surfboard shaped potential with an aspect ratio of $1/\omega_x : 1/\omega_y : 1/\omega_z \approx 8.3 : 44 : 1$ determined from the harmonic trapping frequencies ω_i . More information on the setup of the ODT can be found in [Boh12].

To transfer the atoms from the MOT into the ODT, we ramp down the intensities of the MOT beams. At the end of this ramp, the dipole laser output is ramped quickly to 200 W. Thereby we end up with roughly 10^6 atoms in the ODT. Switching off the cooler beams slightly before the repumper beams ensures that the atoms accumulate in the energetically lower $|F = 1/2\rangle$ hyperfine manifold of the $2^2S^{1/2}$ ground state. Thus, when increasing the magnetic offset field, we end up with a binary mixture of atoms in the hyperfine states labeled $|1\rangle$ and $|2\rangle$. By additionally using a long incoherent rf pulse to drive the transition between these states, we create a balanced fermionic mixture as a starting point.

To reach quantum degeneracy, we use a forced evaporation technique. By continually lowering the trap depth, the hottest atoms are lost while the rest of the sample can re-thermalize via elastic scattering. This relies on sufficiently high scattering rates between the atoms which can be achieved by ramping the magnetic offset field to the vicinity of the broad Feshbach resonance in ^6Li . Hence, by losing particles we can decrease the temperature and thus increase the phase-space density until we reach quantum degeneracy. Depending on the sign of the scattering length, one either ends up with a mixture of fermionic atoms (attractive interactions) or diatomic molecules (repulsive interactions) which eventually condense into a molecular BEC (mBEC). During the course of this thesis we always chose the latter. Thus, we end up with roughly 50,000-100,000 atoms per spin state at temperatures on the order of 100 nK.

Magnetic Field Coils

In the experiment, magnetic offset and gradient fields are used both for trapping as well as manipulating the scattering length via Feshbach resonances. Here, we want to give a short overview about the two coil setups we use throughout the experimental sequence.

The **MOT coils** are two circularly symmetric coils mounted in an approximate anti-Helmholtz configuration which produces the quadrupole field needed for the first trapping step in the MOT (blue part in Figure 3.2). Each coil consists of four axially stacked layers of 25 windings of Kapton coated wire and is mounted onto water cooled copper heat sink. The maximal achievable magnetic field gradient is approximately 85 G/cm at a current of 70 A and the direction of the gradient field can be inverted using a logic circuit. This is used in later stages of the experiment to apply a gradient field which counters the gravitational force experienced by the atoms as well as to apply a strong gradient to achieve a spatial dependent rf transition frequency in tomographic measurements. We can stabilize the gradient to a relative precision of approximately 10^{-3} by measuring the current through the coils with a current transducer and using it as the feedback for a digital PID loop.

The **Feshbach coils** are used to produce the large magnetic offset fields on the order of 1000 G needed to access the Feshbach resonances in our ${}^6\text{Li}$ system. In order to reduce the required currents, they are mounted directly on top of the viewports in the vertical direction as can be seen by the green part in Figure 3.2. However, with our current setup of 33 windings, we still need to operate with currents on the order of 100 A which leads to considerable heating of the coils. Therefore, the coils are directly glued onto custom-designed water cooled heat sinks using a thermally conducting but electrically isolating diamond filled epoxy. This allows us to operate the coils at 120 A continuously without exceeding a temperature of 50 °C. The coils are set up with a slightly larger distance than the Helmholtz criterion. This produces a magnetic field saddle in the horizontal plane and an anti-confinement in the vertical plane. The saddle potential has a trap frequency of approximately $\omega_{r,\text{mag}} = 2\pi \times 12.2 \text{ Hz}$ at 700 G and its magnetic field dependency is $\omega_{r,\text{mag}}(B) = 0.46\sqrt{B} [\text{G}]$. This confinement increases the weak optical one in the horizontal plane and it is an important ingredient for our radial momentum imaging technique [Mur14]. The anti-confinement in the vertical direction is usually negligible compared to our optical trapping frequencies. The stabilization of the magnetic field is done by measuring the current through the coils with a current transducer and using a digital PID feedback loop with a precision of 16 bit and a speed of 100 kHz to control the voltage of the power supply. For magnetic field critical measurements like the rf measurements described in chapter 5, we can increase the precision of the regulation with a differential amplifier circuit. Therefore, we take the difference from the current transducer signal and a high precision reference voltage and amplify it with a differential amplifier. This increases the dynamical range and we can achieve a magnetic field stability of up to 1 mG, which corresponds to a relative stability on the order of $1.25 \cdot 10^{-6}$. More information on the stabilization can be found in [Pre14].

3.1.1. Standing Wave Trap (SWT)

In order to reach the quasi-2D regime as described in section 2.2.1, one needs to introduce a large anisotropy in the trapping potential. In our setup, this is achieved by transferring the atoms from the crossed-beam ODT (CBODT) into a strongly anisotropic optical potential formed by one interference maximum of a standing-wave dipole trap (SWT). In this section we will discuss the conditions which need to be fulfilled to reach the quasi-2D regime. We will then introduce our setup and present the transfer protocol. At last we summarize the relevant measurements to prove experimentally that we fulfill these conditions. All of this can be found in more detail in [Boh12, Nei13, Rie15b].

The Quasi-2D Regime

In a harmonic trap, the strength of the confinement determines the trapping frequency ω and thus the energy needed to populate the excited levels. For a 3D trap where one of the axes has a much stronger confinement³ $\omega_z \gg \omega_{x,y}$, the radial levels

³In our case we define this always to be the z-axis

will be populated first before any excitation along the axial level occurs. Therefore, if both the chemical potential $\mu < \hbar\omega_z$ and the temperature $\kappa_B T < \hbar\omega_z$, then all excitations appear only in the radial plane and the atoms are in their axial ground state. The system can then be treated effectively in a 2D framework. Thus, to reach this regime, we have to reduce both the atom number as well as the temperature.

For $T = 0$ we can calculate the maximal atom number before any excitation in the z-axis occurs by counting the number of possible radial excitations before acquiring any axial excitation. This is given by the relation

$$n_x \hbar\omega_x + n_y \hbar\omega_y < \hbar\omega_z, \quad (3.1)$$

where $n_{x,y}$ is the number of the populated level in the radial plane. The maximum number of atoms per spin state in the axial ground state can then be calculated as

$$N_{\max} = \frac{1}{2} n_{x,\max} n_{y,\max} = \frac{\omega_z^2}{2\omega_x\omega_y}. \quad (3.2)$$

This formula does not account for the effect of interactions, finite temperature or trap anharmonicities. However, these effects do not change the basic need for a large anisotropy in the trapping potential. In our trap geometry we reach an aspect ratio $\omega_z/\omega_r \approx 314 : 1$ and thus we can at most have $\approx 49,000$ atoms per spin state in order to reach the quasi-2D regime.

Experimental Setup

The schematic on how we produce the trap can be seen in Figure 3.3 a). A single elliptical laser beam with wavelength $\lambda = 1064$ nm and aspect ratio 1:8 is focused with a $f = 900$ mm lens and directed under a 45° angle into our custom made interferometer box. There it is split using a 50/50-beamsplitter and the resulting beams are then directed towards our experimental chamber using two 1/2" mirrors where they intersect under an angle of 14° . This intersection leads to an interference pattern and thus a stack of optical potentials as can be seen in b) as the green discs. The distance between the potentials is approximately $4.4 \mu\text{m}$ which is much larger than the typical harmonic oscillator length of $l_z \approx 550$ nm in the axial direction. Therefore, tunneling between the layers can be neglected.

At typical experimental parameters, the axial trap frequency is $\omega_z \approx 2\pi \times 6.95$ kHz and the trap frequencies in the radial plane are $\omega_x \approx 2\pi \times 23.4$ Hz and $\omega_y \approx 2\pi \times 21.2$ Hz including the magnetic confinement from the saddle point potential of the Feshbach coils. This results in an aspect ratio $\omega_x : \omega_y : \omega_z \approx 1.1 : 1 : 327$ and thus we can trap up to 49,000 atoms per spin state while still being in the quasi-2D regime. To avoid parametric heating in the trap, we use a 50 W NUFERN SUB-1174-22 fiber amplifier which is seeded by an Innolight Mephisto-S 500NE solid state laser at 1064 nm with low intensity-noise profile. More information on the laser setup can be found in [Nei13].

In order to transfer the sample from the CBODT into a single layer of the SWT optimally, one has to match both the relative axial position of these traps as well as the axial extension of the sample. To reduce the axial extension in the CBODT, we

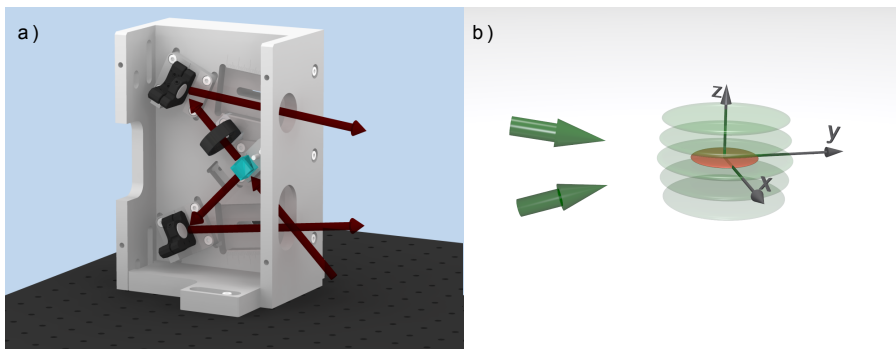


Figure 3.3.: a) CAD drawing of the custom made interferometer box. An elliptical beam enters the case under an angle of 45° . It is then split by a 50/50-beamsplitter and the two resulting beams are directed towards the main experiment chamber using two $1/2$ " mirrors. The beams then intersect under an angle of 14° in the vertical plane and the resulting interference pattern leads to a stack of optical potentials with a large aspect ratio (green discs in b)). By means of an appropriate transfer protocol, we are then able to load almost all atoms into a single potential layer.

flattened the trap in the axial direction by using an elliptical beam with an aspect ratio of 1:5 [Boh12]. In addition, we perform the evaporation on the repulsive side of the Feshbach resonance where molecules form and we end up with a mBEC. This reduces the size of the cloud compared to a Fermi gas considerable due to the absence of the Fermi pressure. To further reduce the axial size, we modulate the frequency of the horizontal AOM of the CBODT beam to create a time-averaged potential in the horizontal plane [Rie15b]. This effectively reduces the axial size and in addition leads to a better mode overlap between the initial flattened cigar-shaped CBODT potential and the round SWT potential. To optimize the positional overlap between the two traps we can adjust the axial position of the mBEC in the CBODT by applying a gradient with the MOT coils of up to ± 6 G/cm. Thereby we can fine tune the vertical position to a precision on the order of the width of one layer.

The total transfer protocol is shown in Figure 3.4. At the beginning of the transfer, we increase the trap depth in the CBODT to reduce the size. We then reduce the magnetic field to decrease the repulsive inter-particle interactions and thus increase the density. We then apply the gradient to shift the cloud in the axial direction and modulate the CBODT to increase the mode overlap between the traps. We then ramp up the power of the SWT and ramp down the power in the CBODT trap before we switch it off. With this scheme we can transfer up to 90% of the atoms into a single layer.

After the transfer, we apply a second evaporative cooling scheme. This has several advantages: first of all the sample is cooled again and thus any heating occurring in the transfer process can be reduced. Secondly, we can set the final atom number in a more controlled manner as any losses in the transfer process can be offset. The evaporative cooling is realized by a spilling technique. We apply a strong magnetic field gradient on the order of 30 G/cm while simultaneously reducing the trapping potential. Thereby hot atoms lost from the central layer are quickly pulled away by

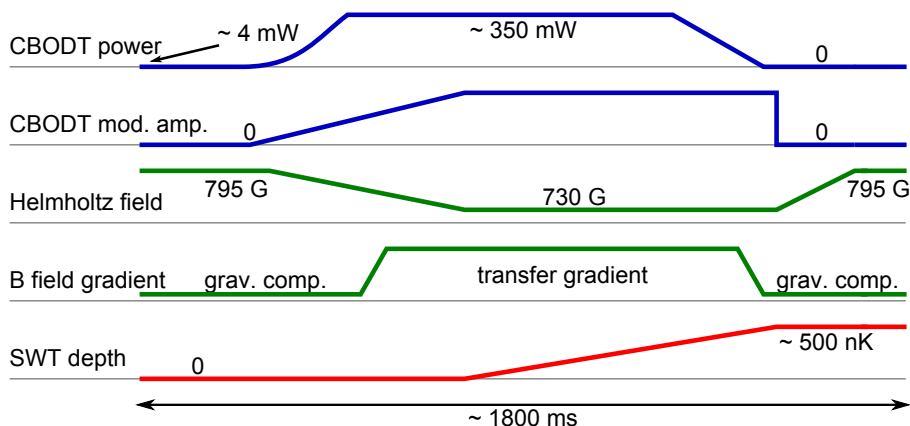


Figure 3.4.: Schematic of the transfer protocol. The CBODT trap as well as its modulation amplitude is ramped up to compress the sample and create the time-averaged potential. At the same time, the magnetic field is reduced to decrease the repulsive inter-particle interactions. By applying a magnetic field gradient, the sample is shifted along the z -axis to achieve the optimal overlap with a single layer of the SWT potential. At last the power in the SWT is ramped up while the power in the CBODT is reduced before it is switched off. We then adjust the magnetic field offset again to the desired value. Taken from [Rie15b]

the gradient and cannot be trapped in adjacent layers. After this spilling process we ramp up the trap potential again and turn off the magnetic field gradient. Hence, by adjusting the final trap depth during the spilling we set the final atom number as well as the temperature. We typically end up with ≈ 35.000 atoms at a temperature of ≈ 70 nK.

Loading a Single Layer

In order to optimize the transfer procedure, we need a method to experimentally measure the transfer efficiency into a single layer. This is challenging as the distance between individual layers is only $\Delta z \approx 4.4 \mu\text{m}$ and therefore to resolve this optically one would need an imaging setup with high enough resolution. However, high resolution always results in a small depth of focus. This is a limiting factor since the weak confinement in the horizontal plane leads to samples with diameters on the order of $300 \mu\text{m}$. Thus, even with the required resolution in the z -axis, our sample is then much larger than the depth of focus and we could not resolve the distance between the layers by optical means.

To circumvent this, we use a method which relies on radio frequency tomography. It has been described in detail in [Nei13, Rie15b] and will be shortly summarized here. After the transfer of our mBEC sample into the SWT, we polarize the sample by illuminating it with a short imaging pulse resonant to the atoms in state $|1\rangle$. As the transferred momentum of the photons is much larger than the trap depth, these atoms are then lost from the trap. For our evaporation scheme where we end up with a molecular sample we cannot set the interaction strength to zero by means of

the Feshbach resonance as the molecules can relax into deeply bound states and are then lost from the trap. Thus, the imaging pulse to remove one of the spin states also transfers momentum to the remaining atoms and heats the sample, which can be either in state $|2\rangle$ or $|3\rangle$ depending on the prepared mixture. To minimize this heating, which is small compared to the trap depth, we ramp the magnetic field to 1100 G, across the resonance, where we have free atoms and the interaction is reduced⁴. We then apply a strong magnetic field gradient of about 70 G/cm along the z-axis using the MOT coils. This gradient leads to a spatial dependent shift in the resonance frequency of the rf transition between state $|2\rangle$ and $|3\rangle$ of about 45 Hz/ μm . Thus, the splitting between neighboring layers is approximately $\Delta\nu_{\text{rf}} \approx 200$ Hz and can be resolved in our setup. However, this large gradient also leads to losses in the trap, predominantly in the central layer. To minimize these, we ramp up the trap depth of the SWT to the maximum feasible value, which increases the trap depth by a factor of roughly 1.4. We then scan the applied rf frequency and take an absorption image of the transferred atoms along the horizontal imaging axis for each frequency. To improve the signal-to-noise ratio, we average the signal at each frequency over 10 repetitions. Additionally, we use long rf pulses with $\tau_{\text{rf}} = 25$ ms such that the Fourier limit is well below 200 Hz. From a Gaussian fit we then obtain the number of transferred atoms at each frequency. This is shown exemplary in Figure 3.5 for the optimized transfer parameters in the 13-mixture. The blue line is a fit of three Gaussian profiles with identical width σ but different position and amplitude. The grey lines are the individual Gaussian profiles. From the fits we obtain that the majority of transferred atoms is in the central layer and only $\approx 10\%$ of atoms is in adjacent layers. The frequency resolution of the rf transition is ≈ 80 Hz and thus we are just on the edge of being able to resolve the individual layers. Note that we perform the rf tomography before we do the final spilling inside the SWT. This will remove particles predominantly in the central layer. Hence, we underestimate the fraction of atoms in adjacent pancakes. This is further discussed in section 5.3.7. This can be improved by doing the rf tomography after the spilling process, but has the disadvantage of a worse signal-to-noise ratio.

The rf tomography relies on a high magnetic field stability as shifts in the magnetic offset field during the measurement would lead to a loss of resolution. This is achieved with the differential offset amplifier circuit described above in the coil section. We measured the long-term magnetic field stability to be better than 1 mG and thus our frequency stability is on the order of 10 Hz [Rie15b].

Reaching the Quasi-2D Regime

To verify experimentally whether we are in the quasi-2D regime, we perform a measurement of the axial momentum distribution as described in [Dyk11]. We ramp the sample across the resonance to the attractive side and weak interactions which are limited by the background scattering length of ${}^6\text{Li}$. For the 13-mixture this is already achieved at $B = 1100$ G whereas we have to ramp to 1400 G for the 12-mixture. We then switch off the SWT and let the sample expand for 3 ms. Due

⁴Note that this still corresponds to about $a_{3\text{D}} \approx -2000 a_0$ as the background scattering length in ${}^6\text{Li}$ is dominated by the triplet state.

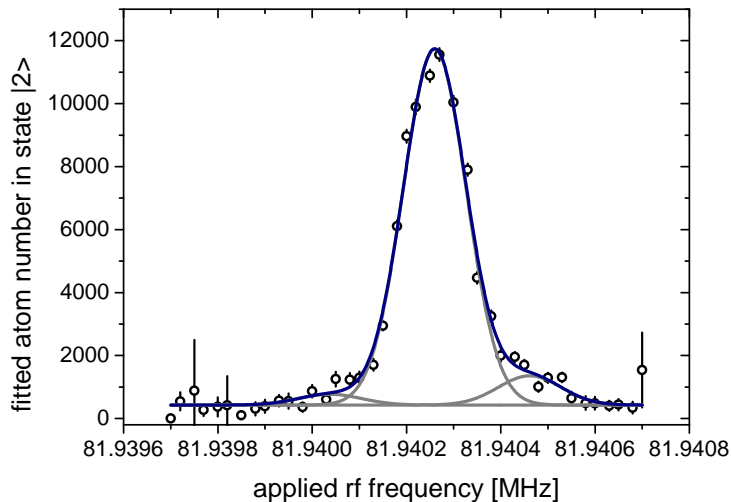


Figure 3.5.: Typical rf tomographic measurement for a sample initially in the 13-mixture. The fitted atom number is plotted against the applied rf frequency. A dominant peak is visible which stems from atoms in the central layer. However, also two smaller peaks on each side can be identified which arise from a small number of atoms in the two adjacent layers. To estimate the relative population in each layer, a sum of three Gaussian profiles with identical width σ is fitted (blue line). The grey lines indicate the individual Gaussian profiles. From this one can estimate that around 90 % of the atoms are in the central layer.

to the strong confinement the sample expands rapidly along the z -axis and thus scattering during the expansion can be neglected. We then image the sample from the side and fit its size along the vertical axis with a Gaussian profile. We perform this measurement for different final spill depths and measure the atom number at each spill depth additionally with our calibrated top-down imaging. From these two measurements we then obtain the plot depicted in Figure 3.6. Here the axial width σ_z after the time-of-flight is plotted versus the atom number in the trap. At low atom numbers the width stays constant until it starts to grow rapidly above a threshold of roughly 50.000 atoms. This behavior can be understood when looking at the evolution of a non-interacting atom in the axial ground state. The ground state of an harmonic oscillator can be described by a Gaussian wave packet. A dispersing Gaussian wave packet keeps its Gaussian form with a time-dependent increasing width $\sigma_z(t)$ of the form [Sch07b]

$$\sigma_z(t) = \sqrt{\frac{\hbar}{2m_{\text{Li}}} \left(\frac{1}{\omega_z} + \omega_z t^2 \right)}. \quad (3.3)$$

In the case of our experimental parameters $\omega_z \approx 6.95$ kHz and $t = 3$ ms, this results in a width of $\sigma_z \approx 45.5 \mu\text{m}$. Our experimentally determined plateau deviates less than 1 % from this estimation and thus treating the expansion as non-interacting is well justified. As the Gaussian wave packet in the ground state has minimal dispersion and initial size, the observed increase in σ_z at larger atom numbers can

be attributed to a gradual population of excited levels in the axial direction. To estimate the point where this starts to happen, we fit both the plateau and the slope linearly (blue lines). We then define the threshold as the intersection of the two lines. This yields $N_{\max} \approx 55,000$ atoms which is roughly what we expect. The larger observed number could be due to the fact that we overestimate our atom number by at least 10% due to atoms in adjacent layers. In our experiments we typically prepare around 35,000 atoms per spin state and hence we are well below this limit and thus assume that our systems behaves quasi-two dimensional.

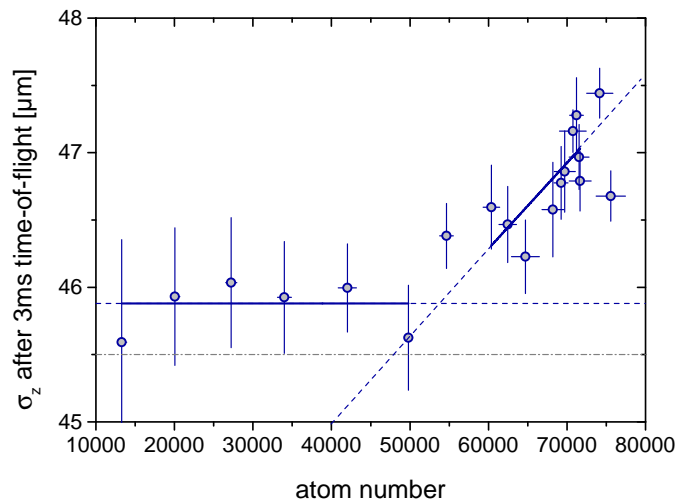


Figure 3.6.: The axial Gaussian width σ_z for a 3 ms time-of-flight is plotted versus the atom number in the trap. Below a threshold atom number N_{\max} , all atoms are in the axial ground state and σ_z shows a plateau. For $N > N_{\max}$, a gradual increase in the population of axial excitations then leads to an increase in σ_z . Each data point is an average of ~ 15 individual measurements and the error bars represent the standard error of the mean (SEM). The gray dash dotted line is the expected width of the axial ground state from theory. The blue lines represent linear fits to the plateau as well as the slope. From an extrapolation of these two fits we obtain a threshold atom number of $N_{\max} \approx 55,000$ atoms per spin state.

Note that this measurement only works for weak interactions and cannot be performed in the strongly interacting regime. However, due to the increased attractive interactions on the BCS side as well as the molecule formation on the BEC side, this gives us a lower bound for the threshold atom number as these effects reduce the energy in the system.

3.1.2. Lattice

In addition to the SWT we also have a square lattice setup which can be additionally switched on to impose a lattice geometry onto the atoms in the single layer. The experimental setup and first experiments are described in detail in [Bay15]. Here

we give a quick overview as we use the lattice to determine the magnification of our top-down imaging system in section 3.2.3.

The principal idea of the lattice setup can be seen in Figure 3.7 a). Two (almost) retro-reflected infrared beams (yellow) are crossed othogonally to produce a square lattice in the xy-plane. Together with the strong axial confinement due to the SWT this then creates a 2D lattice. The lattice beams in each arm are actually not retro-reflected but cross under a small angle of $\approx 14^\circ$ as can be seen in Figure 3.7 b). As we use the same infrared laser source ($\lambda = 1064 \text{ nm}$) as for the SWT, this leads to a lattice spacing $d = \frac{\lambda}{2 \cos \Phi} = 536 \text{ nm}$. Similar to the SWT, we use elliptical beams with an aspect ratio 6.7 : 1 in the vertical axis. This allows us the decrease the focal spot size in the vertical direction and we end up with a focal spot size of $40 \mu\text{m} \times 270 \mu\text{m}$.

In order to avoid any interference between the different lattice arms and the SWT, we detune each arm by passing the laser beam through an AOM. Thereby we also stabilize and control the laser power in each arm. The used frequencies are +100 MHz for the SWT, +110 MHz for lattice 1 and -100 MHz for lattice 2. Additionally, also the polarization is chosen such that the lattice 1 beam is vertically polarized whereas the lattice 2 beam and the SWT beam are horizontally polarized. More information on the setup can be found in [Bay15].

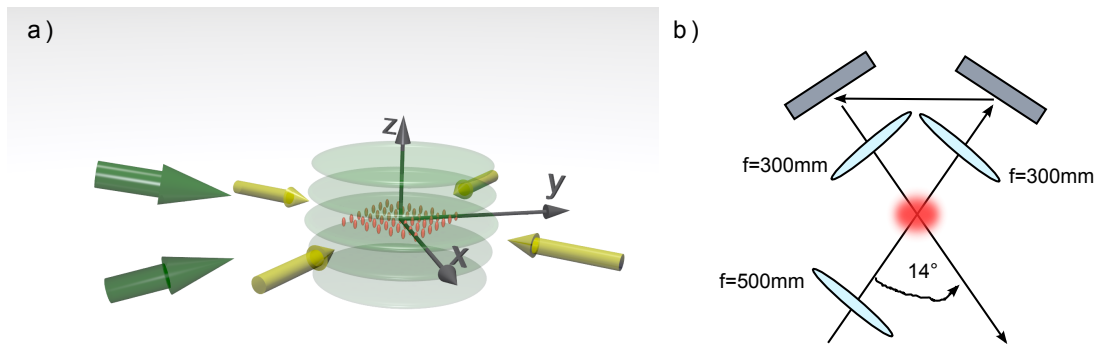


Figure 3.7.: a) Sketch of the combination of the SWT beams (green) and the lattice beams (yellow). The interference of the SWT beams leads to a stack of round anisotropic potentials. Together with interfering retro-reflected lattice beams this leads to a square lattice potential for the atoms (red). b) The lattice beam configuration is not retro-reflected but set up under a small angle 14° .

3.1.3. Preparation of a 13-Mixture

The experimental scheme described so far results in the preparation of a degenerate Fermi mixture in the hyperfine states $|1\rangle$ and $|2\rangle$. Although the tunability of the Feshbach resonance is very similar for all mixtures, it is sometimes advantageous to prepare the sample in a different mixture. This can be seen e.g. in chapter 5, where

we use rf transitions to gain insight into the system. There, one has to consider not only the interactions in the initial state but also the interactions in the final state after the transfer. Thus, it is useful to start with a mixture where the final state interactions are weak. Another aspect is that the hyperfine state $|3\rangle$ is best suited for detection purposes as its imaging transition is closed for all magnetic fields and thus one does not have to deal with dark state decay. This will be discussed in section 3.2.3.

Therefore, we also prepare a balanced $|1\rangle$ - $|3\rangle$ mixture in our experiment in some cases. The overall preparation scheme is very similar to the case of the $|1\rangle$ - $|2\rangle$ mixture but deviates at the start of the evaporative cooling. After reducing the laser power to 40 W, we keep it constant and ramp the magnetic field to a value of 560 G. Since we are still at large temperatures, no molecules have formed yet and thus this ramp does not lead to losses. We then perform a Landau-Zener passage⁵ [Lan32, Zen32] to transfer the population adiabatically from state $|2\rangle$ to state $|3\rangle$. The principle of Landau-Zener passages can be understood in a dressed state picture [Dal85] as an avoided crossing. At the beginning of the passage, the applied rf frequency $\omega_{\text{rf}} = \omega_0 - |\delta|$ has a large detuning $\delta \gg \Omega$ compared to the resonance frequency ω_0 where Ω is the Rabi frequency. The initial state can then be written as a dressed state of the form $|d_{-}\rangle = c_2(\delta, \Omega)|2\rangle - c_3(\delta, \Omega)|3\rangle$ with $c_2 = 1$ and $c_3 = 0$. If one now sweeps the frequency adiabatically across the resonance up to the end frequency $\omega_{\text{rf}} = \omega_0 + |\delta|$, the dressed state evolves and the coefficients are now $c_2 = 0$ and $c_3 = 1$. Thus, one transfers all population into the previously unoccupied state.

Optimizing the ramp speed, detuning and applied rf power, we are then able to transfer roughly 90% of the atoms in state $|2\rangle$ to state $|3\rangle$. Note that we cannot balance the $|1\rangle$ - $|3\rangle$ mixture with a long incoherent rf pulse as we cannot drive a direct transition between these states. Furthermore, since the transfer efficiency is not perfect, we will lose a part of the atoms in three-body collisions between the three different states. Therefore, the evaporation scheme for the $|1\rangle$ - $|3\rangle$ mixture is not as efficient. The evaporation is performed analogously to the $|1\rangle$ - $|2\rangle$ mixture by reducing the trapping potential and setting the magnetic field close to the Feshbach resonance which is now at a magnetic offset field $B \approx 690$ G. Similarly to before, we then end up with a mBEC in our optical dipole trap, which is then the starting point for the experiments.

3.2. Detection of Ultracold Gases

All our experiments are conducted inside a UHV-chamber to avoid any contact of the sample with the environment. Thus, for probing the system one can only rely on optical methods. Different methods like absorption imaging, fluorescence imaging or phase-contrast imaging [Ket99] have been developed. Methods like absorption and fluorescence imaging rely on resonant light scattering and are thus inherently destructive. Other methods like phase-contrast imaging use non-resonant light and

⁵The advantage of the Landau-Zener passage compared to a π -pulse, where one directly drives the transition on resonance, is that it is less sensitive to drifts in the system.

are non-destructive. All these methods have their specific strengths and weaknesses and are used throughout the quantum gas community.

In this work the absorption imaging technique was applied. At its core, absorption imaging measures the transmittance of a sample from which the column density along the imaging axis can be deduced. The section starts by recalling the basic principle of absorption imaging and the deduction of the column density from such measurements in 3.2.1. Subsequently, our experimental imaging setup including the laser stabilization is presented in 3.2.2. Then, a detailed description of our imaging calibration is given in 3.2.3 and the construction of the density profiles from the raw camera images as well as the estimation of the ensuing density uncertainty due to the imaging calibration is shown in 3.2.4. At last, an extension of the setup is presented which allows to image two hyperfine states in quick succession and thus obtain the full information on the system. This option was not utilized yet in this thesis but provides exciting possibilities for future experiments.

3.2.1. Absorption Imaging

To perform absorption imaging, one shines in a resonant laser beam onto the atoms and images the shadow caused by partial absorption of the beam onto a camera. Comparing an image $I_{\text{abs}}(x, y)$ where atoms are present to a reference image $I_{\text{ref}}(x, y)$ without atoms one can then infer the column density of the sample along the imaging axis⁶. For a 3D sample, the attenuation of the imaging beam with intensity I along the sample can then be described via the Lambert-Beer law [Bee52]

$$\frac{dI}{dz} = -n_{3\text{D}}(x, y, z) \sigma(I) I, \quad (3.4)$$

$$\sigma(I) = \frac{\sigma_0}{1 + I/I_{\text{sat}}}, \quad (3.5)$$

where $n_{3\text{D}}$ is the atomic density, σ is the intensity dependent scattering cross section for resonant light, which at low intensities reduces to $\sigma_0 = 3 * \lambda^2/2\pi$, and I_{sat} is the saturation intensity. The saturation intensity I_{sat} depends on the transition and for the D2-line used in the experiment $I_{\text{sat}} = 2.54 \text{ mW/cm}^2$ [Geh03].

In the low intensity limit $I \ll I_{\text{sat}}$, the scattering cross section is constant and equation 3.4 can be solved using the constraints $I(z = -\infty) = I_{\text{ref}}$ and $I(z = \infty) = I_{\text{abs}}$ which results in

$$n_{\text{col}}(x, y) \sigma_0 = -\ln \left(\frac{I_{\text{abs}}(x, y)}{I_{\text{ref}}(x, y)} \right), \quad (3.6)$$

where $n_{\text{col}}(x, y) = \int n_{3\text{D}}(x, y, z) dz$ is now the column-integrated 3D density. In this limit, only relative intensities are of importance. This makes this method very suitable since an exact camera calibration is not needed as long as it operates in a linear regime. However, this limit also has some drawbacks. In order to not be limited by photon-shot noise on the camera, one has to illuminate the sample for

⁶We set the imaging axis to be along the z-axis for the rest of this section.

long exposure times. Since ${}^6\text{Li}$ atoms have a small mass, the recoil momentum is $v_{\text{rec}} \approx 0.1 \text{ m/s}$ [Geh03] and thus the atoms are accelerated out of the focal plane. In addition, they acquire a Doppler shift and due to the isotropic re-emission they also acquire momentum in the orthogonal plane, leading to a decreased resolution. Also for very dense samples the transmitted light can be very small.

The above considerations require us to use large intensities $I \sim I_{\text{sat}}$ in our experiments. Then the intensity dependence of the scattering cross section cannot be ignored and the solution to equation 3.4 is

$$n_{\text{col}}(x, y) \sigma_0 = -\ln\left(\frac{I_{\text{abs}}(x, y)}{I_{\text{ref}}(x, y)}\right) + \frac{I_{\text{ref}}(x, y) - I_{\text{abs}}(x, y)}{I_{\text{sat}}}. \quad (3.7)$$

This effectively adds a correction term to the low intensity solution. In this term the absorption and reference image intensities are now relative to the saturation intensity. Therefore, we now have to calibrate how our camera counts translate into intensity and an exact knowledge of the camera properties is required. Note that the term $n_{\text{col}}\sigma_0$ is commonly referred to as the optical density (OD).

2D Case

The derivation in equation 3.7 relied on the fact that the intensity of the incoming laser beam is continually reduced as it passes through the atomic cloud. In our experiments, however, we have a strongly confined sample in the z -direction with an axial extent l_z on the order of 500 nm. Therefore, all atoms within the plane should experience a similar imaging intensity, making the above ansatz questionable at best. Here we show an alternative derivation using a probabilistic ansatz as introduced in [Yef11, Hun11].

For N atoms inside a small area A , the number of scattered photons N_{sc} is given by $N\gamma\tau$, where $\gamma = \sigma I / (\hbar\omega_L)$ is the scattering rate and $\tau \gg 1/\Gamma$ is the illumination time. In this case ω_L describes the laser frequency and Γ is the linewidth of the transition. Hence, when illuminating the area with N_0 incident photons, the number of transmitted photons N_t is then given as $N_t = N_0 - N\gamma\tau$. Using the definition of γ and the fact that $n = N/A$, we can then convert this into an equation for the transmitted intensity I_t as

$$I_t = I_0 - n\sigma I, \quad (3.8)$$

where I is now an effective intensity determining the scattering rate σ . In addition, the probability of transmitting an incident photon in this area is given by $(1 - \sigma/A)^N$. If the optical density $n\sigma \lesssim 1$, then this can be approximated by $e^{-n\sigma}$ which leads to

$$\frac{I_t}{I_0} = e^{-n\sigma}. \quad (3.9)$$

In our experiments we typically have $n\sigma \lesssim 0.3$ and thus this approximation is justified. Using equation 3.8 and 3.9 as well as the definition of the scattering cross section in equation 3.5, we can then eliminate the effective intensity and end up with

$$n\sigma_0 \approx -\ln\left(\frac{I_t}{I_0}\right) + \frac{I_0 - I_t}{I_{\text{sat}}} \quad (3.10)$$

which is identical to equation 3.7 derived for a 3D sample.

3.2.2. Experimental Imaging Setup

In order to perform absorption imaging, our laser source has to fulfill several criteria: first its linewidth has to be narrow compared to the linewidth $\Gamma = 5.872$ MHz of the used imaging transition. Furthermore, its frequency has to be adjustable over a wide range on the order of GHz as the resonance frequency for the transition tunes with the magnetic field. At last, the frequency stabilization has to be fast on the μ s timescale in order to allow us to adjust the frequency during the imaging. This is needed to compensate for the Doppler effect during imaging which effectively drives the atoms out of resonance. The Doppler-compensation is described in more detail in section 3.2.3.

In the experiment we therefore use a Toptica DL100 Pro diode laser, which is beatoffset-locked [Sch99] to a spectroscopy laser which is frequency stabilized to the D2-line, exciting atoms from the $F = 3/2$ hyperfine ground state at zero magnetic field. A sketch of the setup is shown in Figure 3.8 a). A small part of the laser output is separated for the beatoffset-lock using a glass window. The main part of the laser output passes an acousto-optic modulator (AOM), where its frequency is shifted by 80 MHz, and a laser shutter before it is coupled into an optical fiber which transfers the laser output to the experiment. The AOM is used mainly as a switch to control the imaging pulse duration on a microsecond level. The shutter is added to minimize stray light.

The beatoffset-lock scheme was described in detail in [Bak14, Kra15, Ste16]. It enables us to control and stabilize the laser frequency on an accuracy level of $\Delta f/f \sim 10^{-10}$. To do this, the imaging laser beam is overlapped with the spectroscopy beam on a photodiode. The resulting beat-signal with frequency f_{beat} is then mixed with the frequency output f_{DDS} of a direct digital synthesizer (DDS), which acts as a programmable frequency source. After low-pass filtering, the resulting signal is then split and a phase shift is introduced using a delay line before the signals are mixed again. Subsequently, the signal passes another low-pass filter which results in a constant error signal

$$U_{\text{err}} = \cos(2\pi\Delta\phi), \quad (3.11)$$

where the phase shift $\Delta\phi$ is proportional to the frequency difference $\Delta f = f_{\text{beat}} - f_{\text{DDS}}$. Therefore, using this signal as a feedback for the imaging laser stabilization, we can adjust the laser frequency by changing f_{DDS} . The PID-feedback is done via the Toptica Digilock module. It converts the analog error signal to a digital one with an analogue-digital converter (ADC). The slow part of the signal is fed⁷ to a piezo-controller which sets the diode laser frequency by tuning the angle of the external cavity grating. This enables long-term stability but cannot correct for changes on timescales $< 100 \mu$ s. To correct for changes on smaller timescales, the fast changing part of the error signal is fed to diode laser current with a sampling rate of 100 MHz. For a sudden change in frequency of 20 MHz, the regulation only needs about 1μ s to adjust its frequency within 90% [Ste16]. This is important for the frequency ramps on the order of $1 \text{ MHz}/\mu\text{s}$ we drive in the experiment to compensate for the Doppler effect. This shows that the laser frequency can follow these frequency ramps without

⁷This is done with a DAC with a sampling rate of 100 kHz.

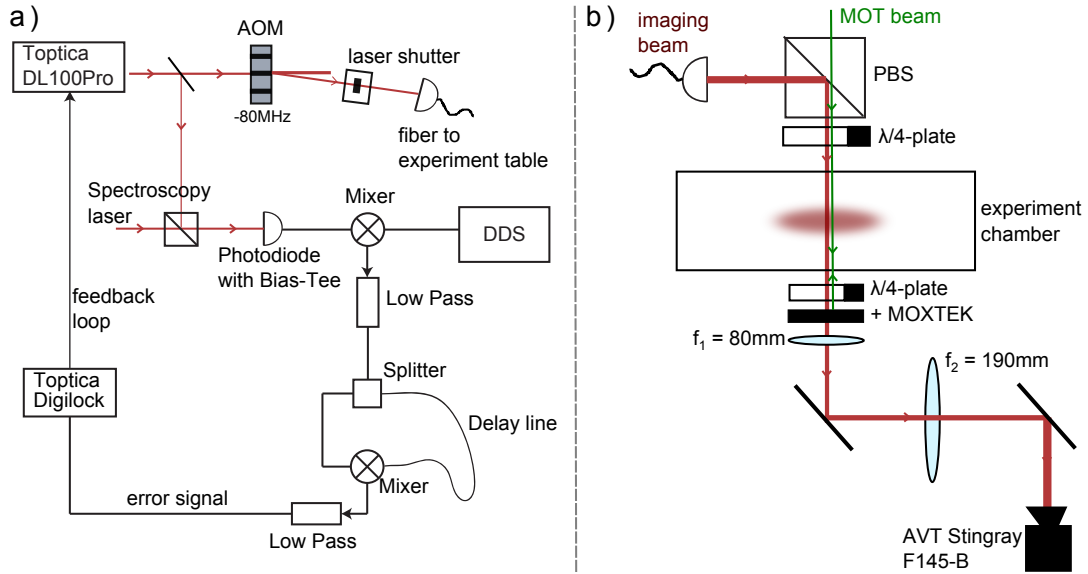


Figure 3.8.: a) Imaging laser setup. The laser output is frequency shifted by an AOM, which also acts as a switch, and coupled into an optical fiber. Additionally, a laser shutter is used to reduce the amount of stray light. A small fraction of the laser output is branched off and overlapped with a spectroscopy laser on a photodiode. The resulting beat signal is mixed with the frequency output of a direct digital synthesizer (DDS) and using shown electronic circuit an error signal is produced. The error signal is then fed into a Toptica Digilock module and used for the control loop of the laser output frequency. b) Imaging setup in the experiment. Both the MOT beam (green) as well as the imaging beam (red) are overlapped with a polarizing beam splitter (PBS) and pass a $\lambda/4$ -waveplate in order to create the required circular polarization. After passing the chamber, another $\lambda/4$ -waveplate transforms the polarization back to linear and a MOXTEK reflective polarizer transmits the imaging beam but reflects the MOT beam. The atoms are then imaged with an AVT Stingray F-145B camera using a combination of a $f_1 = 80\text{mm}$ and $f_2 = 190\text{mm}$ achromatic lenses. This results in an experimentally calibrated magnification of $M \approx 2.14$.

a delay. Apart from the responsiveness, the combined feedback loop also achieves a frequency stability of approximately 120 kHz [Ste16], which is much narrower than the transition linewidth $\Gamma = 5.872$ MHz for the D2-line. Therefore, our assumption of resonant scattering is well fulfilled.

The imaging setup we use for the top-down imaging along the z -axis is displayed in Figure 3.8 b). The imaging beam is overlapped with the MOT beam using a polarizing beam splitter (PBS) cube. Subsequently, both beams pass a $\lambda/4$ -waveplate which results in the σ^- -polarization needed for imaging. It then passes through the vertical viewport of our main experiment chamber where parts of it are scattered by the atom cloud. The viewport is anti-reflection coated and has a reflectivity $R \approx 0.3\%$. After exiting through the opposite viewport, the beam passes another $\lambda/4$ -waveplate and a MOXTEK reflective polarizer. This combination, reverts the polarization of both the imaging and MOT beam to a linear one and the imaging beam is transmitted through the MOXTEK whereas the MOT beam is reflected. To image the atom distribution onto a CCD-camera, we then use the combination of a $f_1 = 80$ mm and a $f_2 = 190$ mm achromatic lens as depicted. As a camera we use an AVT Stingray F145-B which is characterized in section 3.2.3. This setup gives us a magnification of roughly $M \approx f_2/f_1 = 2.38$. In section 3.2.3 we will see that the experimentally deduced value is slightly smaller.

All optical elements between the atomic plane and the camera can cause reflections and thus reduce the light power which reaches the camera. We experimentally calibrate the losses by measuring the imaging beam power with a commercial power meter⁸ in front of the main chamber and directly in front of the camera. Taking into account the reflectivity of the viewport, we then obtain the factor $T = 0.77 \pm 0.03$. This factor is needed when converting the measured counts on the camera into an intensity.

The achievable spatial resolution is limited by the numerical aperture $NA \approx 0.14$ to $d_{\min} = 2.9 \mu\text{m}$. The depth of focus is estimated by $z_{\text{DoF}} = \frac{4\lambda}{NA^2} \approx 137 \mu\text{m}$ and is therefore much larger than the spatial extent of the cloud along the z -axis.

3.2.3. Imaging Calibration

In our experiments, the only available observable we have is the integrated density distribution $n_{\text{col}}(x, y)$ we obtain from absorption imaging along the line of sight. It is therefore crucial to carefully calibrate all the factors which influence its calculation. Here we give a detailed description of the calibration of our imaging system in the vertical direction. The other directions are not calibrated as we only use them for alignment purposes. This section starts with the camera characterization which is needed to convert the measured counts on the camera into an intensity. Next our determination of the imaging magnification M is given. Afterwards we discuss how the Doppler effect influences the imaging and how we experimentally compensate for that. Next, we calibrate the influence of experimental imperfections, for example non-perfect polarizations of the laser beams, and how we can account for this. At last, we debate how decay into a dark state affects the imaging in ${}^6\text{Li}$ for some of

⁸Thorlabs S121C which has a measurement uncertainty of 3% at this wavelength range.

the hyperfine states.

Camera

In the experiment we use CCD cameras to take the images. The CCD sensor chip consists of an array of photosensitive pixel, where incoming light leads to a charge build-up inside a potential for each pixel. The sensitivity of each pixel to the incoming light is characterized by its quantum efficiency $\eta = N_{e^-}/N_{\text{ph}}$, where N_{ph} denotes the number of incoming photons and N_{e^-} describes the number of created electrons. After light exposure, the chip pixels are then read out sequentially and the charge output of each pixel is amplified with a gain $g = N_{e^-}/N_{\text{count}}$ and digitalized with an analogue-to-digital converter (ADC). Here N_{count} denotes the respective number of counts after conversion given in the unit *ADU*. Therefore, to obtain the number of photons per pixel one can use the relation

$$N_{\text{ph}} = \frac{gN_{\text{counts}}}{\eta}. \quad (3.12)$$

From this information and knowing the magnification of the imaging system, one can then determine the incoming intensity of the imaging laser beam.

When analyzing the number of counts on the camera, one also has to take into account the readout noise σ_{read} and dark current i_{dark} . The readout noise is generated in the ADC and sets the lower end of the achievable dynamical range. Experimentally it can be determined from dark images⁹ taken with minimal exposure time τ_{min} . The upper end of the dynamical range is limited by the full well capacity, which sets the saturation limit for each potential well. The dark current i_{dark} stems from thermally excited electrons.

For imaging in the vertical axis we use a 'Stingray F145B' CCD-camera from AVT. It has a Sony ICX285 sensor with 1388×1038 pixels with a pixelsize of $6.45 \mu\text{m} \times 6.45 \mu\text{m}$ and a 14bit ADC. Its output is converted to a 16bit image, which corresponds to a maximal count of 65535 ADU. The camera characterization was performed in our group [Pim16] and will be recapped here. The readout noise and dark current can be obtained by taking images with different exposure times τ_{exp} without illuminating the sensor. From a linear fit of the mean counts over the chip as a function of exposure time, one obtains a dark current of

$$i_{\text{dark}} = (7.573 \pm 0.048) \times 10^{-6} \frac{\text{ADU}}{\mu\text{s}}.$$

The readout noise is determined from a dark image with minimal exposure time by taking the standard deviation of the counts over the chip. Using the gain calibration, the readout noise is given as

$$\sigma_{\text{read}} = 8.7 e^-.$$

To calibrate the gain g of the camera, one repeatedly illuminates the camera with a homogeneous light source for different exposure times τ_{exp} . This is also known as the photon transfer curve (PTC). Experimentally, we achieve the homogeneous

⁹No light on the camera.

illumination by the combination of a LED diode and a diffuser. For each exposure time, we then extract the variance σ_{counts}^2 and mean number of counts N_{counts} by averaging over the whole sensor. Hence, a single image is already sufficient since one averages over roughly 1.4 million pixels. To relate the variance to the mean, one then uses the fact that the detected photoelectrons caused by the the incoming uncorrelated light obey a Poisson distribution and thus the variance scales as

$$\sigma_{e^-}^2 = N_{e^-}. \quad (3.13)$$

This relation can then be used to obtain the variance of the count number is given by

$$\sigma_{\text{counts}}^2 = \frac{\sigma_{e^-}^2}{g^2} = \frac{N_{e^-}}{g^2} = \frac{N_{\text{counts}}}{g}. \quad (3.14)$$

Therefore, in the shot-noise limited region, the gain g can be directly inferred from the linear slope when the variance versus the mean number of counts is plotted.

When averaging the signal from the whole sensor, however, this region is quite small. This is due to non-uniformity of the illumination and slight variations in the sensitivity of each pixel which leads to differences in the mean count number of each pixel. This is often referred to as flat field noise and it leads to a linear contribution $\sigma_{\text{F}} = kN_{\text{counts}}$ to the noise. In order to get rid of this, we expand the procedure slightly. We take a series of images at the same settings and calculate the mean count number for each pixel individually. Thereby we create a map showing us subsets of pixels with a similar mean count number. We then obtain a PTC by calculating the variance over these subsets instead of over the whole sensor. In this way, we obtain a shot-noise limited region for a large dynamic range as can be seen in Figure 3.9. We measure a gain of

$$g = (0.3206 \pm 0.0002) \frac{e^-}{\text{ADU}}.$$

In principal one can also extract a 'gain map' by measuring the gain for each pixel individually by taking a large amount of images at each exposure time and calculating the variance and mean for each pixel separately. However, this requires very long measurement times and thus our approach is a good trade-off. Since each region still consists of more than 10.000 pixels on average, we only need a few images to have very good statistics. Furthermore, a CCD camera contains in general only one¹⁰ amplifier and thus the gain is the same for each pixel. This is in contrast to CMOS cameras where each pixel has its own amplifier and a determination of the gain map is necessary.

At last we determine the quantum efficiency of the sensor. Therefore, we use a collimated laser beam of known power P which is fully captured by the camera and illuminate the sensor for different exposure times τ_{exp} . We convert the detected counts on the camera into photoelectrons by applying our gain calibration and compare the integrated count number N_{e^-} over the chip with the number of photons

¹⁰There are also CCD cameras with more amplifiers where parts of the image are sent to different amplifiers.

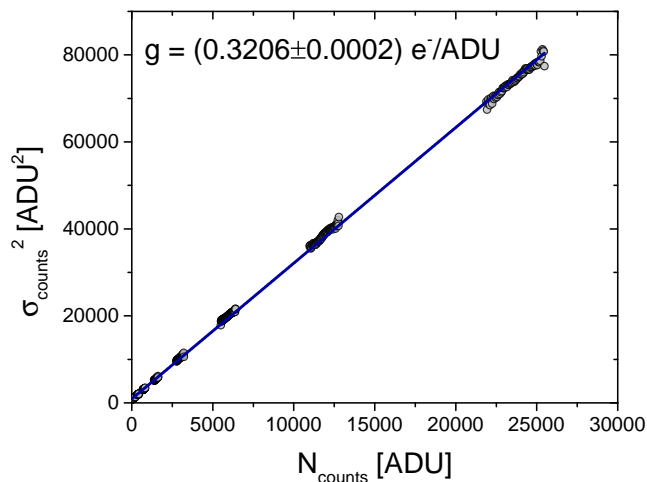


Figure 3.9.: Photon transfer curve for the Stingray F145-B camera. Each subset of data points (grey) corresponds to images taken at a certain exposure time. By applying a statistical approach, we bin together pixels with the same mean count number and derive the variance separately for each binned region. Thereby we circumvent flat field noise and obtain a linear slope (blue line) from which we directly obtain the camera gain g .

from the laser beam given by $N_{\text{ph}} = P\tau_{\text{exp}}\lambda/hc$. The quantum efficiency η is then simply given by the ratio $\eta = N_{e^-}/N_{\text{ph}}$ and we obtain

$$\eta = 0.373 \pm 0.012,$$

where the error is dominated by the uncertainty in the power determination of the laser beam using a commercial power meter. Note that this calibration was performed for different exposure times and thus we extracted η from a linear fit between number of detected photoelectrons N_{e^-} and the exposure time τ_{exp} .

All the aforementioned results are also summarized in Table 3.1.

Symbol	Value	Meaning
σ_{read}	$8.7 e^-$	Readout Noise
i_{dark}	$(7.573 \pm 0.048) \times 10^{-6} \text{ ADU}/\mu\text{s}$	Dark current
g	$(0.3206 \pm 0.0002) e^-/\text{ADU}$	Gain
η	0.373 ± 0.012	Quantum Efficiency

Table 3.1.: Summary of the camera characterization.

Magnification

To determine the magnification of the imaging system, one needs a known reference length to compare the image to. This is similar to pictures of crime scenes where a ruler is put next to the object of interest to have a length scale to compare

the object to. In our case, we can make use of the horizontal square lattice set up in the experiment. We start with a 2D condensate on the BEC side of the resonance where we have deeply bound dimers. By pulsing the lattice beams on for a short time, discrete multiples of the lattice momentum $\hbar k_L$ are transferred to a fraction of the sample. This mechanism is commonly referred to as Kapitza-Dirac scattering [Kap33]. As the transferred lattice momentum is much larger than the initial momentum, one can see the diffracted parts separate in a time-of-flight measurement. This time evolution is shown in Figure 3.10 a) for three different time-of-flights (tof). Note that here, the atoms do not expand in free space but inside a weak harmonic confinement, which is due to the magnetic field saddle of the Feshbach coils. This leads to a mapping of the momenta to real space positions at a time τ corresponding to a quarter of a trapping period T [Mur14]. This mapping only works for ballistic expansion as any scattering during the time-of-flight would perturb it. In our case of a strongly interacting sample this assumption is of course not fulfilled. However, we can use several techniques to circumvent this. First of all, the strong confinement along the z-axis leads to a fast expansion along this axis after switching off the trap. This reduces the density on a short time scale and thus reduces scattering. Furthermore, shortly before the release we quickly ramp the magnetic field to smaller values to quench the interaction strength. This combination then reduces scattering drastically and the expansion can be treated as ballistic. The results can be clearly seen in the center image where the diffraction peaks are in focus. For larger times the peaks are then re-focused to the trap center. A thorough quantum mechanical treatment of this evolution shows that at $\tau_{\text{tof}} = T/4$, the position $x(\tau = T/4)$ in the absorption image is directly related to the initial momenta $k(\tau = 0)$ via

$$k(\tau = 0) = x(\tau = T/4) \left(\frac{m\omega}{\hbar} \right). \quad (3.15)$$

Therefore, we can measure the initial momentum population from the absorption image taken at $T/4$. In Figure 3.10 b) the relative distance between two opposite momentum peaks with $k = \pm k_L$ is plotted as a function of time. From a parabolic fit (red line) one can extract the $T/4$ time experimentally as the maximum distance before the peaks get re-focused towards the center. This is also used to calibrate the magnetic trapping frequency in the experiment.

The lattice momentum $\hbar k_L = \hbar 2\pi/d_{\text{lattice}}$ is given by the lattice spacing $d_{\text{lattice}} = \lambda/(2 \cdot \cos \phi)$, where λ is the laser wavelength and ϕ is the angle between the beams creating the standing wave trap. In the experiment $d_{\text{lattice}} \approx 536$ nm and the beams cross under an angle of $\sim 7^\circ$. We can estimate the relative uncertainty $\Delta d_{\text{lattice}}/d_{\text{lattice}}$ of the lattice spacing to be smaller than 1% when assuming a large angle uncertainty of at most 3° . Thus, we can use the lattice momentum as our 'ruler' to obtain the magnification M .

The distance between two opposite momentum peaks $\pm \hbar k_L$ in the absorption image is given by

$$d(\tau = T/4) = d_{\text{pixel}} \cdot L_{\text{pixel}}/M, \quad (3.16)$$

where d_{pixel} is the distance in pixels and $L_{\text{pixel}} = 6.45 \mu\text{m}$ is the camera pixel size.

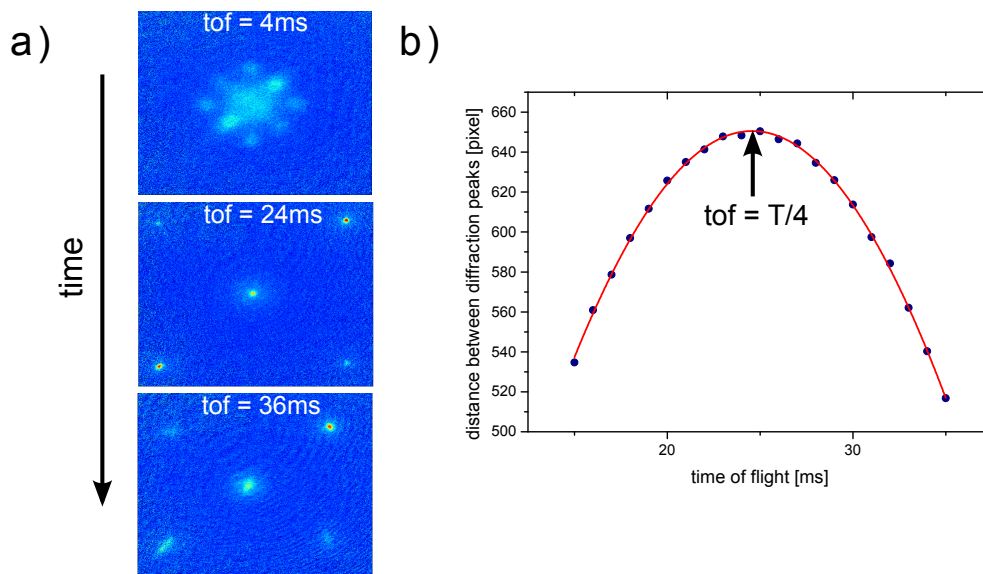


Figure 3.10.: a) A time-of-flight series is shown for a molecular BEC after a square lattice was pulsed on. The time evolution takes place inside the weak harmonic confinement of a magnetic field saddle potential. For a short time-of-flight (tof) of 4 ms the diffraction peaks with lattice momentum k_L from each lattice arm as well as mixed order terms between lattice arms separate. At $\text{tof} = 24$ ms, the diffraction peaks as well as the non-diffracted part in the center are in focus and the evolution has reached its turning point. For longer times the peaks are then re-focused towards the center of the trap. b) The relative distance between the peaks with momentum $\pm \hbar k_L$ is plotted as a function of the time-of-flight. The turning point, and thus the trap frequency of the harmonic confinement can be obtained from a parabolic fit (red line) around the maximum. From the distance between the peaks at $\text{tof} = T/4$ we can also deduce the magnification M . Adapted from [Bay15].

Using equation 3.15, we can then solve for M and obtain

$$M = \frac{d_{\text{pixel}} \cdot L_{\text{pixel}} m \omega}{2 \hbar k_L} = 2.14 \pm 0.06. \quad (3.17)$$

Hence, our experimentally determined magnification is approximately 10 % smaller than what was expected from the imaging system parameters.

Doppler Effect

The scattering of photons during the imaging process leads to a momentum transfer to the atoms along the imaging axis. Due to the light mass of ${}^6\text{Li}$, each absorbed photon adds a recoil velocity $v_{\text{rec}} \approx 0.1$ m/s, thus accelerating the atoms. This results in a Doppler shift of roughly 150 kHz per absorbed photon and thus even scattering of only a few photons leads to a detuning of the transition on the same

order as the linewidth $\Gamma = 5.87$ MHz [Geh03]. Hence, during the imaging the atoms are acquiring a detuning Δf , which effectively reduces the scattering cross section σ_0 . This leads to a decreased signal and an underestimation of the atom number. To correct for this one can either incorporate this time dependent change of the scattering cross section into the derivation of the optical density [Muk16] or adjust the imaging frequency during the imaging pulse.

In the experiment, we opt for the latter by applying a linear ramp of the laser frequency during the exposure. To calibrate the required ramp speed, we proceed as follows. In order to determine the resonance frequency as precisely as possible, we use the shortest experimentally implementable exposure time $\tau_{\text{exp}} = 1 \mu\text{s}$ and image an atomic sample at 900 G^{11} . We then scan the imaging laser frequency to obtain the absorption profile like shown in Figure 3.11 a). From a Lorentzian fit (blue line) we can extract the resonance position as well as the linewidth $\Gamma_{\text{exp}} = 7.44$ MHz of the transition. The linewidth Γ_{exp} is broadened compared to the natural linewidth since we operate at intensities close to the saturation intensity. Using this experimentally determined resonance frequency, we then go back to our usual exposure time of $\tau_{\text{exp}} = 8 \mu\text{s}$ and apply a linear frequency ramp during imaging. We then scan the applied slope ϵ and plot the atom number versus the slope as shown in Figure 3.11 b). We can see that we maximize the detectable atom number at a slope of $\epsilon = 0.765 \text{ MHz}/\mu\text{s}$, which we obtain from a parabolic fit to the data (blue line). The flatness of the slope can be understood when considering that the cross section σ scales with the detuning δ as [Met02]

$$\sigma = \frac{\sigma_0}{1 + s_0 + (2\delta/\Gamma)^2}, \quad (3.18)$$

where $s_0 = I/I_{\text{sat}}$ is the relative intensity. Therefore, in the limit of low intensities $s_0 \rightarrow 0$, a detuning of 1 MHz leads to a reduction in σ of 10%. However, in the experiment we operate at $s_0 \simeq 1$ and therefore this reduction is much smaller as the s_0 term dominates over the detuning term. As we can see from the fit, a change of $0.1 \text{ MHz}/\mu\text{s}$ in the slope changes the detected atom number by less than 2%, making the Doppler compensation a very robust technique.

From both measurements we can obtain an estimate of s_0 . For the linewidth, the intensity broadening is given by $\Gamma_{\text{exp}} = \Gamma_{\text{theory}} \cdot \sqrt{1 + s_0}$ [Met02], which results in $s_0 = (0.61 \pm 0.1)$. From the slope α we can estimate the scattering rate γ as $\gamma = \alpha/\Delta f_{\text{rec}}$ where we used the Doppler shift $\Delta f_{\text{rec}} \approx 150 \text{ kHz}$ per absorbed photon. The scattering rate is also defined as¹²

$$\gamma = \frac{\Gamma}{2} \frac{s_0}{1 + s_0}. \quad (3.19)$$

Therefore, by inserting our measured scattering rate into equation 3.19 we can solve for s_0 and obtain $s_0 = 0.38 \pm 0.07$. Here the error was not taken from the parabolic

¹¹We chose this field in order to have free atoms and no molecules as on the BEC side. The binding energy of the molecule leads to a shift in the resonance frequency which has to be accounted for in the first scattering process. After the first scattering, the molecule is broken apart and the ensuing scattering is from free atoms.

¹²Note that here $\Gamma = 2\pi \times 5.872 \text{ MHz}$ is the linewidth in angular frequency.

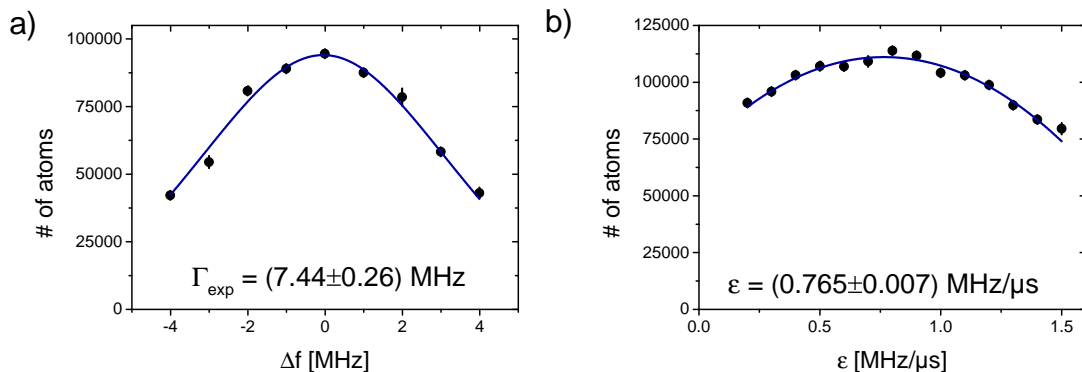


Figure 3.11.: a) Lorentzian absorption profile for a short exposure time $\tau_{\text{exp}} = 1 \mu\text{s}$. The changing cross section is neglected here in the atom number calculation and thus it drops away from resonance. The blue line is a Lorentzian fit and we obtain for the intensity broadened linewidth $\Gamma_{\text{exp}} = (7.44 \pm 0.26)$ MHz. b) The atom number assuming a constant scattering cross section is plotted versus the applied slope for the Doppler compensation. The detected atom number can be increased when applying a frequency ramp during the $8 \mu\text{s}$ long imaging pulse. There is an optimum for which the atoms stay in resonance during the imaging. We obtain this optimal slope $\epsilon = (0.765 \pm 0.007)$ MHz/ μ s from a parabolic fit to our data (blue line).

fit but instead we estimated $\Delta\alpha = 0.1$ MHz/ μ s. Within their errors, both methods roughly agree and they can give us a first estimate of s_0 . For the final image acquisition, we obtain s_0 directly from the reference images using our camera calibration.

The scattering of photons does not only lead to a detuning but also to an acceleration of the atoms along the imaging direction. This leads to a displacement Δz during the imaging pulse. From the scattering rate γ_{sc} , the constant acceleration a_{sc} can be deduced and hence the displacement can be calculated via $\Delta z = 0.5 \cdot a_{\text{sc}} \tau_{\text{exp}}^2$. In our experiments, we use an exposure time $\tau_{\text{exp}} = 8 \mu\text{s}$ and $s_0 \approx 1$. Hence, the scattering rate is roughly $\gamma_{\text{sc}} \approx 9 \frac{\text{photons}}{\mu\text{s}}$, which leads to a mean acceleration of $0.9 \mu\text{m}/\mu\text{s}^2$ when considering the recoil velocity of $v_{\text{rec}} = 0.1$ m/s. This results in a displacement of $\Delta z \approx 28 \mu\text{m}$ during the pulse which is small compared to the depth of focus $z_{\text{DoF}} = 137 \mu\text{m}$ and thus this does not influence our spatial resolution for in-situ measurements.

However, the re-emission of photons in the scattering process leads to an isotropic momentum kick. In the plane orthogonal to the imaging axis, this can be modeled by a random walk. For our typical imaging settings, we scatter around 70 photons per atom and the random walk distance can be estimated to $5 \mu\text{m}$ which effectively limits our total imaging spatial resolution to around $6 \mu\text{m}$ [Kle16].

Experimental Imperfections

In our derivations we used theoretical values for the scattering cross section σ_0 and the saturation intensity I_{sat} so far. However, the experimental values can deviate

due to imperfections in the imaging beam polarization and other effects [Rei07] and therefore effective values σ_0^* and I_{sat}^* have to be calibrated. The deviations can be incorporated via a scaling factor α^* which leads to $\sigma_0^* = \sigma_0/\alpha^*$ and $I_{\text{sat}}^* = \alpha^* I_{\text{sat}}$. We can use this directly in the derivation of equation 3.7 and end up with the modified equation

$$n_{\text{col}}(x, y) \sigma_0 = -\alpha^* \ln \left(\frac{I_{\text{abs}}(x, y)}{I_{\text{ref}}(x, y)} \right) + \frac{I_{\text{ref}}(x, y) - I_{\text{abs}}(x, y)}{I_{\text{sat}}}. \quad (3.20)$$

To calibrate α^* we prepare a sample in the 13-mixture and image state $|3\rangle$ at a magnetic offset field of 1000 G for three different imaging intensities. The state $|3\rangle$ is used since its imaging transition is closed and we do not have dark state losses as will be discussed in the next section. For each intensity, we determine the resonance frequency and optimal Doppler compensation slope as described above. We take 20 shots for each intensity and determine the right side of equation 3.20 from a mean of the central 3×3 pixel area for each individual image. The value of α^* in this case is a free parameter and we perform this calculation for a large set of α^* . If the imaging is calibrated correctly, the detected optical density $OD = n\sigma_0$ should be independent of the used imaging intensity. Hence, to determine the right value of α^* , we have to calculate for which α^* the standard deviation of the optical density at the different intensities is minimal.

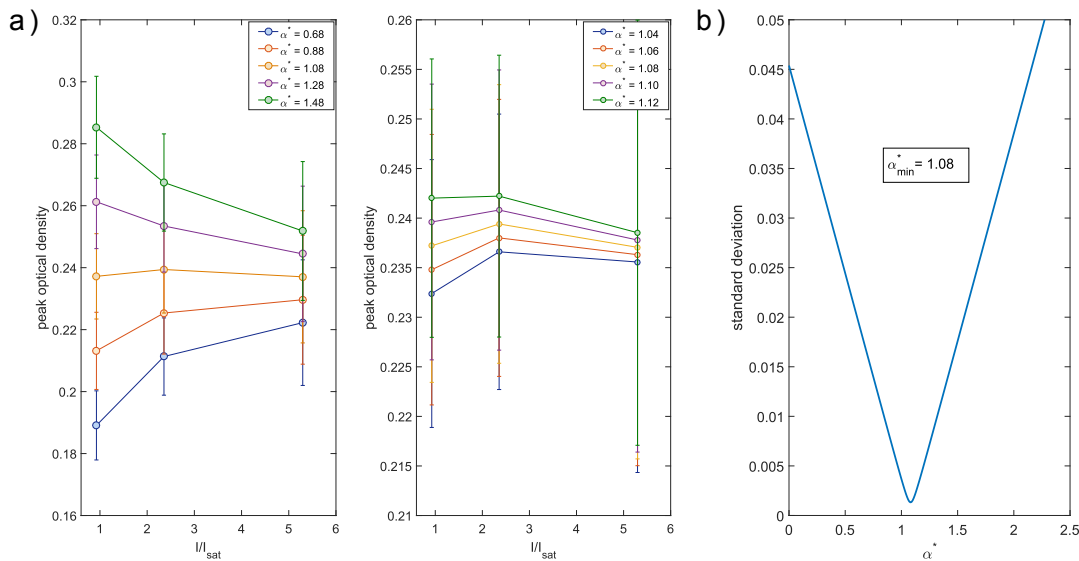


Figure 3.12.: a) The peak optical density as calculated from equation 3.20 is plotted versus the imaging intensity for different values α^* . The right panel shows the same calculation for a finer scale of α^* . b) For $\alpha^* \approx 1.08$ the optical density has the minimal standard deviation.

This calibration is summarized in Figure 3.12. For each intensity, we also calculate the standard deviation of the central OD from the 20 individual shots. We can see that we obtain the minimal standard deviation for $\alpha^* = 1.08 \pm 0.06$. The error is estimated by looking for what values the OD behaves monotonously versus I/I_{sat}

as can be seen in the left panel in a). Within its error $\alpha^* \approx 1$ and thus our imaging setup is well set up.

Decay into Dark State

So far we always assumed a closed transition for the imaging cycle, meaning that when the atom spontaneously decays from the excited state it ends up in its initial state and can be re-excited. However, this assumption does not hold for all lowest hyperfine states $|1 - 3\rangle$ in ${}^6\text{Li}$. This was discussed extensively in [Bec16]. Here we will give a brief summary and show how we can correct our images for this effect.

The six lowest hyperfine ground states $|1 - 6\rangle$ of ${}^6\text{Li}$ were shown in Figure 2.5 a) and can be calculated analytically [Hou98, Geh03] in the basis $|m_J, m_I\rangle$ as

$$\begin{aligned}
 |1\rangle &= A_+ |1/2, 0\rangle - B_+ |-1/2, 1\rangle, \\
 |2\rangle &= A_- |1/2, -1\rangle - B_- |-1/2, 0\rangle, \\
 |3\rangle &= |-1/2, -1\rangle, \\
 |4\rangle &= B_+ |1/2, -1\rangle - A_+ |-1/2, 0\rangle, \\
 |5\rangle &= B_+ |1/2, 0\rangle - A_+ |-1/2, 1\rangle, \\
 |6\rangle &= |1/2, 1\rangle,
 \end{aligned} \tag{3.21}$$

where we omitted the spin amplitudes $J = 1/2$ and $I = 1$. The coefficients are given by $A_{\pm} = 1/\sqrt{1 + (Z^{\pm} + R^{\pm})^2/2}$, $B_{\pm} = \sqrt{1 - A_{\pm}^2}$, $Z^{\pm} = (\mu_n + 2\mu_e) B/A_{2^2S_{1/2}} \pm 1/2$ and $R^{\pm} = \sqrt{(Z^{\pm})^2 + 2}$, where $A_{2^2S_{1/2}} = 152.1368407$ MHz is the magnetic dipole constant and $\mu_{n/e}$ labels the magnetic moment of the neutron and electron respectively. The coefficients A_{\pm} and B_{\pm} are plotted in Figure 3.13 a). Already at magnetic fields B above 300 G, the contribution $|A_{\pm}|^2$ to the states is less than 2% and converges towards 0 at higher fields. Thus, each state can be very well approximated by a single basis state as indicated in Figure 2.5 a). The admixture of different basis states $|m_J, m_I\rangle$ can be understood in terms of a coupling between the nuclear spin I and the angular momentum J of the electrons. At low external magnetic fields B , this coupling is well approximated by eigenstates of the total angular momentum $\vec{F} = \vec{J} + \vec{I}$. When both spins \vec{J} and \vec{I} are parallel, the total angular momentum \vec{F} couples in the same way to the field \vec{B} as both spins would do if they are decoupled. This is the case for the states $|3\rangle$, $|6\rangle$ and therefore they do not have any admixtures. Their magnetic moments $\mu = \frac{\partial E}{\partial B}$ are constant and they have a linear Zeeman shift for all magnetic fields B . In contrast, all other ground states have a coupling dominated regime at magnetic fields $\lesssim 10$ G which then crosses over to the decoupled Paschen-Back regime at larger fields. In between these regimes, the magnetic moment μ changes considerably and can also change sign. At large magnetic fields, the magnetic moment is dominated by the electron spin and is almost constant.

For the imaging transition we use the D2-line which excites the ground state atoms into the excited state $2^2P_{3/2}$ manifold. We use σ_- polarized light and thus the selection rules for the transition are [Dem10]

$$\Delta J = 1, \Delta m_J = -1 \text{ and } \Delta m_I = 0. \tag{3.22}$$

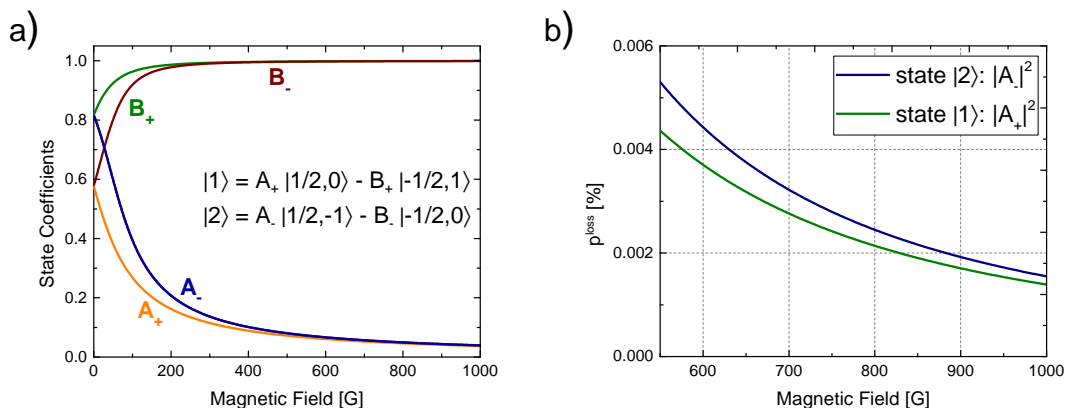


Figure 3.13.: a) The state coefficients used to calculate the ground state levels are plotted versus the applied magnetic field. The used states $|1\rangle$ and $|2\rangle$ are superpositions and can be described by a single basis state $|m_J, m_I\rangle$ for large fields. b) The loss probability to decay into a dark state is shown for the states $|1\rangle$ and $|2\rangle$. Although they are below 0.005 % for fields above 600 G, the effect is still observable when taking absorption images. Note that state $|3\rangle$ does not have any dark state losses. Adapted from [Bec16].

With these selection rules, starting from the three lowest hyperfine states including the admixtures we excite the transitions

$$\begin{aligned}
 |1\rangle &\rightarrow |3'\rangle = |-3/2, 1\rangle, \\
 |2\rangle &\rightarrow |2'\rangle = |-3/2, 0\rangle, \\
 |3\rangle &\rightarrow |1'\rangle = |-3/2, -1\rangle,
 \end{aligned} \tag{3.23}$$

where $|e'\rangle$ indicates the excited states which are labeled from smallest to largest energy as well. Here we used the large field approximation for the excited states. Due to the angular momentum $L = 1$, the orbit of the outer electron does not have much overlap with the nucleus. Therefore, the coupling is weak and the decoupling of the spins already sets in at fields $\lesssim 1$ G which is considerably smaller than the magnetic field for which the ground states with $L = 0$ decouple. Thus, this approximation is valid for the fields we operate at in this thesis.

For the spontaneous decay from the excited state, only $\Delta m_J = +1$ is allowed and thus we can write the decayed into state as a superposition of the initial states as

$$\begin{aligned}
 |1'\rangle &\rightarrow |-1/2, 1\rangle = |3\rangle, \\
 |2'\rangle &\rightarrow |-1/2, 0\rangle = -B_- |2\rangle - A_- |4\rangle, \\
 |3'\rangle &\rightarrow |-1/2, -1\rangle = -B_+ |1\rangle - A_+ |5\rangle.
 \end{aligned} \tag{3.24}$$

Combining equation 3.23 and 3.24, we can deduce that we only have a closed transition when imaging state $|3\rangle$. For the state $|1\rangle$ and $|2\rangle$ we have a finite probability to decay into state $|5\rangle$ and $|4\rangle$ respectively, which is dark to the excitation. This loss probability p^{loss} reduces as the magnetic field is increased as can be seen in Figure

3.13 b). At the magnetic fields we operate the probability for these states to decay into a dark state is less than 0.005%. However, this still has an effect since we scatter ≈ 70 photons per atom and once an atom decays to a dark state it does not scatter photons anymore for the rest of the exposure time τ_{exp} .

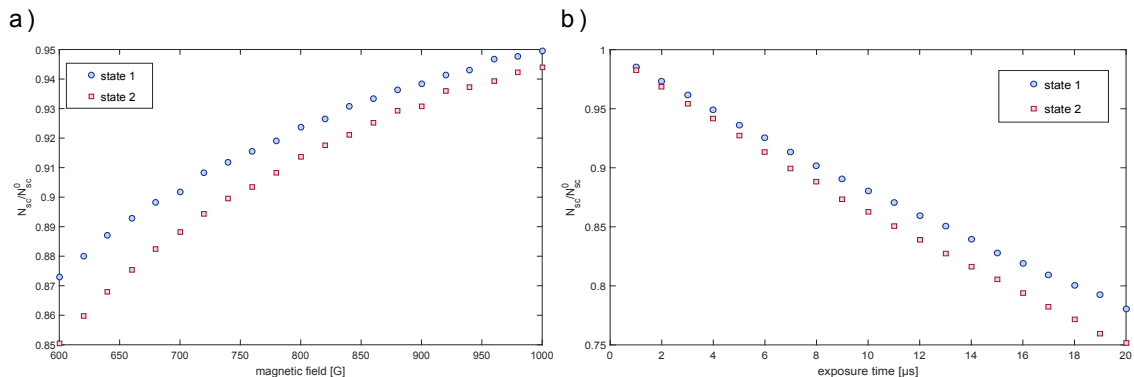


Figure 3.14.: a) The mean number of scattered photons N_{sc} is simulated and compared to the maximal number of scattered photons N_{sc}^0 as a function of magnetic field for both states. The exposure time $\tau_{\text{exp}} = 8 \mu\text{s}$ and $s_0 = 1$ are fixed which results in $N_{\text{sc}}^0 \approx 66$. At larger fields, decay into the dark state becomes suppressed and hence the ratio increases. b) Here the ratio is simulated in dependence of the exposure time at a fixed magnetic field of 700 G and $s_0 = 1$. For larger exposure times, the probability of decaying into a dark state increases and thus the ratio decreases.

This dark state loss results in a reduced number of average photon scattering events per atom. We estimate this effect numerically by simulating the repeated scattering process from an atom. At each out of N_{sc}^0 maximal scattering events, we acquire a random number $0 < p < 1$ and compare it to the loss probability $p^{\text{loss}}(B)$. If $p < p^{\text{loss}}(B)$ the atom decays into a dark state and no further scattering events take place. Otherwise the next scattering event happens. Repeating this process 100.000 times then gives us an average number of scattered photons N_{sc} per atom. In Figure 3.14 the ratio $N_{\text{sc}}/N_{\text{sc}}^0$ is shown both for a fixed exposure time $\tau_{\text{exp}} = 8 \mu\text{s}$ in dependence of the magnetic field a) and at a fixed magnetic field $B = 700 \text{ G}$ for different exposure times b). These simulations assume a fixed intensity $s_0 = 1$ to calculate the scattering rate. As expected, at larger magnetic fields the ratio increases as the branching ratio into the dark state converges to zero. Similarly, for longer exposure times the ratio reduces as the probability that an atom decays at least once into a dark state increases. In the experiments in this thesis we work at magnetic fields between 600 – 1000 G and thus the scattering reduction can reach up to 16%.

In order to correct for these losses, we proceed as follows: from the experimentally acquired absorption image $I_{\text{abs}}(x, y)$ containing the atoms and the reference image

$I_{\text{ref}}(x, y)$ without atoms, we deduce the amount of scattered counts as

$$I_{\text{sc}}(x, y) = I_{\text{ref}}(x, y) - I_{\text{abs}}(x, y), \quad (3.25)$$

which directly relates to the amount of average scattering events. As our imaging beam profile is large compared to the sample and the relative change in intensity over the area of the atoms is less than 10 %, we assume a constant relative intensity $s_{0,\text{mean}}$ to calculate the scattering rate γ_{mean} and simulate the relative amount of scattered photons $(N_{\text{sc}}/N_{\text{sc}}^0)_{\text{mean}}$. Using this factor we correct the scattered images as

$$I_{\text{sc}}^*(x, y) = I_{\text{sc}}(x, y) \cdot \left(\frac{N_{\text{sc}}}{N_{\text{sc}}^0} \right)_{\text{mean}}^{-1}. \quad (3.26)$$

Note that we calculate $s_{0,\text{mean}}$ directly from the reference image using our camera calibration.

With this corrected scattered image we then obtain a modified absorption image

$$I_{\text{abs}}^*(x, y) = I_{\text{ref}}(x, y) - I_{\text{sc}}^*(x, y). \quad (3.27)$$

Subsequently, we then perform the steps outlined in section 3.2.4 to obtain the density $n_{2\text{D}}$. The application of this correction method can be seen in Figure 3.15. Here images were taken for a 13-mixture at 700 G and an average was performed. In the left panel in the lower row, the integrated x-profiles without dark state correction are shown. As expected, the measured density is larger for state $|3\rangle$ (blue) than state $|1\rangle$ (red) since it does not suffer from dark state decay. However, after correcting for the dark state decay in state $|1\rangle$ we find very good agreement between the two profiles (right panel, lower row) which verifies our correction.

3.2.4. Image Composition and Error Estimation

In this section, our method to acquire density profiles is explained and the uncertainty in the acquired densities is estimated. The experimental implementation of absorption imaging is shown in Figure 3.16. In each experimental cycle, three images are recorded with the camera as shown in a). The first image is the absorption image $I_{\text{abs}}(x, y)$, where the atom sample is present and thus part of the imaging beam pulse is scattered. Subsequently, a reference image $I_{\text{ref}}(x, y)$ is taken with the same imaging pulse but without atoms present. Since the recoil of the scattered photons is much larger than the trap depth, the imaging is destructive and one just has to wait a sufficient time before taking the reference image. In our case the timing between these images is roughly 88 ms¹³. At last, a background image is taken where no imaging pulse is applied. This background image I_{bg} is used to eliminate the effect of the camera dark current and readout noise as well as background light from the signal.

From the background subtracted raw images, we calculate both terms in equation 3.7 individually as is shown in the first two images in b). The first term only depends on the relative intensity and thus no further input is needed. To account for possible

¹³The reason for this is explained in section 3.2.5.

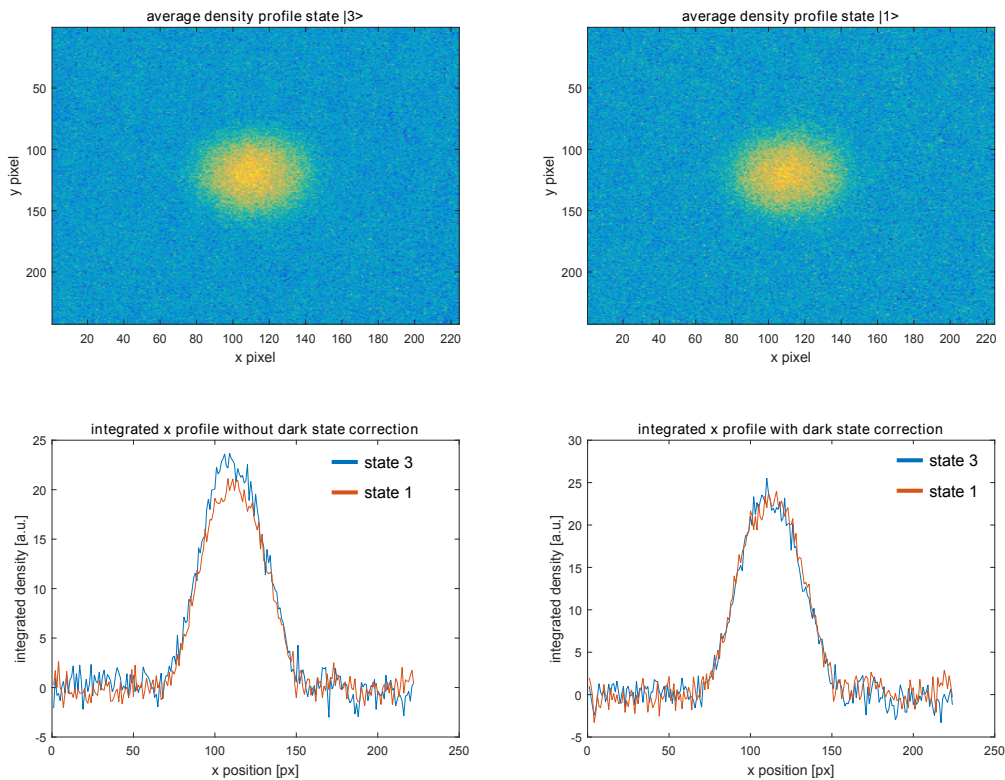


Figure 3.15.: The average density profiles for a 13-mixture are shown for both states in the upper row. In the lower row, the integrated x-profiles are shown without (left) and with (right) the dark state decay correction applied. Without the correction the integrated density in state $|1\rangle$ is smaller as one underestimates the density due to the decreased number of scattered photons during the imaging. After applying the correction, however, both profiles match very well. Taken from [Kle16].

intensity fluctuations in the laser power, we take the computed mean value in the region without atoms and subtract it. Due to the nature of the logarithm, this is identical to rescaling the reference intensity to the absorption intensity. For the second term we have to convert the counts on the camera into an intensity using the conversion factor

$$f_{\text{conv}} = \frac{h \cdot (c/\lambda) \cdot g}{\eta \cdot (A_{\text{pixel}}/M^2) \cdot T \cdot \tau_{\text{exp}}}, \quad (3.28)$$

where h is Planck's constant, c is the speed of light, λ is the imaging laser wavelength, A_{pixel} is the pixel area and the rest of the constants are defined as previously. To account for power fluctuations of the laser in this case too, we rescale the reference intensity to the absorption intensity in the region without atoms. At last one can add these terms to obtain the overall optical density as shown in the last panel.

Both the absorption image as well as the reference image show structure on the imaging beam. From comparisons of the beam profile in front of the main chamber

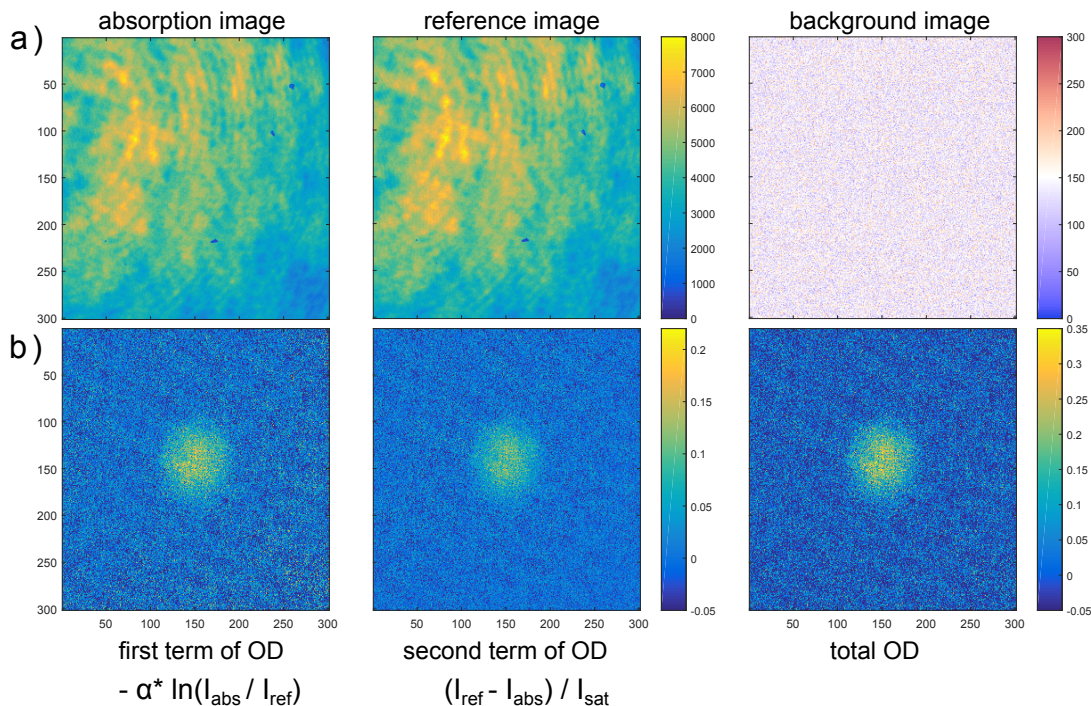


Figure 3.16.: The process of our image acquisition is demonstrated for a single experiment cycle. In a) the raw images are shown: the absorption image is taken first, when atoms are present. After ≈ 88 ms, the reference image is taken where no atoms are present due to the destructive nature of the first pulse. At last, a background image is acquired with the same settings but without the imaging laser pulse on. Using the raw images one can then obtain the optical densities from equation 3.20 as shown in b). The first image shows the logarithmic part. The second image shows the absolute difference $I_{\text{ref}} - I_{\text{abs}}$ normalized with respect to the saturation intensity I_{sat} . At last the sum of these two contributions is shown.

and at the camera position, we know that this structure is due to reflections and interference effects on different surfaces in the imaging path. As a result the image on the camera does not accurately represent the beam profile in the atomic plane and introduces another error source. To get some insight on the structure, for the reference image both cuts along the x- and the y-axis through the center of the cloud are plotted in Figure 3.17. From Gaussian fits one can see that the overall behavior of the beam is described by a Gaussian profile accurately but local deviations are visible due to the aforementioned interference effects. From a 2D Gaussian fit, we can estimate that the overall intensity changes by less than 10% over the size of our samples. These static fringes, however, add local fluctuations with a standard deviation on the order of 11%. For the logarithmic term in equation 3.20 this does not play a role as only the relative signal is of importance. Unfortunately, the absolute intensity difference $I_{\text{ref}}(x, y) - I_{\text{abs}}(x, y)$ in the second term is directly influenced by this structure and thus results in a local over- or underestimation of

the optical density. Note that these fringes are static and depend mainly on the laser frequency.

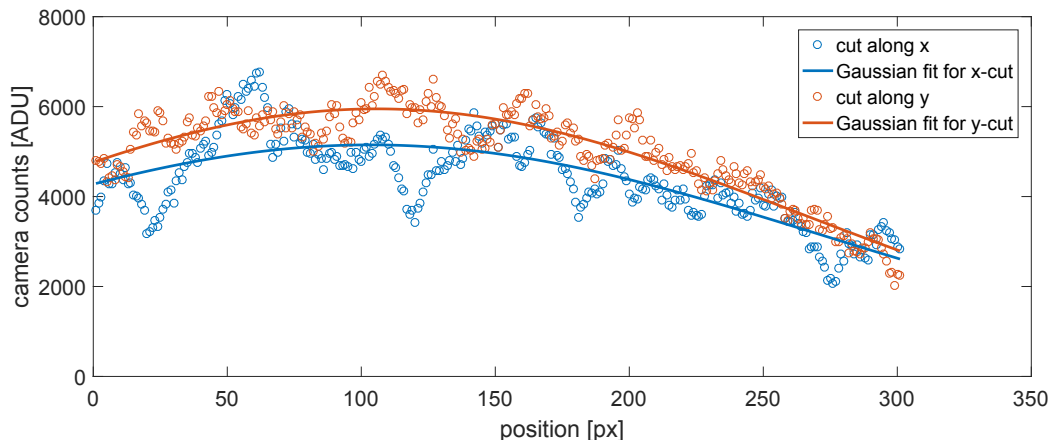


Figure 3.17.: A cut along the x-axis (blue circles) and y-axis (red circles) for the reference image through the center of the atomic cloud is plotted. One can see that the counts fluctuate around a Gaussian profile (fitted lines). This structure is caused by reflections and interference on multiple surfaces in the imaging path.

To estimate the effect each of our imaging calibration uncertainties have on the determination of our local density, we take a typical dataset used in chapter 5 and analyse the density in two 3×3 -regions, one at the center of the cloud where the density is highest and one in the wing of the cloud where the density is lower. This can be seen in Figure 3.18, where the mean density is shown for this dataset. In the zoomed in part below the image, the analyzed regions at the center (black) and further out (red) are depicted. We now vary each of the calibrated parameters in section 3.2.3 within their error, calculate the mean density in the 3×3 -regions and deduce the relative errors $|n - n_0|/n_0$. This is listed in Table 3.2. Apart from the camera gain which can be neglected as an error source, the rest of the contributions show a similar effect on a few percent level. The largest contributions are the magnification M and the imaging imperfections, given by the parameter α^* with 2.3% and 3.15% respectively.

In the table we did not consider the structure we see on the imaging beam so far. By fitting a 2D Gaussian profile to the beam, we estimated the local deviations from this profile to be on the order of 10%. Performing the same error calculation as before results in a relative error of 4.5%. In principle, as these fringes are static and only depend on the laser frequency, assuming a perfect Gaussian beam profile it should be possible to correct this structure and smooth the measured beam profiles with a reference mask. However, this has several drawbacks: first of all, the imaging laser frequency changes with the magnetic field and thus this would require to take a mask at each setting, making it a cumbersome procedure. Furthermore, although the beam profile in front of the main chamber has definitely less structure, it is nevertheless not a perfect Gaussian and thus this assumption would introduce new systematic errors. This is especially important for example, when looking at atomic

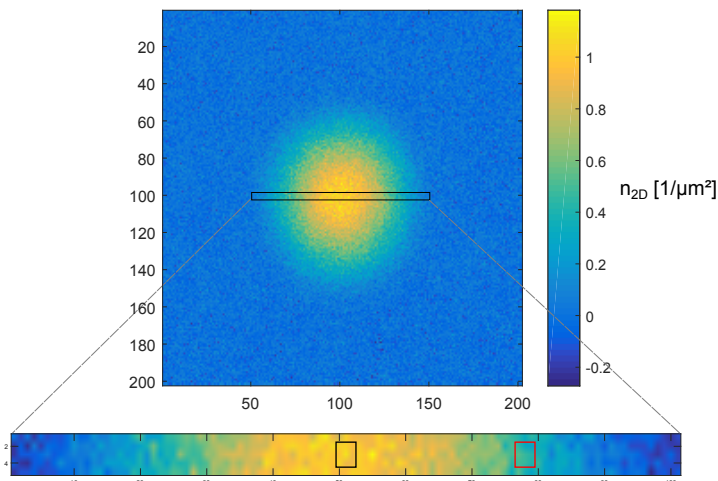


Figure 3.18.: To estimate the different error contributions, we take a subset of our typical experimental data containing 30 images whose mean density profile $n_{2D}(x, y)$ is shown here. We then take a 3×3 region at the center (black rectangle) and a 3×3 region at the wing (red rectangle) to analyze the effect of the uncertainties in our calibration. These regions can be seen in the zoomed in part of the image.

noise correlations as we plan to do in the future. Therefore, we do not attempt to correct this structure but add it to our imaging uncertainty.

To estimate the error due to the Doppler effect, we cannot directly use equation 3.20, as it is based on the assumption of a resonant imaging pulse. However, from the experimental results when changing the slope ϵ of our Doppler compensation ramp, we can infer that the absorption imaging process shows only a weak sensitivity for deviations of ϵ on the order of up to $1 \text{ MHz}/\mu\text{s}$. From the data we estimate that this results in a relative change of the atom number and thus the local density n of less than 2%.

For the two hyperfine states $|1, 2\rangle$, we also have to take the dark state decay and its correction into account. As we explained before, for the correction of the dark state decay we assume a mean relative intensity $s_{0,\text{mean}}$ across the sample. From the reference image profile, we can estimate the error in $s_{0,\text{mean}}$ to be on the order of 10%. However, this uncertainty only results in a small change in the relative amount of scattered photons $N_{\text{ph}}/N_{\text{ph}}^0$ and thus this changes the density by less than 1%. Hence, we can neglect this effect when calculating the overall error and take the same error for all hyperfine states.

Assuming that all these individual error sources are independent, we can then obtain a total error estimate for our density measurement as

$$\left(\frac{\Delta n}{n}\right) \approx 7\%. \quad (3.29)$$

In our 2D systems, since the local Fermi temperature T_F and local Fermi energy E_F are proportional to the density, this directly results in an uncertainty $T_F^{\pm 7\%}$ and $E_F^{\pm 7\%}$.

Parameter	$n_{\text{center}} [1/\mu\text{m}^2]$	$\frac{ n_{\text{center}} - n_0 }{n_0} [\%]$	$n_{\text{wing}} [1/\mu\text{m}^2]$	$\frac{ n_{\text{wing}} - n_0 }{n_0} [\%]$
standard n_0	1.011	-	0.539	-
$T = 0.77 \pm 0.03$	0.994 / 1.025	1.7	0.531 / 0.548	1.6
$\eta = 0.3726 \pm 0.012$	0.997 / 1.025	1.5	0.533 / 0.546	1.2
$g = 0.3206 \pm 0.0002$	1.011 / 1.01	-	0.539 / 0.539	-
$M = 2.14 \pm 0.06$	1.035 / 0.987	2.4	0.531 / 0.527	2.2
$\alpha^* = 1.08 \pm 0.06$	1.043 / 0.979	3.2	0.557 / 0.521	3.3

Table 3.2.: Error estimation of the local density n . For the densities cells, the first value is calculated with positive error and the second one with negative error. For the relative error, the mean is taken.

In general, the choice of the intensity used for imaging depends on several factors. First of all it sets the exposure time needed to obtain a good signal-to-noise ratio. Here one is limited by the large recoil momentum of ${}^6\text{Li}$ and thus it is difficult to reach the low intensity limit without being affected by a reduced spatial resolution. To obtain for example the same number of counts as with the current settings for a relative intensity $s_0 = 0.1$, the imaging pulse would have to be 80 ms long. Although the scattering rate at this intensity is only ≈ 1.6 photons/ μs , this would still lead to a displacement of $512 \mu\text{m}$ along the imaging axis and thus the sample would be accelerated out of the depth of focus. On the other side, the scattering rate saturates at large $s_0 \gg 1$ and thus increasing the intensity further can reduce the required imaging pulse duration for the same signal strength while simultaneously reducing the displacement of the atoms along the imaging axis during the pulse. However, increasing the intensity beyond the saturation limit also shifts the relative influence of the two terms in equation 3.20 towards the second term. Thus, the uncertainty in the imaging is then dominated by this term and the uncertainty in the determination of n increases. In the experiment, we therefore chose a value of $s_0 \approx 0.9$ ¹⁴ as a good experimental trade-off between these considerations. To optimize this in future experiments, one has to measure the shot-to-shot fluctuations in the density as a function of the used intensity [Hue17].

3.2.5. Imaging Two Hyperfine States within an Experimental Cycle

In our experiments, we use a binary mixture of atoms in different hyperfine states. Thus, to get the full information about the system, an absorption image of both states within the same experimental realization of the system is required. This is especially true when working with imbalances or looking at spin-spin correlations.

In order to achieve this, both technical as well as physical solutions have to be found. First of all, imaging one state removes it from the trap. Thus, the remaining atoms in the other state will re-distribute on a time scale given by the trap frequency.

¹⁴Note that in the presentation of the Doppler compensation older data was used where we had a smaller s_0 .

Therefore, the time interval between taking the two images has to be on a much smaller timescale. This requires the laser frequency stabilization to be fast enough to change the frequency by up to 160 MHz in between the two images when imaging state $|1\rangle$ and state $|3\rangle$. Furthermore, the camera itself has to be able to take two images successively on this timescale.

The camera used in the experiment has a method called 'interline transfer'. This means that each pixel has a storage pixel next to it which does not receive any input light. Thus, instead of reading out the camera chip, each pixel can transfer its charge to this storage pixel and the next image can be taken immediately afterwards. This allows us to take two images within $\approx 130 \mu\text{s}$. With our frequency stabilization of the laser, we can follow jumps in the frequency of 20 MHz within a microsecond [Ste16] and thus this is ample time to change the resonance frequency from imaging one state to the other while doing the interline transfer.

In conclusion, we only have to adapt the imaging procedure slightly from the case of imaging only one state. After taking the first absorption image, we ramp the laser frequency within $70 \mu\text{s}$ to the resonance frequency of the second imaged state. During this time we also perform the 'interline transfer'. Subsequently we take the second absorption image. For the reference image, we follow the same procedure. This is because the static fringes we observe on camera depend on the frequency and thus taking only one reference for both states would lead to a structure on the background. This can be seen in Figure 3.19 where we took images without atoms and shifted the laser frequency for the reference image. Already for shifts on the order of 80 MHz one can clearly see a structure on the background which gets even more pronounced for larger shifts. Since in ${}^6\text{Li}$ the difference in resonance frequency between two neighbouring states is on the order of 80 MHz, this would lead to unwanted structure in the images when taking only a single reference image. At last, a single dark image is taken without imaging light. Here there is no difference between these two and thus one is enough.

The two state imaging gives us a useful tool to investigate the imaging process. We can for example check the Doppler shift the atoms acquire during the imaging pulse. For this we imaged the state $|3\rangle$ two times in succession and adjusted the starting frequency for the second image such that we see the most signal. This is shown in Figure 3.20. The optimal relative detuning of the second image is approximately 8 MHz. This matches the slope $\epsilon = 1 \text{ MHz}/\mu\text{s}$ we calibrated as the optimal Doppler compensation ramp. However, we observe that the atom number in the second image is smaller by approximately 10%. The reason for this is not yet understood.

We can also use the two-state imaging to compare our preparation fidelity with our detection fidelity. Therefore, we take a balanced mixture of two hyperfine states and image both states successively. After correcting for the dark state decay, we can then look at the correlation between the atom number in each experimental realization. This is plotted in Figure 3.21. A linear fit (blue line) to the data shows that the atom numbers after the correction match within $\approx 2\%$. We do a principal component analysis (PCA) to find the axis where the data shows the least variance. This corresponds to the blue line and it gives us a measure of how much the atom number varies between the two images within the same realization which is a measure of our detection fidelity. On the other hand, the variance of the data along the blue

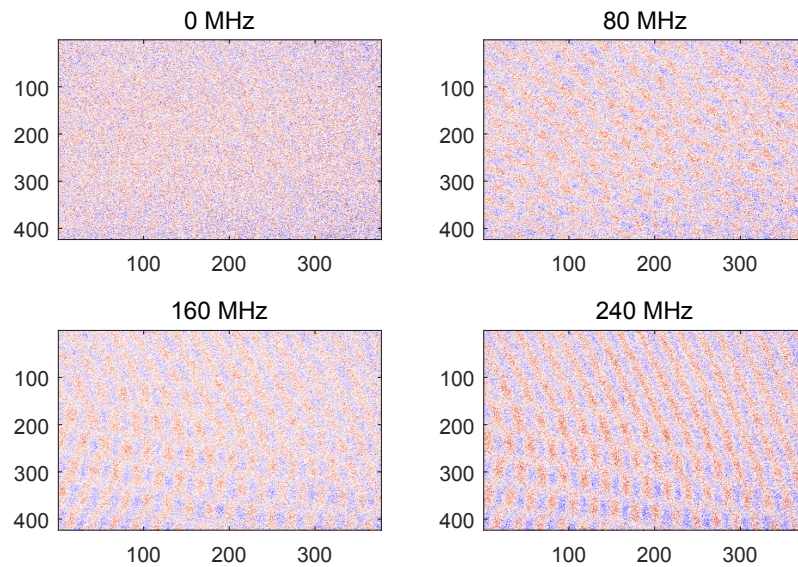


Figure 3.19.: Optical density without atoms for different frequency shifts of the imaging laser in the reference image compared to the absorption image. One can clearly see the structure evolving for larger shifts. This is due to the frequency dependence of the interference due to reflections in the imaging system.

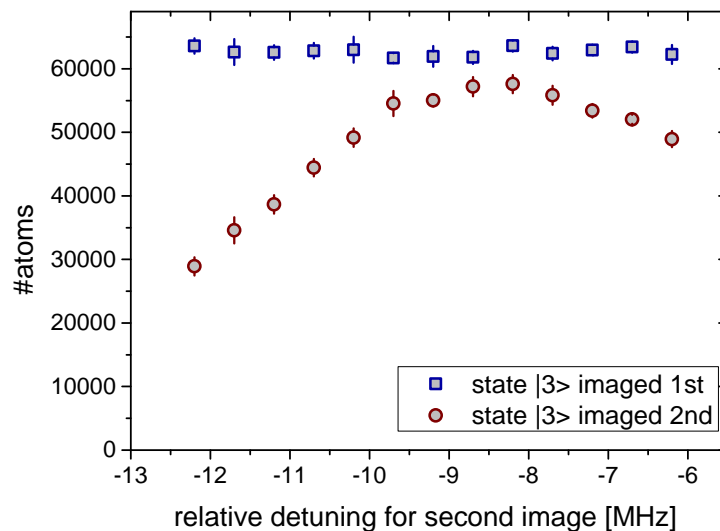


Figure 3.20.: The state $|3\rangle$ is imaged twice in the same cycle. For the second image we adjust the relative detuning of the start frequency compared to the first image. We see an optimal detuning at ≈ -8 MHz which matches the Doppler compensation slope we applied for both images.

line gives us insight of how much the atom number of each preparation varies. This results in a detection uncertainty of $\Delta_{\text{det}} \approx 6\%$ and a preparation uncertainty of $\Delta_{\text{prep}} \approx 14.6\%$. The detection uncertainty is very close to what we estimated from our imaging calibration. We can conclude that we are limited by our preparation to obtain better experimental reproducibility. Note that the preparation uncertainty also depends on the final spilling depth in our standing wave trap.

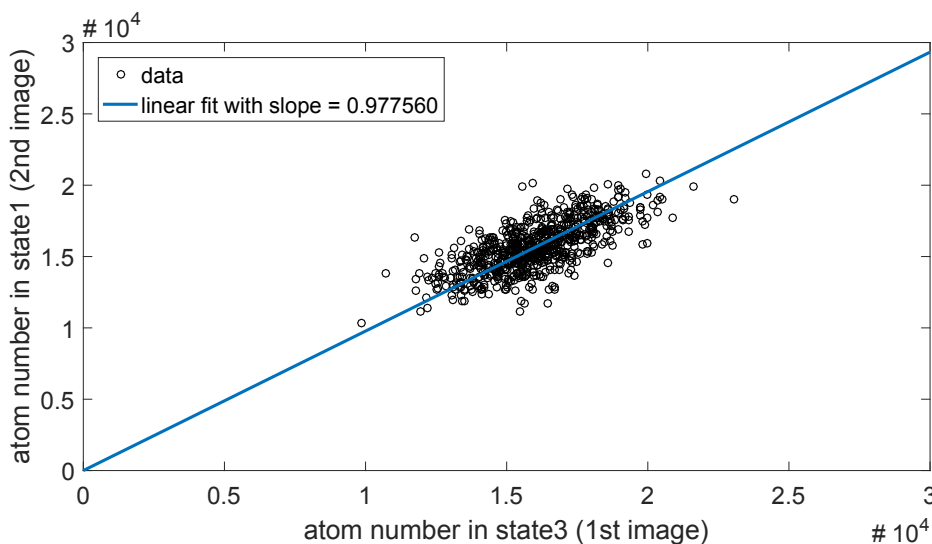


Figure 3.21.: The atom number in state $|3\rangle$, imaged first, is plotted against the atom number in state $|1\rangle$, imaged second. One observes a strong correlation indicating a good detection fidelity. A linear fit (blue line) to the data shows that the detected atom numbers for both states after correcting for dark state decay are within $\approx 2\%$. From a principal component analysis we can estimate the detection uncertainty to be $\Delta_{\text{det}} \approx 6\%$ and the preparation uncertainty to be $\Delta_{\text{prep}} \approx 14.6\%$.

However, when investigating strongly interacting systems one has to be careful. Even for moderately weak interactions, we see that removing atoms from one state heats up the system. Thus, momentum is transferred which can lead to a change of the density distribution already within this $100\ \mu\text{s}$ timescale. This was not studied in detail yet but first experiments observing the superfluid peak in momentum imaging show that the density distribution is considerably broadened for the state imaged second. Hence, this has to be considered in future experiments.

4. Superfluidity in a Shallow Quasi-2D Square Lattice

In this chapter we discuss experiments performed in a two-dimensional square lattice. These experiments have been described in more detail in [Bay15] and hence only a short review is given here with an emphasis on the experimental limitations we encountered.

The starting point for these experiments was a superfluid sample prepared in the SWT on the BEC side of the Feshbach resonance as described in [Rie15a, Mur15] where the atoms are fully paired into dimers and can be treated as bosons. By ramping up the retro-reflected lattice beams and keeping the axial confinement from the SWT, we transfer the sample into a two-dimensional square optical lattice. We observed a superfluid of strongly interacting bosonic molecules in a shallow lattice using a momentum imaging technique [Mur14] similar to the 3D optical lattice case in [Chi06]. For deeper lattices we encountered heating which destroys the superfluid phase. These experiments mark our first step towards our goal of creating low entropy states like the bosonic Mott-insulator in two-dimensional lattice geometries.

This section is organized as follows: first the momentum imaging technique used to observe the superfluid is introduced in 4.1. Subsequently our observations of a superfluid in the shallow lattice are presented in 4.2. At last the possible sources of heating and schemes to mitigate these in the future are discussed in 4.3.

4.1. Probing the Momentum Distribution of a Strongly Interacting Gas

We touched on the momentum imaging method already briefly when discussing our magnification calibration in chapter 3. The basic idea of the momentum imaging technique is to, instead of letting the particles evolve in free-space during the time-of-flight expansion, let them evolve in a weak harmonic trapping confinement in the horizontal plane. This is fulfilled naturally in our experiment as we always have a weak harmonic saddle point potential due to the magnetic Feshbach field coils. In the classical case the trajectory $x(t)$ of a particle moving in a harmonic potential is given by

$$x(t) = x_0 \cos(\omega t) + \frac{p_0}{m\omega} \sin(\omega t), \quad (4.1)$$

where x_0 and p_0 are the initial position and momentum of the particle, m is its mass and ω is the harmonic trapping frequency. After letting the system evolve for a quarter of the trap period $T = 2\pi/\omega$, the initial momentum p_0 is mapped onto the position $x(T/4)$ and vice versa. Thus, by simply doing absorption imaging after a

time-of-flight of $\tau_{\text{tof}} = T/4$ one obtains the in-situ momentum distribution of the cloud. This classical argument can also be shown to work in a quantum field theory framework [Mur14]. In our experiment the trapping frequency of the weak magnetic confinement is on the order of $\omega_{\text{magn}} \approx 2\pi \times 10 \text{ Hz}$ and hence results in a 25 ms time-of-flight to achieve this mapping which is experimentally feasible.

The assumption of a ballistic expansion seems to be at odds with the strongly interacting systems we are studying. However, several factors resolve this issue. First of all the system geometry with the strong axial confinement leads to a rapid initial expansion along the z-axis when switching off the trap. This leads to fast decrease in density and hence a reduction in the scattering rate. An estimation of the amount of scattering events taking place during the expansion yields that less than 10% of the sample scatter once [Mur14]. In addition, approximately 150 μs before the release, the magnetic field is quickly ramped towards the zero-crossing of the scattering length at 527 G¹. This reduces the scattering during the expansion while ensuring that the many-body wave function of the system has no time to adapt and thus remains unaffected. Using these techniques we were able to investigate the momentum distribution of a quasi-2D Fermi gas in the strongly interacting region and observe the phase transition into a condensed phase with a macroscopic occupation of low momentum states [Rie15a, Mur15].

Although the fast expansion along the z-axis quenches the interactions and thus enables this momentum imaging technique, it also poses a problem when imaging the sample along this axis. Due to the long time-of-flight the sample expands considerably and reaches an axial width of several hundred microns. This is larger than the depth-of-focus of the imaging system and thus reduces the resolution. To circumvent this we pulse on the modulated ODT beam after letting the sample expand for 100 μs to reduce the density. Tuning the duration of the pulse and the depth of the ODT beam such that $\tau_{\text{pulse}} = T_{z,\text{ODT}}/4$ we can effectively stop the expansion of the sample in the z-axis. As the radial trap frequency of the modulated ODT beam is on the same order as the magnetic saddle point potential and $T_{z,\text{ODT}} \ll T$, this only weakly perturbs the radial expansion and the $T/4$ time with this additional stopping pulse can be found experimentally. Thereby the sample is still in focus after 25 ms which increases the resolution as well as the signal strength.

For the momentum distribution of a superfluid in a quasi-2D square lattice one expects to observe additionally to a large occupation of low momenta also an increased occupation of momenta with multiple of the lattice momentum k_L . These peaks are challenging to observe as the particles have a large transverse momentum k_L and thus have a larger scattering rate at the beginning of the expansion when the sample is still dense. Thus, to reduce this scattering rate we turn off the SWT 50 μs before we release the particles from the lattice such that the sample already expands in the z-axis and reduces its density.

¹This is for the 12-mixture which was used in this experiment.

4.2. Observation of a Superfluid in the Quasi-2D Square Lattice

The first observation of the transition from a superfluid to a Mott-insulator state has been done in a three-dimensional lattice system using rubidium at small scattering lengths [Gre01]. There the transition was identified by observing the disappearance of sharp peaks in the lattice momentum distribution. For a strongly interacting Fermi gas in a three-dimensional lattice a similar result was obtained using lithium in [Chi06]. Here we report on the observation of the superfluid state in a shallow quasi-2D square lattice geometry.

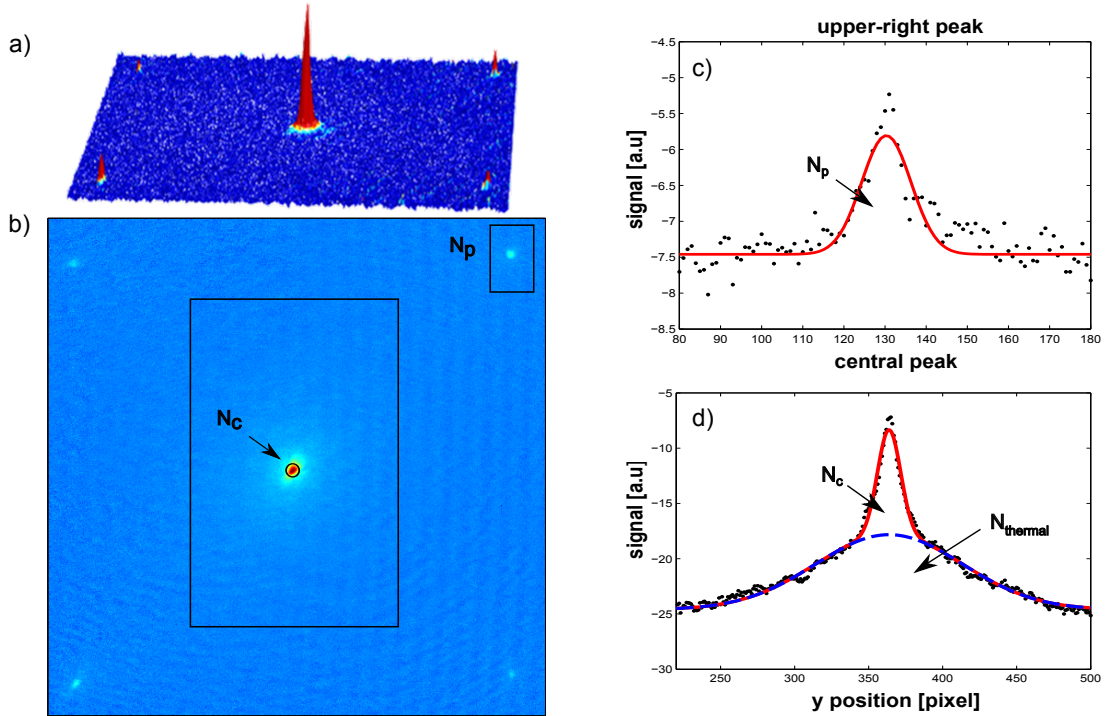


Figure 4.1.: a) 3D image of the averaged momentum distribution over 20 images of a superfluid sample released from a lattice with depth $V = 4.5 E_r$. b) To obtain information about the system both the atom number in the central condensed part (N_c) with zero-momentum as well as the atom number in the part with lattice momentum k_L (N_p) is extracted. This can be seen in c) and d) where the integration of the black region of interests is shown along the x-axis. For the central part a bimodal Gaussian distribution is fitted to differentiate the condensed part from the thermal background. In the lattice peak only the condensed part is visible and thus a single Gaussian is fitted. Adapted from [Bay15].

To transfer the sample from the SWT into the lattice, we linearly ramp up the lattice potential to its final depth on a timescale of 50 ms at a magnetic offset field of $B = 730$ G where the molecule-molecule 3D scattering length is $1500 a_0$. As the overall harmonic confinement of the lattice in the radial plane is stronger than that of the SWT, density has to be redistributed during the ramp up which limits the

speed one can use for the ramp and can introduce heating [Son16]. After the lattice is ramped up, the momentum distribution is obtained using the imaging technique described previously. For shallow lattices this leads to a momentum distribution as can be seen in Figure 4.1 a) as a 3D image and in b) as a 2D projection. There is a large peak at zero-momentum as well as four additional equidistant peaks along the lattice directions. These stem from the expansion of the lattice ground state into plane waves with integer multiples of the lattice momentum k_L as described in equation 2.53 in combination with the macroscopic occupation of low momentum states in the condensate. Here we cannot observe higher orders as they are on the one hand outside the range of our imaging system and their occupation would be furthermore suppressed compared to the $\pm k_L$ peaks and thus very challenging to resolve.

From such momentum distributions we can extract the condensed fraction both in the central peak as well as in the four lattice peaks. The central region has a thermal background and thus to extract the condensed part we employ a bimodal fit as can be seen in d). To obtain the condensed part from the lattice peaks we choose to fit only the upper right peak with a Gaussian as it is consistently the most visible and no thermal fraction could be distinguished from the noise background there as can be seen in c). The stark difference between the lattice axes are possibly due to a calibration issue between the lattice arms.

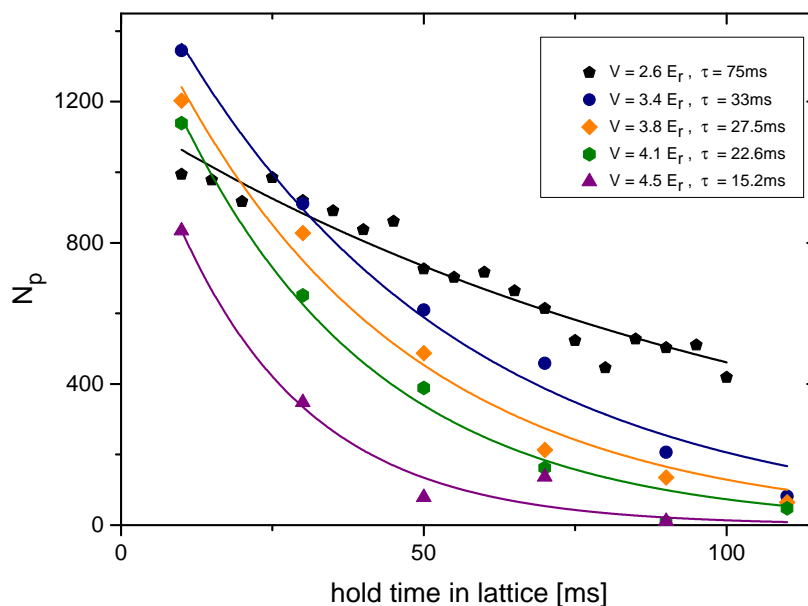


Figure 4.2.: The measured number of atoms in the upper right lattice peak is measured as a function of the hold time of the sample in the lattice for different lattice depths. One observes that the half-life time τ decreases considerably when increasing the lattice depth. Note that this is not atom loss but a loss of coherence due to an increase in temperature which stems from heating in the sample. Taken from [Bay15].

When increasing the lattice depth to drive the transition into a Mott-insulating state one expects these peaks to disappear as each particle is then localized to a single site and thus has broad Gaussian momentum distribution. The resulting momentum distribution from the lattice is then just the incoherent sum of these individual momentum distributions. Qualitatively, we observe this behavior when increasing the lattice depth. However, this broadening of the momentum distribution can also be a sign of heating which destroys the superfluid phase and results in a similar thermal momentum distribution. To investigate this we measured the lifetime of the superfluid in the lattice at different lattice depths by holding the sample for differing times in the lattice before releasing and measuring the number of atoms N_p . The result can be seen in Figure 4.2. We observe a decay in the lattice momentum peak which is strongly dependent on the lattice depth. For shallow lattices on the order of $V = 2.6 E_r$ the half-life time is $\tau = 75$ ms and it is reduced drastically when increasing the lattice depth further such that at $V = 4.5 E_r$ it is already down to $\tau \approx 15$ ms. This limits our ability to prepare and probe the Mott-insulating state. The source of this heating is not yet understood and will be discussed in the next section.

4.3. Heating in the Lattice

In optical traps fluctuations in the laser power or positional instabilities can lead to parametric heating [Geh98] as particles can be excited to higher trap levels. The heating rate scales with the trapping frequency as ω^2 and thus this is especially important for lattices where in our setup the on-site trapping frequencies can reach up to 100 kHz.

To establish if the observed heating is a single particle effect and does not stem from many-body physics, we prepared a polarized sample by removing one spin component with a resonant imaging pulse. After holding the sample for a variable time either in the SWT only or in a combination of the SWT and the lattice with a depth of $40 E_r$, we measured the vertical width of the sample after a short time-of-flight of 3 ms. The result is shown in Figure 4.3. In the SWT we do not observe significant heating as the width is constant for all hold times. In the combined trap including the lattice we observe an overall larger width which is expected due to the increased confinement. But here we also see an increase of the width over time indicating the presence of a heating mechanism already for a non-interacting sample which points towards technical noise.

That this heating manifests itself in the z-axis is not surprising as this axis rapidly becomes the axis of weakest confinement when turning on the lattice beams. This is due to the axial confinement $\omega_z \approx 2\pi \times 7$ kHz being fixed by the SWT and having negligible influence from the lattice beams. For deep lattices, as it is the case here, the band gap exceeds $h \cdot 100$ kHz and thus band excitations are suppressed. To confirm this, we also checked for radial excitations using a band-mapping technique [Blo08]. There we did not observe any increase in population of higher bands within our resolution. From this measurement of the polarized sample we also observe that the timescale where the increase in axial width occurs is much longer than

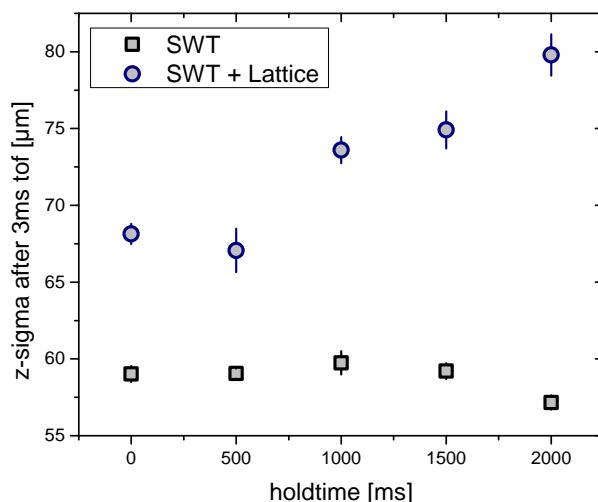


Figure 4.3.: The Gaussian width of the sample in the z -axis after a time-of-flight of 3 ms is shown as a function of the holdtime in the trap. This was done both for a polarized sample in the SWT only (black squares) and for a polarized sample in the combined potential of the SWT and the lattice with depth $40 E_r$ (blue circles). Whereas for the SWT no increase in the width is observable on a 2 s timescale, the width in the combined trap increases significantly on this timescale, indicating the presence of a heating mechanism.

the timescale in the coherence measurement in the previous section. This might be partially explainable by energy arguments when one considers that the axial trapping frequency corresponds to an energy $\hbar \cdot \omega_z / k_B \approx 300$ nK and thus already a small population transfer of atoms into excited states as measured in Figure 4.3 can heat the sample considerably upon thermalization and lead to the observed loss of coherence. Even at the more shallow lattices used in the coherence loss measurements in Figure 4.2 where the band gap is small compared to $\hbar \cdot \omega_z$, the excitation energy needed to excite particles around the condensed part $q = 0$ is on the order of $4 E_r$ which is much larger than $\hbar \cdot \omega_z$ considering the molecular recoil energy $E_{r,\text{molecules}} = 0.5 E_{r,\text{atom}} = h \cdot 14.5$ kHz (see numerical calculations in Figure 2.10) and thus the same argument that the axial confinement is weakest applies here. Apart from these single-particle effects, the strong interactions present in the molecular sample can also lead to interaction energies on the order of the axial confinement and thus it is not yet clear if solving these single particle heating effects due to noise will be enough to prepare a low entropy Mott-insulator.

During the course of this thesis we examined the relative intensity noise (RIN) of our laser. The power stabilization is done by measuring the transmitted beam power behind a mirror with a photodiode and using this signal as feedback for a PID-loop to control the rf power of an AOM. Improving the PID-loop by replacing the digital version with a faster analogue one we were not able to improve on the heating despite some decrease in RIN. We also tested exchanging the seed of the fiber amplifier with an Innolight Mephisto laser which has reduced RIN compared to the Innolight Mephisto S version we employ. Although we measured a reduction of RIN

after the fiber amplifier of 10 dB we did not observe any significant improvement in the heating rate. Another possibility could be phase noise as we do not actively stabilize the phase. This might be an issue in the lattice arms as there the travel distance of the retro-reflected beam is up to 1 m before it interferes in the experiment chamber. This could be tested in the future by setting up an interferometer.

In the immediate future, we will implement a high numerical aperture objective in combination with a spatial light modulator (SLM) into the setup. Thereby we can project a wide variety of potentials onto the atom plane [Hol14]. We will then revisit these heating questions and hopefully resolve them.

5. Pairing in the Normal Phase of a Quasi-2D Fermi Gas

In previous work in our group we investigated the phase transition to a superfluid throughout the two-dimensional BEC-BCS crossover [Rie15a, Mur15]. Superfluidity emerges from an instability in the normal phase and hence - to understand its origin - a better understanding of the normal phase is required. In high- T_c cuprates it has been shown that some effects like the suppression in the static magnetic susceptibility which occur in the superfluid phase, already set in at temperatures T^* larger than T_c [War89, All89, Joh89]. This part of the phase diagram is known as the pseudogap region. However, in these materials effects like doping and the underlying lattice structure play an important role and hence the influence of pairing is not easy to separate [Che05].

Here, ultracold Fermi gases can provide further insight. In these systems the interaction between the particles is tunable via Feshbach resonances and the superfluid phase transition is inherently connected to pairing as long-range phase coherence requires a bosonic degree of freedom. Depending on the interaction, these pairs can be either two-body dimer states or (many-body) Cooper-pairs in momentum space. On the BEC side where the binding energy of these dimers E_B is much larger than the thermal energy $k_B T$, these pairs are trivially formed above the critical temperature T_c and the ensuing phase transition is well understood. In the weakly attractive fermionic limit where BCS theory is applicable, the pairing temperature for Cooper pairs is identical with the critical temperature. This leaves the question what happens in the strongly interacting crossover region around the Feshbach resonance. Is there a pseudogap phase with preformed Cooper pairs already above the critical temperature or is the normal phase a Fermi liquid with well-defined quasiparticles [Zwi16]? In three dimensional systems, theoretical models predict such a pseudogap phase above the critical temperature at unitarity [Che09b, Mag09, Pie09]. Momentum-resolved rf spectroscopy experiments [Gae10] showed for example back-bending in the dispersion relation near k_F similar to the BCS case. However, the existence of back-bending far from k_F is predicted to be a universal feature of Fermi gases with contact interactions and thus is not unambiguously a sign of a pseudogap. Moreover, thermodynamic measurements of the specific heat of the system above T_c showed no signal of a pseudogap [Ku12].

In a two-dimensional system, the pseudogap region is expected to be enhanced compared to the 3D case due to the increased role of quantum fluctuations [Mar15]. Similarly to the 3D case, momentum-resolved rf spectroscopy revealed signs of back-bending in the spectra for a quasi-2D system [Fel11]. However, a theoretical model using a high-temperature Virial expansion can reproduce these spectra [Nga13] and thus the evidence for a pseudogap is not conclusive. Furthermore, rf spectroscopy

measurements studying the evolution from a 3D to a 2D system [Som12] showed that the pairing gap measured up to interaction strengths of $\ln(k_F a_{2D}) < 0.5$ is still in agreement with the binding energy of simple two-body dimers which exist at all interaction strengths in two dimensions. This supports the argument of [Lev15] obtained from QMC calculations that a pseudogap is only expected for $\ln(k_F a_{2D}) > 0.5$ where remnants of a Fermi surface are present and the chemical potential $\mu > 0$. Note however that there are also T-matrix calculations which predict this transition from a molecular to a pseudogap regime to happen already at interaction strengths $\ln(k_F a_{2D}) \approx 0 - 0.1$ [Mar15] and thus it is still an open question.

In general, rf spectroscopy is a very sensitive tool to study pairing as demonstrated e.g. in 3D systems in [Chi04, Sch07a, Sch08b, Sch08a, Sch09, Gae10, Sag15] as well as in quasi-2D systems [Fel11, Frö11, Bau12, Frö12, Kos12, Som12, Zha12]. During the course of this thesis we studied the pairing in a quasi two-dimensional system in the BEC-BCS crossover using a spatially resolved rf spectroscopy technique similar to [Sch08a]. The local rf response is crucial as our system is inhomogeneous and hence both the relative temperature scale T/T_F as well as the interaction strength $\ln(k_F a_{2D})$ vary considerably when comparing the high-density center of the cloud to the low-density wings. From theoretical predictions [Fis14], we expect to see a gapped excitation spectrum: a paired branch indicating either the population of dimer states or many-body Cooper pairs and an unpaired branch. In a spin balanced system the unpaired branch can only be excited thermally whereas in a slightly spin imbalanced mixture the excess atoms of the majority can populate this branch additionally. The energy difference between these branches then gives us access to study the pairing gap as a function of interaction strength and temperature. In this thesis we employed both approaches. We took an imbalanced dataset to investigate the pairing gap in the crossover region and a balanced dataset to study the onset of pairing at high temperatures and the interaction induced density dependent energy shifts in the rf spectra.

This chapter is organized as follows: first the basic principles of spatially resolved rf spectroscopy are summarized in section 5.1. Then mean-field BCS theory as a qualitative description of the crossover is discussed in section 5.2. Subsequently the experimental methods, calibrations and systematics to obtain the spatially resolved rf spectra are presented in section 5.3. Our experimental results are discussed next. We start by investigating the initial state interaction induced shifts as a function of interaction strength by looking at the rf spectra of balanced samples in section 5.4. Next we investigate the onset of pairing at large temperatures $T/T_F > 1$ in the crossover regime in section 5.5. At last, we use an imbalanced mixture to estimate the pairing gap as a function of interaction strength and temperature in section 5.6 and identify a region where the system cannot be described simply in terms of two-body physics and thus many-body effects play a role.

5.1. RF Spectroscopy as a Tool

In ^6Li the three lowest hyperfine states used in the experiment have a level spacing on the order of $\Delta E \approx h \cdot 80 \text{ MHz}$ and differ in their nuclear spin projection m_I .

Therefore, by applying a resonant oscillating radio frequency field, we can flip the nuclear spin and drive transitions between neighbouring states. This is exemplary shown in Figure 5.1 a). If one starts with a non-interacting atom in state $|3\rangle$ (red), one can drive a transition to state $|2\rangle$ (blue) by applying a rf pulse with energy $E_{\text{free-free}}$. However, if the atom in state $|3\rangle$ is initially paired¹, its energy is lowered and hence a smaller energy $E_{\text{bound-free}}$ is required to flip its spin. This difference in the required rf frequency can be measured in experiments, making rf spectroscopy a very good tool to probe pairing as well as interactions as the involved transitions between different states are very sensitive to such shifts.

This section covers the basics of rf spectroscopy and its application in our ${}^6\text{Li}$ system. It starts by introducing coherent as well as incoherent rf transitions in section 5.1.1 and 5.1.2. Next interaction effects which can shift the observed resonance positions are motivated in section 5.1.3 and the lineshape of the rf spectrum is discussed in section 5.1.4. Then the concept of locally resolved rf spectroscopy as a means to obtain information from homogeneous subsamples in our inhomogeneous trap is explained in section 5.1.5. At last the specific situation in our ${}^6\text{Li}$ system is presented in section 5.1.6.

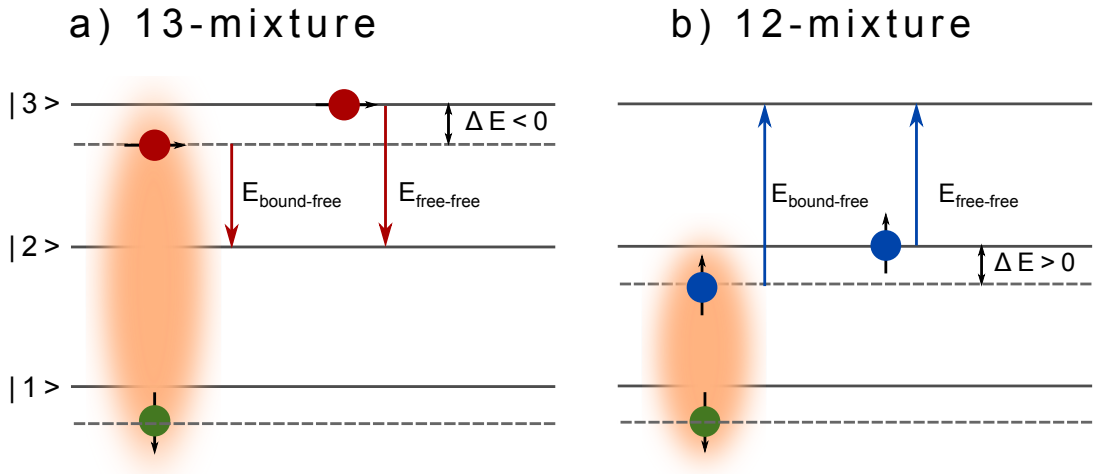


Figure 5.1.: These sketches show the transition scheme in our ${}^6\text{Li}$ system. In a) the case for the 13-mixture is shown. The bound-free transition is shifted to smaller energies with respect to the free-free transition. In b) the case for the 12-mixture is shown. Here the energy shift of the bound-free transition is positive compared to the free-free transition.

5.1.1. Coherent RF Transitions

In the case of a non-interacting system without decoherence or dephasing, the application of rf pulses to obtain population transfer can be described in the framework of Rabi oscillations [Bra03]. Here the assumption is a two-level system $\{|g\rangle, |e\rangle\}$ where a harmonic perturbation $V(t) \propto \sin(\omega t)$ is applied. In our case the two

¹In this case a dimer with an atom in state $|1\rangle$ is sketched.

level system consists of either a $\{|2\rangle, |3\rangle\}$ or $\{|1\rangle, |2\rangle\}$ combination of the hyperfine states, which we call in the following 12- or 13-mixtures, and the harmonic perturbation is the rf pulse which can be approximated for a long pulse by a plane wave $\vec{B}_{\text{rf}}(t) = \vec{B}_0 \cos(\omega_{\text{rf}}t)$.

This coupling then leads to a superposition² $\psi(t) = \cos\left(\frac{\Omega t}{2}\right)|g\rangle + \sin\left(\frac{\Omega t}{2}\right)|e\rangle$ between the states, and the population oscillates with the Rabi frequency Ω . This behavior can be seen in Figure 5.2 b) where the population in state $|2\rangle$ is plotted versus the applied pulse duration τ_{rf} . The Rabi frequency can then be extracted from a damped³ sine fit (blue line). In general, the Rabi frequency depends on the coupling between the magnetic field and the magnetic moment μ_s as

$$\Omega \propto \mu_s \vec{B}_0 \vec{e}_s, \quad (5.1)$$

where \vec{e}_s is the spin axis. Hence, we can adjust the Rabi frequency experimentally by changing the rf power P_{rf} we put into the rf coil as $|\vec{B}_0| \propto \sqrt{P_{\text{rf}}}$.

So far we assumed the driving oscillating field to be on resonance. If the field is off-resonant with a detuning $\Delta\omega_{\text{rf}}$, the effective Rabi frequency Ω_{eff} increases as $\Omega_{\text{eff}} = \sqrt{\Omega^2 + \Delta\omega_{\text{rf}}^2}$ and the observed contrast in the population oscillation decreases as $(\Omega/\Omega_{\text{eff}})^2$. This determines the lineshape of the coherent rf transition to be Lorentzian. This can be seen in Figure 5.2 a). Here the loss of atoms in state $|2\rangle$ is plotted versus the detuning when applying a 25 ms long, weak rf pulse. The blue line is a Lorentzian fit which nicely reproduces the data. Due to the long pulse duration, the width of the rf transition is mostly given by our achievable magnetic field stability. From the experimental data we can also notice that the population oscillation gets damped with an exponential decay constant $\tau_{\text{decoherence}} \approx 20$ ms. This is due to magnetic field inhomogeneities which lead to variations of the resonance frequency over the sample and hence to decoherence.

So far only the spin degree of freedom was included in the derivation. However, for a general treatment also the spatial degree of freedom has to be included. The transition can then be described in terms of a wave function for the initial state $|\Phi_i\rangle$ and the final state $|\Phi_f\rangle$. The Rabi frequency is then proportional to the wave function overlap regarding the rf operator $\hat{R}F$ as

$$\Omega \propto \langle \Phi_f | \hat{R}F | \Phi_i \rangle. \quad (5.2)$$

The momentum of the rf photon is negligible compared to the atom momentum and thus for systems where the spin and spatial degree of freedom separate, the spin Rabi frequency Ω_s as derived before is then modified by the spatial wave function overlap as

$$\Omega \propto \Omega_s \langle \Psi_{\text{spatial},f} | \Psi_{\text{spatial},i} \rangle. \quad (5.3)$$

This can lead to a reduction of the Rabi frequency and thus the coupling decreases when driving for example bound-bound transitions.

²Here we assume the atoms to be initially in state $|g\rangle$ at $t = 0$.

³The damping is due to decoherence in the sample.

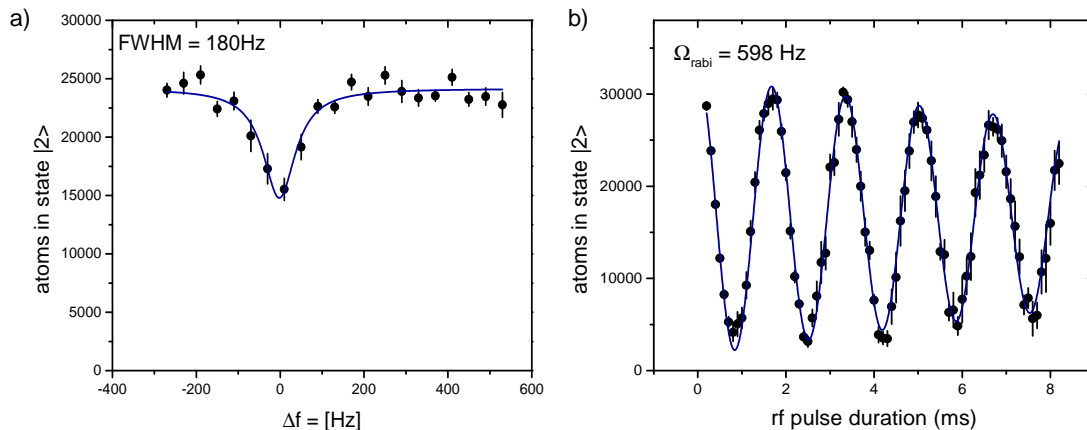


Figure 5.2.: a) State $|2\rangle$ population versus detuning Δf for a pulse duration $\tau = 25$ ms in a polarized sample. One can see a loss feature at resonance with a FWHM ≈ 180 Hz obtained from a Lorentzian fit (blue line). b) Rabi oscillations in a polarized sample of state $|2\rangle$ atoms. By tuning the applied pulse duration τ_{rf} , population is transferred in a two-level system and oscillations are observed. Due to decoherence, the contrast reduces for longer times and the Rabi frequency Ω can be extracted from a damped sine fit (blue line).

5.1.2. Incoherent RF Transitions in Interacting Systems

In the experiment we are interested in strongly interacting Fermi gases and thus the previously described coherent framework is not applicable. When one starts e.g. with a 12-mixture and drives the transition from state $|2\rangle$ into state $|3\rangle$, then scattering between the superposition state $\psi = \alpha |2\rangle + \beta |3\rangle$ and the atoms in state $|1\rangle$ quickly lead to decoherence, thus destroying the superposition. Since the scattering rate in our system in the strongly interacting regime is on the order of kHz, the timescale of decoherence is now below milliseconds. In order to still make predictions about the driven transition, we use Fermi's Golden rule [Sch07b] and consider a linear response of the system. The transition rate Γ is then given by

$$\Gamma(\omega) = \pi\Omega^2 \sum_{\mathbf{k}} A_{|2\rangle}(\mathbf{k}, \xi_{\mathbf{k}} - \hbar\omega) f(\xi_{\mathbf{k}} - \hbar\omega), \quad (5.4)$$

where $A_{|2\rangle}(\mathbf{k}, \epsilon)$ is the spectral function of the interacting state $|2\rangle$, $f(x)$ is the Fermi function and $\xi_{\mathbf{k}} = \hbar^2 k^2 / 2m - \mu$ is the fermion dispersion relation measured from the chemical potential μ . The spectral function describes the probability to find a single particle excitation with both momentum \mathbf{k} and energy $\hbar\omega$ [Gia13] and it has to be calculated by a suitable many-body approach. Hence, the sum basically integrates over all initial momentum states which can be transferred via an rf photon into a different internal state with the same momentum. To account for the initial occupation we have to multiply by the Fermi function.

Interactions can also lead to pairing in the system. This will influence the form of the spectral function and results in an energy shift ΔE in the observed transition

rate. Let us consider for example a dimer with binding energy E_B . Then, to drive the transition of one constituent atom into a third, unoccupied state, the rf photon has to additionally bring up the energy required to break the dimer. Hence, the observed resonance frequency $\nu_{\text{res}} = \nu_{\text{free-free}} + \nu_B$ is shifted. This makes rf spectroscopy a sensitive tool to probe pairing in the system.

5.1.3. Interaction Shifts

In the previous section we did not consider the effect interactions have on the observed rf transitions, apart from the pairing. Interactions can lead to an energy shift in the observed rf transitions and are thus a source of systematic error. In the literature these energy shifts are either known as Hartree shifts or clock-shifts and only occur when driving a rf transition into a third state [Ket08].

Both interactions in the initial as well as in the final state can affect the observed rf transition energy. When driving e.g. the transition $|3\rangle \rightarrow |2\rangle$ in a 13-mixture, the initial interaction in the 13-mixture as well as the final state interactions between the transferred atoms in state $|2\rangle$ and state $|1\rangle$ will play a role. However, the interaction between state $|2\rangle$ and state $|3\rangle$ does not affect the transition as the system is in a superposition state during the pulse duration [Ket08].

In section 5.2 we showed that the pairing dissociation peak occurs at positive energies $\hbar \cdot \omega_{rf} > 0$ for the 12-mixture and at negative energies $\hbar \cdot \omega_{rf} < 0$ in the 13-mixture. The Hartree energy shift for an initial 12- or 13-mixture respectively is then given by

$$\Delta E_{\text{Hartree},12} = E_{\text{H},\text{final}} - E_{\text{H},\text{initial}} \quad \text{and} \quad \Delta E_{\text{Hartree},13} = E_{\text{H},\text{initial}} - E_{\text{H},\text{final}} \quad (5.5)$$

where $E_{\text{H},\text{initial}}$ is the energy shift due to the initial state interaction and $E_{\text{H},\text{final}}$ is the energy shift due to the final state interaction. We now adopt the convention to define the pairing dissociation peak to be at positive energies also in the 13-mixture. Then we can write the Hartree shift for all cases as

$$\Delta E_{\text{Hartree}} = E_{\text{H},\text{final}} - E_{\text{H},\text{initial}}. \quad (5.6)$$

In general, the description of the strongly interacting regime is challenging and an analytic formula for the Hartree shift does not exist. In the weak coupling regime $|\ln(k_F a_{2D})| \gg 1$, however, the energy shifts can be described in a mean-field picture. There the energy shift $\Delta E = g_{2D} \cdot n$ is proportional to the density n with a coupling constant g given by [Blo75]

$$g_{2D} = -\frac{2\pi\hbar^2}{m \ln(k_F a_{2D})} \quad (5.7)$$

and thus one can also write the energy shift in terms of the Fermi energy as

$$\Delta E_{\text{Hartree},\text{mean-field}} = -\frac{E_F}{\ln(k_F a_{2D})}. \quad (5.8)$$

For the strongly interacting region $|\ln(k_F a_{2D})| \simeq 1$ this mean-field formula diverges and is not applicable. From the existence of a bound state at all interaction

strengths in a two-dimensional system and the absence of a divergence in the scattering length a_{2D} , we know that the two limits have to be smoothly connected. For a two-body system one can calculate the change in energy in the crossover region analytically and obtain

$$\Delta E_{Hartree,interpolated} = -\frac{\ln(k_F a_{2D})}{(\ln(k_F a_{2D})^2 + \pi^2)} E_F \quad (5.9)$$

which converges in the limits $|\ln(k_F a_{2D})| \gg 1$ towards equation 5.8. We use this as a first estimate to compare our measured Hartree shifts to in section 5.4. For a better comparison one would have to apply QMC or Luttinger-Ward calculations.

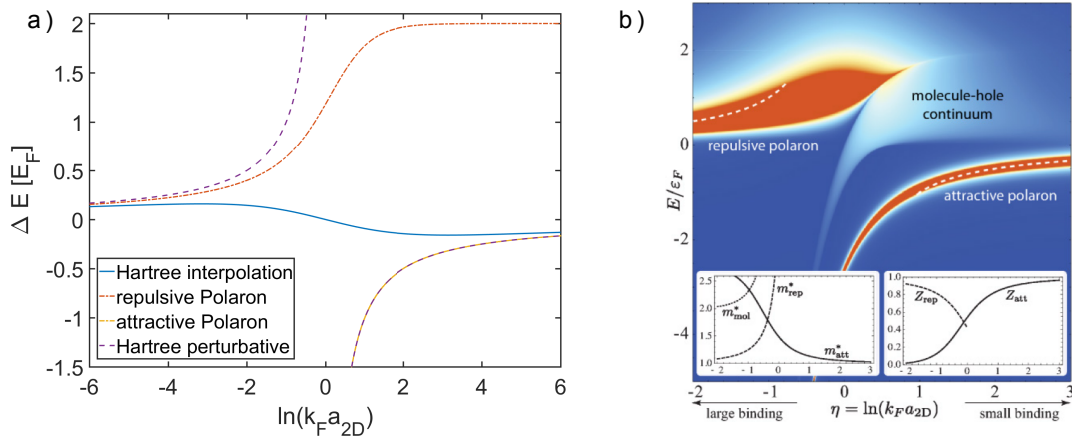


Figure 5.3.: a) Interaction induced Hartree shift given in units of the Fermi energy E_F as a function of the interaction strength $\ln(k_F a_{2D})$ for the different models. b) Plot of the zero-momentum spectral function of the Fermi polaron taken from [Sch12]. A broad repulsive polaron with positive energy and a narrow attractive polaron with negative energy exist. The white dashed lines are from the mean-field theory in equation 5.8 and are not applicable in the strongly interacting regime.

For the final state interactions one has to additionally consider that only a fraction of the atoms are transferred into the final state. Thus, the final state system can be often described as a minority interacting with a sea of majority atoms and hence a Fermi polaron model is more suitable [Zha12, Sch12, Nga12]. The zero-momentum spectral function of the Fermi polaron in two-dimensions has been calculated in [Sch12] using a T-matrix approach and result in two branches: a broad and thus short lived repulsive polaron branch with positive energy for negative (extending to small positive) $\ln(k_F a_{2D})$ and a narrower attractive polaron branch with negative energy for positive (extending to small negative) $\ln(k_F a_{2D})$. The graph from [Sch12] is shown in Figure 5.3 b). Here the branches are shown in red and the white dashed lines are the perturbative theory. One can see that the repulsive polaron energy in the strongly interacting region is bounded to energies smaller $2E_F$.

In the weak coupling limit $E_B/E_F \rightarrow \infty$, the repulsive polaron branch can be calculated as [Nga12]

$$E_{\text{polaron}}^{\text{rep}} = \frac{2E_F}{\ln(E_B/E_F)}. \quad (5.10)$$

For the strongly interacting region this leads to a divergence and thus cannot be applied. To estimate the repulsive polaron energy in this regime we use a heuristic function which describes the maximum of the spectral function obtained from T-matrix calculations [Sch12] as [Ens17]

$$E_{\text{polaron}}^{\text{rep}} = \frac{2E_F}{1 + \ln(1 + \exp[-\ln(2 \cdot E_F/E_B)])}, \quad (5.11)$$

which gives a valid approximation at least in the regime $\ln(k_F a_{2D}) < 0$.

The attractive polaron is approximated in the weak coupling limit $E_B \ll E_F$ by [Zha12]

$$E_{\text{polaron}}^{\text{attr}} = -\frac{2E_F}{\ln(2E_F/E_B)} = -\frac{E_F}{\ln(k_F a_{2D})}. \quad (5.12)$$

This approximation is within 2% of a more rigorous T-matrix calculation in the regime $\ln(k_F a_{2D}) \geq 5$ which is the final state regime we operate in for the 12-mixture. Note that all these derivations are done in a true two-dimensional system and thus do not consider the quasi-2D regime. This is important as on the BEC side, the binding energy approaches the 3D binding energy and thus the relation in equation 2.44 between a_{2D} and E_B does not hold. Thus, to calculate the final state repulsive polaron shift we use the quasi-2D binding energy obtained from equation 2.45. The different interaction models are shown Figure 5.3 a) as a function of the interaction strength.

For the measurements described in this thesis, the knowledge of the interaction shift is important in the case where we only observe a single branch in our rf spectrum. In the case where we observe both the pairing branch as well as the thermally (or by imbalance) populated free-free branch, we are only interested in the relative distance between these peaks as the interaction induced shift is for both branches the same. In general, ${}^6\text{Li}$ is challenging to use for rf measurements as there exists no non-interacting final state, unlike e.g. in ${}^{40}\text{K}$. However, this can also be useful if one is interested in the study of such final state effects.

5.1.4. Lineshape

The rf transition rate $\Gamma_{\text{rf}}(\omega)$ contains the information about the spectral function of the state. In a two-body system it can be derived at all interactions strengths. However, in a many-body system the description becomes challenging especially in a 2D system where a bound dimer state exists at all interaction strengths. Still, one can find a universal relation for the large frequency rf tail in the 2D system [Lan12]

$$\Gamma(\omega) \rightarrow \frac{\ln^2(E'_B/E_B) \Omega^2 C}{4m\omega^2 [\ln^2(\omega/E'_B) + \pi^2]}, \quad (5.13)$$

where E'_B is the dimer energy of the final state, E_B is the dimer energy of the initial state and C is the Tan contact of the system. The Tan contact [Tan08] is related to the universal power-law tail $n_\sigma(k) \rightarrow C/k^4$ of the momentum distribution of each spin state and there exist other relations linking it to thermodynamic properties of the system as well. Thus, a measurement of the large frequency tail can also give access to the contact [Frö12]. From the formula we can see that in the high-frequency tail we obtain the simple scaling $\Gamma(\omega) \sim 1/\omega^2$ if $|\ln(\omega/E'_B)| \ll \pi$ or if the final state interactions are negligible.

For a two-body system consisting of dimers one can obtain a general expression for the transition rate $\Gamma(\omega)$ as [Lan12]

$$\Gamma(\omega) = \frac{\pi E_B \Omega^2 \ln^2(E'_B/E_B)}{4m\omega^2 (\ln^2[(\omega - E_B)/E'_B] + \pi^2)} \Theta(\hbar\omega - E_B). \quad (5.14)$$

Here, the possible bound-bound transition between E_B and E'_B occurring at $\delta(\hbar\omega - E_B + E'_B)$ has been ignored. For the data taken with the 13-mixture the bound-bound transition is shifted far away from the region of interest and can be measured independently. In the 12-mixture, the final state binding energy is $E'_B < 1$ Hz and thus much smaller than typical system temperatures on the order of $k_B T/h \approx 2$ kHz. Hence, the transition rate there is highly suppressed and can be neglected.

The lineshape of the transition rate is thus strongly dependent on the final state dimer also for the bound-free transition. This can be seen in Figure 5.4, where the rf lineshape obtained from equation 5.14 is plotted for a fixed initial state dimer energy $E_B = 10$ kHz for three different final state dimer energies E'_B . We can see that the final dimer energy has a very strong effect on the lineshape and the drop off of the large frequency tail. This affects also the relation between the observed peak energy E_{peak} and the threshold energy E_B . This is plotted in the inlay where the ratio between the peak and the threshold energy is plotted as a function of the ratio E_B/E'_B . The peak has a maximal shift from the threshold at around $E_B/E'_B \simeq 0.3$, where the corresponding lineshape has the most pronounced high frequency tail. For small final dimer energies E'_B on the other hand, the lineshape gets very narrow with a fast drop off. As the ratio between the peak position and the threshold energy can reach up to 20%, we cannot rely on the peak position as an estimate for the threshold energy.

In the experiment the rf lineshape is also affected by our experimental rf frequency resolution as well as interactions. The frequency resolution is in our case limited by the Fourier limited width of the rf pulse due to our short pulse lengths of $\tau = 4$ ms which leads to a frequency resolution of $\sigma_{\text{rf}} \approx 220$ Hz⁴. This leads to a broadening of the lineshape which can be simulated by convolving the lineshape with a Gaussian profile of width σ_{rf} . This is shown in Figure 5.5 for two different settings. In general this will shift the observed peak to larger frequencies and blur out the sharp threshold. Thus, to determine the threshold energy experimentally we include this convolution in the modeling of our measured spectra. In addition other final state effects can effect the lineshapes as well.

⁴We apply a square pulse and use the time-bandwidth product $\Delta t \cdot \Delta\nu \geq 0.886$ to estimate the frequency resolution.

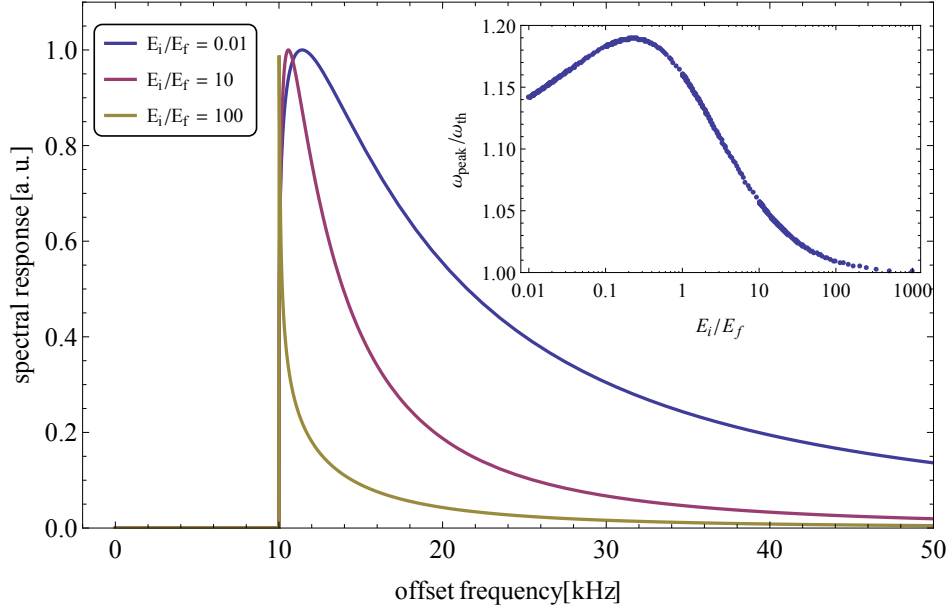


Figure 5.4.: Dependence of the rf lineshape on the final state dimer energy. The threshold function equation 5.14 is plotted for 3 different values of final state interactions for an initial state dimer energy $E_{B,i} = 10$ kHz. For deeply bound final state dimers (blue line), the lineshape is very broad and the peak position ω_{peak} is shifted upwards compared to the threshold position ω_{th} . When the final state dimer energy gets smaller (red, yellow), the lineshape becomes narrower and the peak position ω_{peak} approaches the threshold position ω_{th} . The ratio $\omega_{\text{peak}}/\omega_{\text{th}}$ is shown as a function of the initial to final state dimer energy ratio $E_{B,i}/E_{B,f}$ in the inset where we again set $E_{B,i} = 10$ kHz. For $E_{B,i}/E_{B,f} \sim 1$, the peak is shifted by up to almost 20% compared to the threshold. For $E_{B,i}/E_{B,f} \gg 10$, the peak position approaches the threshold position.

Furthermore, possible many-body effects in the strongly interacting region can additionally alter the lineshape. For this, however, we do not have a suitable model as a theoretical description in this regime is challenging. The modeling of our experimentally measured lineshapes is described in more detail in 5.3.8.

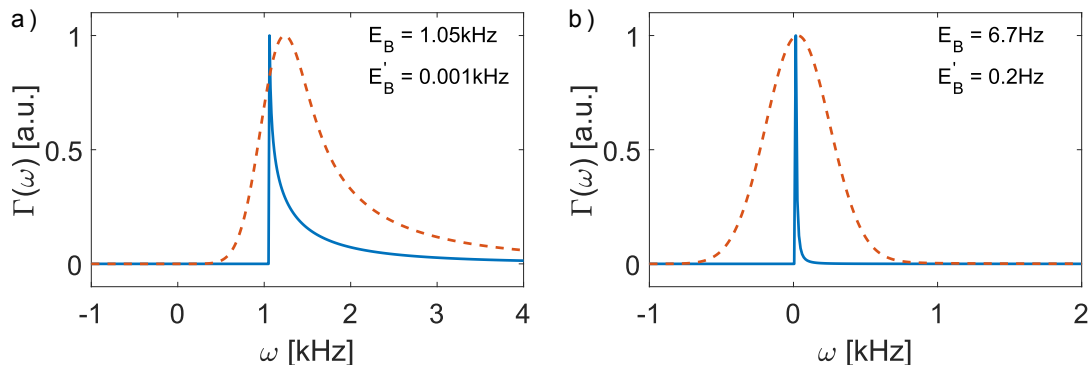


Figure 5.5.: The experimental rf resolution leads to a convolution of the rf lineshapes. This is shown here for two examples in the 12-mixture where the final state binding energy is negligible. This corresponds to a) $B = 844$ G and b) $B = 1002$ G. The blue line is the model from equation 5.14 and the red dashed line is the same model convoluted with a Gaussian profile with our experimental frequency resolution $\sigma_{\text{rf}} = 220$ Hz. One can see that the convolution leads to a shift of the observed peak to larger frequencies which depends strongly on the form of the rf tail.

5.1.5. Spatially Resolved RF Spectra

In section 2.3.1 we discussed how the physics changes in our 2D Fermi mixture when changing the interaction strength $\ln(k_F a_{2D})$. As the interaction strength is explicitly density dependent, it changes in our inhomogeneous samples as we move from the center with higher density to the low density wings. This is also the case for the relative temperature T/T_F as in a 2D system, T_F is directly proportional to the density n_{2D} . Therefore, in the wings of the sample the system is non-degenerate and behaves as a thermal gas. Hence, it is necessary to locally probe the system to avoid averaging over different physical regimes which can potentially hide relevant features. Such locally resolved measurements have been performed e.g. in a 3D system in [Sch08a]. Here we explain the procedure for a 2D system.

In the normal phase, there is no long-range phase coherence present and since our potential is smooth we can use the local density approximation (LDA). Then at each point \mathbf{r} in the trap we describe the system as homogeneous with density $n_{2D}(\mathbf{r})$, relative temperature $T/T_F(\mathbf{r})$ and interaction strength $\ln(k_F a_{2D})(\mathbf{r})$. This is shown exemplary in Figure 5.6. In the upper panel, radial density profiles are plotted corresponding to images where a rf pulse was applied (blue, green) and a reference where no rf pulse was applied (orange). Depending on the applied frequency, only

parts of the sample are transferred which shows up e.g. as a ring in the image when taking the difference between the rf sample and the reference as shown in the inlay. In the lower panel the evolution of the local variables $T/T_F(r)$ and $\ln(k_F a_{2D})(r)$ is shown across the sample. The relative temperature $T/T_F(r)$ is lowest in the center where the density and thus T_F is maximal. In contrast, the interaction strength $\ln(k_F a_{2D})(r)$ decreases when going towards the wing as k_F is reduced.

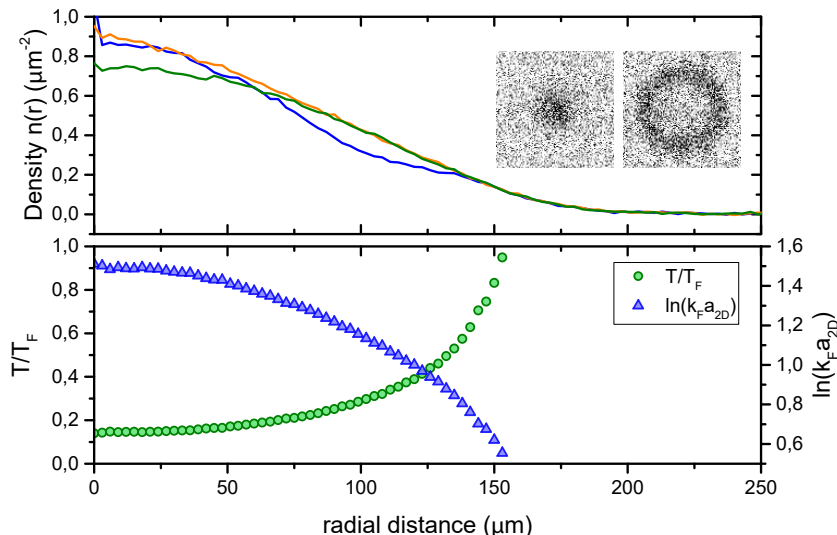


Figure 5.6.: The upper panel shows different radial density profiles: the blue and green profiles have been taken with an applied rf pulse. One can see that the density is locally reduced compared to the reference profile (orange) where no rf pulse has been applied. From these profiles one can infer the locally transferred density as shown in the inlays. In the lower panel the local variables $T/T_F(r)$ and $\ln(k_F a_{2D})(r)$ are plotted versus the radius. One can see that the relative temperature increases as one approaches the wings of the sample. The interaction strength however decreases in the low density region. This highlights again the need to resolve the rf spectra spatially.

To ensure that the rf probing is only done locally such that the atoms have no time to redistribute inside the trap during the rf pulse, we apply rf pulses which are short compared to the trapping period. We then image the sample directly at the end of the pulse and obtain thus a local rf response $n_{2D}(\mathbf{r}, \omega)$ as was shown in Figure 5.6. Subsequently, we then compare this density to a reference density $n_{2D,\text{ref}}(\mathbf{r})$ taken at the same conditions without application of the rf pulse. From this we infer the fraction of transferred atoms as

$$I(\mathbf{r}, \omega) = \frac{(n_{2D,\text{ref}}(\mathbf{r}) - n_{2D}(\mathbf{r}, \omega))}{n_{2D,\text{ref}}(\mathbf{r})}. \quad (5.15)$$

This can then be plotted as a rf spectrum as showcased in Figure 5.7. In section 5.3.5, we will give a more detailed explanation on the limits of our achievable frequency resolution.

Note that the transfer of atoms into a third state leads to three-body losses. However, these occur however on timescales longer than the rf pulse duration and thus we do not observe an influence of this loss process in the rf spectra. Furthermore, the spectra obtained with this method are momentum integrated and hence we do not have direct access to the single particle spectral function $A(\mathbf{k}, \omega)$. Performing a momentum resolved spectroscopy like e.g. in [Fel11], however, averages over the inhomogeneous sample, thus introducing again the problem of the different temperatures and interactions strengths across the sample. In future experiments this can be resolved by preparing homogeneous systems and then performing momentum resolved spectroscopy.

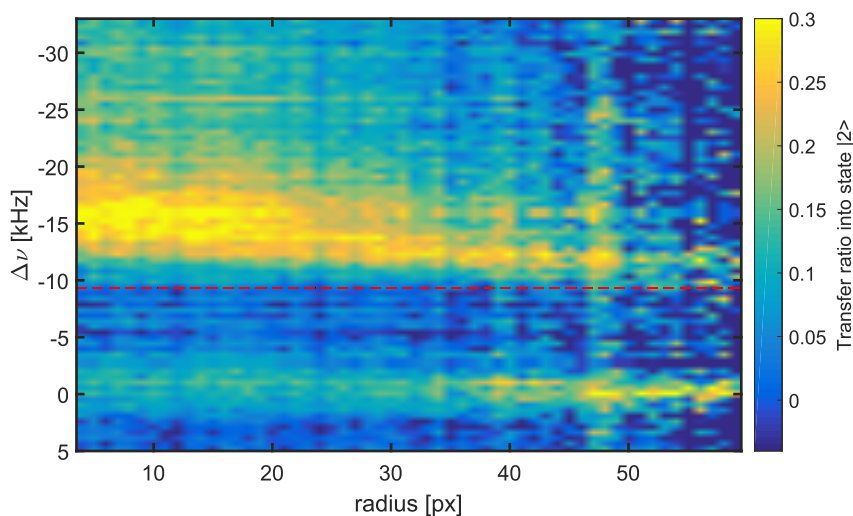


Figure 5.7.: RF spectrum of an imbalanced mixture on the BEC side. One can differentiate between a free-free transition around $\Delta\nu = 0$ and the bound-free transition with dimer binding energy E_B (red dashed line). Due to the local resolution one can observe the density dependent interaction shifts.

5.1.6. The ${}^6\text{Li}$ System

In the experiment we use the three lowest hyperfine states of ${}^6\text{Li}$. There exists a broad Feshbach resonance for all binary mixtures in close vicinity to each other (see Figure 2.5 b)). Thus, when performing rf spectroscopy one has to consider both initial and final state interactions. Large final state interactions then complicate the description of the system and should be avoided. In our ${}^6\text{Li}$ system we can minimize these final state effects by preparing either a 12- or 13-mixture depending on the initial interaction strength we want to realize.

This is depicted in Figure 5.8 where both the 3D scattering length (upper panel) as well as the corresponding quasi-2D interaction strength $\ln(k_F a_{2D})$ for a typical experimental Fermi momentum $k_F \approx 3.5 \mu\text{m}^{-1}$ in the trap center (lower panel) are shown as a function of the external magnetic offset field B in the regime we use in the experiment.

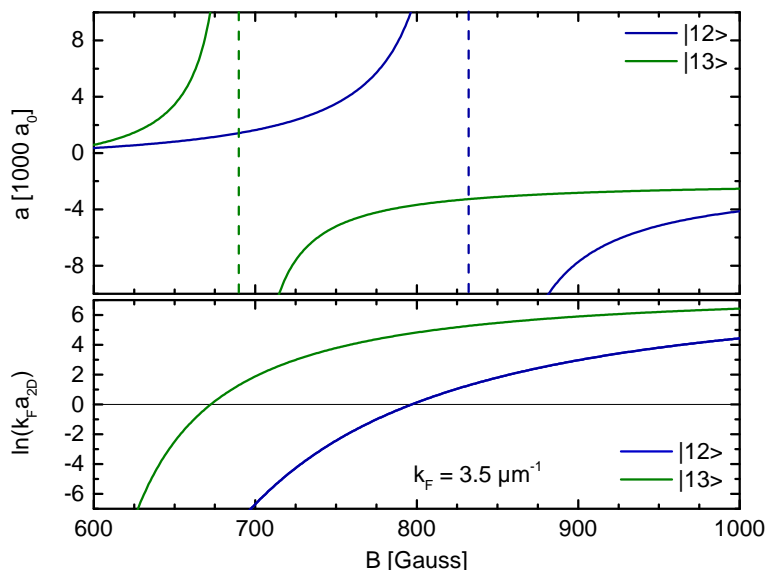


Figure 5.8.: In the upper panel the 3D scattering length in units of the Bohr radius is plotted versus the magnetic offset field for both the 12- and the 13-mixture. On the BCS side of the 13-resonance the interaction strength in the 12-mixture increases. On the BCS side of the 12-resonance, the interaction in the 13-mixture is limited to the background scattering length. In the lower panel the 2D interaction parameter $\ln(k_F a_{2D})$ is plotted as a function of the magnetic offset field. Adapted from [Rie15b].

In the experiment we want to explore the strongly interacting region around $\ln(k_F a_{2D})^{\text{initial}} \sim 0$. When starting in the 13-mixture, the final interaction strength is $\ln(k_F a_{2D})^{\text{final}} < -6$ up to magnetic fields of around $B \approx 700$ G. Hence, there the assumption of a weakly coupled final state is valid. For magnetic fields larger than $B \approx 700$ G one approaches the region of strong interactions and thus final state influences become important. This can be seen when looking at the rf spectra in this regime in section 5.4.

For an initial 12-mixture, the final state interactions in the 13-mixture begin to saturate towards $\ln(k_F a_{2D})^{\text{final}} \approx 6$ above the Feshbach resonance in the 12-mixture at $B_{12} \approx 832$ G. This is due to the 3D background scattering length having a large negative value $a_{3D,\text{bg}} \approx -2000 a_0$. Thus, when operating above the Feshbach resonance we can again assume the weak coupling limit to be an adequate description of the final state interaction. Here we do not consider the interaction in a 23-mixture as it has no influence on the transitions we use during these experiments.

5.2. Mean-Field Treatment of the Crossover Region

For the crossover region in a quasi-2D system there is no complete theory describing the normal phase and thus the expected pseudogap behavior. Advances have been made [Fis14, Mar15] but a complete picture is still missing. Here we will present the often used mean-field BCS approach to motivate the expected rf spectra in the

crossover region.

Technically, mean-field BCS theory only describes the superfluid phase in the weakly attractive limit and does not incorporate the notion of a pseudogap. However, when extending the theory into the strongly interacting regime one can still extract a critical temperature. It is however much larger than the experimentally observed critical temperatures and thus it is assumed that this temperature now does not signal the onset of superfluidity but rather the onset of many-body pairing and thus gives an estimate of the crossover temperature T^* . Note however that this ansatz does not incorporate quantum fluctuations which play an increased role in two dimensions and thus the obtained results are not expected to show good agreement with experiments but rather aim to give an intuitive picture.

In zero-temperature mean-field BCS theory, the spectral function $A_{\text{BCS}}(\mathbf{k}, \omega)$ of the ground state shows two branches which can be associated with the population of many-body pairs in the lower branch and the thermal excitations which break up the pairs in the upper branch. The single-particle dispersion relation for these two branches is then given by [Zwe16]

$$E_{\mathbf{k}, \text{BCS}}^{(\pm)} = \mu \pm \sqrt{\eta_k^2 + \Delta^2} \quad (5.16)$$

with $\eta_k = \frac{\hbar^2 k^2}{2m} - \mu$ being the free particle dispersion and $\Delta^2 = 2E_B E_F$ being the excitation gap where E_B is the two-body dimer energy as defined in equation 2.45. On the BCS side the excitation gap Δ can be written as $\Delta = \sqrt{\Delta_{\text{sc}}^2 + \Delta_{\text{pg}}^2}$, where Δ_{sc} is the superfluid gap and Δ_{pg} is the pseudogap. On the BEC side where $\mu = -E_B/2$ at zero temperature the gap vanishes. The BCS single-particle dispersion from equation 5.16 is plotted in Figure 5.3 a) as the blue (red) curve where also the free particle dispersion $E_{\text{free}} = \frac{\hbar^2 k^2}{2m}$ is given as the green curve. At zero temperature the system is fully paired and only the lower branch (blue) is occupied. For finite temperatures, also the upper branch can be thermally excited if the temperature is on the order of the excitation gap Δ .

The rf response of the system at low temperatures can then be explained as depicted in Figure 5.3 b). Here the system is paired and the lower BCS branch is dominantly occupied as indicated by the blue line. The upper excited BCS branch in contrast is only thermally populated with most of the population occurring around $k = k_F$ where the excitation gap is minimal. In addition the free particle dispersion of the initial state $|i\rangle$ is given as the green dashed line and the free particle dispersion of the final state $|f\rangle$ is given as the green line. For the following we presume that $E_f > E_i$ and that the energy offset between these states is $E_{\text{free-free}} = \hbar \cdot \omega_{\text{free-free}}$. The minimal rf energy required to break a pair and transfer an atom from the lower BCS branch to the final state $|f\rangle$ is then given at $k = 0$ and results in a rf transition energy threshold $\hbar \cdot \omega_{\text{th}}^+$ relative to $E_{\text{free-free}}$ with

$$\omega_{\text{th}}^+ = \sqrt{\mu^2 + \Delta^2} - \mu > 0. \quad (5.17)$$

Using the relation $\mu = E_F - E_B/2$ we can derive $\hbar \cdot \omega_{\text{th}}^+ = E_B$ at zero temperature. For the thermally excited atoms in the upper branch, the situation is slightly different. There the required rf transition energy is now bounded at both sides. The maximal

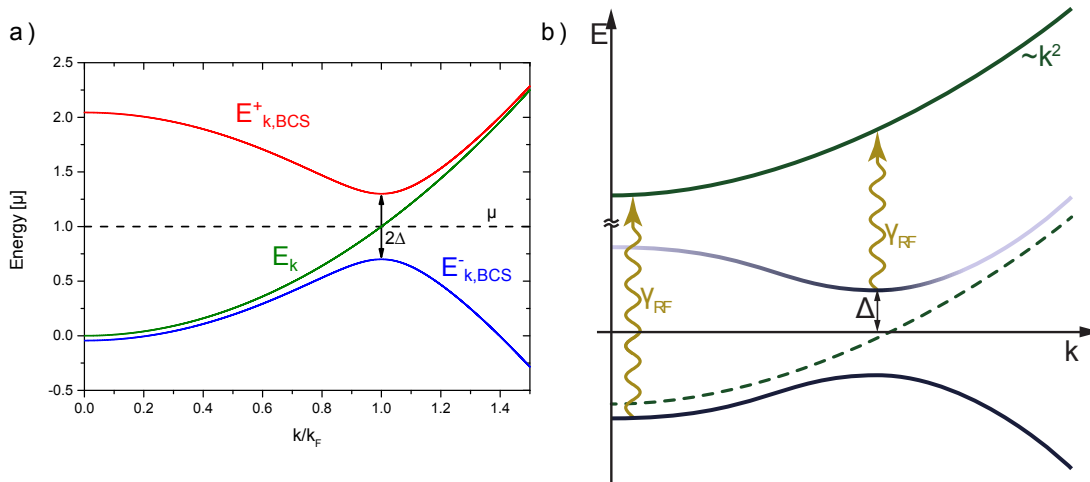


Figure 5.9.: a) Single-particle dispersion relation $E_{\mathbf{k},\text{BCS}}^{(\pm)}$ (red/blue) for zero temperature BCS theory ($\Delta = 0.3E_F$) as well as the dispersion relation $E_{\mathbf{k}}$ for free particles (green). They indicate the energy required to remove or add a single particle. The excitation gap Δ is defined in BCS theory as the minimal energy required to place an excitation in the system and is thus given by the minimal distance between the chemical potential μ and the upper BCS branch (red). b) Sketch of the rf response when driving the system from an initial state $|i\rangle$ into a final state $|f\rangle$. The minimum required energy to break a pair in the lower BCS branch and project it onto the free final state is given by $\hbar \cdot \omega_{\text{th}} = E_B + E_{\text{free-free}}$. In contrast the energy required to drive an atom from the excited BCS branch to the free final state is reduced by the excitation gap Δ .

required energy for the rf transition approaches $E_{\text{free-free}}$ at $k \gg k_F$, resulting in $\Delta\omega < 0$ relative to the free-free transition. On the other hand the minimal required energy is again given at $k = 0$ and results in the threshold

$$\omega_{\text{max}}^- = -\sqrt{\mu^2 + \Delta^2} - \mu = -2E_F < \omega < 0 \quad (5.18)$$

at zero temperature. Note that this definition only applies in the fermionic regime for $\mu > 0$ and that this peak coincides with the free-free peak once the excitation gap $\Delta = 0$. On the BEC side at large temperatures there will be an equilibrium between dimers and free atoms and thus the upper branch will just be the free particle excitations at $\omega = 0$. This is depicted in Figure 5.10. In a) the BEC side is shown. There, one expects a bound-free branch with threshold energy E_B and a free-free branch at $\omega = 0$. In contrast on the BCS side (b)) we expect the free-free branch to be modified at temperatures where the excitation gap starts to open up. Then most of the weight of this peak is shifted to negative frequencies at $-\Delta$ as the thermal excitations mostly populate the momentum states $k \approx k_F$. The threshold of the bound-free branch is still at E_B as in the BEC case. Thus, the distance between these peaks is a measure of the excitation gap Δ . However, the exact relation between the peak of the negative frequency branch and the excitation gap depends strongly on the thermal population and thus a quantitative determination of the excitation gap is difficult [Che09a]. However, the occurrence of a shift towards negative frequencies is still a strong sign to determine whether a pseudogap region is present or not.

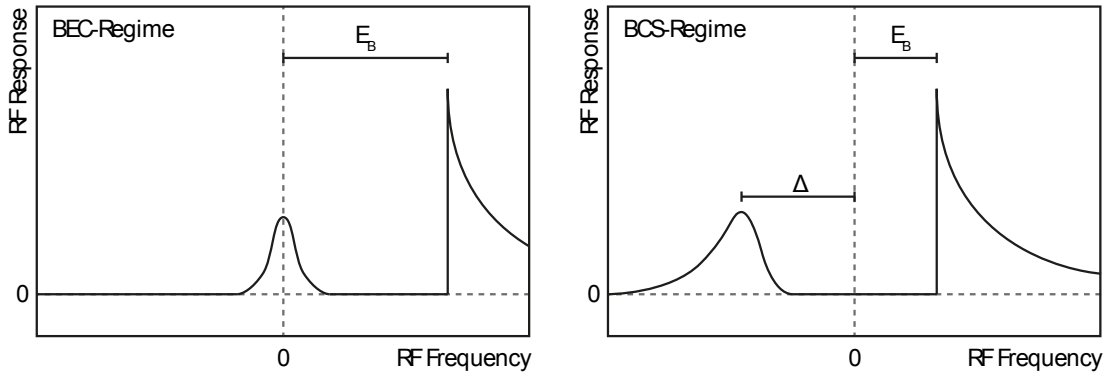


Figure 5.10.: Sketch of the expected lineshapes for the different regimes. On the BEC side (left panel) there is no gapped excitation spectrum and thus one expects to see a peak at zero detuning indicating the free-free transition and a peak with threshold at E_B indicating the dissociation of the bound dimer pairs. On the BCS side (right panel), however, thermal excitations are still subject to many-body effects for a non-zero excitation gap Δ and thus the free-free branch is shifted to negative frequencies. The shift of the transition gives an estimate of Δ . The exact form and peak position depend however on the population of the free atom branch.

To increase the visibility of the unpaired particle branch, one can also introduce a small spin imbalance into the system. Thereby the excess atoms of the majority will populate the upper branch and thus mimic the thermal occupation, under the assumption that the presence of a small imbalance does not change the dispersion relation. This was first done in a 3D system [Sch08a] and is applied in this work as well.

The above derivations all assumed the zero temperature limit of BCS theory where the free atom branch would not be populated. One can extend these to finite temperatures [Bab98] which results in a temperature dependent excitation gap $\Delta(T/T_F)$ as well as a temperature dependent $\mu(T/T_F)$. However, these results can only give a qualitative description of the expected physics like the temperature dependent gap and the single particle excitations around the Fermi momentum. For quantitative results they cannot be relied on as they do not incorporate quantum fluctuations which play an important role especially in two-dimensional systems.

Note that the picture painted above for the rf transition assumed that the final state energy $E_f > E_i$. In our ${}^6\text{Li}$ system this is the case if we for example start with the 12-mixture and drive the transition from state $|2\rangle$ to state $|3\rangle$. However, if we start in the 13-mixture and drive the transition from state $|3\rangle$ to state $|2\rangle$, the signs are changed and the bound-free peak occurs now at negative frequencies. This has to be considered when investigating our rf spectra in the following sections.

5.3. Experimental Implementation and Methods

This section covers the experimental implementation and the methods we use to analyze the data. It starts with the data preparation in subsection 5.3.1 and the way we tune the interaction strength and temperature in the system in subsection 5.3.2. Next, our method to imbalance the system is introduced in subsection 5.3.3 and the determination of the free-free peak as a reference for our measurements is discussed in subsection 5.3.4. Subsequently, the limitations of our frequency resolution are debated in subsection 5.3.5 and the thermometry of our samples is explained in subsection 5.3.6. At last, the atom number in adjacent layers is discussed in subsection 5.3.7 and the modeling of the rf lineshapes is explained in subsection 5.3.8.

5.3.1. Data Preparation

In order to obtain a good signal-to-noise ratio for the rf spectra, we have to average over a large enough data set. Hence, at each magnetic field of interest we take at least 50 shots for each applied rf frequency as well as for the reference image. For each rf frequency subset, we calculate the density profile for each shot as described in section 3.2. We then integrate along the x- and y-axis respectively and perform a Gaussian fit to obtain the center of the cloud. Subsequently, we shift all images such that their centers are at the same position to account for trap center fluctuation we see in our experiment on the order of $6\ \mu\text{m}$ along the standing wave trap beam direction. We then obtain the atom number for each shot by integrating over the region containing atoms.

In section 3.2.5, we showed that our imaging detection fidelity is higher than the preparation fidelity. Therefore, we use the previously obtained atom number to post-select our data such that we only consider shots which are within 20% of the mean atom number. Thus, we avoid any outliers in the preparation to influence our results.

We then average over the remaining data and perform an elliptical average to account for the non-ellipticity in our horizontal trap frequencies of $\omega_x : \omega_y = 1.1 : 1$. Thus, we end up with an averaged radial profile $n_{2D}(r)$. From these radial profiles we then obtain the rf spectra $I(\mathbf{r}, \omega) = \frac{n_{2D,ref}(\mathbf{r}) - n_{2D}(\mathbf{r}, \omega)}{n_{2D,ref}(\mathbf{r})}$ at each magnetic field.

5.3.2. Tuning the Interaction Strength and Temperature

In order to access the phase diagram, we need to tune both the relative temperature T/T_F as well as the interaction strength $\ln(k_F a_{2D})$. Equation 2.24 shows that in a 2D system, the Fermi energy E_F and thus also T_F scales linearly with the density n . Similarly, also the interaction strength is density dependent as k_F scales with the square root of the density n . Therefore, in our inhomogeneous trapping potential we sample over a trace of the phase diagram as we go from the center of the cloud towards the wing. This can be seen in Figure 5.6, where both the relative temperature T/T_F as well as the interaction strength $\ln(k_F a_{2D})$ are plotted as a function of the radial distance from the trap center (lower panel). This emphasizes the need to resolve the rf response locally, as otherwise one would average over different parts of the phase diagram as shown in Figure 5.6.

To access the crossover in the interaction strength, we change the magnetic offset field we apply with the Feshbach coils. Thereby we can make use of the broad Feshbach resonances present in ${}^6\text{Li}$ and can go from the BEC side with $\ln(k_F a_{2D}) \leq -1$ to the BCS side with $\ln(k_F a_{2D}) \geq 1$. This can be seen in Figure 5.11 A for the 13-mixture. The relative temperature T/T_F in comparison already changes from $T/T_F \simeq 0.1$ to $T/T_F > 1$ as we go towards the wing of the trap. To investigate the normal phase just above the superfluid transition, this is already sufficient. However, to study the onset of pair formation in the gas, as done in section 5.5, we need to achieve larger temperatures. We accomplish this by modulating the trap depth of our standing wave trap sinusoidally by 10% with twice the trapping frequency ω_z for a varying time τ_{shake} . After applying the modulation, we hold the sample for 200 ms to ensure re-thermalization. We check that no atoms are lost due to this procedure. This leads to an increase in T/T_F as shown in Figure 5.11 B. At last, we can also tune the system by changing the final evaporation depth in the standing wave trap. Thereby we change both the absolute temperature T as well as the density n and thus T_F and k_F . The result can be seen exemplary in Figure 5.11 C, where a smaller trap depth indicates less atoms and thus a reduced density.

5.3.3. Creating Spin Imbalance

A part of the experiments were performed in a spin imbalanced sample in the 13-mixture. Our current evaporation scheme revolves around producing a molecular BEC in the ODT by performing the evaporative cooling on the repulsive side of

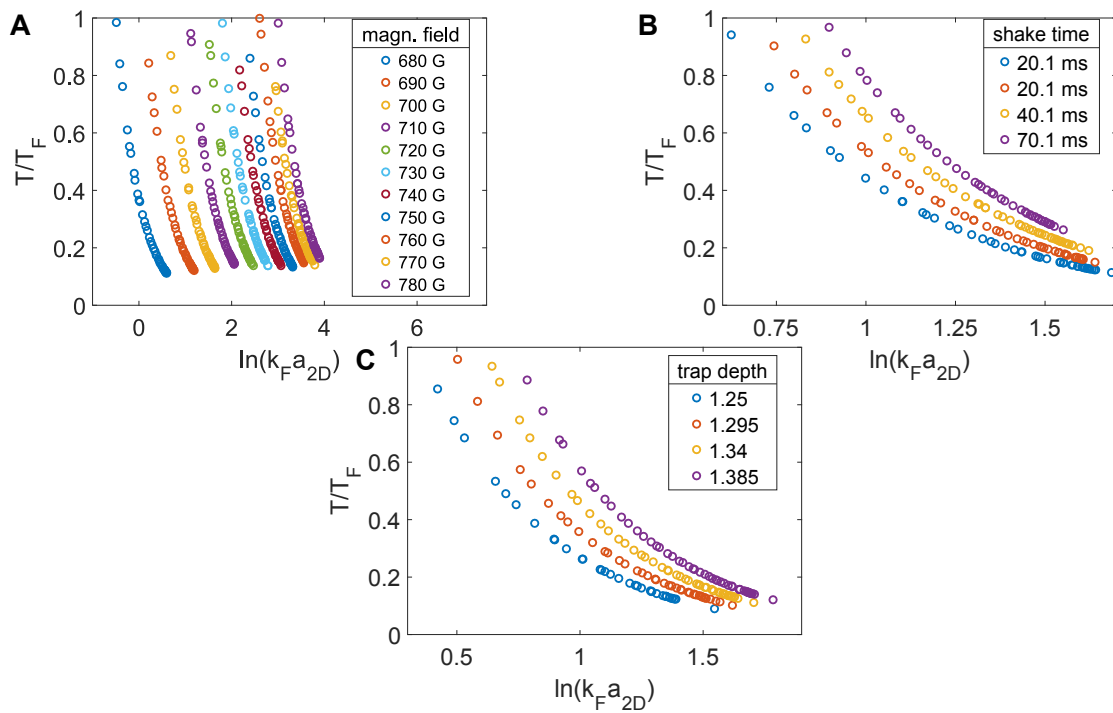


Figure 5.11.: Traces through the phase diagram obtained from a sample at different magnetic fields in **A**, for different shake times of the trap modulation and thus an increasing temperature in **B** and for different final spill depths of the SWT and different atomnumber in **C**.

the Feshbach resonance and subsequent transfer into a single layer of the SWT (see chapter 3.1). Thus, we end up with a spin balanced sample in the SWT and have to introduce a spin imbalance at this stage. Therefore, we again use a Landau-Zener passage as described for the preparation of a 13-mixture. By adjusting the parameters such that we reduce the transfer efficiency, we can transfer a small part of the atoms from state $|1\rangle$ to state $|2\rangle$ at a magnetic field of $B = 1000$ G where the atoms are unpaired and the interaction is relatively weak. The atoms transferred to state $|2\rangle$ are then lost in three-body collisions which reduces the overall atom number but results in an imbalance with the majority of atoms in state $|3\rangle$ and the minority in state $|1\rangle$. This is shown in Figure 5.12 for three different settings of the ramp speed in our Landau-Zener passage. The radial density profiles show that by increasing the amount of transferred atoms, we increase the local polarization $p_{\text{loc}} = \frac{n_{|3\rangle} - n_{|1\rangle}}{n_{|3\rangle} + n_{|1\rangle}}$ as shown in the inlays in the plots. As we operate in the normal phase, we do not observe a phase separation into a balanced core and a polarized wing as one observes in a superfluid [Sch08a, Mit16] but rather see a constant local polarization only increasing slightly in the wings of the sample. For the experiments performed in section 5.6 we used a setting close to B with a local polarization on the order of 10 – 15 %. We can also see the limitations of this imbalance scheme. When creating larger imbalances, one loses a considerable amount of atoms in three-body collisions. This loss process introduces heating and thus limits the achievable temperatures to about $T/T_F \geq 0.5$.

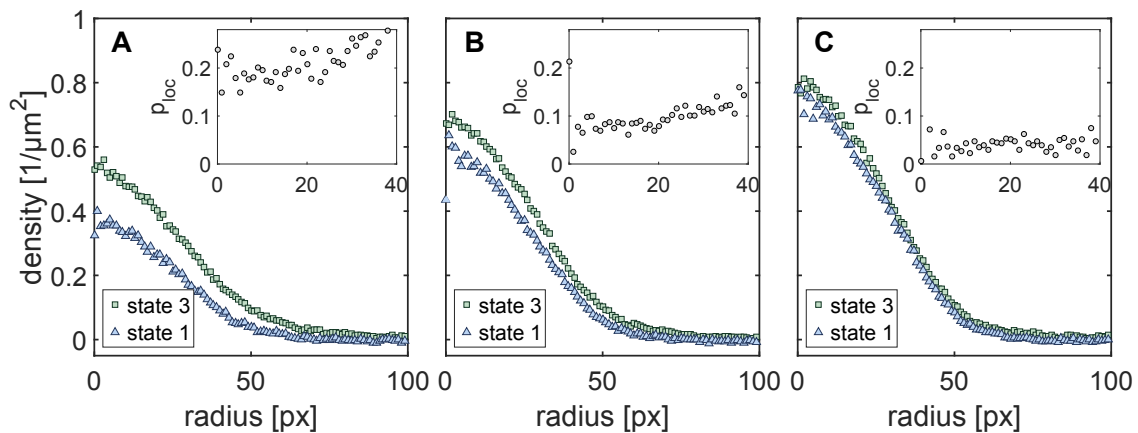


Figure 5.12.: Majority ($|3\rangle$) and minority ($|1\rangle$) radial density profiles after introducing spin imbalance using a Landau-Zener passage with varying ramp speed. For lower ramp speed **A** the introduced imbalance increases at the cost of increased atom loss. For larger ramp speed **C** the losses are small and the system is only slightly imbalanced. In the experiment we use the setting shown in **B**. The inlays show the local polarization p_{loc} as a function of the radius in pixel, resulting in A: $p_{\text{loc}} \approx 0.2$, B: $p_{\text{loc}} \approx 0.1$ and C: $p_{\text{loc}} \approx 0.05$ across the sample. As we operate in the normal phase, we do not observe a phase separation with a balanced core.

5.3.4. Determination of the Free-Free Transition

In order to obtain a reference frequency for our experiments, we measure the bare rf transition $\nu_{\text{free-free}}$ of a non-interacting sample. This can be achieved by using a polarized sample, since identical fermions do not interact at low energies. Experimentally, we do this by ramping our sample across the Feshbach resonance to a magnetic field of 1100 G where the interaction for both the 12-mixture as well as the 13-mixture is weak. We then pulse on the imaging beam for $8 \mu\text{s}$ and set it to be resonant to state $|1\rangle$. This removes the atoms in state $|1\rangle$ from the trap while still keeping the atoms in the other state trapped. Due to the weak interactions present, the remaining atoms are nevertheless heated up. However, this has no influence on the determination of the free-free resonance position.

To determine the free-free resonance positions we then use a long rf pulse ($\tau_{\text{rf}} = 25 \text{ ms}$) at low power and scan the applied rf frequency. Thus, we obtain a precise determination of $\nu_{\text{free-free}}$ as can be seen exemplarily in Figure 5.1 a).

5.3.5. Frequency Resolution

In order to resolve the local response of the system, we have to make sure that the perturbation we introduce by transferring population into an unoccupied state has no time to evolve in the trap. Hence, we want to use rf pulses which are short compared to the trapping period and image the sample directly after applying the pulse. However, short rf pulses lead to a Fourier limited frequency resolution and therefore we have to find a good trade-off.

To investigate this experimentally, we prepare a 12-mixture at $B \approx 854 \text{ G}$ and record the rf spectrum for different pulse durations τ_{rf} as can be seen exemplarily in Figure 5.13 A. For all applied rf pulse durations, the density dependence of the bound-free transition is readily visible and one can observe qualitatively that the observed maximum shift decreases for longer rf pulse durations. For each pulse duration we adjust the rf power such that a similar fraction of atoms is transferred. This leads to Rabi frequencies between 60 Hz for the longest and 240 Hz for the shortest τ_{rf} and hence the effect of power broadening is small compared to the Fourier limit. Binning the spectra over two pixels and taking a cut at a fixed radius, we can then compare the peak positions and widths of the bound-free transition. This is shown in B for the peak FWHM and in C for the peak position. One can see that for short rf pulses on the order of 1 ms, the width increases as the Fourier limit there is on the order of 1 kHz. Although the Fourier limit decreases for longer pulse durations, we see the FWHM increase for longer times which we attribute to diffusion of particles during the application of the rf pulse. We find a minimum at around $\tau_{\text{rf}} \approx 4 \text{ ms}$ which is the value we use throughout this thesis. The peak position, which indicates the interaction induced Hartree shift, seems to be relatively constant for short durations. There are some outliers at around 6 – 8 ms which we neglect. For longer pulse durations the observed peak position decreases. Hence, we argue that for short pulse durations the observed peak is not influenced by diffusion and gives reliable results.

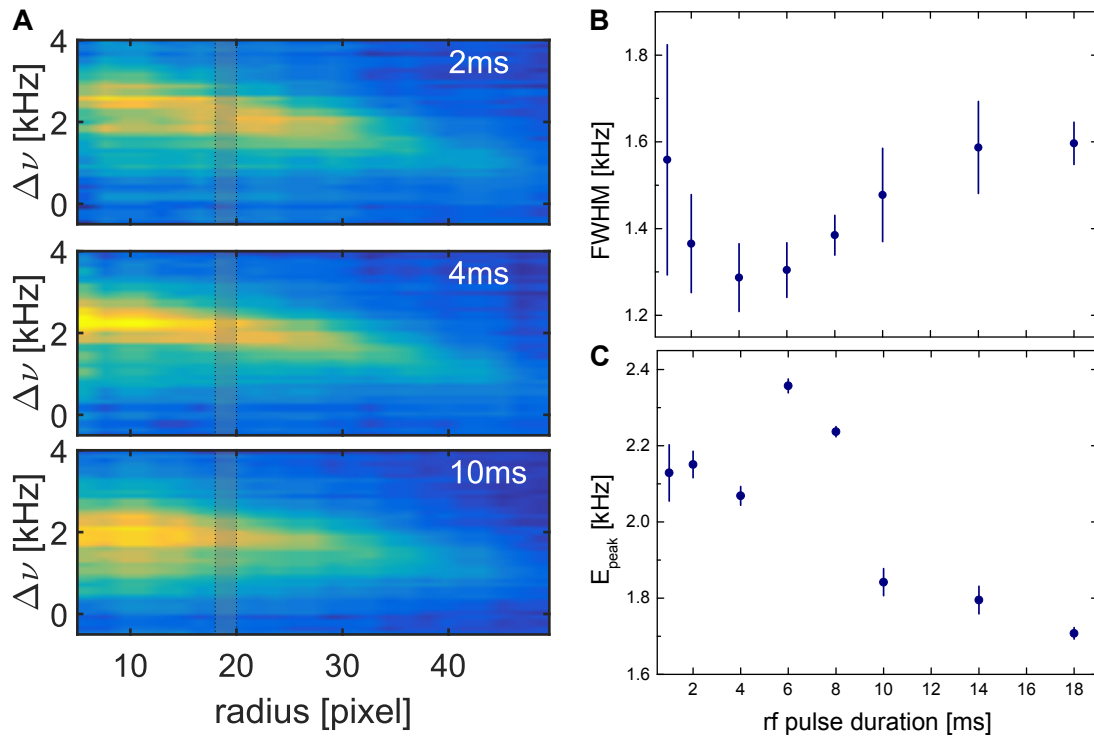


Figure 5.13.: Influence of the rf pulse duration on the measured rf response spectra measured at 854 G. In **A** the spectra are shown for rf pulse durations of 2 ms, 4 ms and 10 ms. Along the cuts marked as the shaded area in the spectra, the lineshape is obtained and in **B** the FWHM and in **C** the peak position are determined from fits. It can be stated that $\tau_{\text{rf}} = 4$ ms gives a good trade-off between frequency resolution and the effect of diffusion on the sample.

5.3.6. Thermometry

The relevant energy scale of the system is given by the Fermi energy E_F and therefore the relevant temperature scale is given by T/T_F . The Fermi temperature T_F can be obtained directly from the density n assuming the local density approximation. To determine the absolute temperature T in the sample, we fit a reference equation of state (EOS) $n(\mu, T)$ to the outer region of the cloud. The EOS of a 2D Fermi gas in the BEC-BCS crossover was determined in [Boe16, Fen16] and we will use the temperature determination as shown in the supplementary material of [Boe16] in this work.

To interpolate between the bosonic and the fermionic limit of the 2D BEC-BCS crossover, a second order virial expansion for a homogeneous system is used. It is defined by

$$n_0^{\text{virial}} = (1/\lambda_T)^2 \{ \ln(1 + e^{\beta\mu}) + 2b_2 e^{2\beta\mu} \} \quad (5.19)$$

where

$$b_2 = e^{\beta\epsilon_B} - \int_{-\infty}^{\infty} ds \frac{\exp(-e^s/(2\pi))}{\pi^2 + (s - \ln(2\pi\beta\epsilon_B))^2} \quad (5.20)$$

is the interaction induced correction to the second virial coefficient [Cha13, Nga13]. This equation becomes exact in the whole 2D BEC-BCS crossover for a small fermion fugacity $z = e^{\beta\mu}$. In the bosonic limit of $\beta\epsilon_B \gg 1$, the fermion fugacity $z \rightarrow 0$ and $b_2 \simeq e^{\beta\epsilon_B}$ and equation 5.19 approaches the Boltzmann formula

$$n_0^{\text{boltzmann}} = (\alpha_{\text{eff}}/\lambda_T^2) e^{\alpha_{\text{eff}}\beta\tilde{\mu}}, \quad (5.21)$$

with the limit $\alpha_{\text{eff}} = 2$ indicating the bosonic case of deeply bound molecules. Here the two-body binding energy ϵ_B is defined as

$$\epsilon_B = \frac{\hbar^2}{ma_{2D,0}^2} e^{\Delta w(\frac{\tilde{\mu}_0}{\hbar\omega_z})}, \quad (5.22)$$

where $\Delta w(x)$ is the filling correction to the scattering introduced in section 2.2.1 and $\tilde{\mu} = \mu + \epsilon_B/2$.

As $\beta\epsilon_B$ becomes smaller, the virial expansion approaches the ideal Fermi gas formula. Comparing this to Luttinger-Ward (LW) and quantum Monte-Carlo (QMC) simulations shows that this leads to an overestimation of the temperature when using the virial expansion. On the other hand we can use the Boltzmann formula with an interaction dependent coefficient α_{eff} as a lower bound for the temperature. The parameter α_{eff} interpolates here between the bosonic limit of molecules with mass $m = 2m_{\text{Li}}$ and the fermionic limit of free atoms with mass $m = m_{\text{Li}}$. Thus, we take the average between these two methods to obtain our temperature

$$T = \frac{T_{\text{virial}} + T_{\text{boltzmann}}}{2}. \quad (5.23)$$

In order to fit our obtained density profiles $n(r)$ with this EOS of a homogeneous system, we apply the local density approximation (LDA). This assigns a local chemical potential $\mu(r) = \mu_0 - V(r)$ to each position in the trapping potential $V(r)$. We can then locally approximate the atom density as

$$n(\mu, T, r) = n_0(\mu_0 - V(r), T). \quad (5.24)$$

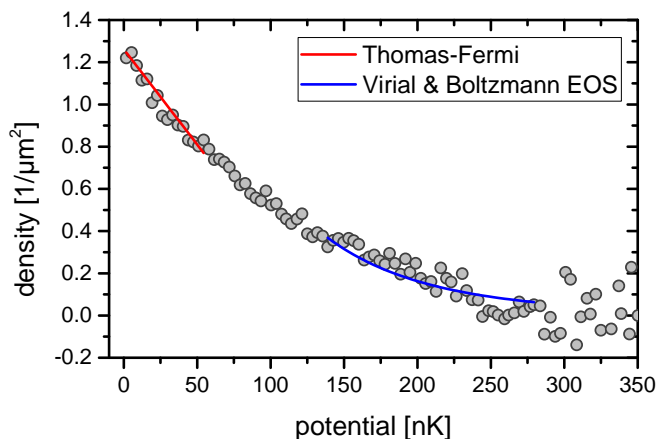


Figure 5.14.: Thermometry of a single shot. First, to obtain the central $\tilde{\mu}_0$ we fit a Thomas-Fermi model to the central part of the cloud (red line). The temperature is then determined by fitting two reference EOS to the wing of the data (grey dots), namely a virial expansion and a Boltzmann function. Both are shown as a single blue line as the obtained density profiles do not differ significantly. From this we can then extract a temperature estimate as the average between the virial expansion and the Boltzmann model.

In order to obtain the most accurate value for $\tilde{\mu}_0$ to determine ϵ_B from equation 5.22, we fit a Thomas-Fermi model of the form

$$n(\mu, T) = c \cdot (\tilde{\mu}_0 - V(r)) \quad (5.25)$$

to the central part of the cloud. This is justified when the parameter c is independent of temperature and fitting range [Boe16]. This improves the signal-to-noise ratio compared to the value $\tilde{\mu}_0$ obtained from the Boltzmann fit in the wing where the signal is smaller. This fitting procedure is depicted exemplary in Figure 5.14. Here, the Thomas Fermi fit and its fit range is shown as the red line and both the Boltzmann fit and the virial expansion fit are shown as the blue line in the wing.

The obtained results for the temperature determination of both the virial expansion and the Boltzmann model are shown in Figure 5.15 a) in the crossover region. Here we show the result of the Boltzmann model both in the bosonic limit where $\alpha_{\text{eff}} = 2$ and in the fermionic limit where $\alpha_{\text{eff}} = 1$. Up to $\ln(k_F a_{2D}) \leq 0.5$, the virial fit as well as the bosonic Boltzmann fit agree very well. As $\ln(k_F a_{2D})$ increases, we then observe that the bosonic Boltzmann fit yields larger temperatures than the virial expansion. This is expected as α_{eff} is reduced in the crossover region. At large $\ln(k_F a_{2D}) \approx 2$, the virial expansion gives an upper limit of the temperature whereas a Boltzmann fit with $\alpha_{\text{eff}} \approx 1$ yields a lower limit for the temperature. To obtain an interaction dependent α_{eff} , we hence interpolate between $1 \leq \alpha_{\text{eff}} \leq 2$ in this region. This is depicted in Figure 5.15 b). This interpolation scheme is similar to the one deployed in [Rie15b].

The results of such fits to individual realizations in a measurement run at different interactions strengths $\ln(k_F a_{2D})$ are shown in Figure 5.16. In the BEC limit, the

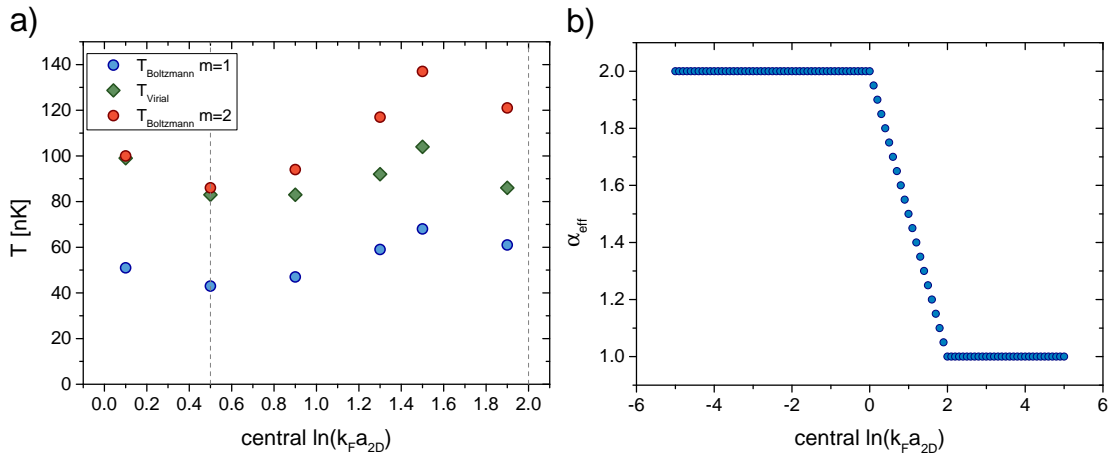


Figure 5.15.: a) Temperature estimation from both the virial expansion as well as the Boltzmann fit at different interaction strengths $\ln(k_F a_{2D})$. Close to the BEC side, both the virial expansion (green diamonds) and the bosonic Boltzmann model (red dots) yield the same result. In the crossover region, the bosonic Boltzmann model overestimates the temperature and the virial expansion can be considered as an upper bound of the temperature. The lower bound is then a Boltzmann model with interaction dependent α_{eff} which converges to the fermionic Boltzmann model (blue dots) at large positive scattering lengths. b) We interpolate $1 \leq \alpha_{\text{eff}} \leq 2$ in the crossover region between $0.5 \leq \ln(k_F a_{2D}) \leq 2$. This interpolated value is then used to obtain the lower bound of the temperature in this regime.

temperatures obtained from both methods are identical and the average is trivial. In the crossover, however, the temperatures obtained from both methods differ and the virial expansion is used as an upper bound whereas the Boltzmann fit is a lower bound. The spread in the measured temperatures is between 15 – 20 %. This uncertainty is mainly due to the fitting and does not depend on the preparation of the sample. We checked this by dividing each image in two parts and taking the radial average over each half. The obtained fitted temperature differences between the two halves then show the same spread. In addition, when comparing the temperature obtained from one half of one image with the temperature obtained from the other half of the next image, we observe the same behavior. Therefore, we take the average temperature of each dataset as the temperature estimate and use the standard error of the mean as the temperature uncertainty.

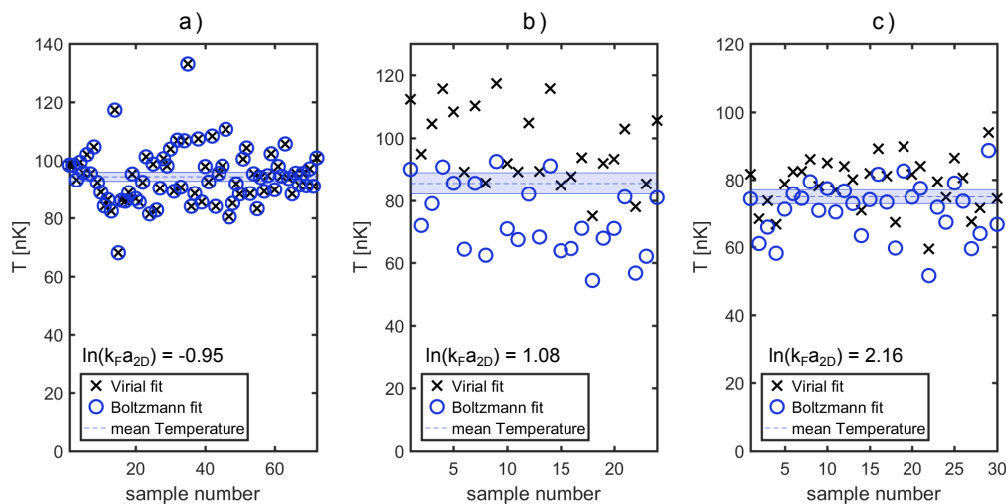


Figure 5.16.: Fitted temperatures with both the virial fit (black crosses) as well as the Boltzmann fit (blue circles) with the effective parameter α_{eff} used from Figure 5.15 b) for three different interaction strengths on the BEC side a), in the crossover b) and on the BCS side c). The mean averaged temperature as well as the standard error of the mean are given as the blue dashed line with the shaded area.

5.3.7. Atoms in Adjacent Layers

From the rf tomography results in section 3.1.1 we know that a fraction of at least 10 % of the atoms is transferred into adjacent layers of the central SWT potential. This results in an overestimation of the local density n and thus it influences our determination of both the Fermi energy E_F as well as the relative temperature T/T_F . We can also detect the population of adjacent layers in our locally resolved rf spectra. This gives us another measurement to estimate this fraction and it provides furthermore insight into the size of the sample in the adjacent layers. Note that the results presented here were obtained for the data taken with the balanced samples.

For the imbalanced samples we reduced the atom number before the transfer into the SWT and thus there the population of atoms in adjacent layers is further reduced.

In Figure 5.17 A the spatially resolved rf spectrum is shown for a sample in the 12-mixture at a magnetic offset field of $B \approx 854$ G. Here we show the total transferred density in order to make the contribution from the adjacent layer better visible. One can distinguish the bound-free branch above the binding energy E_B (red dashed line) with a density dependent transition frequency. Below the white dashed line which serves as a guide to the eye, one observes a second smaller branch which also lies above the binding energy. This branch we identify with atoms in adjacent layers. The arguments for this assumption are the following: The observed energy shift of this additional feature is larger than the calculated confinement induced binding energy E_B for all magnetic fields where we have the necessary rf frequency resolution to separate the bound-free and the free-free branch. This indicates that the atoms in the adjacent layers are paired as well at these fields although their relative temperature is larger due to the smaller density. Furthermore, the radial extent of this second branch is reduced, as one would expect for a distribution of a small atom number in adjacent pancakes. At last, it cannot stem from unpaired atoms in the central layer as then one would have to observe a much stronger contribution in the wings where the relative temperature T/T_F is large.

To estimate the systematics in our determination of the local density, we bin the rf spectra over two pixels along the radius and look at the lineshapes at a fixed radius. Such lineshapes are plotted for the rf spectrum shown in A at three different radii in Figure 5.17 B. We observe a bimodal structure where we attribute the large peak to the bound-free transition in the central layer and the smaller peak to the bound-free transition in the adjacent layers. When approaching the wing of the sample, one observes that both peaks shift to smaller frequencies and the lower peak cannot be identified for larger radii. The density dependence of the frequency shift is due to interaction effects which depend on the density and the interaction strength. Ultimately, we are interested in these density dependent shifts and they will be analyzed later on in section 5.4. From the relative weight of these two peaks we can infer the population ratio between the central layer and the adjacent ones. Therefore, we fit the lineshapes using a sum of two Gumbel distributions (orange line) with identical form as defined later on in section 5.3.8. From the relative weight of the two peaks we can then infer the fraction of density in the central layer, p_{central} , as a function of the radius. This is plotted in C for the data shown here at $B = 854$ G in the 12-mixture (red squares) as well as for data taken at $B = 682$ G in the 13-mixture (blue circles). Furthermore, the average of these two measurements is shown as the green diamonds. In the center, the fraction of atoms in the central layer is on the order of 80% and it smoothly increases as one approaches the wing of the sample. Note that the fitting procedure breaks down at some point in the wing and thus we set the observed fraction there to $p_{\text{central}} = 1$.

The interaction strength at the center of the sample for these fields is $\ln(k_F a_{2D}) \approx 0.54$ for the 13-mixture and $\ln(k_F a_{2D}) \approx 1.5$ for the 12-mixture. Hence, both are on the attractive side where the density profiles only change marginally. On the BEC side the density distribution is more narrow and thus there the size of the adjacent layers is also reduced. For our determination of the interaction induced energy shift

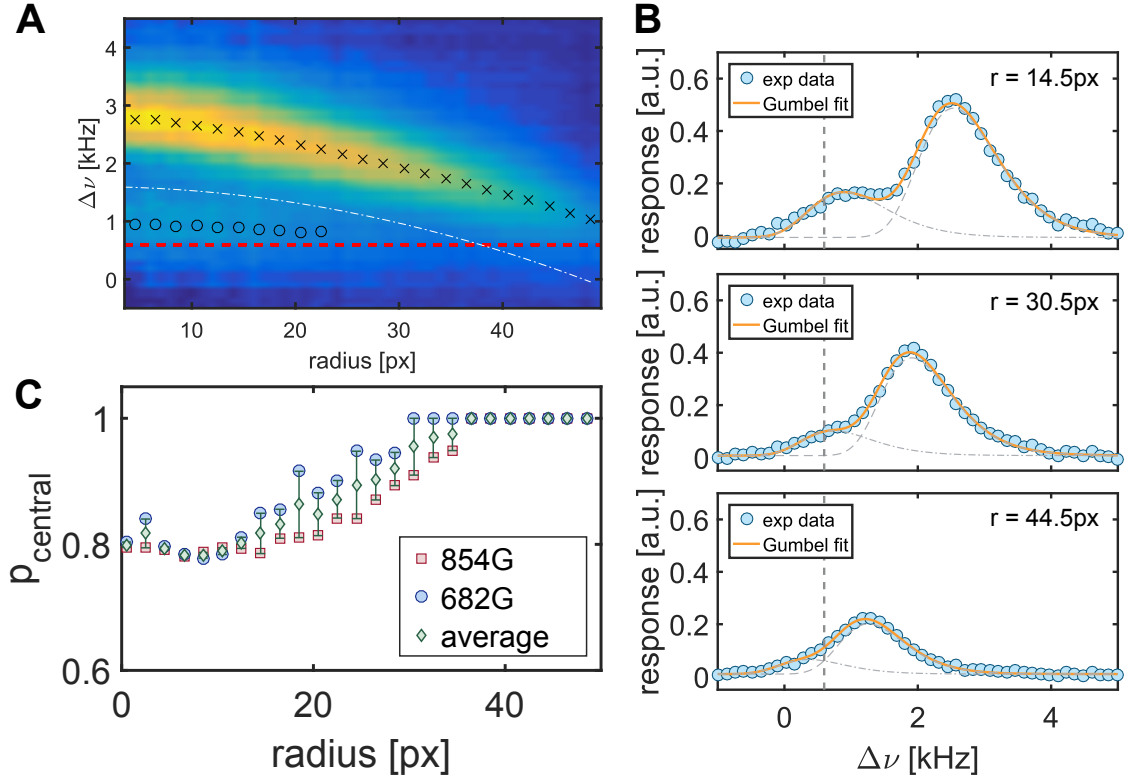


Figure 5.17.: **A** RF spectrum at $B = 854$ G in the 12-mixture. The red dashed line indicates the energy shift due to the confinement induced bound state E_B . The white dash dotted line is a guide to the eye to separate the main contribution in the central layer from the smaller one of the adjacent layers. The black crosses (circles) are the peak positions from fits to the central (adjacent) layer. **B** Vertical cuts along three different radii $r = 14.5$ px, $r = 30.5$ px and $r = 44.5$ px. The fitted line (orange) is the sum of two Gumbel distributions with identical form but independent peak position and amplitude. **C** Fraction of density in the central layer p_{central} as a function of the radius for data obtained at $B = 854$ G in the 12-mixture (red squares) and at $B = 680$ G in the 13-mixture (blue circles). In addition the average of these two is plotted as the green diamonds. The central layer fraction is smallest in the trap center where $p_{\text{central}} \approx 0.8$.

in section 5.4, we will thus use this estimated fraction of atoms in the central layer as a systematic error on the density determination.

5.3.8. Modeling the Spectra

Here the modeling of our lineshapes as it was done for the balanced dataset in section 5.4 is described. For the imbalanced datasets where we observe both the bound-free as well as the free-free peak the modeling is described directly in section 5.6.

To obtain the threshold energy at each radial position in the cloud, we first bin the spectra over two pixels along the radius to improve the signal-to-noise ratio. We then model the spectra according to the following procedure: For interaction strengths $\ln(k_F a_{2D}) \leq 0.8$ we use the 13-mixture, where the initial dimer energy is large compared to the thermal energy in the system, $E_B \geq k_B T$. Therefore, we assume the system to be describable in terms of two-body dimers and use equation 5.14 to model our spectra. This assumption might break down in the strongly interacting region around $\ln(k_F a_{2D}) \sim 0.5$, however as we do not have a prediction for the lineshape based on a many-body model this is the most reasonable approach. Due to the small repulsive scattering length a_{12}^{3D} for the final state, it supports deeply bound final state dimers $E'_B > 100$ kHz. Thus, we end up with ratios $0.03 < E_B/E'_B < 0.07$ and observe strongly asymmetric rf lineshapes with a long rf-tail. From the considerations in section 5.1.4 we know that the observed peak position can deviate by up to 20% from the threshold position, which can be even increased due to the finite frequency resolution as well as other final state effects. We therefore model our observed lineshapes using an adapted version of equation 5.14,

$$\Gamma_{\text{model}}(\omega) = \frac{A}{(\omega - \omega_0)^2 \left(\ln^2 \left[(\omega - E_{\text{th}}) / E'_B \right] + \pi^2 \right)} \Theta(\omega - E_{\text{th}}), \quad (5.26)$$

where we convolve the lineshape with a Gaussian profile of width σ , which is a free fitting parameter as the width is also affected by interaction effects. Here we treat ω as an energy via $E = \hbar\omega = hf$ and we fix the final dimer energy E'_B to the theory calculation. Since we measure the energy ω relative to the previously determined free-free energy, we introduce the free parameter ω_0 since the energy threshold is now relative to the interaction shifted free-free energy $\hbar \cdot \omega_0$ and leave the threshold energy E_{th} as a free fitting parameter as well. As a comparison to extract the peak position, we also fit a Gumbel distribution of the form

$$\Gamma_{\text{Gumbel}}(\omega) = A e^{-\frac{\omega - \omega_{\text{peak}}}{\alpha}} - \beta e^{-\frac{\omega - \omega_{\text{peak}}}{\alpha\beta}}, \quad (5.27)$$

which can describe the asymmetric data quite well.

In Figure 5.18 A and B we show the experimentally measured lineshape and the corresponding fits at a fixed radius both for the magnetic fields $B \approx 672$ G and $B \approx 682$ G, corresponding to a central interaction strength of $\ln(k_F a_{2D}) \approx -0.24$ and $\ln(k_F a_{2D}) \approx 0.54$ respectively. For the data in A, we do not resolve the atoms in the adjacent pancake and hence we fit a single peak to it⁵. This is likely due to the

⁵This was only the case for the data at two magnetic fields, namely $B \approx 662$ G and $B \approx 672$ G.

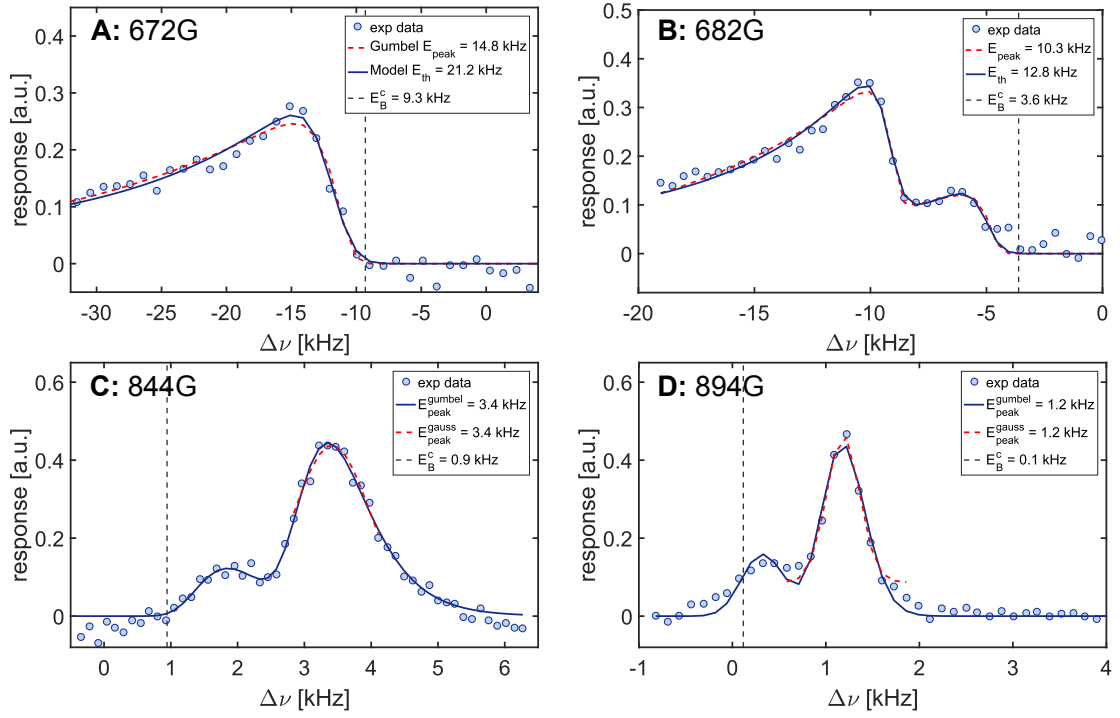


Figure 5.18.: Spectral lineshapes for the 13-mixture at **A**: $\ln(k_F a_{2D}) \approx -0.24$ and at **B**: $\ln(k_F a_{2D}) \approx 0.54$ as well as for the 12-mixture at **C**: $\ln(k_F a_{2D}) \approx 1.26$ and **D**: $\ln(k_F a_{2D}) \approx 2.16$. The black dashed vertical line indicates the position of the confinement induced binding energy E_B without considering Hartree shifts. In the case of the 13-mixture, the blue line is a fit using the model function from equation 5.26 and the red dashed line is a fit using a Gumbel function (equation 5.27). In the case of the 12-mixture, the blue line is a fit using the Gumbel distribution from equation 5.27 and the red dashed line is a Gaussian fit around the peak position. For all the lineshapes except in A where it is not resolvable, the sum of two contributions was fitted to account for atoms in adjacent layers.

fact that the interaction shift is small compared to the binding energy which makes a separation of the peaks hard to observe. Since our preparation scheme is the same for all fields, we still assume the systematic error in the density determination as before. For the data in B, both peaks can be identified and thus we adapt our fit to consist of a sum of the model function with independent interaction shifts ω_0 but the same convolution width σ . We observe that our model describe the data quite well and gives us a reliable method to extract the threshold energy in this regime. The fitted convolution width σ is on the order of 700 Hz and thus higher than the Fourier limited resolution of ≈ 220 Hz. This is most likely due to the final state being a repulsive polaron which broadens the transition. From the fits we obtain an uncertainty of $E_{\text{th}} \approx 5\%$.

For the data taken in the 12-mixture we take a slightly different approach. There, the dimer energy in the final state is minuscule ($E_B' < 1$ Hz) and thus the ratio E_B/E_d'

ranges from $E_B/E'_B \approx 800$ in the crossover regime at $B \approx 844$ G to $E_B/E'_B \approx 30$ in the BCS limit at 1000 G. Thus, assuming again an initial dimer state and using equation 5.14, we can expect the lineshapes to be much narrower and less asymmetric as discussed in section 5.1.4. The validity of this assumption is not clear in the crossover regime and it breaks down far on the BCS side where one expects a free-free transition which we experimentally cannot differentiate from a bound-free transition due to our limited frequency resolution and the small binding energies. There we measure very symmetric lineshapes which can be fitted by a Gaussian profile with width $\sigma = 220$ Hz which fits very well with our experimentally limited frequency resolution. Since in this regime the thermal energy is much larger than the binding energy $k_B T/E_B \gg 1$, we expect the initial state to be a Fermi liquid with free atoms [Frö12] which is consistent with our interpretation of an interaction shifted free-free transition.

As the model function used on the 13-mixture did not provide robust fit results in the crossover region for the 12-mixture and it is not expected to be applicable far on the BCS side, we use a heuristic approach by fitting a Gumbel distribution (equation 5.27) as well as a Gaussian profile around the peak to the data. We then estimate the shift of the peak from the threshold from simulations of equation 5.14 convoluted with the experimental frequency resolution. This assumption is reasonable in this regime as the final state attractive polaron has a narrow lineshape and we measure experimentally the widths of the peaks to agree very well with our experimental frequency resolution for magnetic fields $B \geq 872$ G. This estimation yields a shift of the peak energy compared to the threshold energy of about 200 Hz at $B \approx 844$ G and 90 Hz at $B \approx 894$ G.

In Figure 5.18 C and D we show the experimentally observed lineshapes and the corresponding fits for the magnetic fields $B \approx 844$ G and $B \approx 892$ G, corresponding to a central interaction strength of $\ln(k_F a_{2D}) \approx 1.26$ and $\ln(k_F a_{2D}) \approx 2.16$ respectively. In both cases, a double peak structure due to atoms in adjacent trap layers is visible. The lineshapes in C show an asymmetry, indicating that here the initial state still consists of paired atoms. In D the lineshape is very symmetric, suggesting that here the signal is due to a free-free transition. The uncertainty on the determination of the peak is on the order of 20 Hz and thus the main source of error is the systematic overestimation of the threshold energy when equating it to the peak position.

5.4. Determination of Initial State Interaction Shifts

Initially, we started investigating rf spectra in the crossover regime for balanced samples close to the critical temperature T_c . There we mostly observe only one branch in the rf spectra. Far on the BEC side the binding energy E_B is much larger than the thermal energy $k_B T$ and thus only the bound-free branch is occupied. Far on the BCS side, the binding energy is negligible and cannot be resolved. There the observed branch is identified as the free-free branch. In the crossover region, for most of our data we observe only one peak, indicating that pairs are already formed at considerably high temperatures as discussed in section 5.5. As we thus

do not have a reference to compare to we could not use this data to extract a pairing gap. However, comparing the measured density dependent energy shift of the visible branch relative to the free-free transition energy of a polarized sample, we can estimate the density dependent interaction induced shifts. Such shifts have been measured previously [Frö11], however there the signal was averaged over the inhomogeneous trapping potential as well as over multiple traps and thus different densities contributed. In our case we have the advantage of (almost) all atoms being in a single trap in combination with the locally resolved spectra. Thus, we can use a local density approximation (LDA) to obtain the rf response of homogeneous subsamples and can directly look at the evolution of the Hartree shifts as a function of density and interaction strength in the trap. This is especially important in quasi-2D systems where one can drive the crossover physics by changing the density of the sample. However, as we use ${}^6\text{Li}$ we do not have access to non-interacting final states and thus our calculation of the initial interaction shift relies on theoretical models for the final state interactions. This is especially a problem on the repulsive side of the Feshbach resonance as there the binding energy E_B for true 2D and quasi-2D systems differ and thus theoretical models for the final state which are done for a 2D system might deviate from the experimental situation.

As was shown in section 5.1.6, we can decrease final state effects by choosing an appropriate initial state mixture of ${}^6\text{Li}$. Thus, we took rf spectra both for the 13-mixture extending from the BEC side at a central $\ln(k_F a_{2D}) \approx -1$ up to the far BCS side with $\ln(k_F a_{2D}) \approx 3.6$ (see Figure 5.19) as well as for the 12-mixture starting in the crossover region for $\ln(k_F a_{2D}) \approx 1.26$ up to the BCS side with $\ln(k_F a_{2D}) \approx 3.6$ (see Figure 5.20). These measurements were performed with roughly 30.000 – 40.000 atoms per spin state, corresponding to a central Fermi energy of $E_F \approx h \cdot 10$ kHz. As our axial trapping frequency is $\omega_z = 2\pi \times 6.9$ kHz, the experiments are in the quasi-2D regime with $E_F / (\hbar\omega_z) \simeq 1$.

From these rf spectra one can get a qualitative understanding of the BEC-BCS crossover. For a non-negligible two-body binding energy E_B , the rf transition energy in the low-density wing approaches E_B which is plotted as the red dashed line in the rf spectra thus showing that at large temperatures the physics can be explained by two-body physics. In the high-density center we observe strong density dependent shifts which are due to interaction effects both in the initial and final state. The contribution of these final state effects becomes evident when comparing the rf spectra on the BCS side $\ln(k_F a_{2D})_{\text{initial}} > 2$ between the data taken in the 13-mixture and in the 12-mixture. There the initial state interaction is comparable but the final state interaction changes drastically.

This can be seen e.g. when comparing the data taken at $B = 782$ G in the 13-mixture with the data taken at $B = 1002$ G in the 12-mixture. There the final state interaction strength is $\ln(k_F a_{2D})_{\text{final}} \approx -0.7$ and $\ln(k_F a_{2D})_{\text{final}} \approx 5.7$ respectively. Whereas the final state for the 13-mixture is strongly interacting, the final state for the 12-mixture is still in the weak coupling regime. This results in different interaction shifts at the same density and initial interaction strength. This is shown exemplary in Figure 5.21 A where a cut for both mixtures at a radius corresponding to $\ln(k_F a_{2D})_{\text{initial}} = 3.36$ and $E_F = 6.5$ kHz is shown. As the system is far on the BCS side one expects it to be a Fermi-liquid resulting in symmetric lineshapes and thus

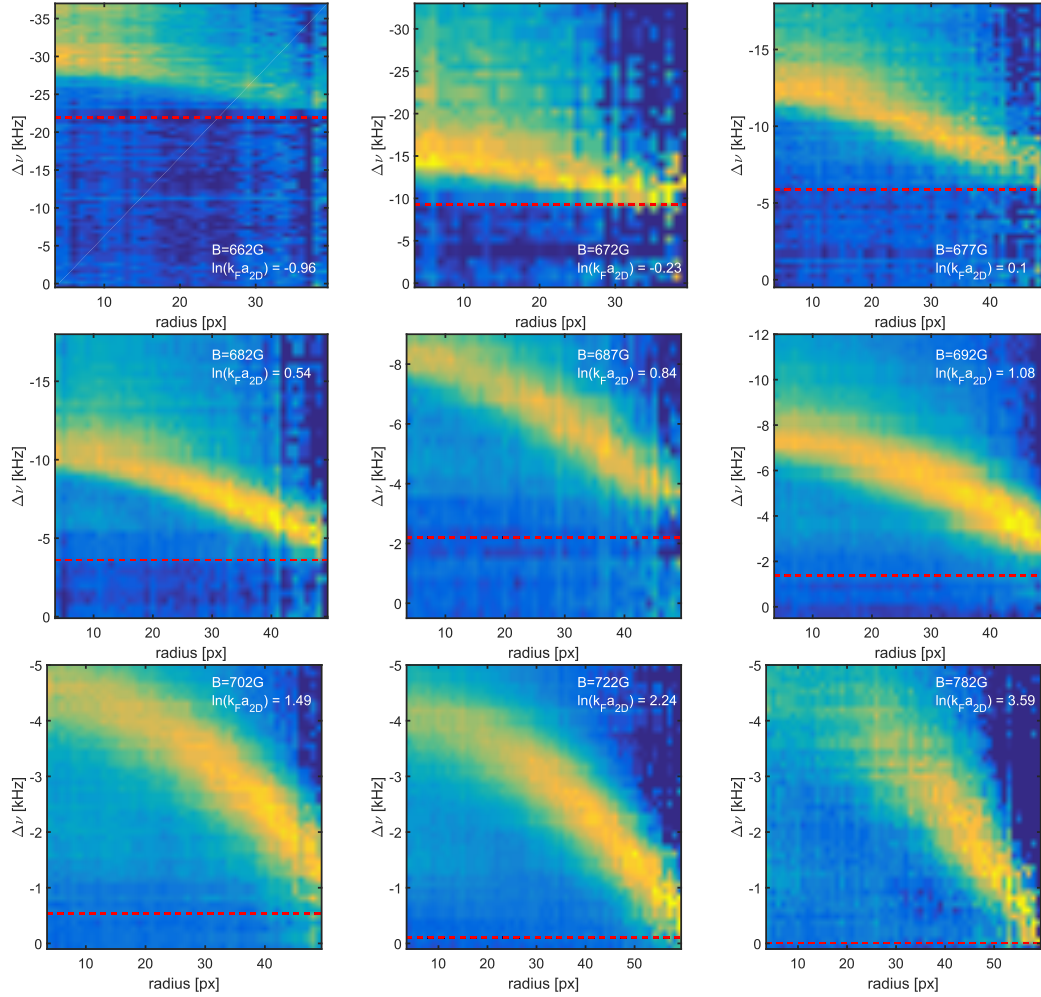


Figure 5.19.: Spatially resolved RF spectra for a balanced 13-mixture in the crossover region. The red dashed lines indicate the confinement induced binding energy E_B . In the low density limit at large radius where the expected interaction shift is small and the temperature $T/T_F > 1$, the observed rf transition energy approaches the two-body binding energy. In the high-density limit, interaction shifts both in the initial and final state lead to a density dependent shift in the observed rf transition energy.

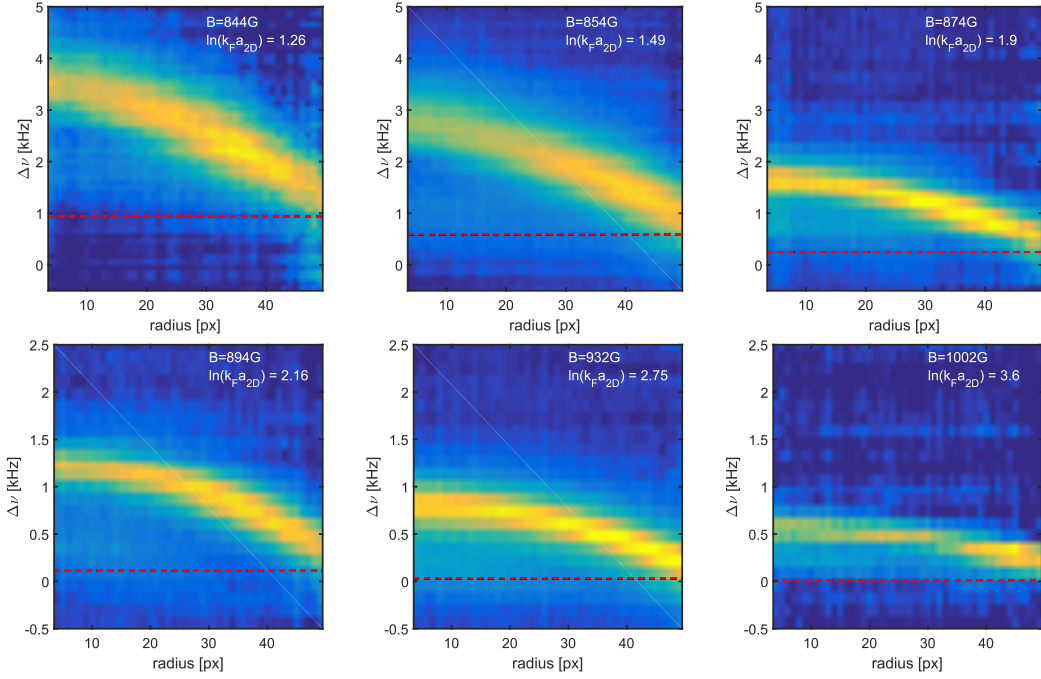


Figure 5.20.: Spatially resolved RF spectra for a balanced 12-mixture in the crossover region. The red dashed lines indicate the confinement induced binding energy E_B . In the low density limit at large radius where the expected interaction shift is small and the temperature $T/T_F > 1$, the observed rf transition energy approaches the two-body binding energy. In the low density limit at large radius where the expected interaction shift is small and the temperature $T/T_F > 1$, the observed rf transition energy approaches the two-body binding energy. In the high-density limit, interaction shifts both in the initial and final state lead to a density dependent shift in the observed rf transition energy. Far on the BCS side ($\ln(k_F a_{2D}) \geq 2$) the two-body binding energy E_B is negligible and cannot be resolved.

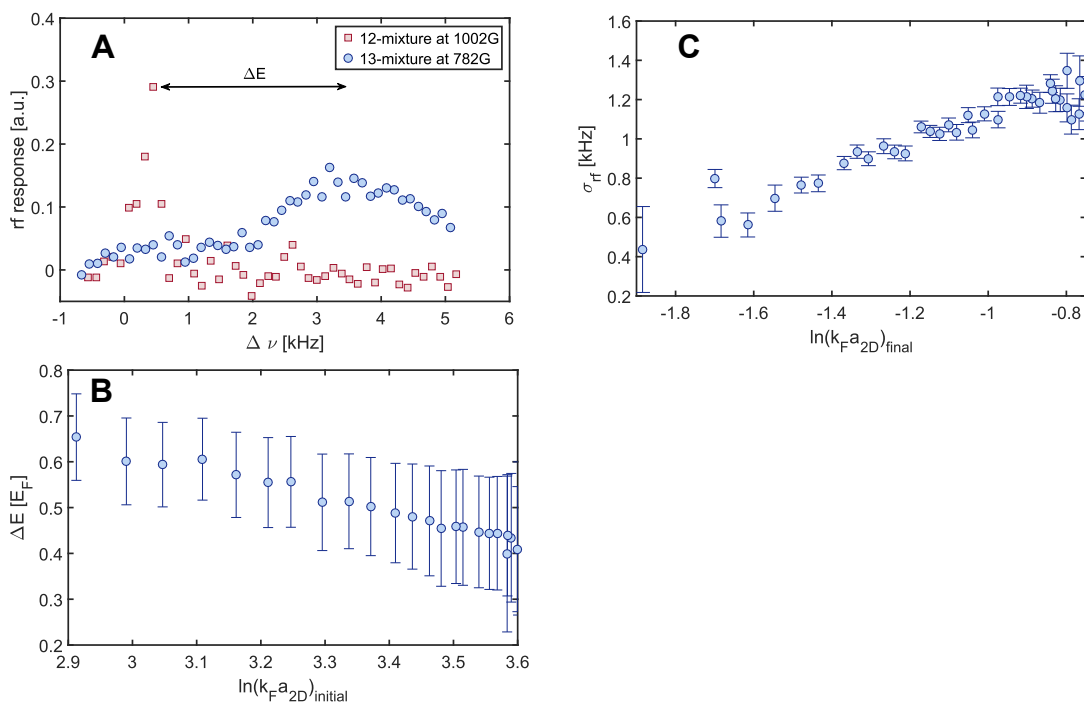


Figure 5.21.: **A** Radial cut through the rf spectrum at $\ln(k_F a_{2D})_{\text{initial}} = 3.36$ with $E_F = 6.5$ kHz. Due to the different final state interactions the observed interaction shift differs. **B** Difference in the final state interaction shift in units of the Fermi energy between the 12- and 13-mixture for identical initial state interaction strength. **C** Gaussian width of the free-free peak in the 13-mixture as a function of the final state interaction strength. The increase in the observed width corresponds to a decrease in the lifetime of the final state polaron [Nga12].

the peak positions can be directly compared. The difference ΔE between the peaks which corresponds to the difference in the final state interaction shift is plotted in B as a function of the initial state interaction strength and one observes a deviation $\Delta E \sim 0.5 E_F$ and thus a substantial difference in the final state interaction shifts in this regime. This behavior can be explained by the existence of a final state repulsive polaron when starting in the 13-mixture. This increases the final state interaction energy shift substantially as was shown in Figure 5.3 a). The presence of the polaron can also be seen by the increasing width of the peak for the 13-mixture which is shown in Figure 5.21 C as a function of the interaction strength in the final state. As the repulsive polaron is not the ground state of the system it has a short lifetime and can decay further for example into a molecular state or into the attractive polaron branch depending on the system [Nga12]. This results in a broadening of the transition which we can directly observe as our experimental rf resolution is smaller. From the measured widths on the order of 1 kHz we can estimate a lifetime $\tau \sim 1$ ms which is in agreement with measurements performed for the repulsive polaron in a quasi-2D system [Kos12]. Furthermore, we observe that the lifetime decreases as $\ln(k_F a_{2D}) \rightarrow 0_-$ as is expected [Nga12]. For the 12-mixture

the final state is most likely a stable attractive polaron state. There we measure a constant width of the peak which is in very good agreement with our experimental rf frequency resolution of 220 Hz.

It is interesting to note that we observe a positive energy shift $\Delta E_{\text{Hartree}} > 0$ as defined in equation 5.6 at all interaction strengths and for both mixtures we investigated. This fact already gives us some insights into the interaction induced energy shifts in the different regimes. In the 13-mixture the final state is most probably a repulsive polaron as discussed above and thus in this regime $E_{\text{H,final}} > 0$ holds. For the initial state however we pass the zero-crossing in the interaction strength $\ln(k_{\text{F}}a_{2\text{D}})$ and thus we expect to see a change in the sign of the initial state interaction energy $E_{\text{H,initial}}$. Thus, we can deduce $E_{\text{H,initial}} < E_{\text{H,final}}$ in this regime. In the 12-mixture, the interaction strength both for the initial and the final state is $\ln(k_{\text{F}}a_{2\text{D}}) < 0$ throughout our data. Hence, to observe a positive $\Delta E_{\text{Hartree}}$, the attractive initial state interaction energy has to be stronger than the attractive final state interaction, $|E_{\text{H,initial}}| > |E_{\text{H,final}}|$.

To get a more quantitative insight about the interaction shifts we do the following: to limit the final state interactions to the weak coupling regime we use the data taken in the 13-mixture for magnetic fields $B \leq 692$ G corresponding to $\ln(k_{\text{F}}a_{2\text{D}}) < 0.8$ and the data taken in the 12-mixture for magnetic fields $B \geq 844$ G corresponding to $\ln(k_{\text{F}}a_{2\text{D}}) > 0.8$. There the final state interaction strength is limited to $\ln(k_{\text{F}}a_{2\text{D}}) < -6$ and $\ln(k_{\text{F}}a_{2\text{D}}) > 4$ respectively and hence one can use the weak coupling approximations as an estimate for the final state interaction shifts. With this estimate we then calculate the initial state interaction shift from our experimentally determined threshold energy E_{th} as

$$E_{\text{H,initial}} = -\frac{E_{\text{th}} - E_{\text{B}} - E_{\text{H,final}}}{E_{\text{F}}} \quad (5.28)$$

where we used the the theoretically calculated dimer energy E_{B} . By interpolating our data to a fixed temperature T/T_{F} , we obtain the initial state interaction shift as a function of interaction strength as shown in Figure 5.22. Here we use red (blue) data points to differentiate between data taken in the 13-mixture (12-mixture). The dominant error in equation 5.28 stems from the determination of the Fermi energy and thus the density. For the error bars we thus consider the uncertainty on the order of 7% in the imaging calibration as described in chapter 3 as well as the systematic overestimation of the atom number of up to 20% due to a small number of atoms in adjacent layers as described in section 5.3.7. The error in the estimation of $\ln(k_{\text{F}}a_{2\text{D}})$ is small and can be neglected in the plots.

For both temperatures $T/T_{\text{F}} = 0.25$ a) and $T/T_{\text{F}} = 0.5$ b) one observes that the initial state interaction shift E_{initial} crosses over from a positive to a negative shift in energy as one proceeds from the BEC side to the BCS side. When approaching the weak coupling regimes $\ln(k_{\text{F}}a_{2\text{D}}) \gg 1$, the data seems to converge towards the perturbative (blue dashed line) and interpolated (black dashed line) Hartree shift at least on the BCS side. In the strong coupling regime a matching with the interpolated Hartree shift from equation 5.9 is not observed although it is also not expected as this interpolation does not take into account the strong interactions. Here further theoretical input is required. Another question is how the finite lifetime

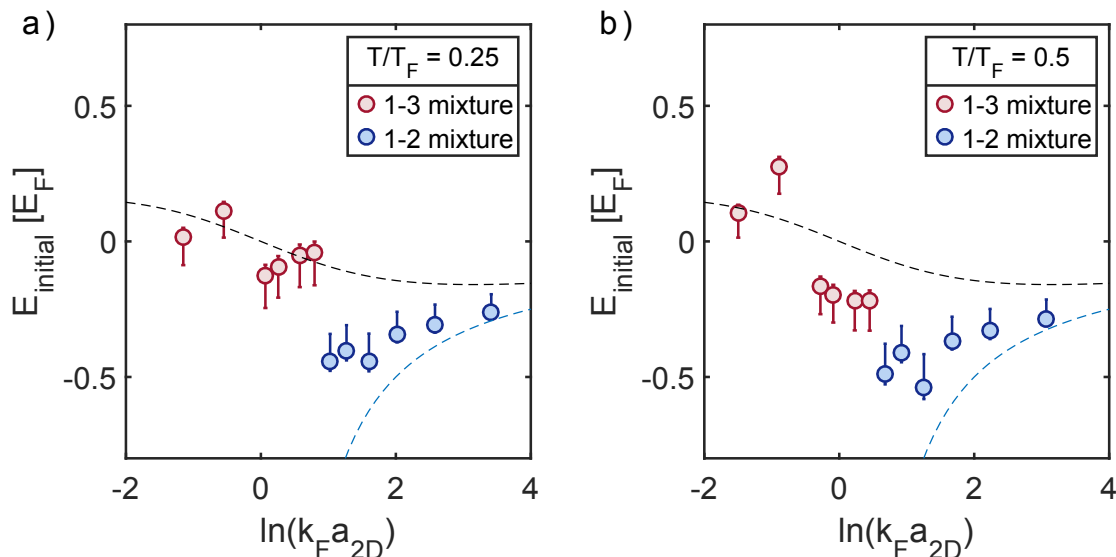


Figure 5.22.: The initial state interaction shift E_{initial} in units of the Fermi energy E_F is plotted as a function of the interaction strengths for two temperatures a) $T/T_F = 0.25$ and b) $T/T_F = 0.5$. It was calculated by subtracting both the dimer binding energy E_B as well as the final state interaction energy E_{final} obtained from a theoretical model from the measured threshold energy E_{th} . The data at each magnetic field was interpolated to match the temperature. The data points in red were obtained from the 13-mixture whereas the data points in blue are extracted from the 12-mixture. The black dashed line indicates the Hartree energy obtained from the interpolation in equation 5.9 whereas the blue dashed line is the perturbative approach in equation 5.8.

of the final state in the 13-mixture influences the transition as our rf pulse duration $\tau = 4$ ms is on a similar order as the estimated lifetime.

In conclusion we find that interaction effects can lead to considerable shifts of the transition energy on the order of up to half the Fermi energy E_F . As these shifts are highly density dependent it is crucial to separate the rf response from different parts of an inhomogeneous trap. Furthermore, these shifts also depend on the interaction strength. As the interaction strength in a quasi-2D system depends on the density itself, this separation is even more important in 2D systems. Experimentally we observe that with our combination of a single layer quasi-2D system and the spatially resolved rf spectroscopy using short pulse durations, we are able to study the density dependent evolution of the interaction shifts. This is an improvement compared to previous experiments [Frö11] where the signal was averaged over the inhomogeneous trap and several layers. When employing a theoretical model for the final state interaction shifts we can deduce the initial state interaction shift and find a smooth behavior when crossing over from the BEC to the BCS side. For a more quantitative analysis further theoretical input is required. Future experiments can improve on this technique by employing a uniform trap. This would improve the signal-to-

noise ratio and one could potentially use longer rf pulses improving the frequency resolution. Furthermore, by using ${}^6\text{Li}$ we were limited by final state interactions being present at all initial interaction strengths in the crossover. This complicates the study of the interaction shifts and could be avoided by using atomic species like e.g. ${}^{40}\text{K}$ where the final state interaction is negligible.

5.5. Onset of Pairing at High Temperatures in the Crossover Region

In this section we investigate how pairing sets in at large temperatures in the crossover region. Far on the BEC side where we have $E_B \gg k_B T$, we observe that the system is fully paired also when heating it up considerably. In the crossover region where $E_B \simeq k_B T$, however, we observe a co-existence of the bound-free and free-free branch when heating the system and we can investigate this onset experimentally.

For this purpose we performed a local rf spectroscopy with a balanced sample in the 12-mixture at $B \approx 844\text{ G}$ with a central interaction strength $\ln(k_F a_{2D}) \approx 0.8$ and Fermi energy $E_F = h \cdot 4.8\text{ kHz}$ which was heated up such that the relative temperature in the center was on the order of $T/T_F \approx 1.2$ with a Boltzmann factor $k_B T/E_B \approx 6.49$. Note that the interaction strength in the sample varies and reaches $\ln(k_F a_{2D}) \approx -0.6$ in the low-density wing. Thus, although the sample is in the strongly interacting regime throughout, the sign of the interaction strength changes.

The experimentally obtained rf spectrum $I(\nu, r)$ is shown in Figure 5.23 A. One can clearly distinguish two branches in the rf signal: the branch close to $\Delta\nu = 0$ is the free-free transition of unpaired atoms. The branch above the two-body binding energy E_B/h (red dashed line) is the bound-free transition of paired atoms. In the center of the cloud where the density is large and thus the relative temperature scale T/T_F is smallest we see a co-existence of these branches with an increased weight in the bound-free transition. The relative weight of these two branches then shifts towards the free-free transition until at around a radius of roughly $r \approx 53\text{ px} = 160\text{ }\mu\text{m}$, corresponding to a temperature $T/T_F \approx 7$, only the free-free transition has considerable weight.

In thermal equilibrium, the density ratio between free fermions n_F and fermions bound in dimers n_B can be calculated for a non-interacting system to be [Bar14, Nga13]

$$\frac{n_F^2}{n_B} = \frac{mk_B T}{4\pi\hbar^2} e^{-\frac{E_B}{k_B T}}, \quad (5.29)$$

which is known as the Saha formula. As the dimers are only weakly bound with a binding energy E_B much smaller than the linewidth Γ of the optical transition, $E_B \ll \Gamma$, we cannot differentiate between dimers and free atoms in the absorption imaging and our measured density is thus $n_{2D} = n_F + n_B$. Combining this with the definition of the Fermi energy in equation 2.24, we can derive for the relative weight $p = \frac{n_F}{n_F + n_B}$ of free atoms

$$\frac{p}{\frac{1}{p} - 1} = \frac{T}{T_F} e^{-\frac{E_B}{k_B T}}, \quad (5.30)$$

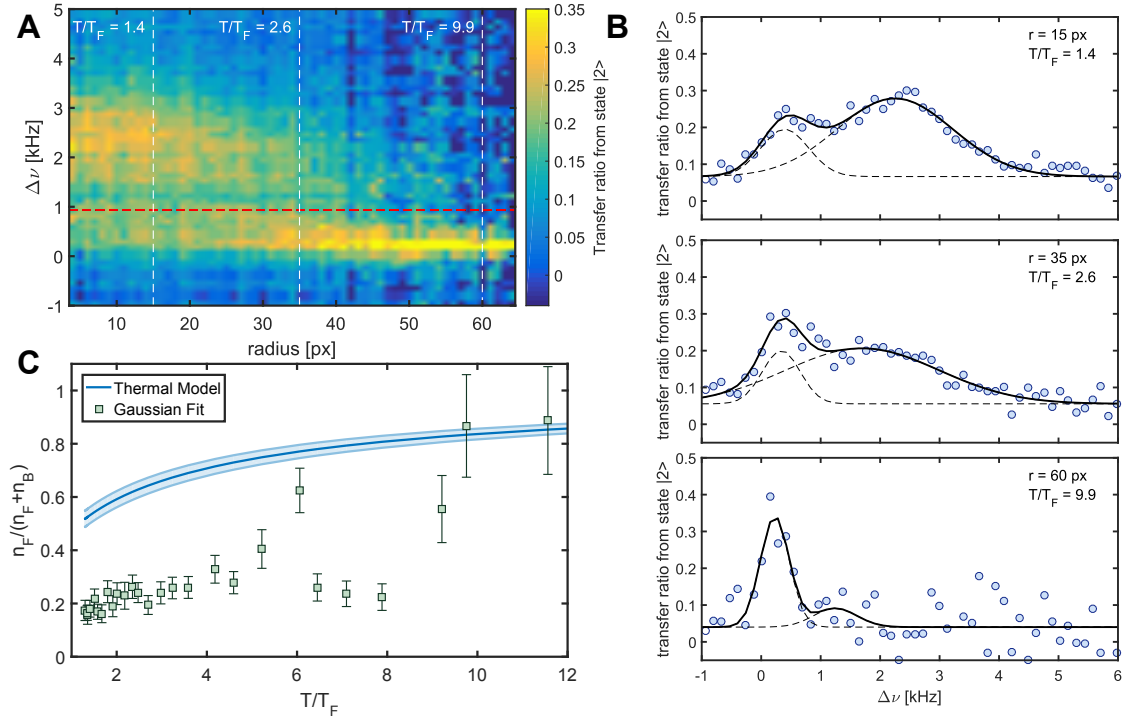


Figure 5.23.: **A** Spatially resolved rf spectrum for the 12-mixture at a central $\ln(k_F a_{2D}) \approx 0.8$ at temperatures $T/T_F > 1$. The horizontal red dashed line indicates the energy of the confinement induced two-body state, whereas the vertical white dashed lines indicate the local temperature T/T_F which is non-linear in the radius. In the low density limit in the wings of the cloud one observes a single peak at $\Delta\nu \approx 0$ indicating free thermal atoms. Already at temperatures $T/T_F \sim 3$ a second peak starts to occur whose relative distance is at least the two-body binding energy $E_B \approx 1$ kHz. We identify this with the bound-free transition of dimer pairs. For both branches one observes a density dependence related to interaction shifts. **B** Radial cuts along the vertical dashed white lines in A. The black dashed line is a double Gaussian fit from which we obtain the relative weights. In the high-density region in the center (upper panel) one observes a two peak structure and thus co-existence between free atoms and dimer pairs with similar weight. Towards the low-density wings the weight of the dimer branch diminishes until only free thermal atoms exist (lower panel). **C** Relative population of the free-free branch expected from a thermal model (blue line) [Bar14] and obtained from the data using the fit (green squares). The blue shaded region indicates the uncertainty due to our temperature and density calibration.

which we can solve numerically for our local T/T_F . In Figure 5.23 B this solution is shown as a function of T/T_F as the blue line. In the center of the cloud the expected relative free spectral weight is $p \approx 50\%$ and it increases consistently towards the wing until only free atoms are present. To compare this to our data we take cuts along fixed radii. In Figure 5.23 C three cuts along the white vertical dashed lines in A are shown as an example. In the central region (upper panel), both peaks are clearly visible and thus there is considerable weight in both of them. Further out towards the wing (middle panel) the free atom fraction increases and the relative spectral weight changes towards the free atom peak. In the wing at a radius of $r \approx 60$ px where the density is only 10% of its central value we cannot discriminate the molecular peak from the noise (lower panel) and thus the free atom fraction approaches one. Due to our finite frequency resolution and the small binding energy we cannot fully separate the two peaks and thus fitting a model as described in section 5.3.8 has not been robust. To extract some quantitative insight about the change of the free spectral weight we employ a double Gaussian fit as shown as the black lines. The relative weight of each peak is additionally plotted as the black dashed lines. As the symmetric Gaussian profile cannot describe the asymmetry of the bound-free lineshape, this will overestimate the contribution of the bound-free branch and hence underestimate the free spectral weight p . The result of this estimation of the relative free spectral weight is shown in Figure 5.23 B as the green squares including the 1σ -confidence interval. We can observe that in the wings at large temperatures T/T_F the results are in agreement. In the region $6 < T/T_F < 8$, the fitting procedure overestimates the small bound-free contribution and thus severely underestimates the free-free fraction. Towards the center the relative free spectral weight p decreases and lies consistently below the thermal model. Some of this systematic deviation can be attributed to our determination of the weights using a double Gaussian profile and the model which assumes non-interacting particles although we are in the strongly interacting regime. Nevertheless the observed decline of the free spectral weight is steeper than predicted by the thermal model. Thus, interactions and quantum effects play a considerable role in the onset of pairing which are not captured by the model.

In conclusion we observed the onset of pairing in the crossover regime for a strongly interacting Fermi gas as a function of the temperature T/T_F . We found that the measured relative free spectral weight is not in agreement with a thermal model and hence interactions and quantum effects play a role in the pairing. A better quantitative comparison, however, is challenging as the free-free and the bound-free branch have considerable overlap due to the small dimer binding energy $E_B = 1$ kHz, making the extraction of the relative weights model dependent. Increasing the axial confinement ω_z to enlarge the dimer energy E_B , however, would also lead to a reduction in the Boltzmann factor and thus reduce the relative free spectral weight further, making a comparison in the central region difficult.

5.6. Many-Body Pairing above the Critical Temperature

In this section we investigate the gap between the free atom branch and the paired branch in the rf spectrum. As the thermal occupation of the free atom branch is small in the interesting temperature region close to the superfluid phase transition, we imbalance the system with a local polarization of $p_{\text{loc}} \approx 15\%$ in order to increase the population of the free atom branch by the excess atoms of the majority [Sch08a, Che09a]. This enables us to detect both branches in our locally resolved rf spectra and measure the relative distance between them.

In the experiment we use the 13-mixture and prepare the imbalance as described in section 5.3.3. Here the majority is the state $|3\rangle$ and the minority is the state $|1\rangle$. By using the 13-mixture we can drive both the transition $|1\rangle \rightarrow |2\rangle$ to obtain the minority spectrum as well as the transition $|3\rangle \rightarrow |2\rangle$ to obtain the majority spectrum. This allows us to compare the spectra in the crossover region where the pairing is most interesting.

To obtain a reference we start by investigating a system on the BEC side at $B \approx 672$ G where $E_B/k_B T \gg 1$ and the system is fully paired into dimers. Here $E_B = 9.3$ kHz and we can separate the two branches well. The Fermi energy in the center is $E_F = 8$ kHz and thus the system is in the quasi-2D regime. The measured rf spectrum is shown in Figure 5.24 A. Here we observe only a small density dependent shift on the order of 1 kHz and the width of the free-free peak increases by $\approx 30\%$ in the center compared to the low-density regions in the wing. From radial cuts averaged along 3 pixel as shown in B, we can extract the distance ΔE between the (symmetric) free atom peak energy $E_{\text{free-free}}^{\text{peak}}$ near $\Delta\nu = 0$ and the threshold energy E_{th} for the (asymmetric) bound-free peak which we obtain from a fit according to equation 5.26. This model is shown as the green line where in addition we also show the fit we obtain with a Gumbel distribution (blue dashed line) as a comparison. We see that the fits are in good agreement with the data and that the threshold energy we obtain from the model (grey dashed vertical line) is close to the energy $E_{\text{free-free}}^{\text{peak}} + E_B$ one expects for the bound-free branch. In C the distance $\Delta E = E_{\text{th}} - E_{\text{free-free}}^{\text{peak}}$ is plotted in units of the binding energy E_B as a function of the temperature T/T_F . As one would expect for a mixture of two-body dimers and free excess majority atoms we observe a value in good agreement with $\Delta E = E_B$ throughout the sample and no temperature dependence. Note that due to the broadening of the transition towards the high density center, the peak energy $E_{\text{bound-free}}^{\text{peak}}$ changes more drastically than the threshold energy and is thus not a reliable quantity to describe the relative distance. This is shown in the inset in C where the peak energy for the free-free transition (green), the threshold energy (blue) and the peak energy for the bound-free transition obtained from the Gumbel fit (red) are shown as a function of T/T_F .

We now extend our study to the crossover region where $\ln(k_F a_{2D}) \approx 0.8$ in the central region at a magnetic field $B \approx 692$ G and the dimer binding energy is $E_B = 1.37$ kHz. Here we take rf spectra of both the minority and the majority as shown in Figure 5.25 A. We see a good overlap between the branches with the main difference

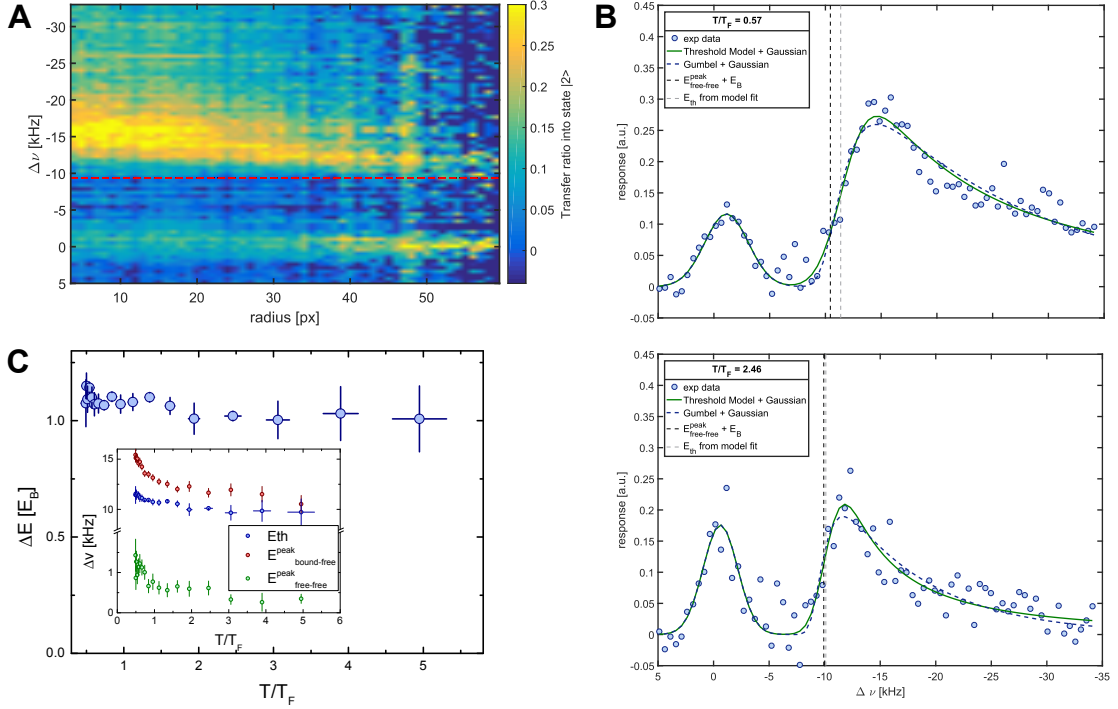


Figure 5.24.: **A** RF spectrum of the majority component $|3\rangle$ of an imbalanced 13-mixture at $B \approx 672$ G corresponding to a central $\ln(k_F a_{2D}) \approx -0.4$. Both the bound-free branch above the binding energy E_B (red dashed line) as well as the free-free branch close to $\Delta\nu = 0$ are visible and well separated. **B** Radial cuts in the high density center (upper panel, $r = 13$ px) and towards the low density wing (lower panel, $r = 43$ px). The green line fits a combination of the threshold model in equation 5.26 and a Gaussian to the data whereas the blue dashed line fits a Gumbel function (equation 5.27) in combination with a Gaussian to extract the peak position of the bound-free peak. **C** The relative distance ΔE between the free-free peak and the bound-free threshold energy is plotted in units of the binding energy E_B as a function of T/T_F . The result is consistent with the binding energy E_B throughout the sample. The inlay shows the fit results for both the peak energies (green for the free-free branch and red for the bound-free branch) and the threshold energy (blue).

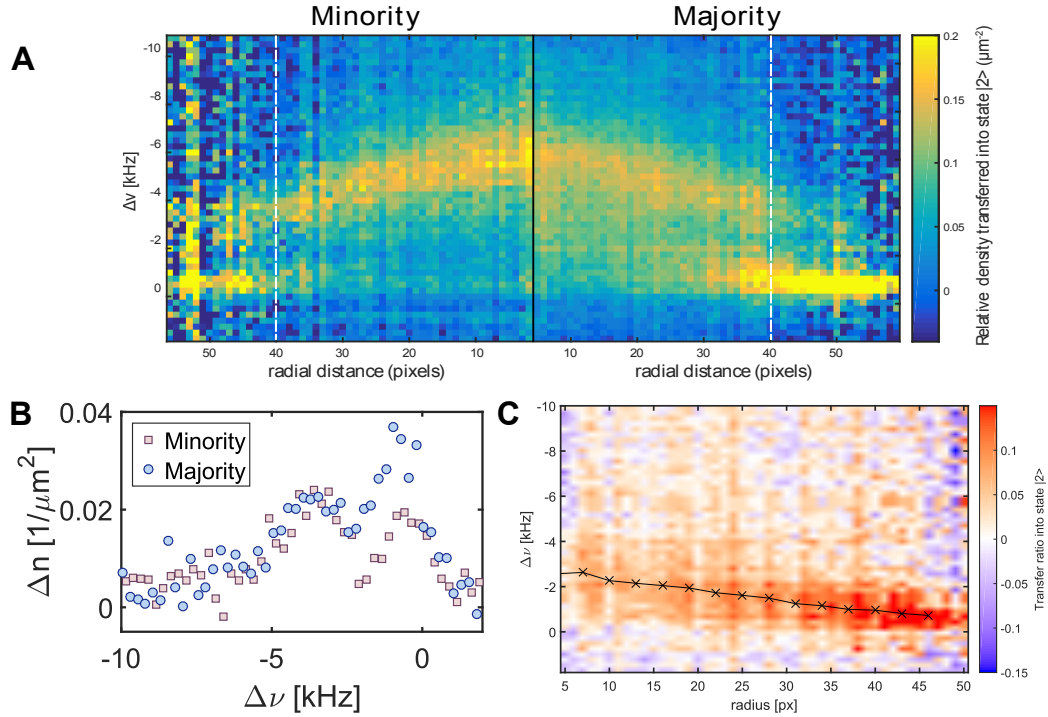


Figure 5.25.: **A** RF spectrum of both the minority component $|1\rangle$ and the majority component $|3\rangle$ of an imbalanced 13-mixture at $B \approx 692$ G corresponding to a central $\ln(k_F a_{2D}) \approx 0.8$. For the minority spectrum the frequency axis has been inverted. The bound-free branch for both components match very well indicating that the system is indeed paired. The free-free branch in the minority is only weakly occupied in the high temperature wings whereas we see a larger population for the majority due to the excess atoms. The white dashed vertical lines indicate the radial cut at $r = 40$ px shown in **B** for both spectra. Here the transferred density Δn is plotted. **C** Taking the difference between the majority and the minority spectrum reveals the free-free branch for the excess atoms. One observes a broadening at the center which is due to final state interaction effects. The black crosses indicate the peak position obtained from a Gaussian fit.

being the reduced occupation of the free branch for the minority component as it is only weakly thermally occupied. In B a cut at a radius of $r = 40$ px is plotted for the absolute transferred density Δn . One observes that the paired branch overlaps very well showing that the atoms in state $|1\rangle$ and $|3\rangle$ are indeed paired and that the unpaired branch for the majority component is larger as there the excess atoms lead to a bigger population. For the minority we observe a clear signal of the free branch only in the wing of the sample at large T/T_F whereas for the majority we can see a signal also towards the center. However, the width of the transition broadens when going towards the center which is most likely due to interaction effects. To get a better estimate for the free-free branch we can subtract the minority rf spectrum⁶ from the majority rf spectrum to obtain the excess majority atom rf spectrum. This is shown in Figure 5.25 C where the black crosses mark the peak positions obtained from a Gaussian fit to vertical cuts averaged over 3 pixels. We observe that the width of the free-free branch is severely broadened towards the center, indicating a transition into a short-lived repulsive final state polaron as discussed in section 5.4. This limits the frequency resolution and makes it difficult to separate the branches.

The question is now whether the relative distance between the free-free peak and the threshold energy changes significantly already before the critical temperature for superfluidity. This would hint at beyond two-body physics and thus indicate many-body effects. We perform the same analysis scheme as for the BEC data as shown in Figure 5.26. From the radial cuts in B we can see that especially in the center the branches do not separate well and thus the fitting of a threshold model is challenging. For the fit we set the width of the free-free branch to the measured width obtained from Figure 5.25 C to reduce the number of free parameters. Looking at the radial cuts in Figure 5.26 B, we find that our fits describe the data adequately. However, to do so the threshold energy of the bound free branch relative to the free-free branch is increased considerably compared to the dimer binding energy E_B . This can be seen as the distance between the black dashed vertical line which is the expected distance of E_B from the free-free peak and the actually fitted threshold energy which is the gray dashed vertical line. In C the extracted relative distance ΔE is plotted as a function of the temperature T/T_F . In addition the gray dashed vertical line indicates the part of the sample where the interaction strength $\ln(k_F a_{2D}) > 0.5$ as this is the regime where one would expect a Fermi surface to be present with $\mu > 0$ [Lev15]. We observe a value $\Delta E \gtrsim 1.6 \cdot E_B$ throughout the sample and thus a result which is not consistent with the picture of simple two-body dimers. While some of this deviation might be explainable by the fitting procedure, it is nevertheless considerable and hints towards many-body effects playing a role in this regime. This might also be an explanation for the increased critical temperature T_c/T_F we observed in this interaction regime in earlier experiments as shown in Figure 2.8 b) [Rie15b]. In this regime the pair size is predicted to be on the order of the inter-particle spacing and thus many-body effects become feasible.

However, with our method we cannot give a definite answer to the question of the existence of a pseudogap, as we do not observe a strong temperature dependence of the pairing gap above the critical temperature T_c/T_F . Theory predictions for the

⁶Here we do not normalize the rf spectra but take the absolute transferred density.

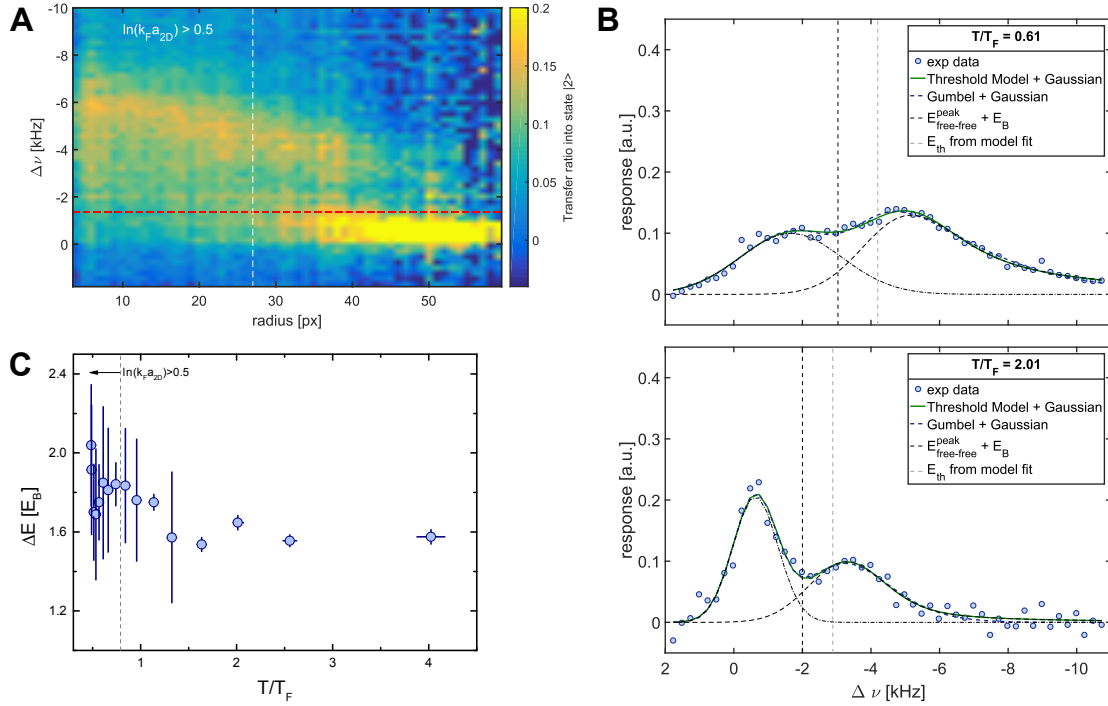


Figure 5.26.: **A** RF spectrum of the majority component $|3\rangle$ of an imbalanced 13-mixture at $B \approx 692$ G corresponding to a central $\ln(k_F a_{2D}) \approx 0.8$. Both the bound-free branch above the binding energy E_B (red dashed line) as well as the free-free branch close to $\Delta\nu = 0$ are visible but not well separated. **B** Radial cuts in the high density center (upper panel, $r = 13$ px) and towards the low density wing (lower panel, $r = 43$ px). The green line fits a combination of the threshold model in equation 5.26 and a Gaussian to the data where the width of the Gaussian was fixed according to the result in Figure 5.25 C. The blue dashed line fits a Gumbel function (equation 5.27) in combination with a Gaussian to extract the peak position of the bound-free peak. **C** The relative distance ΔE between the free-free peak and the bound-free threshold energy is plotted in units of the binding energy E_B as a function of T/T_F . We observe a deviation from the dimer binding energy which hints towards many-body effects playing a role in the pairing process.

temperature T^* where the pseudogap opens up for interaction strengths $\ln(k_F a_{2D}) \approx 0.8$ are in the range $T^*/T_F \approx 0.6$ [Mar15] and thus we barely probe this temperature regime.

In conclusion, we identified a region where the measured rf spectra cannot be explained by two-body physics alone. This is strong indication that in this regime many-body pairing plays a role and thus further experimental investigations as well as theory input e.g. regarding the expected lineshapes for many-body paired systems are required. To improve the experiment or build upon our investigations, different steps can be taken. In our ${}^6\text{Li}$ system, it would be of advantage to use the 12-mixture in the strongly interacting regime as there the final state is much narrower as shown in section 5.4. This could improve the achievable frequency resolution and thus help to resolve the branches better. Furthermore, the imbalance creation introduces heating into the system. Thus, reducing the temperature while keeping the imbalance is an aim for the future. Performing such experiments in a homogeneous trap as might be achievable soon in the setup would also be an improvement.

6. Conclusion and Outlook

During the course of this thesis ultracold gases have been used as a quantum simulator to investigate different quantum mechanical systems. Our experimental setup offers the ability to prepare a strongly interacting, two-component Fermi mixture in a single layer of a strongly anisotropic standing wave trapping potential. Thereby we can create a single realization of a quasi-2D system and we have direct access to the two-dimensional density distribution using absorption imaging without averaging over several realizations. Furthermore, we can add two perpendicular retro-reflected beams in the radial plane to realize a two-dimensional square lattice geometry.

In chapter 3 the preparation procedure of our sample was described and the calibration of our imaging system, performed during this thesis, was presented in detail. Furthermore, the possibility to image both spin states within a single experiment cycle has been implemented during the course of this thesis which will give us the full information about the system in future experiments.

In chapter 4 the momentum distribution of a sample in the two-dimensional square lattice geometry was measured using a time-of-flight evolution in a weakly harmonic potential in the radial plane [Mur14]. The momentum distribution contains information about the coherence of the system by means of the macroscopic occupation of specific momentum states. For a sample on the BEC side of the Feshbach resonance where deeply bound bosonic dimers are formed we observed sharp peaks in the momentum distribution at zero-momentum as well as at positive and negative lattice momenta k_L along the lattice axes for shallow lattices. This shows that a macroscopic part of the sample is condensed and hence in a superfluid state. Increasing the lattice depth to drive the transition into a Mott-insulator, we observed heating which leads to an increased loss of coherence on a timescale of 20 ms at a lattice depth of $V = 4 E_r$. Thus, we made first steps towards our goal of realizing low entropy systems in a two-dimensional lattice geometry.

In chapter 5 a spatially resolved rf spectroscopy method was employed for a single realization of a quasi-2D Fermi gas in a harmonic trap. This enabled us to separate the varying density, relative temperature T/T_F and interaction strength $\ln(k_F a_{2D})$ regimes one inevitable has in the harmonic trapping potential. Using a local density approach (LDA), the rf lineshapes for two-component Fermi mixtures in the normal phase were measured as a function of these parameters.

For spin-balanced samples the interaction induced energy shifts were measured as a function of the interaction strength. As there are always final state interactions present in ${}^6\text{Li}$, we used both a 12-mixture as well as a 13-mixture to minimize these final state effects. This allowed us to use weakly coupled theories to disentangle these final state shifts from the initial state interactions in the strongly interacting regime. We found these interaction induced shifts to be substantial in the strongly interacting regime reaching up to half the Fermi energy E_F . Furthermore, by comparing samples

with the same initial interaction strength but differing final state interactions one can directly contrast their influence on the obtained spectra. This showed that the final state can also be influenced by polaron like physics leading to strong shifts and broad transitions in the case of a short-lived repulsive final state polaron [Nga12, Sch12]. These measurements emphasize the need to use either spatially resolved spectra or homogeneous systems. Otherwise the averaging over the trap leads to broadening effects as well as systematics. This can be seen as for example the dominant part of the unpaired atom signal stems from the wings of the cloud at large temperature but low density whereas the paired atom signal is dominantly from the low temperature, large density region at the center.

Heating up the sample by modulating the harmonic potential, we studied the onset of pairing at high temperatures in the strongly interacting regime. There we observed the transition from a system of mostly unpaired atoms in the wings to a co-existence of paired and unpaired atoms, where the fraction of paired atoms increases as one decreases the temperature T/T_F . Measuring the relative fraction by fitting the lineshapes with a model incorporating both these branches, we extracted that the fraction of paired atoms increases faster as one approaches the low temperature regime than one would expect from a non-interacting, thermal model. This indicates that interactions play a role in the formation of the paired atoms.

At last, we looked at the pairing gap in a slightly spin-imbalanced sample. There, the excess atoms of the majority populate the unpaired atom branch and its signal is enhanced, making it possible to observe both branches also at low temperatures and far on the BEC side where deeply bound molecules are formed. Inferring the distance between these branches from the measured rf spectra, we find that on the BEC side our results are in agreement with two-body theory. In the strongly interacting regime, however, we observe a deviation from two-body physics. Although we cannot unambiguously identify a pseudogap regime, this nevertheless implies that many-body effects play a role and that this regime includes interesting physics thus inviting further studies. For future experiments, combining the ability to create uniform potentials as e.g. shown in [Muk16] with momentum-resolved rf spectroscopy as used in [Fel11, Frö12, Gae10] could improve on our results, especially when using atomic species where the final state interactions are negligible.

In the immediate future we plan to expand our existing experimental setup in several steps. We will implement a spatial light modulator (SLM) [Hol14] together with a high numerical aperture objective [Ser11] to project tailor made trapping potentials on top of the strong axial confinement provided by the SWT (see Figure 6.1). This will enable us to prepare various trapping geometries, ranging from uniform systems to different lattice geometries. In addition, a single particle, spatial and spin resolved fluorescence imaging method has been developed and successfully tested in the other experiment of our group [Bec16, Ber17]. The combination of these techniques together with our momentum imaging technique [Mur14] will provide a rich playground for future experiments.

One idea is to prepare a uniform, quasi-2D system with low atom number where we can still resolve the atoms individually and perform momentum resolved rf spectroscopy. This could give us direct access to multi-particle correlation functions and thus the possible onset of many-body effects in the pairing could be studied as a

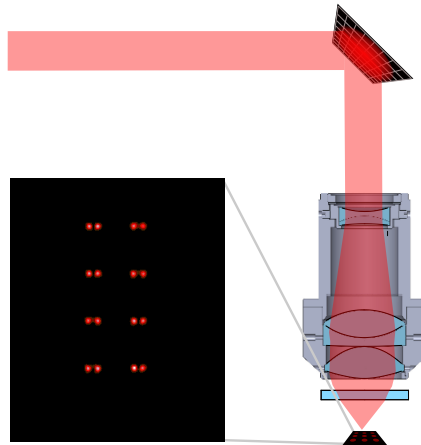


Figure 6.1.: Using the combination of a spatial light modulator (SLM) and a custom made high numerical aperture objective we will be able to create a large variety of trapping geometries to study correlations in strongly interacting Fermi systems.

function of system size and interaction.

Another direction the SLM offers is to create lattices of varying sizes and geometry. One goal would then be to prepare a Mott-insulator of molecules as a low entropy state. Breaking up the molecules in a deep lattice and adiabatically changing the lattice geometry to a superlattice can then potentially create a state with strong anti-correlations in the spin domain [Lub11] which we could measure with our spin resolved imaging technique.

These experimental implementations will bring us further towards our aim of a flexible quantum simulator and allow us to study the crossover from few- to many-body physics in more detail in the future.

A. Appendix

A.1. Polylogarithmic Function

In the context of density distributions for ideal Fermi or Bose gases, we introduced the polylogarithmic functions $Li_\nu(z)$. Therefore we give here a definition and summarize its properties. The polylogarithmic function can be either defined in an integral form or as a power series [Pit03]

$$Li_\nu(z) = \frac{1}{\Gamma(\nu)} \int_0^\infty dx x^{\nu-1} \frac{1}{z^{-1}e^x - 1} = \sum_{l=1}^{\infty} \frac{z^l}{l^\nu}, \quad (\text{A.1})$$

where $\Gamma(\nu)$ is the Gamma function and $|z| < 1$. In the case of a Bose gas, $z = \exp(\beta\mu)$ is the so-called fugacity which is always smaller than one since $\mu \leq 0$. In the case of fermions one uses a slightly different definition

$$-Li_\nu(-z) = \frac{1}{\Gamma(\nu)} \int_0^\infty dx x^{\nu-1} \frac{1}{z^{-1}e^x + 1} = \sum_{l=1}^{\infty} (-1)^{l+1} \frac{z^l}{l^\nu}. \quad (\text{A.2})$$

Another useful property of the polylogarithm is the relation

$$z \frac{d}{dz} Li_{\nu+1}(z) = Li_\nu(z). \quad (\text{A.3})$$

Bibliography

- [All89] H. Alloul, T. Ohno, P. Mendels, *Y89NMR evidence for a fermi-liquid behavior in $YBa_2Cu_3O_{6+x}$* , Physical Review Letters **63**(16), 1700–1703 (1989).
- [Alt10] A. Altland, B. Simons, *Condensed Matter Field Theory* (Cambridge University Pr., 2010).
- [And95] M. H. Anderson, J. R. Ensher, M. R. Matthews, C. E. Wieman, E. A. Cornell, *Observation of Bose-Einstein Condensation in a Dilute Atomic Vapor*, Science **269**(5221), 198–201 (1995).
- [Ash76] N. W. Ashcroft, N. Mermin, *Solid State Physics* (Cengage Learning, Inc, 1976).
- [Bab98] E. Babaev, H. Kleinert, *Crossover from Weak- to Strong-Coupling Superconductivity and to Normal State with Pseudogap*, arXiv (1998).
- [Bak10] W. S. Bakr, A. Peng, M. E. Tai, R. Ma, J. Simon, J. I. Gillen, S. Folling, L. Pollet, M. Greiner, *Probing the Superfluid-to-Mott Insulator Transition at the Single-Atom Level*, Science **329**(5991), 547–550 (2010).
- [Bak14] M. Bakircioglu, *Simultane Absorptionsabbildung zweier Spin-Zustände bei hohen Magnetfeldern* (2014), B.Sc. Thesis, University of Heidelberg.
- [Bar57] J. Bardeen, L. N. Cooper, J. R. Schrieffer, *Theory of Superconductivity*, Phys. Rev. **108**, 1175–1204 (1957).
- [Bar04] M. Bartenstein, A. Altmeyer, S. Riedl, S. Jochim, C. Chin, J. H. Denschlag, R. Grimm, *Collective Excitations of a Degenerate Gas at the BEC-BCS Crossover*, Phys. Rev. Lett. **92**, 203201 (2004).
- [Bar14] M. Barth, J. Hofmann, *Pairing effects in the nondegenerate limit of the two-dimensional Fermi gas*, Physical Review A **89**(1) (2014).
- [Bau12] S. K. Baur, B. Fröhlich, M. Feld, E. Vogt, D. Pertot, M. Koschorreck, M. Köhl, *Radio-frequency spectra of Feshbach molecules in quasi-two-dimensional geometries*, Phys. Rev. A **85**, 061604 (2012).
- [Bau14] M. Bauer, M. M. Parish, T. Enss, *Universal Equation of State and Pseudogap in the Two-Dimensional Fermi Gas*, Phys. Rev. Lett. **112**, 135302 (2014).
- [Bay15] L. Bayha, *A Strongly Interacting Fermi Gas in a Two-Dimensional Optical Lattice*, Masters Thesis, Ruprecht-Karls-Universität Heidelberg (2015).
- [Bec16] J. H. W. Becher, *Towards Spin and Site-Resolved, Single-Atom Imaging of $6Li$ Atoms in a Multiwell Potential*, Masters Thesis, Ruprecht-Karls-Universität Heidelberg, <http://www.lithium6.de/publications> (2016).

- [Bed86] J. Bednorz, K. Müller, *Possible highT c superconductivity in the Ba-La-Cu-O system*, Zeitschrift für Physik B Condensed Matter **64**(2), 189–193 (1986).
- [Bee52] Beer, *Bestimmung der Absorption des rothen Lichts in farbigen Flüssigkeiten*, Annalen der Physik und Chemie **162**(5), 78–88 (1852).
- [Ber72] V. L. Berezinskii, *Destruction of long-range order in one-dimensional and two-dimensional systems possessing a continuous symmetry group. II. Quantum systems*, Sov. Phys. JETP **34**, 610 (1972).
- [Ber17] A. Bergschneider, *TBD*, Dissertation, Ruprecht-Karls Universität Heidelberg (2017), to be published.
- [Bis78] D. J. Bishop, J. D. Reppy, *Study of the Superfluid Transition in Two-Dimensional ⁴He Films*, Phys. Rev. Lett. **40**, 1727–1730 (1978).
- [Blo75] P. Bloom, *Two-dimensional Fermi gas*, Physical Review B **12**(1), 125–129 (1975).
- [Blo08] I. Bloch, J. Dalibard, W. Zwerger, *Many-body physics with ultracold gases*, Reviews of Modern Physics **80**(3), 885–964 (2008).
- [Blo12] I. Bloch, J. Dalibard, S. Nascimbene, *Quantum simulations with ultracold quantum gases*, Nat Phys **8**(4), 267–276 (2012).
- [Boe16] I. Boettcher, L. Bayha, D. Kedar, P. Murthy, M. Neidig, M. Ries, A. Wenz, G. Zürn, S. Jochim, T. Enss, *Equation of State of Ultracold Fermions in the 2D BEC-BCS Crossover Region*, Physical Review Letters **116**(4) (2016).
- [Boh12] J. E. Bohn, *Towards an ultracold three-component Fermi Gas in a two-dimensional optical lattice* (2012), Diploma thesis, Ruprecht-Karls-Universität Heidelberg.
- [Bot06] S. S. Botelho, C. A. R. Sá de Melo, *Vortex-Antivortex Lattice in Ultracold Fermionic Gases*, Phys. Rev. Lett. **96**, 040404 (2006).
- [Bra03] B. H. Bransden, C. J. Joachain, *Physics of Atoms and Molecules* (Prentice Hall, 2003).
- [Bro23] L. de Broglie, *Waves and Quanta*, Nature (London) **112**, 540 (1923).
- [Car03] J. Carlson, S.-Y. Chang, V. R. Pandharipande, K. E. Schmidt, *Superfluid Fermi Gases with Large Scattering Length*, Phys. Rev. Lett. **91**, 050401 (2003).
- [Cha13] C. Chafin, T. Schäfer, *Scale breaking and fluid dynamics in a dilute two-dimensional Fermi gas*, Physical Review A **88**(4) (2013).
- [Che05] Q. Chen, J. Stajic, S. Tan, K. Levin, *BCS-BEC crossover: From high temperature superconductors to ultracold superfluids*, Physics Reports **412**(1), 1–88 (2005).
- [Che09a] Q. Chen, Y. He, C.-C. Chien, K. Levin, *Theory of radio frequency spectroscopy experiments in ultracold Fermi gases and their relation to photoemission in the cuprates*, Reports on Progress in Physics **72**(12), 122501 (2009).

-
- [Che09b] Q. Chen, K. Levin, *Momentum Resolved Radio Frequency Spectroscopy in Trapped Fermi Gases*, Physical Review Letters **102**(19) (2009).
- [Chi04] C. Chin, M. Bartenstein, A. Altmeyer, S. Riedl, S. Jochim, J. H. Denschlag, R. Grimm, *Observation of the Pairing Gap in a Strongly Interacting Fermi Gas*, Science **305**, 1128–1130 (2004).
- [Chi06] J. K. Chin, D. E. Miller, Y. Liu, C. Stan, W. Setiawan, C. Sanner, K. Xu, W. Ketterle, *Evidence for superfluidity of ultracold fermions in an optical lattice*, Nature **443**(7114), 961–964 (2006).
- [Chi10] C. Chin, R. Grimm, P. Julienne, E. Tiesinga, *Feshbach resonances in ultracold gases*, Rev. Mod. Phys. **82**(2), 1225 (2010).
- [Cla09] P. Cladé, C. Ryu, A. Ramanathan, K. Helmerson, W. D. Phillips, *Observation of a 2D Bose Gas: From Thermal to Quasicondensate to Superfluid*, Phys. Rev. Lett. **102**, 170401 (2009).
- [Dal85] J. Dalibard, C. Cohen-Tannoudji, *Dressed-atom approach to atomic motion in laser light: the dipole force revisited*, Journal of the Optical Society of America B **2**(11), 1707 (1985).
- [Dal98] J. Dalibard, *Collisional dynamics of ultracold atomic gases*, in M. Inguscio, S. Stringari, C. Wieman (Ed.), *Bose-Einstein Condensation in Atomic Gases*, Vol. Course CXL of *Proceedings of the International School of Physics Enrico Fermi* (IOS Press, Varenna, 1998).
- [Dal99] J. Dalibard, *Collisional dynamics of ultra-cold atomic gases*, Proceedings of the International School of Physics “Enrico Fermi” **140**(Bose-Einstein Condensation in Atomic Gases), 321–349 (1999).
- [Dav95] K. B. Davis, M. O. Mewes, M. R. Andrews, N. J. van Druten, D. S. Durfee, D. M. Kurn, W. Ketterle, *Bose-Einstein Condensation in a Gas of Sodium Atoms*, Physical Review Letters **75**(22), 3969–3973 (1995).
- [Dem10] W. Demtröder, *Experimentalphysik 3: Atome, Moleküle und Festkörper (Springer-Lehrbuch) (German Edition)* (Springer, 2010).
- [Des12] R. Desbuquois, L. Chomaz, T. Yefsah, J. Leonard, J. Beugnon, C. Weitenberg, J. Dalibard, *Superfluid behaviour of a two-dimensional Bose gas*, Nature Physics **8**(9), 645 (2012).
- [Din96] H. Ding, T. Yokoya, J. C. Campuzano, T. Takahashi, M. Randeria, M. R. Norman, T. Mochiku, K. Kadowaki, J. Giapintzakis, *Spectroscopic evidence for a pseudogap in the normal state of underdoped high-Tc superconductors*, Nature **382**(6586), 51–54 (1996).
- [Dyk11] P. Dyke, E. D. Kuhnle, S. Whitlock, H. Hu, M. Mark, S. Hoinka, M. Lingham, P. Hannaford, C. J. Vale, *Crossover from 2D to 3D in a Weakly Interacting Fermi Gas*, Phys. Rev. Lett. **106**, 105304 (2011).
- [Eag69] D. M. Eagles, *Possible Pairing without Superconductivity at Low Carrier Concentrations in Bulk and Thin-Film Superconducting Semiconductors*, Phys. Rev. **186**, 456–463 (1969).

- [Ens17] T. Enss (2017), private Communication.
- [Fel11] M. Feld, B. Fröhlich, E. Vogt, M. Koschorreck, M. Köhl, *Observation of a pairing pseudogap in a two-dimensional Fermi gas*, *Nature* **480**(7375), 75–78 (2011).
- [Fen16] K. Fenech, P. Dyke, T. Pepler, M. Lingham, S. Hoinka, H. Hu, C. Vale, *Thermodynamics of an Attractive 2D Fermi Gas*, *Physical Review Letters* **116**(4) (2016).
- [Fes58] H. Feshbach, *Unified theory of nuclear reactions*, *Annals of Physics* **5**(4), 357 – 390 (1958).
- [Fet03] A. Fetter, J. Walecka, *Quantum Theory of Many-particle Systems*, Dover Books on Physics (Dover Publications, 2003).
- [Fey82] R. P. Feynman, *Simulating physics with computers*, *International journal of theoretical physics* **21**(6), 467–488 (1982).
- [Fis14] A. M. Fischer, M. M. Parish, *Quasi-two-dimensional Fermi gases at finite temperatures*, *Physical Review B* **90**(21) (2014).
- [Foo04] C. J. Foot, *Atomic Physics* (Oxford University Press, 2004).
- [Frö11] B. Fröhlich, M. Feld, E. Vogt, M. Koschorreck, W. Zwerger, M. Köhl, *Radio-Frequency Spectroscopy of a Strongly Interacting Two-Dimensional Fermi Gas*, *Physical Review Letters* **106**(10) (2011).
- [Frö12] B. Fröhlich, M. Feld, E. Vogt, M. Koschorreck, M. Köhl, C. Berthod, T. Giamarchi, *Two-Dimensional Fermi Liquid with Attractive Interactions*, *Physical Review Letters* **109**(13) (2012).
- [Gae10] J. P. Gaebler, J. T. Stewart, T. E. Drake, D. S. Jin, A. Perali, P. Pieri, G. C. Strinati, *Observation of pseudogap behaviour in a strongly interacting Fermi gas*, *Nature Physics* **6**(8), 569–573 (2010).
- [Geh98] M. E. Gehm, K. M. O’Hara, T. A. Savard, J. E. Thomas, *Dynamics of noise-induced heating in atom traps*, *Physical Review A* **58**(5), 3914–3921 (1998).
- [Geh03] M. Gehm, *Properties of 6Li* (2003), <http://www.physics.ncsu.edu/jet/techdocs/pdf/PropertiesOfLi.pdf>.
- [Gia13] T. Giamarchi, A. Iucci, C. Berthod, *Introduction to Many Body physics*, Lecture Notes (2008-2013), University of Geneva.
- [Gio08] S. Giorgini, L. P. Pitaevskii, S. Stringari, *Theory of ultracold atomic Fermi gases*, *Rev. Mod. Phys.* **80**, 1215–1274 (2008).
- [Gor61] L. P. Gorkov, T. K. Melik-Barhudarov, *Contribution to the theory of superfluidity in an imperfect Fermi gas*, *Soviet Physics JETP* **13**, 1018 (1961).
- [Gre01] M. Greiner, I. Bloch, O. Mandel, T. W. Hänsch, T. Esslinger, *Exploring Phase Coherence in a 2D Lattice of Bose-Einstein Condensates*, *Physical Review Letters* **87**(16) (2001).

-
- [Gre05] M. Greiner, C. A. Regal, D. S. Jin, *Probing the Excitation Spectrum of a Fermi Gas in the BCS-BEC Crossover Regime*, Phys. Rev. Lett. **94**, 070403 (2005).
- [Gri00] Rudolf Grimm, Matthias Weidemüller, Yurii B. Ovchinnikov, *Optical dipole traps for neutral atoms*, Adv. At. Mol. Opt. Phys. **Vol. 42**, 95–170 (2000).
- [Gub13] K. Gubbels, H. Stoof, *Imbalanced Fermi gases at unitarity*, Physics Reports **525**(4), 255 – 313 (2013).
- [Had06] Z. Hadzibabic, P. Krüger, M. Cheneau, B. Battelier, J. Dalibard, *Berezinskii-Kosterlitz-Thouless crossover in a trapped atomic gas*, Nature **441**, 1118 (2006).
- [Had11] Z. Hadzibabic, J. Dalibard, *Two-dimensional Bose fluids: An atomic physics perspective*, Rivista del Nuovo Cimento, vol. **34**, pp.389–434 (2011).
- [Hoh67] P. C. Hohenberg, *Existence of Long-Range Order in One and Two Dimensions*, Physical Review **158**(2), 383–386 (1967).
- [Hol14] M. Holten, *Hamiltonian Engineering in Ultracold Atom Experiments using a Spatial Light Modulator* (2014), b.Sc. Thesis, University of Heidelberg.
- [Hou98] M. Houbiers, H. T. C. Stoof, W. I. McAlexander, R. G. Hulet, *Elastic and inelastic collisions of ^6Li atoms in magnetic and optical traps*, Physical Review A **57**(3), R1497–R1500 (1998).
- [Hua57] K. Huang, C. N. Yang, *Quantum-Mechanical Many-Body Problem with Hard-Sphere Interaction*, Physical Review **105**(3), 767–775 (1957).
- [Hua87] K. Huang, *Statistical Mechanics* (John Wiley & Sons, 1987).
- [Hue17] K. Hueck, N. Luick, L. Sobirey, J. Siegl, T. Lompe, H. Moritz, L. W. Clark, C. Chin, *Calibrating High Intensity Absorption Imaging of Ultracold Atoms*, ArXiv e-prints (2017).
- [Hun11] C.-L. Hung, *In Situ Probing of Two-Dimensional Quantum Gases*, Dissertation, University of Chicago (2011).
- [Ino98] S. Inouye, M. R. Andrews, J. Stenger, H.-J. Miesner, D. M. Stamper Kurn, W. Ketterle, *Observation of Feshbach resonances in a Bose-Einstein condensate*, Nature **392**, 151–154 (1998).
- [Joc04] S. Jochim, *Bose-Einstein Condensation of Molecules*, Dissertation, Leopold-Franzens-Universität Innsbruck (2004).
- [Joh89] D. C. Johnston, *Magnetic Susceptibility Scaling in $\text{La}_{2-x}\text{Sr}_x\text{CuO}_4$* , Physical Review Letters **62**(8), 957–960 (1989).
- [Jos13] J. V. José (Ed.), *40 years of Berezinskii-Kosterlitz-Thouless Theory* (World Scientific, New Jersey, 2013).
- [Kap33] P. L. Kapitza, P. A. M. Dirac, *The reflection of electrons from standing light waves*, Mathematical Proceedings of the Cambridge Philosophical Society **29**(02), 297 (1933).

- [Ket99] W. Ketterle, D. S. Durfee, D. M. Stamper Kurn, *Making, probing and understanding Bose-Einstein condensates*, in M. Inguscio, S. Stringari, C. Wieman (Ed.), *Bose-Einstein Condensation in Atomic Gases*, Vol. CXL of *Proceedings of the International School of Physics Enrico Fermi*, 67–176 (IOS Press, Amsterdam, 1999).
- [Ket08] W. Ketterle, M. W. Zwierlein, *Making, probing and understanding ultracold fermi gases*, Proc. of the International School of Physics 'Enrico Fermi', Course CLXIV (2008).
- [Kle16] R. A. Klemt, *Many-body correlations in quasi-two-dimensional, ultracold atomic Fermi gas*, Masters Thesis, Ruprecht-Karls-Universität Heidelberg, <http://www.lithium6.de/publications> (2016).
- [Kos73] J. M. Kosterlitz, D. J. Thouless, *Ordering, metastability and phase transitions in two-dimensional systems*, Journal of Physics C: Solid State Physics **6**(7), 1181 (1973).
- [Kos12] M. Koschorreck, D. Pertot, E. Vogt, B. Fröhlich, M. Feld, M. Köhl, *Attractive and repulsive Fermi polarons in two dimensions*, Nature **485**(7400), 619–622 (2012).
- [Kra15] G. Krause, *Simultaneous absorption imaging of two Li6 hyperfine states* (2015), B.Sc. Thesis, University of Heidelberg.
- [Krü07] P. Krüger, Z. Hadzibabic, J. Dalibard, *Critical Point of an Interacting Two-Dimensional Atomic Bose Gas*, Phys. Rev. Lett. **99**, 040402 (2007).
- [Ku12] M. J. H. Ku, A. T. Sommer, L. W. Cheuk, M. W. Zwierlein, *Revealing the Superfluid Lambda Transition in the Universal Thermodynamics of a Unitary Fermi Gas*, Science **335**(6068), 563–567 (2012).
- [Lan32] L. Landau, *Zur Theorie der Energieübertragung. II*, Phys. Z. Sowjetunion **2**(46), 1–13 (1932).
- [Lan81] L. Landau, E. Lifshitz, *Quantum Mechanics: Non-Relativistic Theory*, Vol. 3 (Elsevier Science, 1981).
- [Lan96] L. Landau, E. Lifshitz, *Statistical Physics*, Vol. 5 (Elsevier Science, 1996).
- [Lan12] C. Langmack, M. Barth, W. Zwerger, E. Braaten, *Clock Shift in a Strongly Interacting Two-Dimensional Fermi Gas*, Physical Review Letters **108**(6) (2012).
- [Leg80] A. J. Leggett, *Cooper pairing in spin-polarized Fermi systems*, J. Phys. (Paris) Coll. **41**, C7–19 (1980).
- [Lev15] J. Levinsen, M. M. Parish, *Strongly Interacting Two-Dimensional Fermi Gases*, in *Annual Review of Cold Atoms and Molecules*, 1–75 (World Scientific Pub Co Pte Lt, 2015).
- [Lew12] M. Lewenstein, A. Sanpera, V. Ahufinger, *Ultracold Atoms in Optical Lattices* (Oxford University Press, 2012).

-
- [Lub11] M. Lubasch, V. Murg, U. Schneider, J. I. Cirac, M.-C. Bañuls, *Adiabatic Preparation of a Heisenberg Antiferromagnet Using an Optical Superlattice*, Physical Review Letters **107**(16) (2011).
- [Mag09] P. Magierski, G. Wlazłowski, A. Bulgac, J. E. Drut, *Finite-Temperature Pairing Gap of a Unitary Fermi Gas by Quantum Monte Carlo Calculations*, Physical Review Letters **103**(21) (2009).
- [Mar10] K. Martiyanov, V. Makhalov, A. Turlapov, *Observation of a Two-Dimensional Fermi Gas of Atoms*, Phys. Rev. Lett. **105**, 030404 (2010).
- [Mar15] F. Marsiglio, P. Pieri, A. Perali, F. Palestini, G. C. Strinati, *Pairing effects in the normal phase of a two-dimensional Fermi gas*, Physical Review B **91**(5) (2015).
- [Mer66] N. D. Mermin, H. Wagner, *Absence of Ferromagnetism or Antiferromagnetism in One- or Two-Dimensional Isotropic Heisenberg Models*, Physical Review Letters **17**(22), 1133–1136 (1966).
- [Met02] H. J. Metcalf, P. v. Straten, *Laser cooling and trapping*, Graduate texts in contemporary physics (Springer, New York ; Berlin ; Heidelberg [u.a.], 2002), corr. 2. print Edn.
- [Mit16] D. Mitra, P. T. Brown, P. Schauß, S. S. Kondov, W. S. Bakr, *Phase Separation and Pair Condensation in a Spin-Imbalanced 2D Fermi Gas*, Physical Review Letters **117**(9) (2016).
- [Moe95] A. J. Moerdijk, B. J. Verhaar, A. Axelsson, *Resonances in ultracold collisions of ${}^6\text{Li}$, ${}^7\text{Li}$, and ${}^{23}\text{Na}$* , Phys. Rev. A **51**, 4852–4861 (1995).
- [Mue17] E. J. Mueller, *Pseudogaps in strongly interacting Fermi gases*, arXiv (2017).
- [Muk16] B. Mukherjee, Z. Yan, P. B. Patel, Z. Hadzibabic, T. Yefsah, J. Struck, M. W. Zwierlein, *Homogeneous Atomic Fermi Gases*, arXiv (2016).
- [Mur14] P. A. Murthy, D. Kedar, T. Lompe, M. Neidig, M. G. Ries, A. N. Wenz, G. Zürn, S. Jochim, *Matter-wave Fourier optics with a strongly interacting two-dimensional Fermi gas*, Physical Review A **90**(4) (2014).
- [Mur15] P. Murthy, I. Boettcher, L. Bayha, M. Holzmann, D. Kedar, M. Neidig, M. Ries, A. Wenz, G. Zürn, S. Jochim, *Observation of the Berezinskii-Kosterlitz-Thouless Phase Transition in an Ultracold Fermi Gas*, Physical Review Letters **115**(1) (2015).
- [Nei13] M. Neidig, *A realization of a two-dimensional Fermi gas in a standing wave trap* (2013), Master thesis, Ruprecht-Karls-Universität Heidelberg.
- [Nga12] V. Ngampruetikorn, J. Levinsen, M. M. Parish, *Repulsive polarons in two-dimensional Fermi gases*, EPL (Europhysics Letters) **98**(3), 30005 (2012).
- [Nga13] V. Ngampruetikorn, J. Levinsen, M. M. Parish, *Pair Correlations in the Two-Dimensional Fermi Gas*, Physical Review Letters **111**(26) (2013).
- [Nor05] M. R. Norman, D. Pines, C. Kallin, *The pseudogap: friend or foe of highTc?*, Advances in Physics **54**(8), 715–733 (2005).

- [Nor11] M. R. Norman, *The Challenge of Unconventional Superconductivity*, *Science* **332**(6026), 196–200 (2011).
- [Onn11] H. K. Onnes, *The resistance of pure mercury at helium temperatures*, *Commun. Phys. Lab. Univ. Leiden* **12**, 120+ (1911).
- [Pau25] W. Pauli, *Über den Zusammenhang des Abschlusses der Elektronengruppen im Atom mit der Komplexstruktur der Spektren*, *Zeitschrift für Physik* **31**(1), 765–783 (1925).
- [Pau40] W. Pauli, *The Connection Between Spin and Statistics*, *Phys. Rev.* **58**, 716–722 (1940).
- [Peh13] N. Pehoviak, *Laserstabilisierung durch Modulationstransferspektroskopie in 6 Li* (2013), Bachelor thesis, Ruprecht-Karls-Universität Heidelberg.
- [Pet00] D. S. Petrov, M. Holzmann, G. V. Shlyapnikov, *Bose-Einstein Condensation in Quasi-2D Trapped Gases*, *Phys. Rev. Lett.* **84**, 2551–2555 (2000).
- [Pet01] D. S. Petrov, G. V. Shlyapnikov, *Interatomic collisions in a tightly confined Bose gas*, *Physical Review A* **64**(1) (2001).
- [Pet02] C. J. Pethick, H. Smith, *Bose-Einstein Condensation in Dilute Gases* (Cambridge University Press, 2002).
- [Pet03a] D. S. Petrov, *Three-body problem in Fermi gases with short-range interparticle interaction*, *Physical Review A* **67**(1) (2003).
- [Pet03b] D. S. Petrov, M. A. Baranov, G. V. Shlyapnikov, *Superfluid transition in quasi-two-dimensional Fermi gases*, *Phys. Rev. A* **67**, 031601 (2003).
- [Pet04] D. S. Petrov, C. Salomon, G. V. Shlyapnikov, *Weakly Bound Dimers of Fermionic Atoms*, *Physical Review Letters* **93**(9) (2004).
- [Pet05] D. S. Petrov, C. Salomon, G. V. Shlyapnikov, *Scattering properties of weakly bound dimers of fermionic atoms*, *Physical Review A* **71**(1) (2005).
- [Pie09] P. Pieri, A. Perali, G. C. Strinati, *Enhanced paraconductivity-like fluctuations in the radiofrequency spectra of ultracold Fermi atoms*, *Nature Physics* **5**(10), 736–740 (2009).
- [Pim16] R. F. R.-M. Pimentel, *Towards Detection of Noise Correlations in a System of Ultracold 6Li Atoms* (2016), B.Sc. Thesis, University of Heidelberg.
- [Pit03] L. P. Pitaevskii, S. Stringari, *Bose-Einstein Condensation* (Oxford University Press, 2003).
- [Pre14] S. Pres, *BKT-phase transition in a strongly interacting 2d Bose gas*, Masters Thesis, Ruprecht-Karls Universität Heidelberg (2014), Master thesis, Ruprecht-Karls-Universität Heidelberg.
- [Pro01] N. Prokof'ev, O. Ruebenacker, B. Svistunov, *Critical Point of a Weakly Interacting Two-Dimensional Bose Gas*, *Phys. Rev. Lett.* **87**, 270402 (2001).

-
- [Pro02] N. Prokof'ev, B. Svistunov, *Two-dimensional weakly interacting Bose gas in the fluctuation region*, Phys. Rev. A **66**, 043608 (2002).
- [Ran90] M. Randeria, J.-M. Duan, L.-Y. Shieh, *Superconductivity in a two-dimensional Fermi gas: Evolution from Cooper pairing to Bose condensation*, Physical Review B **41**(1), 327–343 (1990).
- [Reg04] C. A. Regal, M. Greiner, D. S. Jin, *Observation of Resonance Condensation of Fermionic Atom Pairs*, Phys. Rev. Lett. **92**(4), 040403–4 (2004).
- [Rei07] G. Reinaudi, T. Lahaye, Z. Wang, D. Guéry-Odelin, *Strong saturation absorption imaging of dense clouds of ultracold atoms*, Optics Letters **32**(21), 3143 (2007).
- [Rie10] M. G. Ries, *A magneto-optical trap for the preparation of a three-component Fermi gas in an optical lattice* (2010), Diploma thesis, Ruprecht-Karls-Universität Heidelberg.
- [Rie15a] M. Ries, A. Wenz, G. Zürn, L. Bayha, I. Boettcher, D. Kedar, P. Murthy, M. Neidig, T. Lompe, S. Jochim, *Observation of Pair Condensation in the Quasi-2D BEC-BCS Crossover*, Physical Review Letters **114**(23) (2015).
- [Rie15b] M. G. Ries, *A Two-Dimensional Fermi Gas in the BEC-BCS Crossover*, Dissertation, Ruprecht-Karls-Universität Heidelberg, <http://www.lithium6.de/publications> (2015), PhD thesis, Ruprecht-Karls-Universität Heidelberg.
- [Sag15] Y. Sagi, T. E. Drake, R. Paudel, R. Chapurin, D. S. Jin, *Breakdown of the Fermi Liquid Description for Strongly Interacting Fermions*, Physical Review Letters **114**(7) (2015).
- [Sak10] J. J. Sakurai, J. J. Napolitano, *Modern Quantum Mechanics* (ADDISON WESLEY PUB CO INC, 2010).
- [Sch93] A. Schilling, M. Cantoni, J. D. Guo, H. R. Ott, *Superconductivity above 130 K in the Hg-Ba-Ca-Cu-O system*, Nature **363**(6424), 56–58 (1993).
- [Sch99] U. Schünemann, H. Engler, R. Grimm, M. Weidemüller, M. Zielonkowski, *Simple scheme for tunable frequency offset locking of two lasers*, Rev. Sci. Instrum. **70**(1), 242–243 (1999).
- [Sch00] F. Schwabl, *Statistische Mechanik*, Springer-Lehrbuch (Springer-Verlag GmbH, 2000).
- [Sch07a] C. H. Schunck, Y. Shin, A. Schirotzek, M. W. Zwierlein, W. Ketterle, *Pairing Without Superfluidity: The Ground State of an Imbalanced Fermi Mixture*, Science **316**(5826), 867–870 (2007).
- [Sch07b] F. Schwabl, *Quantenmechanik (QM I)* (Springer, 2007).
- [Sch08a] A. Schirotzek, Y. il Shin, C. H. Schunck, W. Ketterle, *Determination of the Superfluid Gap in Atomic Fermi Gases by Quasiparticle Spectroscopy*, Physical Review Letters **101**(14) (2008).

- [Sch08b] C. H. Schunck, Y. il Shin, A. Schirotzek, W. Ketterle, *Determination of the fermion pair size in a resonantly interacting superfluid*, *Nature* **454**(7205), 739–743 (2008).
- [Sch09] A. Schirotzek, C.-H. Wu, A. Sommer, M. W. Zwierlein, *Observation of Fermi Polarons in a Tunable Fermi Liquid of Ultracold Atoms*, *Physical Review Letters* **102**(23) (2009).
- [Sch12] R. Schmidt, T. Enss, V. Pietilä, E. Demler, *Fermi polarons in two dimensions*, *Physical Review A* **85**(2) (2012).
- [Ser11] F. Serwane, *Deterministic preparation of a tunable few-fermion system*, Dissertation, Ruprecht-Karls-Universität Heidelberg, <http://www.mpi-hd.mpg.de/biblio/preprints/2011-048.pdf> (2011).
- [Sim10] P. Simon, *Apparatus for the preparation of ultracold Fermi gases* (2010), Diploma thesis, Ruprecht-Karls-Universität Heidelberg.
- [Som12] A. T. Sommer, L. W. Cheuk, M. J. H. Ku, W. S. Bakr, M. W. Zwierlein, *Evolution of Fermion Pairing from Three to Two Dimensions*, *Physical Review Letters* **108**(4) (2012).
- [Son16] M. Soni, M. Dolfi, M. Troyer, *Density redistribution effects in fermionic optical lattices*, *Physical Review A* **94**(6) (2016).
- [Ste16] T. Steinle, *Implementation of Simultaneously Imaging two Hyperfine States of Ultracold ^6Li Atoms in a Magnetic Field* (2016), B.Sc. Thesis, University of Heidelberg.
- [Tan08] S. Tan, *Energetics of a strongly correlated Fermi gas*, *Annals of Physics* **323**(12), 2952–2970 (2008).
- [Wan37] G. H. Wannier, *The Structure of Electronic Excitation Levels in Insulating Crystals*, *Physical Review* **52**(3), 191–197 (1937).
- [War89] W. W. Warren, R. E. Walstedt, G. F. Brennert, R. J. Cava, R. Tycko, R. F. Bell, G. Dabbagh, *Cu spin dynamics and superconducting precursor effects in planes above T_c in $\text{YBa}_2\text{Cu}_3\text{O}_{6.7}$* , *Physical Review Letters* **62**(10), 1193–1196 (1989).
- [Wei09] M. Weidemüller, C. Zimmermann, *Cold Atoms and Molecules*, Physics textbook (Wiley, 2009).
- [Wen08] A. Wenz, *Few-Body Physics in a Three-Component Fermi Gas*, <http://www.mpi-hd.mpg.de/biblio/preprints/2008-023.pdf> (2008), Diploma thesis, Ruprecht-Karls-Universität Heidelberg.
- [Wen13] A. Wenz, *From Few to Many: Ultracold Atoms in Reduced Dimensions*, Dissertation, Ruprecht-Karls-Universität Heidelberg, <http://www.lithium6.de/publications> (2013).
- [Wes04] S. Wessel, F. Alet, M. Troyer, G. G. Batrouni, *Quantum Monte Carlo simulations of confined bosonic atoms in optical lattices*, *Physical Review A* **70**(5) (2004).

-
- [Wu87] M. K. Wu, J. R. Ashburn, C. J. Torng, P. H. Hor, R. L. Meng, L. Gao, Z. J. Huang, Y. Q. Wang, C. W. Chu, *Superconductivity at 93 K in a new mixed-phase Y-Ba-Cu-O compound system at ambient pressure*, Phys. Rev. Lett. **58**, 908–910 (1987).
- [Yef11] T. Yefsah, R. Desbuquois, L. Chomaz, K. J. Günter, J. Dalibard, *Exploring the Thermodynamics of a Two-Dimensional Bose Gas*, Physical Review Letters **107**(13) (2011).
- [Zü13] G. Zürn, T. Lompe, A. N. Wenz, S. Jochim, P. S. Julienne, J. M. Hutson, *Precise Characterization of Li_6 Feshbach Resonances Using Trap-Sideband-Resolved RF Spectroscopy of Weakly Bound Molecules*, Physical Review Letters **110**(13) (2013).
- [Zen32] C. Zener, *Non-Adiabatic Crossing of Energy Levels*, Proceedings of the Royal Society A: Mathematical, Physical and Engineering Sciences **137**(833), 696–702 (1932).
- [Zha12] Y. Zhang, W. Ong, I. Arakelyan, J. E. Thomas, *Polaron-to-Polaron Transitions in the Radio-Frequency Spectrum of a Quasi-Two-Dimensional Fermi Gas*, Physical Review Letters **108**(23) (2012).
- [Zwe03] W. Zwerger, *Mott-Hubbard transition of cold atoms in optical lattices*, Journal of Optics B: Quantum and Semiclassical Optics **5**, S9–S16 (2003).
- [Zwe16] W. Zwerger, *Strongly interacting Fermi gases*, Proceedings of the International School of Physics 'Enrico Fermi' **191**(Quantum Matter at Ultralow Temperatures), 63–141 (2016).
- [Zwi05] M. W. Zwierlein, J. R. Abo Shaeer, A. Schirotzek, C. H. Schunck, W. Ketterle, *Vortices and superfluidity in a strongly interacting Fermi gas*, Nature (London) **435**(7045), 1047–1051 (2005).
- [Zwi16] M. Zwierlein, *Thermodynamics of strongly interacting Fermi gases*, Proceedings of the International School of Physics 'Enrico Fermi' **191**(Quantum Matter at Ultralow Temperatures), 143–220 (2016).

Danksagung

An dieser Stelle bedanke ich mich bei allen die zum Gelingen dieser Arbeit beigetragen haben.

- Selim, für das Vertrauen und die Möglichkeit die Doktorarbeit in deiner tollen Gruppe auszuführen. Du hast mich stets unterstützt und in den Diskussionen mit Dir konnte ich viel lernen.
- Allen Mitgliedern der Gruppe Ultracold, den aktuellen rund um Andrea, Vincent, Puneet, Luca, Jan Hendrik, Ralf, Marvin, Philipp, Justin, Rodrigo, Thomas und Gerhard sowie den ehemaligen Andre, Martin, Simon, Thomas und Dhruv. Vom täglichen Kickern, den Pizza- und Feuerzangenbowle-abende bei Selim, dem Doktorhut bauen bis spät in die Nacht sowie der täglichen Arbeit im Labor herrschte stets eine ausgezeichnete Atmosphäre. Danke auch nochmals für das ausführliche Korrekturlesen der Arbeit.
- Prof. Markus Oberthaler für die freundliche Übernahme der Zweitkorrektur dieser Arbeit.
- Tilman Enss für Theoriediskussionen rund um 2D Gase.
- Prof. Peter Bachert und Prof. Joerg Jaeckel für die Bereitschaft Teil der Prüfungskommission zu sein.
- Der Gruppe von Prof. Matthias Weidemüller für die generelle Hilfe und Diskussionen rund um die Experimente, den gemeinsamen Weihnachtsfeiern sowie der freundlichen Ausleihe eines Lasers als unserer kaputt war. Er läuft immer noch stabil.
- Dominic Litsch, der als Beauftragter für Lasersicherheit immer ansprechbar war und uns in vielen Belangen geholfen hat.
- Frau Krämer die uns bei vielen bürokratischen Aufgaben Arbeit abgenommen hat.
- Der gesamten PI-Werkstatt, insbesondere Ralf Ziegler. Außerdem einen extra Dank an Esther Danzeisen, die uns tatkräftig beim Bau der neuen Feshbach-Spulen unterstützt hat als unsere alten den Geist aufgegeben hatten.
- Der EDV-Abteilung die den Umzug unseres Servers übernommen hat und immer erreichbar war.
- All meinen Freunden, die mir eine schöne Zeit in Heidelberg beschern und mich auf andere Gedanken bringen wenn es im Labor mal nicht so rund läuft.

- Nathalie, ohne dich hätte ich das nicht geschafft.